Heavy Flavor Decays of the Z^0 and a Search for Flavor Changing Neutral Currents*

Sean Eric Walston

Stanford Linear Accelerator Center
Stanford University
Stanford, CA 94309

SLAC-Report-728

*Ph.D. Thesis, University of Oregon, Eugene, OR.

HEAVY FLAVOR DECAYS OF THE Z^0 AND A SEARCH FOR

FLAVOR CHANGING NEUTRAL CURRENTS

by

SEAN ERIC WALSTON

A DISSERTATION

Presented to the Department of Physics
and the Graduate School of the University of Oregon
in partial fulfillment of the requirements
for the degree of
Doctor of Philosophy

June 2004

"Heavy Flavor Decays of the Z^0 and a Search for Flavor Changing Neutral Currents," a dissertation prepared by Sean Eric Walston in partial fulfillment of the requirements for the Doctor of Philosophy degree in the Department of Physics. This dissertation has been approved and accepted by:

_____

Dr. James E. Brau, Chair of the Examining Committee

_____

Date

Committee in charge: Dr. James E. Brau, Chair
                          Dr. Raymond E. Frey
                          Dr. Davison E. Soper
                          Dr. Robert L. Zimmerman
                          Dr. Michael E. Kellman

Accepted by:

_____

Dean of the Graduate School

An Abstract of the Dissertation of

Sean Eric Walston   for the degree of   Doctor of Philosophy

in the Department of Physics   to be taken   June 2004

Title: HEAVY FLAVOR DECAYS OF THE Z^0 AND A SEARCH FOR

FLAVOR CHANGING NEUTRAL CURRENTS

Approved: _____
Dr. James E. Brau

Presented here are the results of a direct search for flavor changing neutral currents via the rare process $Z^0 \rightarrow bs$ and a measurement of $R_{bs} = \frac{\Gamma(Z^0 \rightarrow bs)}{\Gamma(Z^0 \rightarrow \text{hadrons})}$. Because the decays $Z^0 \rightarrow b\bar{b}$ and $Z^0 \rightarrow c\bar{c}$ contribute significant backgrounds to $Z^0 \rightarrow bs$, simultaneous measurements of $R_b = \frac{\Gamma(Z^0 \rightarrow b\bar{b})}{\Gamma(Z^0 \rightarrow \text{hadrons})}$ and $R_c = \frac{\Gamma(Z^0 \rightarrow c\bar{c})}{\Gamma(Z^0 \rightarrow \text{hadrons})}$ were also made. The standard double tag technique was extended and self calibrating tags were used for s, c, and b quarks. These measurements were made possible by the unique capabilities of the SLAC Large Detector (SLD) at the Stanford Linear Accelerator Center (SLAC): The b and c tags relied upon the SLD's VXD3 307 megapixel CCD vertex detector for topological and kinematic reconstruction of the B and D decay vertices; the s tag identified $K^{\pm}$ mesons using the particle identification capabilities of SLD's Cherenkov Ring Imaging Detector (CRID), and K^0_S mesons and Λ hadrons by kinematic reconstruction of their decay vertices in SLD's 5120 channel central drift chamber (CDC) particle tracking system.

CURRICULUM VITA

NAME OF AUTHOR: Sean Eric Walston

PLACE OF BIRTH: Walnut Creek, California

DATE OF BIRTH: 10 January, 1971

GRADUATE AND UNDERGRADUATE SCHOOLS ATTENDED:

    University of Oregon
    University of New Mexico

DEGREES AWARDED:

    Doctor of Philosophy, 2004, University of Oregon
    Bachelor of Science, 1996, University of New Mexico

AREAS OF SPECIAL INTEREST:

    Electroweak physics
    Heavy flavor physics

PROFESSIONAL EXPERIENCE:

    Stanford Linear Accelerator Center, Stanford University, CA.
        SLD Collaboration, 1997 - present.

    University of Oregon, Eugene, OR.
        Graduate Teaching Fellow, 1996 - present.

    Los Alamos National Laboratory, Los Alamos, NM.
        Non-proliferation and International Security Division, NIS-1 Space and
        Atmospheric Sciences Group, summer 1994, summer 1995, and summer
        1996.
        Physics Division, P-3 Weak Interactions Group, 1993-1994.

PUBLICATIONS:

1. SLD Collaboration, K. Abe, et al. Heavy Flavor Decays of the Z^0 and a Search for Flavor Changing Neutral Currents. in preparation.

2. SLD Collaboration, K. Abe, et al. First measurement of the double-inclusive $B/\overline{B}$ hadron energy distribution in e^+e^- annihilations, and of angle-dependent correlations between the B and $\overline{B}$ energies. submitted to *Phys. Lett. B*, 2003, [SLAC-PUB-9966].

3. SLD Collaboration, K. Abe, et al. Search for time dependent B_S^0 - $\overline{B_s^0}$ oscillations using a vertex charge dipole technique. *Phys. Rev. D*, **67**:012006, 2003, [e-Print Archive: hep-ex/0209002, SLAC-PUB-9285].

4. SLD Collaboration, K. Abe, et al. Improved direct measurement of the parity violation parameter A_b using a mass tag and momentum weighted track charge. *Phys. Rev. Lett.*, **90**:141804, 2003, [e-Print Archive: hep-ex/0208044, SLAC-PUB-9188].

5. SLD Collaboration, K. Abe, et al. A search for time dependent B_s^0 - $\overline{B_s^0}$ oscillations using exclusively reconstructed $D_s^{\pm}$ mesons. *Phys. Rev. D*, **66**:032009, 2002, [e-Print Archive: hep-ex/0207048, SLAC-PUB-9286].

6. SLD Collaboration, K. Abe, et al. An improved study of the structure of $e^+e^- \to b\bar{b}g$ events and limits on the anomalous chromomagnetic coupling of the b quark. *Phys. Rev. D*, **66**:052001, 2002, [e-Print Archive: hep-ex/0205066, SLAC-PUB-9206].

7. SLD Collaboration, K. Abe, et al. Measurement of the b quark fragmentation function in Z^0 decays. *Phys. Rev. D*, **65**:092006, 2002, *Erratum-ibid. Phys. Rev. D*, **66**:079905, 2002, [e-Print Archive: hep-ex/0202031, SLAC-PUB-9087].

8. SLD Collaboration, K. Abe, et al. Improved direct measurement of A_b and A_c at the Z^0 pole using a lepton tag. *Phys. Rev. Lett.*, **88**:151801, 2002, [e-Print Archive: hep-ex/0111035, SLAC-PUB-8951].

9. SLD Collaboration, K. Abe, et al. Improved measurement of the probability for gluon splitting into $b\bar{b}$ in Z^0 decays. *Phys. Lett. B*, **507**:61-69, 2001, [e-Print Archive: hep-ex/0102002, SLAC-PUB-8737].

10. SLD Collaboration, K. Abe, et al. An improved direct measurement of leptonic coupling asymmetries with polarized Z bosons. *Phys. Rev. Lett.*, **86**:1162-1166, 2001, [e-Print Archive: hep-ex/0010015, SLAC-PUB-8618].

11. SLD Collaboration, K. Abe, et al. Measurement of A_c with charmed mesons at SLD. *Phys. Rev. D*, **63**:032005, 2001, [e-Print Archive: hep-ex/0009035, SLAC-PUB-8447].

12. SLD Collaboration, K. Abe, et al. First direct measurement of the parity violating coupling of the Z^0 to the s quark. *Phys. Rev. Lett.*, **85**:5059-5063, 2000, [e-Print Archive: hep-ex/0006019, SLAC-PUB-8408].

13. SLD Collaboration, K. Abe, et al. A high precision measurement of the left-right Z boson cross-section asymmetry. *Phys. Rev. Lett.*, **84**:5945-5949, 2000, [e-Print Archive: hep-ex/0004026, SLAC-PUB-8401].

14. SLD Collaboration, K. Abe, et al. Precise measurement of the b quark fragmentation function in Z^0 boson decays. *Phys. Rev. Lett.*, **84**:4300-4304, 2000, [e-Print Archive: hep-ex/9912058, SLAC-PUB-8316].

15. SLD Collaboration, K. Abe, et al. Search for charmless hadronic decays of B mesons with the SLD detector. *Phys. Rev. D*, **62**:071101, 2000, [e-Print Archive: hep-ex/9910050, SLAC-PUB-8280].

16. SLD Collaboration, K. Abe, et al. Direct measurement of the neutral weak dipole moments of the tau lepton. submitted to *Phys. Rev. Lett.*, [SLAC-PUB-8163].

17. SLD Collaboration, K. Abe, et al. Direct measurement of A_b in Z^0 decays using charged kaon tagging. *Phys. Rev. Lett.*, **83**:1902-1907, 1999, [SLAC-PUB-7959].

18. SLD Collaboration, K. Abe, et al. Direct measurement of A_b and A_c at the Z^0 pole using a lepton tag. *Phys. Rev. Lett.*, **83**:3384-3389, 1999, [SLAC-PUB-7798].

19. SLD Collaboration, K. Abe, et al. First study of the structure of $e^+e^- \rightarrow b\bar{b}g$ events and limits on the anomalous chromomagnetic coupling of the b quark. *Phys. Rev. D*, **60**:092002, 1999, [e-Print Archive: hep-ex/9903004, SLAC-PUB-7920].

ACKNOWLEDGEMENTS

I owe special thanks to my advisor Jim Brau for supporting me all of these years and allowing me to work on so many interesting projects. Working with the Oregon group has indeed been a privilege. I would like to thank Tracy Usher for allowing me to apprentice with him on tuning backgrounds at SLC – I really do have fond memories of all those long hours spent at the SLAC Main Control Room. And I would also like to thank Hermann Stängle and especially Dong Su whose massive amounts of assistance over the years were absolutely essential for completing this dissertation.

Thanks also to all of the SLD students and postdocs I had the privilege of getting know and work with: Hidemi Akimoto, Giulia Bellodi, Aaron Chou, Danning Dong, Dave Jackson, Hyejoo Kang, Matt Langston, Vincenzo Lia, Cheng-Ju Lin, Thomas Moore, Gavin Nesom, PerReinertsen, Hermann Stängle, Julia Thom, Jodi Wittlin, and Tom Wright. I could not have asked for a nicer group of colleagues.

I also wish to thank my colleagues at the University of Oregon for their friend-ship: David Caley, Dave Mason, Amy McGrew, Rauha Rahkola, Brian Stubbs, and Paula White. All the discussions over lunch, coffee at Starbucks, and Burger and Brew at the Sixth Street Grill were enormously enjoyable.

Most of all, I would like to thank my very good friend George Nickel for sustaining my interest in physics – especially during those times when the going got tough, and especially my father Bob Walston for stimulating my interest in physics in the first place with all those wonderful discussions over pie and coffee.

These two amazing men are my source of inspiration and I shall always endeavor to emulate their incredible spirit of inquiry.

DEDICATION

To Pa.

TABLE OF CONTENTS

LIST OF FIGURES

Page

Page

LIST OF TABLES

Page

CHAPTER I

INTRODUCTION

"All these things being considered, it seems probable to me that God in the beginning formed matter in solid, massy, hard, impenetrable, moveable particles of such sizes and figures, and with such other properties, and in such proportion to space, as most conduced to the end for which he formed them; and that these primitive particles being solids, are incomparably harder than any porous bodies compounded of them; even so very hard, as never to wear or break in pieces; no ordinary power being able to divide what God himself made in the first creation....

"It seems to me farther, that those particles have not only a force of inertia accompanied with such passive laws of motion as naturally result from that force, but also that they are moved by certain active principles, such as is that of gravity..."

Sir Isaac Newton, as the quote above from *Optics* (1730) indicates, understood that a central goal of physics was to discover the most fundamental bits of matter and comprehend the nature of the forces acting between them. This dis-

sertation presents three modern measurements of the nature of one of the known fundamental forces – the electroweak force.

Up until the 1930s, all natural phenomena appeared to have their origins within two fundamental forces – gravitation and electromagnetism. Both forces were described by classical fields that permeated all of space and extended to infinity from well defined sources – mass in the case of gravitation, and electric charge in the case of electromagnetism. But as people started looking more closely at atomic and subatomic phenomena, it became clear that two new forces were needed: The "strong force" was introduced to describe how the nucleus of the atom stayed together despite the electromagnetic repulsion of its constituents, and the "weak force" was introduced to explain how the neutron could morph into a proton during a particular form of radioactive decay known as beta decay.

The four forces have radically different relative strengths, and are manifestly different in character; for example two forces – gravity and electromagnetism – extend to infinity, while the two nuclear forces have very short ranges. But despite these differences, there has long been a latent hope that all four fundamental forces are manifestations of a single interaction or principle, described by a single unified theory. This hope is not without precedent: Recall that the apparently different electric and magnetic forces were unified by James Clerk Maxwell in 1865 [1] into electromagnetism; There was the fleeting success of Theodor Kaluza's theory – first proposed in 1919 [2] – to unify classical electromagnetism with gravitation in the form of a vacuum solution to Einstein's general theory of relativity written in five dimensions instead of the orthodox four; and the most recent example was the

unification of the weak with the electromagnetic interactions into the electroweak interaction achieved by the Standard Model.

At the present moment in history, 12 matter particles have been identified which interact through the agencies of these four fundamental forces. Gravitation has proven the most difficult of these to understand, and no one has yet written down a consistent quantum field theory for gravity. By comparison, much more progress has been made in understanding the strong, electromagnetic, and weak interactions.

Particle accelerators have played a critical role throughout this progress. The proton accelerator E. O. Lawrence and graduate student M. S. Livingston successfully demonstrated in January of 1931 was later improved on independently by E. McMillan and V. Veksler by varying the frequency of the RF fields used to accelerate the protons. In a synchrotron, the protons must be confined to a narrow range of orbits which requires large magnetic fields, and in 1953 at Brookhaven, a group of accelerator physicists invented the principle of "strong focusing" which allowed much smaller magnets to be used to confine the protons to the required orbits. Successive generations of proton accelerators achieved higher and higher energies, from the AGS (Alternating Gradient Syncrotron) to the accelerator at Fermilab to the CERN (originally Centre Européenne pour la Recherche Nucléaire, now Organisation Européenne pour la Recherche Nucléaire) SPS (Super Proton Synchrotron) [3].

Meanwhile, electron accelerators – which had their origins in the cathode ray tubes of the nineteenth century – saw similar progress and achieved successively higher energies with each generation, very much in parallel with their proton-

accelerating counterparts. Many electron accelerators used a linear configuration in order to avoid the problem of energy losses due to synchrotron radiation, which is a much more serious problem for lightweight electrons than for relatively heavy protons. The development of electron accelerators culminated with the two mile long linear accelerator (linac) at SLAC (Stanford Linear Accelerator Center) and the 27 km circumference LEP (Large Electron Positron) ring at CERN.

Continuing this historical trend, the LHC (Large Hadron Collider), now under construction at CERN, and the LC (Linear Collider), presently on the drawing boards at laboratories and universities around the world, respectively represent the next logical steps in proton and electron collider developments. Proton and electron colliders naturally complement one another because, while higher energies can generally be achieved with a proton collider, thus leading to discoveries of new particles, the precisely known properties of electron-positron collisions provide an optimum environment for precision measurements [4].

This was the case with the Z^0 boson of the electroweak interaction, its discovery having been made at a proton collider – the CERN SPS – leaving precision measurements to be carried out at e^+e^- colliders – namely the SLC (SLAC Linear Collider) and LEP at CERN. Such precision measurements of the Z^0 resonance are important to constrain the Standard Model and also to point the way to alternative theories which attempt to go beyond the Standard Model. To this end, data taking with e^+e^- colliders running on the Z^0 resonance began in 1989 at both the LEP ring and the SLC.

The present analysis includes two such precision tests, the $Z^0 \rightarrow b\bar{b}$ and $Z^0 \rightarrow c\bar{c}$ couplings, R_b and R_c. Measurement of R_b by itself provides an excellent

test of the electroweak portion of the Standard Model. The $Z^0 \to b\bar{b}$ coupling, in contrast to the couplings associated with other flavor quarks, includes relatively significant radiative corrections from the large top quark mass due to the relevant term in the quark mixing matrix, $|V_{tb}|$, being ≈ 1. The $Z^0 \to c\bar{c}$ coupling is likewise a valuable test of the electroweak portion of the Standard Model.

However, the original objective of this analysis was to make a direct search for one of a group of rare processes within the Standard Model known as flavor changing neutral currents (FCNC). In general, FCNC are decays of a Z^0 into a quark and an antiquark (or a lepton and antilepton for that matter) of differing flavors. In the search for the process $Z^0 \to bs$, by which we mean the sum of the two charge-conjugate final states $b\bar{s}$ and $\bar{b}s$, the processes $Z^0 \to b\bar{b}$ and $Z^0 \to c\bar{c}$ are both important backgrounds – hence measurements of the $Z^0 \to b\bar{b}$ and $Z^0 \to c\bar{c}$ couplings are needed.

Chapter II begins with a detailed review of the theory of electroweak interactions in the Standard Model by deriving the electroweak Lagrangian. The CKM (Cabbibo Kobayashi Maskawa) quark mixing matrix and its origins are also discussed in detail. Standard Model predictions for R_b and R_c are examined, and the calculation of R_{bs} in the Standard Model is reviewed and updated.

Chapters III and IV provide details of the SLD and SLC, respectively. Chapter IV also includes a discussion of the issues associated with beam induced backgrounds in the SLD detector resulting from its operating in the linear collider environment – something this author got involved in during the latter half of the 1997-98 run.

Chapter V provides a primer on detector triggering and other important aspects necessary for initial event characterization.

Chapter VI gives the overall method of the analysis whereby R_b, R_c, and R_{bs} are extracted simultaneously using self-calibrating quark tags.

Chapter VII and chapter VIII examine the methods used for tagging heavy-flavor bottom and charm quarks, and strange quarks, respectively.

Chapter IX contains the results of the analysis and a discussion of all the statistical and systematic uncertainties associated with each of the three measurements.

CHAPTER II

THEORETICAL

FOUNDATIONS

The Standard Model of electroweak and strong interactions consists of a relativistically invariant quantum field theory with two distinct interactions – the strong and the electroweak interactions – and incorporates all the known phenomenology of these fundamental interactions. It describes spinless, spin-1/2, and spin-1 fields interacting with one another in a manner determined by the Lagrangian. Although quite complex in the details, the Lagrangian for the Standard Model is based on two basic ideas beyond those necessary for any quantum field theory: The concept of a local symmetry, and the concept of spontaneous symmetry breaking. The local symmetry determines the form of the interactions between fields that carry the charges associated with the symmetry (not necessarily the electric charge), and the interaction is mediated by spin-1 "gauge" particles called vector bosons. Spontaneous symmetry breaking posits that the vacuum itself has a nonzero charge distribution (again, not necessarily the electric charge) which gives rise to the masses of the particles in the theory [5].

The electroweak portion of the Standard Model is based on the local gauge group $SU(2)_L \times U(1)$, with resulting gauge bosons W_μ^i and B_μ for the $SU(2)_L$ and $U(1)$ factors respectively. This is a theory with a very long Lagrangian with many

fields, and has the terms

$$\mathcal{L}_{\text{electroweak}} = \mathcal{L}_{\text{K-G}} + \mathcal{L}_{\text{Y-M}} + \mathcal{L}_{\text{Dirac}} + \mathcal{L}_{\text{Yukawa}} \tag{2.1}$$

where $\mathcal{L}_{\text{K-G}}$ describes spinless Klein-Gordon scalar fields, $\mathcal{L}_{\text{Y-M}}$ is the Yang-Mills kinetic energy term for the spin-1 vector gauge fields, $\mathcal{L}_{\text{Dirac}}$ describes spin-1/2 Dirac spinor fields, and $\mathcal{L}_{\text{Yukawa}}$ describes the Yukawa interaction between the spinor and scalar fields. The motivations behind this construction will become clear in due course. The following sections deal with each of the terms in turn.

2.1 Local Gauge Invariance of a Klein-Gordon Field

Consider the Lagrangian for a complex self-interacting Klein-Gordon field,

$$\mathcal{L}_{\text{K-G}} = \partial^\mu \phi^\dagger \partial_\mu \phi - m^2 \phi^\dagger \phi - \lambda (\phi^\dagger \phi)^2. \tag{2.2}$$

The local gauge transformation which represents the $SU(2)_L \times U(1)$ gauge symmetries is defined by

$$\phi' = e^{i\left[\frac{Y^W}{2}\Lambda(x) + I_a^W \Lambda_a(x)\right]} \phi \tag{2.3}$$

where the weak hypercharge, Y^W (numerically 1 for ϕ and -1 for $\phi^\dagger$), is the generator of the $U(1)$ gauge symmetry, and the weak isospin, I_a^W, is the generator of the $SU(2)_L$ gauge symmetry. The matrices I_a^W turn out to be the Pauli spin matrices times the factor one half, $\sigma_a/2$.

The potential terms, $m^2\phi^\dagger\phi + \lambda(\phi^\dagger\phi)^2$, in equation 2.2 are already symmetric under the local gauge transformation defined in equation 2.3, but in order to eliminate any $\Lambda(x)$ and $\Lambda_a(x)$ dependence in the kinetic term, $\partial^\mu\phi^\dagger\partial_\mu\phi$, the gauge fields B_μ for $U(1)$ and $W_{a\mu}$ for $SU(2)_L$ must be added by generalizing the derivative, ∂_μ, to the gauge covariant derivative,

$$D_\mu \;=\; \partial_\mu - ig'\frac{Y^W}{2}IB_\mu - igI_a^W W_{a\mu} \tag{2.4}$$

such that $D_\mu\phi$ transforms as an $SU(2)$ doublet under the local gauge transformation, i.e.

$$(D_\mu\phi)' \;=\; e^{i\left[\frac{Y^W}{2}\Lambda(x)+I_a^W\Lambda_a(x)\right]}(D_\mu\phi). \tag{2.5}$$

Simply replacing $\partial_\mu\phi$ by $D_\mu\phi$ produces field equations for B_μ and $W_{a\mu}$ which contain no space-time derivatives, meaning that B_μ and $W_{a\mu}$ do not propagate. To rectify this oversight, locally gauge invariant kinetic terms for B_μ and $W_{a\mu}$ must be added to the Lagrangian of equation 2.2. The trick is to define a field tensor which is invariant under the local gauge transformation of equation 2.3, such that $F_{\mu\nu}$ transforms as

$$F'_{\mu\nu} = F_{\mu\nu}. \tag{2.6}$$

It turns out that the combination of covariant derivatives $D_\mu D_\nu - D_\nu D_\mu = [D_\mu, D_\nu]$, when acting on any function, contains no derivatives of the function. Thus $F_{\mu\nu} \propto [D_\mu, D_\nu]$ is a good choice. The invariant field strength tensor for the $U(1)$ gauge

field B_μ is

$$F_{\mu\nu} \;\; = \;\; \partial_\mu B_\nu - \partial_\nu B_\mu. \tag{2.7}$$

The correct invariant field strength tensor for the $SU(2)_L$ gauge field $W_{a\mu}$ is analogously

$$G_{a\mu\nu} \;\; = \;\; \partial_\mu W_{a\nu} - \partial_\nu W_{a\mu} + g\epsilon_{abc} W_{b\mu} W_{c\nu}. \tag{2.8}$$

An appropriate kinetic energy term for a gauge field is one which is quadratic in the derivatives of the field. Thus it is trivial to write down a term which is quadratic in derivatives of B_μ and $W_{a\mu}$ resulting in the Yang-Mills kinetic energy term [5]

$$\mathcal{L}_{\text{Y-M}} \;\; = \;\; -\frac{1}{4} F^{\mu\nu} F_{\mu\nu} - \frac{1}{4} G_a^{\mu\nu} G_{a\mu\nu}. \tag{2.9}$$

The locally gauge invariant Lagrangian for the scalar fields becomes

$$\mathcal{L}_{\text{K-G}} \;\; = \;\; (D^\mu\phi)^\dagger D_\mu\phi - m^2\phi^\dagger\phi - \lambda(\phi^\dagger\phi)^2. \tag{2.10}$$

Since we desire to end up with one massless and three massive vector bosons, we require $1 + 3 = 4$ independent scalar fields. The simplest choice is a doublet of complex scalar fields,

$$\phi \;\; = \;\; \begin{pmatrix} \frac{\phi_3 + i\phi_4}{\sqrt{2}} \\[2mm] \frac{\phi_1 + i\phi_2}{\sqrt{2}} \end{pmatrix} \tag{2.11}$$

$$\phi^\dagger \;\; = \;\; \begin{pmatrix} \frac{\phi_3 - i\phi_4}{\sqrt{2}} & \frac{\phi_1 - i\phi_2}{\sqrt{2}} \end{pmatrix} \tag{2.12}$$

where the fields ϕ_1, ϕ_2, ϕ_3, and ϕ_4 are all real. Note also that

$$\phi^\dagger \phi \;=\; \frac{1}{2}(\phi_1^2 + \phi_2^2 + \phi_3^2 + \phi_4^2). \tag{2.13}$$

The energy density of the field is the Hamiltonian,

$$\mathcal{H} \;=\; \pi^\dagger \pi + \nabla \phi^\dagger \nabla \phi + m^2 \phi^\dagger \phi + \lambda (\phi^\dagger \phi)^2 \tag{2.14}$$

with $\lambda > 0$ and where $\pi = \dot{\phi}$. Note that $\pi^\dagger \pi + \nabla \phi^\dagger \nabla \phi$ is nonnegative, and is zero if $\phi^\dagger$ or ϕ is constant. $\mathcal{H}$ is zero for $\phi^\dagger$ or $\phi = 0$, but if $m^2 < 0$, there are nonzero values of $\phi^\dagger \phi$ for which $\mathcal{H} < 0$. The minimum energy will therefore have a nonzero field configuration. $\mathcal{H}$ will have a minimum when both potential and kinetic energies are at their lowest values [5]. Thus, the vacuum solution is found by considering

$$\delta \mathcal{H} \;=\; 0 \tag{2.15}$$

$$\delta \left[m^2 \phi^\dagger \phi + \lambda (\phi^\dagger \phi)^2 \right] \;=\; 0 \tag{2.16}$$

$$m^2 \delta \phi^\dagger \phi + m^2 \phi^\dagger \delta \phi + 2\lambda \phi^\dagger \phi (\delta \phi^\dagger \phi + \phi^\dagger \delta \phi) \;=\; 0. \tag{2.17}$$

The $\delta \phi^\dagger$ and $\delta \phi$ are independent, but what really matters is that the coefficients on both be zero (and because $\mathcal{H}$ is symmetrical in $\phi^\dagger$ and ϕ, the coefficients are the same):

$$m^2 + 2\lambda (\phi^\dagger \phi)_{vacuum} \;=\; 0 \tag{2.18}$$

$$2\lambda (\phi^\dagger \phi)_{vacuum} \;=\; -m^2 \tag{2.19}$$

$$(\phi^\dagger\phi)_{vacuum} = -\frac{m^2}{2\lambda} \tag{2.20}$$

$$(\phi^\dagger\phi)_{vacuum} = \frac{1}{2}|\phi_V|^2. \tag{2.21}$$

Note that ϕ_V is not completely specified; it may lie at any point on the circle in complex field space corresponding to the minimum of the potential [5].

Suppose ϕ_V is real and given by

$$\phi_V = \sqrt{-\frac{m^2}{\lambda}}. \tag{2.22}$$

We can choose to have

$$\phi_{1_{vacuum}} = \frac{\phi_V}{\sqrt{2}}$$

$$\phi_{2_{vacuum}} = 0$$

$$\phi_{3_{vacuum}} = 0$$

$$\phi_{4_{vacuum}} = 0$$

$$\tag{2.23}$$

with the result that

$$\phi_{vacuum} = \begin{pmatrix} 0 \\ \frac{\phi_V}{\sqrt{2}} \end{pmatrix} \tag{2.24}$$

$$\phi^\dagger_{vacuum} = \begin{pmatrix} 0 & \frac{\phi_V}{\sqrt{2}} \end{pmatrix} \tag{2.25}$$

$$(\phi^\dagger\phi)_{vacuum} = \frac{1}{2}\phi_V^2. \tag{2.26}$$

The scalar fields require a representation such that the field with a nonzero vacuum value is electrically neutral to ensure that the photon A_μ remains massless. At the same time this field must carry nonzero values of I_3^W and Y^W so that Z_μ^0 acquires a mass from spontaneous symmetry breaking. The simplest assignment is [5]

$$\phi = \begin{pmatrix} \phi^+ \\ \phi^0 \end{pmatrix} \tag{2.27}$$

$$\phi^\dagger = \begin{pmatrix} -\phi^- & \phi^{0\dagger} \end{pmatrix}. \tag{2.28}$$

By being clever, it is possible to avoid an inordinate amount of computation, and in this case being clever means taking full advantage of the $SU(2)_L$ gauge symmetry. First we write the four degrees of freedom in ϕ so that it looks like the product of a local symmetry transformation and a simpler version of ϕ:

$$\phi = \begin{pmatrix} \phi^+ \\ \phi^0 \end{pmatrix} = e^{\frac{i\pi_a(x)I_a^W}{\phi_V}} \begin{pmatrix} 0 \\ \frac{H(x)+\phi_V}{\sqrt{2}} \end{pmatrix}. \tag{2.29}$$

This amounts to an isospin rotation at each point in space. We have stuffed three of the four degrees of freedom of the original complex scalar doublet into the three fields $\pi_a(x)$. We are, in effect, choosing a gauge by making an operator gauge transformation using $\pi_a(x)$. The field $H(x)$, the fourth degree of freedom, is the Higgs field. Because of local gauge invariance, we can then write ϕ in a very simple form with the phases removed [5]:

$$\phi_{new}(x) = e^{-\frac{i\pi_a(x)I_a^W}{\phi_V}} \phi(x) \tag{2.30}$$

$$\phi_{new}(x) \;=\; \begin{pmatrix} 0 \\ \frac{H(x)+\phi_V}{\sqrt{2}} \end{pmatrix}. \tag{2.31}$$

This choice, called the unitary gauge [5], will make it easy to write out $D_\mu\phi$ in explicit matrix form. Let us thus drop all the "*new*" subscripts on the fields in the unitary gauge.

$$
\begin{aligned}
D_\mu\phi &= \left(\partial_\mu - ig'\frac{Y^W}{2}IB_\mu - igI_a^W W_{a\mu} \right)\phi \\[2mm]
&= \left[\partial_\mu - ig'\frac{Y^W}{2}\begin{pmatrix} B_\mu & 0 \\ 0 & B_\mu \end{pmatrix} \right. \\[2mm]
&\quad \left. -ig\frac{1}{2}\begin{pmatrix} W_{3\mu} & W_{1\mu}-iW_{2\mu} \\ W_{1\mu}+iW_{2\mu} & -W_{3\mu} \end{pmatrix} \right]\begin{pmatrix} 0 \\ \frac{H(x)+\phi_V}{\sqrt{2}} \end{pmatrix} \\[2mm]
&= \left[\partial_\mu - i\begin{pmatrix} g'\frac{Y^W}{2}B_\mu + g\frac{1}{2}W_{3\mu} & g\frac{1}{2}(W_{1\mu}-iW_{2\mu}) \\ g\frac{1}{2}(W_{1\mu}+iW_{2\mu}) & g'\frac{Y^W}{2}B_\mu - g\frac{1}{2}W_{3\mu} \end{pmatrix} \right]\begin{pmatrix} 0 \\ \frac{H(x)+\phi_V}{\sqrt{2}} \end{pmatrix} \\[2mm]
&= \begin{pmatrix} -\frac{1}{2\sqrt{2}}ig\,(W_{1\mu}-iW_{2\mu})\,(H+\phi_V) \\ \frac{1}{\sqrt{2}}\partial_\mu H - \frac{1}{2\sqrt{2}}i\left(g'Y^W B_\mu - gW_{3\mu}\right)(H+\phi_V) \end{pmatrix}.
\end{aligned} \tag{2.32}
$$

Substituting $\phi(x)$ and $D_\mu\phi$ from equations 2.31 and 2.32 into $\mathcal{L}_{\text{K-G}}$ of equation 2.2, we have

$$
\begin{aligned}
\mathcal{L}_{\text{K-G}} &= \frac{g^2}{8}\left(W_1^\mu + iW_2^\mu\right)\left(W_{1\mu}-iW_{2\mu}\right)(H+\phi_V)^2 + \frac{1}{2}\partial^\mu H \partial_\mu H \\[2mm]
&\quad + \frac{1}{8}\left(g'Y^W B^\mu - gW_3^\mu\right)\left(g'Y^W B_\mu - gW_{3\mu}\right)(H+\phi_V)^2 \\[2mm]
&\quad - \frac{m^2}{2}(H+\phi_V)^2 - \frac{\lambda}{4}(H+\phi_V)^4
\end{aligned} \tag{2.33}
$$

Terms quadratic in the fields are mass terms. After a simple rearrangement of equation 2.33, we can begin to easily see the mass terms.

$$
\begin{aligned}
\mathcal{L}_{\text{K-G}} &= \frac{1}{2}\partial^\mu H \partial_\mu H + \frac{g^2 \phi_V^2}{8}\left(W_1^\mu + iW_2^\mu\right)\left(W_{1\mu} - iW_{2\mu}\right) \\
&\quad + \frac{\phi_V^2}{8}\left(g'Y^W B^\mu - gW_3^\mu\right)\left(g'Y^W B_\mu - gW_{3\mu}\right) \\
&\quad + \frac{g^2}{8}\left(W_1^2 + W_2^2\right)H^2 + \frac{1}{8}\left(g'Y^W B^\mu - gW_3^\mu\right)\left(g'Y^W B_\mu - gW_{3\mu}\right)H^2 \\
&\quad + \frac{g^2 \phi_V}{4}\left(W_1^2 + W_2^2\right)H + \frac{\phi_V}{4}\left(g'Y^W B^\mu - gW_3^\mu\right)\left(g'Y^W B_\mu - gW_{3\mu}\right)H \\
&\quad - \frac{\lambda}{4}H^4 - \lambda\phi_V H^3 - \frac{1}{2}\left(m^2 + 3\lambda\phi_V^2\right)H^2 \\
&\quad - (m^2 \phi_V + \lambda\phi_V^3)H - \frac{m^2 \phi_V^2}{2} - \frac{\lambda\phi_V^4}{4}
\end{aligned}
\tag{2.34}
$$

If we define

$$
\left(W_1^\mu + iW_2^\mu\right) = \sqrt{2}W^{-\mu} \tag{2.35}
$$

$$
\left(W_{1\mu} - iW_{2\mu}\right) = \sqrt{2}W_\mu^+ \tag{2.36}
$$

then the term

$$
\begin{aligned}
\frac{g^2 \phi_V^2}{8}\left(W_1^\mu + iW_2^\mu\right)\left(W_{1\mu} - iW_{2\mu}\right) &= \frac{g^2 \phi_V^2}{4}W^{-\mu}W_\mu^+ \\
&= M_W^2 W^{-\mu}W_\mu^+ \tag{2.37}
\end{aligned}
$$

and is quadratic in the $W^\pm$ fields, and they will acquire a mass of

$$
M_W = \frac{g\phi_V}{2}. \tag{2.38}
$$

The combination $\left(g'Y^W B_\mu - gW_{3\mu}\right)$ will also have mass. It can be rewritten as

$$
\begin{aligned}
\left(g'Y^W B_\mu - gW_{3\mu}\right) &= \sqrt{(g'Y^W)^2 + g^2} \\
&\times \left(\frac{g'Y^W}{\sqrt{(g'Y^W)^2 + g^2}} B_\mu - \frac{g}{\sqrt{(g'Y^W)^2 + g^2}} W_{3\mu} \right).
\end{aligned}
\tag{2.39}
$$

It is convenient to define the following:

$$
\sin\theta_W = \frac{g'Y^W}{\sqrt{(g'Y^W)^2 + g^2}} \tag{2.40}
$$

$$
\cos\theta_W = \frac{g}{\sqrt{(g'Y^W)^2 + g^2}} \tag{2.41}
$$

with the consequence that

$$
\frac{g'Y^W}{\sqrt{(g'Y^W)^2 + g^2}} B_\mu - \frac{g}{\sqrt{(g'Y^W)^2 + g^2}} W_{3\mu} = \sin\theta_W B_\mu - \cos\theta_W W_{3\mu}.
\tag{2.42}
$$

We now define

$$
Z^0_\mu = \sin\theta_W B_\mu - \cos\theta_W W_{3\mu} \tag{2.43}
$$

$$
A_\mu = \cos\theta_W B_\mu + \sin\theta_W W_{3\mu}. \tag{2.44}
$$

Thus we "rotate" [5] B_μ and $W_{3\mu}$ into the physical fields Z^0_μ and A_μ with the result that only the Z^0 gains mass. Mass terms for neutral fields are written with an additional factor of $\frac{1}{2}$ (so that when you take the derivative, the factor of two which

results from the square of the field cancels with the factor of one half),

$$
\begin{aligned}
\frac{\phi_V^2}{8}\left(g'Y^W B^\mu - gW_3^\mu\right)\left(g'Y^W B_\mu - gW_{3\mu}\right) &= \frac{[(g'Y^W)^2 + g^2]\phi_V^2}{8}Z^{0\mu}Z_\mu^0 \\
&= \frac{1}{2}\frac{[(g'Y^W)^2 + g^2]\phi_V^2}{4}Z^{0\mu}Z_\mu^0 \\
&= \frac{M_Z^2}{2}Z^{0\mu}Z_\mu^0
\end{aligned}
\tag{2.45}
$$

with

$$
M_Z = \frac{\sqrt{(g'Y^W)^2 + g^2}\,\phi_V}{2}
\tag{2.46}
$$

and the interesting result that

$$
\frac{M_W}{M_Z} = \frac{g\phi_V}{2}\frac{2}{\sqrt{(g'Y^W)^2 + g^2}\,\phi_V} = \frac{g}{\sqrt{(g'Y^W)^2 + g^2}} = \cos\theta_W.
\tag{2.47}
$$

Finally, the Lagrangian from equation 2.34 can be written

$$
\begin{aligned}
\mathcal{L}_{\text{K-G}} &= \frac{1}{2}\partial^\mu H\partial_\mu H + M_W^2 W^{-\mu}W_\mu^+ + \frac{M_Z^2}{2}Z^{0\mu}Z_\mu^0 - \frac{1}{2}\left(m^2 + 3\lambda\phi_V^2\right)H^2 \\
&\quad + \frac{g^2}{4}W^{-\mu}W_\mu^+ H^2 + \frac{(g'Y^W)^2 + g^2}{8}Z^{0\mu}Z_\mu^0 H^2 \\
&\quad + gM_W W^{-\mu}W_\mu^+ H + \frac{\sqrt{(g'Y^W)^2 + g^2}\,M_Z}{2}Z^{0\mu}Z_\mu^0 H \\
&\quad - \frac{\lambda}{4}H^4 - \lambda\phi_V H^3 - (m^2\phi_V + \lambda\phi_V^3)H - \frac{m^2\phi_V^2}{2} - \frac{\lambda\phi_V^4}{4}.
\end{aligned}
\tag{2.48}
$$

2.2 Local Gauge Invariance of a Dirac Field

Now consider the Lagrangian for a massless free Dirac field

$$\mathcal{L}_{\text{Dirac}} = \overline{\psi} i \gamma^{\mu} \partial_{\mu} \psi. \tag{2.49}$$

Because right-handed fields have zero weak isospin, i.e. they are isospin singlets, right- and left-handed fields behave differently. It will therefore be uesful to consider separately the left- and right-handed components of the Dirac field in order to derive the electroweak model in terms of the physical fields. To that end, the following relations will prove helpful:

$$\psi = \psi_L + \psi_R = \left(\frac{1 - \gamma^5}{2} \right) \psi + \left(\frac{1 + \gamma^5}{2} \right) \psi, \tag{2.50}$$

where

$$\psi_L = \left(\frac{1 - \gamma^5}{2} \right) \psi \tag{2.51}$$

$$\psi_R = \left(\frac{1 + \gamma^5}{2} \right) \psi \tag{2.52}$$

and for the antiparticles

$$\overline{\psi} = \overline{\psi}_R + \overline{\psi}_L = \overline{\psi} \left(\frac{1 + \gamma^5}{2} \right) + \overline{\psi} \left(\frac{1 - \gamma^5}{2} \right) \tag{2.53}$$

where

$$\overline{\psi}_R = \overline{\psi} \left(\frac{1 + \gamma^5}{2} \right) \tag{2.54}$$

$$\overline{\psi}_L \;\; = \;\; \overline{\psi}\left(\frac{1-\gamma^5}{2}\right). \tag{2.55}$$

The "L" and "R" on ψ_L and ψ_R refer to the handedness, a Lorentz invariant quantity which is related in a nontrivial way to the helicity, the projection of the spin s along the momentum p [6]. The corresponding anti-particle for a left-handed particle, for example, is right-handed; and vice-versa. Another way to put it is that $\overline{\psi}_R$ is the conjugate of ψ_L, i.e.

$$\overline{\psi}_R \;\; = \;\; (\psi_L)^\dagger \gamma^0. \tag{2.56}$$

We again generalize the derivative, ∂_μ, to the gauge covariant derivative, but this time separately for left- and right-handed fields since they are each invariant under different gauge symmetries: The left-handed fields are invariant under $SU(2)_L \times U(1)$ while the right-handed fields are only invariant under $U(1)$. Thus ∂_μ becomes D_μ for the left- and right-handed fields respectively,

$$D_\mu^{SU(2)\times U(1)} \;\; = \;\; \partial_\mu - ig'\frac{Y^W}{2}IB_\mu - igI_a^W W_{a\mu} \tag{2.57}$$

$$D_\mu^{U(1)} \;\; = \;\; \partial_\mu - ig'\frac{Y^W}{2}IB_\mu. \tag{2.58}$$

A fully phase invariant generalization of equation 2.49 is then

$$\begin{aligned}
\mathcal{L}_{\text{Dirac}} \;\; = \;\; & \overline{\psi}_L i\gamma^\mu \left(\partial_\mu - ig'\frac{Y^W}{2}IB_\mu\right)\psi_R \\
& +\overline{\psi}_R i\gamma^\mu \left(\partial_\mu - ig'\frac{Y^W}{2}IB_\mu - igI_a^W W_{a\mu}\right)\psi_L.
\end{aligned} \tag{2.59}$$

Equation 2.59 can be rewritten explicitly in matrix form:

$$
\begin{aligned}
\mathcal{L}_{\text{Dirac}} &= \overline{\psi}_L i\gamma^\mu \left(\partial_\mu - ig'\frac{Y^W}{2}B_\mu\right)\psi_R + \overline{\psi}_R i\gamma^\mu \left[\partial_\mu - ig'\frac{Y^W}{2}\begin{pmatrix} B_\mu & 0 \\ 0 & B_\mu \end{pmatrix}\right.\\
&\quad \left. -ig\frac{1}{2}\begin{pmatrix} W_{3\mu} & W_{1\mu} - iW_{2\mu} \\ W_{1\mu} + iW_{2\mu} & -W_{3\mu} \end{pmatrix}\right]\psi_L \\
&= \overline{\psi}_L i\gamma^\mu \left(\partial_\mu - ig'\frac{Y^W}{2}B_\mu\right)\psi_R \\
&\quad + \overline{\psi}_R i\gamma^\mu \left[\partial_\mu - i\begin{pmatrix} g'\frac{Y^W}{2}B_\mu + g\frac{1}{2}W_{3\mu} & g\frac{1}{2}(W_{1\mu} - iW_{2\mu}) \\ g\frac{1}{2}(W_{1\mu} + iW_{2\mu}) & g'\frac{Y^W}{2}B_\mu - g\frac{1}{2}W_{3\mu} \end{pmatrix}\right]\psi_L.
\end{aligned}
$$

$$(2.60)$$

The definitions for Z_μ^0 and A_μ from equations 2.43 and 2.44 yield reciprocal definitions for B_μ and $W_{3\mu}$,

$$
\begin{aligned}
B_\mu &= \cos\theta_W A_\mu + \sin\theta_W Z_\mu^0 & (2.61) \\
W_{3\mu} &= \sin\theta_W A_\mu - \cos\theta_W Z_\mu^0; & (2.62)
\end{aligned}
$$

the relations

$$
\begin{aligned}
g'\cos\theta_W &= g\sin\theta_W = e & (2.63) \\
g'\sin\theta_W &= \frac{g\sin^2\theta_W}{\cos\theta_W}; & (2.64)
\end{aligned}
$$

and the definitions for W_μ^- and W_μ^+ from equations 2.35 and 2.36 may all be substituted into equation 2.60:

$$
\begin{aligned}
\mathcal{L}_{\text{Dirac}} = {}& \overline{\psi}_L i\gamma^\mu \partial_\mu \psi_R + \overline{\psi}_R i\gamma^\mu \partial_\mu \psi_L \\
& + \overline{\psi}_L \gamma^\mu \frac{Y^W}{2} e A_\mu \psi_R - \overline{\psi}_L \gamma^\mu \left(-\frac{Y^W}{2} \frac{g\sin^2\theta_W}{\cos\theta_W} \right) Z_\mu^0 \psi_R \\
& + \overline{\psi}_R \gamma^\mu \begin{pmatrix} \frac{Y^W}{2} + \frac{1}{2} & 0 \\ 0 & \frac{Y^W}{2} - \frac{1}{2} \end{pmatrix} e A_\mu \psi_L \\
& - \overline{\psi}_R \gamma^\mu \begin{pmatrix} -\frac{Y^W}{2}\frac{g\sin^2\theta_W}{\cos\theta_W} + \frac{1}{2}\frac{g\cos^2\theta_W}{\cos\theta_W} & 0 \\ 0 & -\frac{Y^W}{2}\frac{g\sin^2\theta_W}{\cos\theta_W} - \frac{1}{2}\frac{g\cos^2\theta_W}{\cos\theta_W} \end{pmatrix} Z_\mu^0 \psi_L \\
& + \overline{\psi}_R \gamma^\mu \begin{pmatrix} 0 & g\frac{1}{\sqrt{2}} W_\mu^+ \\ g\frac{1}{\sqrt{2}} W_\mu^- & 0 \end{pmatrix} \psi_L.
\end{aligned}
\tag{2.65}
$$

Now, for reasons which will only become apparent towards the end, we are going to add zero to the right-handed couplings of A_μ and Z_μ^0, making equation

2.65 look like

$$
\begin{aligned}
\mathcal{L}_{\text{Dirac}} \quad = \quad & \overline{\psi}_L i\gamma^\mu \partial_\mu \psi_R + \overline{\psi}_R i\gamma^\mu \partial_\mu \psi_L + \overline{\psi}_L \gamma^\mu \left(\frac{Y^W}{2} + 0 \right) eA_\mu \psi_R \\
& + \overline{\psi}_R \gamma^\mu \begin{pmatrix} \frac{Y^W}{2} + \frac{1}{2} & 0 \\ 0 & \frac{Y^W}{2} - \frac{1}{2} \end{pmatrix} eA_\mu \psi_L \\
& - \overline{\psi}_L \gamma^\mu \left(-\frac{Y^W}{2} \frac{g\sin^2\theta_W}{\cos\theta_W} - 0 \right) Z^0_\mu \psi_R \\
& - \overline{\psi}_R \gamma^\mu \begin{pmatrix} -\frac{Y^W}{2}\frac{g\sin^2\theta_W}{\cos\theta_W} + \frac{1}{2}\frac{g\cos^2\theta_W}{\cos\theta_W} & 0 \\ 0 & -\frac{Y^W}{2}\frac{g\sin^2\theta_W}{\cos\theta_W} - \frac{1}{2}\frac{g\cos^2\theta_W}{\cos\theta_W} \end{pmatrix} Z^0_\mu \psi_L \\
& + \overline{\psi}_R \gamma^\mu \begin{pmatrix} 0 & g\frac{1}{\sqrt{2}}W^+_\mu \\ g\frac{1}{\sqrt{2}}W^-_\mu & 0 \end{pmatrix} \psi_L.
\end{aligned}
\tag{2.66}
$$

This can be rewritten as

$$
\begin{aligned}
\mathcal{L}_{\text{Dirac}} \quad = \quad & \overline{\psi}_L i\gamma^\mu \partial_\mu \psi_R + \overline{\psi}_R i\gamma^\mu \partial_\mu \psi_L \\
& + \overline{\psi}_L \gamma^\mu \left(\frac{Y^W}{2} + 0 \right) eA_\mu \psi_R + \overline{\psi}_R \gamma^\mu \begin{pmatrix} \frac{Y^W}{2} + \frac{1}{2} & 0 \\ 0 & \frac{Y^W}{2} - \frac{1}{2} \end{pmatrix} eA_\mu \psi_L \\
& - \frac{g}{\cos\theta_W} \overline{\psi}_L \gamma^\mu \left[-\left(\frac{Y^W}{2} + 0 \right)\sin^2\theta_W \right] Z^0_\mu \psi_R - \frac{g}{\cos\theta_W}\overline{\psi}_R\gamma^\mu \\
& \times \begin{pmatrix} -\left(\frac{Y^W}{2} + \frac{1}{2}\right)\sin^2\theta_W + \frac{1}{2} & 0 \\ 0 & -\left(\frac{Y^W}{2} - \frac{1}{2}\right)\sin^2\theta_W - \frac{1}{2} \end{pmatrix} \\
& \times Z^0_\mu \psi_L + \overline{\psi}_R\gamma^\mu \begin{pmatrix} 0 & g\frac{1}{\sqrt{2}}W^+_\mu \\ g\frac{1}{\sqrt{2}}W^-_\mu & 0 \end{pmatrix}\psi_L.
\end{aligned}
\tag{2.67}
$$

Now comes a little slight of hand: Those zeros we added earlier in the right-handed couplings for the A_μ and the Z^0_μ are really the weak isospin of the right-handed

fields for which, because right-handed fields are isospin singlets, $I_3^W = 0$. Not only that, but in the left-handed couplings for the A_μ and the Z_μ^0, those $+\frac{1}{2}$s and $-\frac{1}{2}$s are also from I_3^W. Left-handed fields are doublets, and the top half of the doublet has $I_{3,11}^W = \frac{1}{2}$ whilst the bottom half of the doublet has $I_{3,22}^W = -\frac{1}{2}$. With our feat of legerdemain, equation 2.67 becomes

$$
\begin{aligned}
\mathcal{L}_{\text{Dirac}} \;=\; & \overline{\psi}_L i\gamma^\mu \partial_\mu \psi_R + \overline{\psi}_R i\gamma^\mu \partial_\mu \psi_L \\
& + \overline{\psi}_L \gamma^\mu \left(\frac{Y^W}{2} + I_3^W \right) e A_\mu \psi_R + \overline{\psi}_R \gamma^\mu \begin{pmatrix} \frac{Y^W}{2} + I_{3,11}^W & 0 \\ 0 & \frac{Y^W}{2} + I_{3,22}^W \end{pmatrix} e A_\mu \psi_L \\
& - \frac{g}{\cos\theta_W} \overline{\psi}_L \gamma^\mu \left[-\left(\frac{Y^W}{2} + I_3^W \right) \sin^2\theta_W \right] Z_\mu^0 \psi_R - \frac{g}{\cos\theta_W} \overline{\psi}_R \gamma^\mu \\
& \times \begin{pmatrix} -\left(\frac{Y^W}{2} + I_{3,11}^W \right) \sin^2\theta_W + I_{3,11}^W & 0 \\ 0 & -\left(\frac{Y^W}{2} + I_{3,22}^W \right) \sin^2\theta_W + I_{3,22}^W \end{pmatrix} \\
& \times Z_\mu^0 \psi_L + \overline{\psi}_R \gamma^\mu \begin{pmatrix} 0 & g\frac{1}{\sqrt{2}} W_\mu^+ \\ g\frac{1}{\sqrt{2}} W_\mu^- & 0 \end{pmatrix} \psi_L, \quad (2.68)
\end{aligned}
$$

and we can now identify the electric charge

$$
q_{ii} \;=\; \frac{Y^W}{2} I_{ii} + I_{3,ii}^W \quad (2.69)
$$

where once again $I^W_{3,ii} = 0$ and $I_{ii} = 1$ for right-handed fields. This allows us to simplify equation 2.68 accordingly

$$
\begin{aligned}
\mathcal{L}_{\text{Dirac}} = \ & \overline{\psi}_L i\gamma^\mu \partial_\mu \psi_R + \overline{\psi}_R i\gamma^\mu \partial_\mu \psi_L \\
& + \overline{\psi}_L \gamma^\mu q e A_\mu \psi_R + \overline{\psi}_R \gamma^\mu \begin{pmatrix} q_{11} & 0 \\ 0 & q_{22} \end{pmatrix} e A_\mu \psi_L \\
& - \frac{g}{\cos\theta_W} \overline{\psi}_L \gamma^\mu \left(-q \sin^2\theta_W \right) Z^0_\mu \psi_R \\
& - \frac{g}{\cos\theta_W} \overline{\psi}_R \gamma^\mu \begin{pmatrix} -q_{11}\sin^2\theta_W + I^W_{3,11} & 0 \\ 0 & -q_{22}\sin^2\theta_W + I^W_{3,22} \end{pmatrix} Z^0_\mu \psi_L \\
& + \overline{\psi}_R \gamma^\mu \begin{pmatrix} 0 & g\frac{1}{\sqrt{2}} W^+_\mu \\ g\frac{1}{\sqrt{2}} W^-_\mu & 0 \end{pmatrix} \psi_L.
\end{aligned}
\tag{2.70}
$$

The right and left handed couplings for the Z^0 are defined as

$$
g_R = -q\sin^2\theta_W \tag{2.71}
$$

$$
g_{L,ii} = I^W_{3,ii} - q_{ii}\sin^2\theta_W \tag{2.72}
$$

which makes equation 2.70

$$
\begin{aligned}
\mathcal{L}_{\text{Dirac}} \;=\;& \overline{\psi}_L i\gamma^\mu \partial_\mu \psi_R + \overline{\psi}_R i\gamma^\mu \partial_\mu \psi_L \\[4pt]
& + \overline{\psi}_L \gamma^\mu q e A_\mu \psi_R + \overline{\psi}_R \gamma^\mu
\begin{pmatrix} q_{11} & 0 \\ 0 & q_{22} \end{pmatrix} e A_\mu \psi_L \\[4pt]
& - \frac{g}{\cos\theta_W} \overline{\psi}_L \gamma^\mu g_R Z^0_\mu \psi_R
- \frac{g}{\cos\theta_W} \overline{\psi}_R \gamma^\mu
\begin{pmatrix} g_{L,11} & 0 \\ 0 & g_{L,22} \end{pmatrix} Z^0_\mu \psi_L \\[4pt]
& + \overline{\psi}_R \gamma^\mu
\begin{pmatrix} 0 & g\frac{1}{\sqrt{2}}W^+_\mu \\ g\frac{1}{\sqrt{2}}W^-_\mu & 0 \end{pmatrix} \psi_L .
\end{aligned}
\tag{2.73}
$$

Finally, it is time to recombine the terms for the left and right handed interactions. We use the commutation rules for γ^μ with γ^5 and other properties of γ^5 to write at last

$$
\begin{aligned}
\mathcal{L}_{\text{Dirac}} \;=\;& \overline{\psi} i\gamma^\mu \partial_\mu \psi \\[4pt]
& + \overline{\psi} \gamma^\mu q e A_\mu \psi \\[4pt]
& - \frac{g}{2\cos\theta_W} \overline{\psi}\gamma^\mu \left[\left(1+\gamma^5\right) g_R + \left(1-\gamma^5\right) g_L \right] Z^0_\mu \psi \\[4pt]
& + \frac{g}{2\sqrt{2}} \overline{\psi}\gamma^\mu \left(1-\gamma^5\right)
\begin{pmatrix} 0 & W^+_\mu \\ W^-_\mu & 0 \end{pmatrix} \psi .
\end{aligned}
\tag{2.74}
$$

This is a popular way to write the Lagrangian for it shows explicitly how the Z^0 couples differently to left and right handed particles. However, by defining the vector coupling, g_V

$$
g_V \;=\; g_L + g_R
$$

$$= I_3^W - 2q \sin^2 \theta_W, \tag{2.75}$$

and axial vector coupling, g_A,

$$g_A = g_L - g_R$$
$$= I_3^W, \tag{2.76}$$

we can rewrite the Lagrangian for a Dirac field in its simplest form and as it most often appears in the literature

$$
\begin{aligned}
\mathcal{L}_{\text{Dirac}} &= \overline{\psi} i \gamma^\mu \partial_\mu \psi \\
&\quad + \overline{\psi} \gamma^\mu q e A_\mu \psi \\
&\quad - \frac{g}{2\cos\theta_W} \overline{\psi} \gamma^\mu \left(g_V - g_A \gamma^5 \right) Z_\mu^0 \psi \\
&\quad + \frac{g}{2\sqrt{2}} \overline{\psi} \gamma^\mu \left(1 - \gamma^5 \right) \begin{pmatrix} 0 & W_\mu^+ \\ W_\mu^- & 0 \end{pmatrix} \psi.
\end{aligned}
\tag{2.77}
$$

2.3 The Yukawa Coupling and the Origin of Mass

There is but one loose end. So far, we have the interaction of scalars with vectors and spinors with vectors. We still need the interaction of scalars with spinors. This is done with $\mathcal{L}_{\text{Yukawa}}$. One desired outcome is for $\mathcal{L}_{\text{Yukawa}}$ to be the source of mass for the fermions. Recall that terms quadratic in the fields are mass terms. Fermions with mass have an additional constraint – they must exist in both right handed and left handed states. The only field operators that yield a non-zero

mass for fermions are bilinear products of fields that flip the particle's handedness [7]: $\overline{\psi}\psi = \overline{\psi}_R\psi_R + \overline{\psi}_L\psi_L$ and $\overline{\psi}_R\psi_L = \overline{\psi}_L\psi_R = 0$. However, the weak isospin symmetry forbids such mass operators because they are not invarient under that symmetry: ψ_L is a weak doublet whereas ψ_R is a weak singlet, and the product of the two is not a singlet as it ought to be to preserve the weak isospin symmetry. But recall that the Higgs field is an isospin doublet. Thus $\mathcal{L}_{\text{Yukawa}}$ has the form $\overline{\psi}\phi Y \psi$ where Y gives the strength of the interaction between the fermion in question and the Higgs boson. It is once again useful to consider left and right handed particles separately, using the definitions from equations 2.51, 2.52, 2.54, and 2.55. Clarity will be further improved by considering the various isospin singlets and doublets explicitly:

$$
\psi_{Li} = \begin{cases} \begin{pmatrix} u'_{Li} \\ d'_{Li} \end{pmatrix} & \text{Quarks} \\[6pt] \begin{pmatrix} \nu'_{Li} \\ e^{-'}_{Li} \end{pmatrix} & \text{Leptons} \end{cases} \tag{2.78}
$$

$$
\psi_{Ri} = \begin{cases} \begin{matrix} u'_{Ri} & \text{Quarks} \\ d'_{Ri} & \end{matrix} \\[6pt] \begin{matrix} \nu'_{Ri} & \text{Leptons} \\ e^{-'}_{Ri} & \end{matrix} \end{cases} \tag{2.79}
$$

$$
\overline{\psi}_{Ri} = \begin{cases} \begin{pmatrix} \overline{u'}_{Ri} & \overline{d'}_{Ri} \end{pmatrix} & \text{Quarks} \\[6pt] \begin{pmatrix} \overline{\nu'}_{Ri} & e^{+'}_{Ri} \end{pmatrix} & \text{Leptons} \end{cases} \tag{2.80}
$$

$$\overline{\psi}_{Li} = \begin{cases} \overline{u'}_{Li} & \text{Quarks} \\ \overline{d'}_{Li} \\ \overline{\nu'}_{Li} & \text{Leptons} \\ e^{+\prime}_{Li} \end{cases} \tag{2.81}$$

where i and j denote the three generations of the quarks and leptons. The primes denote the weak eigenstate basis. The Higgs doublet along with its complex conjugate are [8]

$$\phi = \begin{pmatrix} \phi^+ \\ \phi^0 \end{pmatrix} \tag{2.82}$$

$$\phi^\dagger = \begin{pmatrix} -\phi^- & \phi^{0\dagger} \end{pmatrix} \tag{2.83}$$

$$\overline{\phi} = \begin{pmatrix} \overline{\phi}^0 \\ -\phi^- \end{pmatrix} = i\sigma_2 \phi^* \tag{2.84}$$

$$\overline{\phi}^\dagger = \begin{pmatrix} \overline{\phi}^0 & \phi^+ \end{pmatrix} \tag{2.85}$$

where $\overline{\phi}^0 = \phi^{0\dagger}$. The Yukawa term in the Lagrangian can be written down explicitly as

$$
\begin{aligned}
\mathcal{L}_{\text{Yukawa}} &= \left(\begin{array}{cc} \overline{u'}_{Rj} & \overline{d'}_{Rj} \end{array} \right) \left(\begin{array}{c} \phi^+ \\ \phi^0 \end{array} \right) Y_{ji}^{d\dagger} d'_{Ri} + \overline{d'}_{Li} Y_{ij}^d \left(\begin{array}{cc} -\phi^- & \phi^{0\dagger} \end{array} \right) \left(\begin{array}{c} u'_{Lj} \\ d'_{Lj} \end{array} \right) \\
&+ \left(\begin{array}{cc} \overline{u'}_{Rj} & \overline{d'}_{Rj} \end{array} \right) \left(\begin{array}{c} \overline{\phi}^0 \\ -\phi^- \end{array} \right) Y_{ji}^{u\dagger} u'_{Ri} + \overline{u'}_{Li} Y_{ij}^u \left(\begin{array}{cc} \overline{\phi}^0 & \phi^+ \end{array} \right) \left(\begin{array}{c} u'_{Lj} \\ d'_{Lj} \end{array} \right) \\
&+ \left(\begin{array}{cc} \overline{\nu'}_{Rj} & e_{Rj}^{+'} \end{array} \right) \left(\begin{array}{c} \phi^+ \\ \phi^0 \end{array} \right) Y_{ji}^{e\dagger} e_{Ri}^{-'} + e_{Li}^{+'} Y_{ij}^e \left(\begin{array}{cc} -\phi^- & \phi^{0\dagger} \end{array} \right) \left(\begin{array}{c} \nu'_{Lj} \\ e_{Lj}^{-'} \end{array} \right) \\
&+ \left(\begin{array}{cc} \overline{\nu'}_{Rj} & e_{Rj}^{+'} \end{array} \right) \left(\begin{array}{c} \overline{\phi}^0 \\ -\phi^- \end{array} \right) Y_{ji}^{\nu\dagger} \nu'_{Ri} + \overline{\nu'}_{Li} Y_{ij}^\nu \left(\begin{array}{cc} \overline{\phi}^0 & \phi^+ \end{array} \right) \left(\begin{array}{c} \nu'_{Lj} \\ e_{Lj}^{-'} \end{array} \right).
\end{aligned}
$$

$$(2.86)$$

Particle mass arises directly from the Yukawa interaction because of the non-zero vacuum expectation value of ϕ:

$$
\phi_{vacuum} = \left(\begin{array}{c} 0 \\ \frac{\phi_V}{\sqrt{2}} \end{array} \right) \tag{2.87}
$$

$$
\phi_{vacuum}^\dagger = \left(\begin{array}{cc} 0 & \frac{\phi_V}{\sqrt{2}} \end{array} \right) \tag{2.88}
$$

$$
\overline{\phi}_{vacuum} = \left(\begin{array}{c} \frac{\phi_V}{\sqrt{2}} \\ 0 \end{array} \right) \tag{2.89}
$$

$$
\overline{\phi}_{vacuum}^\dagger = \left(\begin{array}{cc} \frac{\phi_V}{\sqrt{2}} & 0 \end{array} \right). \tag{2.90}
$$

This can be seen explicitly by letting $\phi \rightarrow \phi_{vacuum}$ and so on in equation 2.86: Thus $\mathcal{L}_{\text{Yukawa}} \rightarrow \mathcal{L}_{Mass}$

$$
\begin{aligned}
\mathcal{L}_{Mass} &= \frac{\phi_V}{\sqrt{2}} \left[\overline{d'}_{Rj} Y_{ji}^{d\dagger} d'_{Ri} + \overline{d'}_{Li} Y_{ij}^{d} d'_{Lj} \right] + \frac{\phi_V}{\sqrt{2}} \left[\overline{u'}_{Rj} Y_{ji}^{u\dagger} u'_{Ri} + \overline{u'}_{Li} Y_{ij}^{u} u'_{Lj} \right] \\
&\quad + \frac{\phi_V}{\sqrt{2}} \left[e_{Rj}^{+'} Y_{ji}^{e\dagger} e_{Ri}^{-'} + e_{Li}^{+'} Y_{ij}^{e} e_{Lj}^{-'} \right] + \frac{\phi_V}{\sqrt{2}} \left[\overline{\nu'}_{Rj} Y_{ji}^{\nu\dagger} \nu'_{Ri} + \overline{\nu'}_{Li} Y_{ij}^{\nu} \nu'_{Lj} \right] \\
&= \frac{\phi_V}{\sqrt{2}} \left[\overline{d'}_i Y_{ij}^{d} d'_j + \overline{u'}_i Y_{ij}^{u} u'_j + e_i^{+'} Y_{ij}^{e} e_j^{-'} + \overline{\nu'}_i Y_{ij}^{\nu} \nu'_j \right]. \quad (2.91)
\end{aligned}
$$

In the garden variety Standard Model, $\overline{\nu'}_L = \nu'_R = 0$ and the neutrinos have no mass, but as recent empirical evidence suggests, this may not in fact be true. In any case, I will leave these terms in for the sake of quark-lepton universality.

The Y are actually complex matrices called Yukawa matrices, and since there are three generations of quarks and leptons, the Yukawa matrices are really complex 3×3 matrices which in general are not diagonal [9]. The consequence of this is that there may be mixing across generations. To look at things in the mass eigenstate basis, we would have to diagonalize the Yukawa matrices Y. This is done by two unitary transformation matrices, as follows:

$$
\hat{Y} = VYV^{\dagger} \quad (2.92)
$$

$$
VV^{\dagger} = I. \quad (2.93)
$$

Writing $\mathcal{L}_{Mass}$ in the mass basis (unprimed) rather than the weak basis (primed) yields

$$
\mathcal{L}_{Mass} = \frac{\phi_V}{\sqrt{2}} \left[\overline{d}_i V_{ik}^{d} Y_{kn}^{d} V_{nj}^{d\dagger} d_j + \overline{u}_i V_{ik}^{u} Y_{kn}^{u} V_{nj}^{u\dagger} u_j + e_i^{+} V_{ik}^{e} Y_{kn}^{e} V_{nj}^{e\dagger} e_j^{-} + \overline{\nu}_i V_{ik}^{\nu} Y_{kn}^{\nu} V_{nj}^{\nu\dagger} \nu_j \right]
$$

$$= \frac{\phi_V}{\sqrt{2}} \left[\overline{d}_i \hat{Y}_i^d d_i + \overline{u}_i \hat{Y}_i^u u_i + e_i^+ \hat{Y}_i^e e_i^- + \overline{\nu}_i \hat{Y}_i^\nu \nu_i \right]. \tag{2.94}$$

Finally, we can write

$$\mathcal{L}_{Mass} = \hat{\mathcal{M}}_i^d \overline{d}_i d_i + \hat{\mathcal{M}}_i^u \overline{u}_i u_i + \hat{\mathcal{M}}_i^e e_i^+ e_i^- + \hat{\mathcal{M}}_i^\nu \overline{\nu}_i \nu_i \tag{2.95}$$

where the mass matrices $\hat{\mathcal{M}}_i$ have replaced the constants and the diagonalized Yukawa matrices, $\frac{\phi_V}{\sqrt{2}} \hat{Y}_i$.

2.4 The CKM Matrix

The weak states (primed) are thus related to the mass states (unprimed) by

$$
\begin{aligned}
u_i' &= V_{ik}^{u\dagger} u_k & \overline{u'}_i &= \overline{u}_k V_{ki}^u \\
d_i' &= V_{ik}^{d\dagger} d_k & \overline{d'}_i &= \overline{d}_k V_{ki}^d \\
\nu_i' &= V_{ik}^{\nu\dagger} \nu_k & \overline{\nu'}_i &= \overline{\nu}_k V_{ki}^\nu \\
e_i^{-'} &= V_{ik}^{e\dagger} e_k^- & e_i^{+'} &= e_k^+ V_{ki}^e.
\end{aligned}
\tag{2.96}
$$

In light of this, let's reexamine the charged current interaction, the last term in equation 2.77, once again to derive an important result.

$$\mathcal{L}_{CC} = \frac{g}{2\sqrt{2}} \overline{\psi} \gamma^\mu \left(1 - \gamma^5 \right) \begin{pmatrix} 0 & W_\mu^+ \\ W_\mu^- & 0 \end{pmatrix} \psi. \tag{2.97}$$

In the weak basis (primed), equation 2.97 looks like

$$
\begin{aligned}
\mathcal{L}_{CC} &= \frac{g}{2\sqrt{2}} \left[\overline{u'}_{Ri} \gamma^\mu W_\mu^+ d'_{Li} + \overline{d'}_{Ri} \gamma^\mu W_\mu^- u'_{Li} \right. \\
&\qquad \left. + \overline{\nu'}_{Ri} \gamma^\mu W_\mu^+ e_{Li}^{-\prime} + e_{Ri}^{+\prime} \gamma^\mu W_\mu^- \nu'_{Li} \right],
\end{aligned}
\tag{2.98}
$$

but in the mass basis (unprimed), equation 2.97 looks like

$$
\begin{aligned}
\mathcal{L}_{CC} &= \frac{g}{2\sqrt{2}} \left[\overline{u}_i V_{ik}^u \gamma^\mu W_\mu^+ V_{kj}^{d\dagger} d_j + \overline{d}_i V_{ik}^d \gamma^\mu W_\mu^- V_{kj}^{u\dagger} u_j \right. \\
&\qquad \left. + \overline{\nu}_i V_{ik}^\nu \gamma^\mu W_\mu^+ V_{kj}^{e\dagger} e_j^- + e_i^+ V_{ik}^e \gamma^\mu W_\mu^- V_{kj}^{\nu\dagger} \nu_j \right] \\
&= \frac{g}{2\sqrt{2}} \left[\overline{u}_i \gamma^\mu W_\mu^+ (V_{CKM})_{ij} d_j + \overline{d}_i \left(V_{CKM}^\dagger \right)_{ij} \gamma^\mu W_\mu^- u_j \right. \\
&\qquad \left. + \overline{\nu}_i \left(V_{MNSP}^\dagger \right)_{ij} \gamma^\mu W_\mu^+ e_j^- + e_i^+ \gamma^\mu W_\mu^- (V_{MNSP})_{ij} \nu_j \right],
\end{aligned}
\tag{2.99}
$$

where $V^u V^{d\dagger} = V_{CKM}$, the Cabibbo-Kobayashi-Maskawa matrix, and where $V^e V^{\nu\dagger} = V_{MNSP}$, the Maki-Nagakawa-Sakata-Pontecorvo matrix [10]. V_{CKM} and V_{MNSP} are both unitary because V^u, $V^{d\dagger}$, V^e, and $V^{\nu\dagger}$ are all unitary transformation matrices, and any matrix which is the product of two unitary matrices is itself unitary. This may be proved as follows: If A and B are both unitary matrices, then $A^\dagger A = A A^\dagger = 1$ and $B^\dagger B = B B^\dagger = 1$. If $A^\dagger B = C$, then $B^\dagger A = C^\dagger$, and $C^\dagger C = B^\dagger A A^\dagger B = B^\dagger (A A^\dagger) B = B^\dagger B = 1$. V_{CKM} would be the identiy matrix were it not for the difference between the rotation matrices for the up-type quarks, V^u, and the down-type quarks V^d. It is that difference that determines the amount of generation mixing in weak interaction processes [9]. For that reason, all the mixing can be placed in either the up-type or down-type quarks, and convention has favored the down-type quarks. The upshot is that weak charged currents change flavors.

Let's also reexamine the the neutral current interaction, the third term in equation 2.77.

$$\mathcal{L}_{NC} = -\frac{g}{2\cos\theta_W}\overline{\psi}\gamma^\mu\left(g_V - g_A\gamma^5\right)Z^0_\mu\psi. \tag{2.100}$$

In the weak basis (primed), equation 2.100 looks like

$$\mathcal{L}_{NC} = -\frac{g}{2\cos\theta_W}\left[\overline{u'}_i\gamma^\mu\left(g_V - g_A\gamma^5\right)Z^0_\mu u'_i + \overline{d'}_i\gamma^\mu\left(g_V - g_A\gamma^5\right)Z^0_\mu d'_i \right. $$
$$\left. + e^{+'}_i\gamma^\mu\left(g_V - g_A\gamma^5\right)Z^0_\mu e^{-'}_i + \overline{\nu'}_i\gamma^\mu\left(g_V - g_A\gamma^5\right)Z^0_\mu \nu'_i\right], \tag{2.101}$$

but in the mass basis (unprimed), equation 2.100 looks like

$$\mathcal{L}_{NC} = -\frac{g}{2\cos\theta_W}\left[\overline{u'}_i V^u_{ij}\gamma^\mu\left(g_V - g_A\gamma^5\right)Z^0_\mu V^{u\dagger}_{jk}u'_k \right.$$
$$+ \overline{d'}_i V^d_{ij}\gamma^\mu\left(g_V - g_A\gamma^5\right)Z^0_\mu V^{d\dagger}_{jk}d'_k$$
$$+ e^{+'}_i V^e_{ij}\gamma^\mu\left(g_V - g_A\gamma^5\right)Z^0_\mu V^{e\dagger}_{jk}e^{-'}_k$$
$$\left. + \overline{\nu'}_i V^\nu_{ij}\gamma^\mu\left(g_V - g_A\gamma^5\right)Z^0_\mu V^{\nu\dagger}_{jk}\nu'_k\right]$$
$$= -\frac{g}{2\cos\theta_W}\left[\overline{u}_i\gamma^\mu\left(g_V - g_A\gamma^5\right)Z^0_\mu u_i + \overline{d}_i\gamma^\mu\left(g_V - g_A\gamma^5\right)Z^0_\mu d_i \right.$$
$$\left. + e^+_i\gamma^\mu\left(g_V - g_A\gamma^5\right)Z^0_\mu e^-_i + \overline{\nu}_i\gamma^\mu\left(g_V - g_A\gamma^5\right)Z^0_\mu \nu_i\right]. \tag{2.102}$$

Because $V^f V^{f\dagger} = I$, $\mathcal{L}_{NC}$ is the same in both the weak (primed) and mass (unprimed) bases. The weak neutral current is therefore flavor-diagonal: There are no tree-level flavor changing neutral currents.

2.5 R_{bs} in the Standard Model

Just because there are no tree-level flavor changing neutral currents does not mean that they are forbidden at higher orders. Indeed, loop order "penguin" diagrams specifically allow for flavor changing neutral currents.

The curious name "penguin" has its origins in a game of darts which occurred at a Geneva pub in the summer of 1977 among experimentalist Melissa Franklin and theorists John Ellis, Mary K. Gaillard, Dimitri Nanopoulos, and Serge Rudaz. Somehow the telling of a joke about penguins evolved into a bet whereby the loser of the dart game had to use the word penguin in his or her next paper. It seems that at some point Rudaz took Franklin's place in the game and proceeded to defeat Ellis [11]. Ellis recalls that "for some time, it was not clear to me how to get the word into this quark paper that we were writing at the time. Then, one evening I stopped on my way back to my apartment to visit some friends living in Meyrin, where I smoked some illegal substance. Later, when I got back to my apartment and continued working on our paper, I had a sudden flash that the famous diagrams looked like penguins. So we put the name into our paper, and the rest, as they say, is history" [12]. At the end, the paper contains an acknowledgment to Franklin for "helpful discussions" [13].

The Standard Model prediction for the branching ratio for $Z^0 \rightarrow b\bar{s} + s\bar{b}$ has been worked out by M. Clements *et al* [14]. We have calculated $R_{bs} = \frac{\Gamma(Z^0 \rightarrow b\bar{s} + s\bar{b})}{\Gamma(Z^0 \rightarrow \text{hadrons})}$ from their computation assuming the current experimental values for the various quark masses, CKM matrix elements, and so on.

The calculation is done in the 't Hooft-Feynman gauge because the vector boson propagators assume their simplest form and the unphysical scalars take on

the masses of their physical partners. The ten diagrams to be calculated are shown in Figure 1. Note that the tree-level diagram is conspicuously absent.

The matrix element for $Z^0 \to b\bar{s} + s\bar{b}$ in the massless b, s approximation is then

$$\mathcal{M} = \frac{g^3}{(4\pi)^2} \bar{u}(p_b)\not{\epsilon}(1 - \gamma^5)v(p_s)[\mathcal{A}(m_t)V_{ts}^*V_{tb} + \mathcal{A}(m_c)V_{cs}^*V_{cb} + \mathcal{A}(m_u)V_{us}^*V_{ub}]$$

(2.103)

where $\mathcal{A}(m_j)$ represents the sum of the ten diagrams in Figure 1 and is a function of the internal quark mass m_j. Summing over the spins of b and s gives

$$\sum_{\text{spins}} |\mathcal{M}|^2 = \left[\frac{g^3}{(4\pi)^2}\right]^2 8(p_b^\alpha p_s^\beta + p_s^\alpha p_b^\beta - g^{\alpha\beta}p_b \cdot p_s)\epsilon_\alpha \epsilon_\beta^*$$
$$\times |\mathcal{A}(m_t)V_{ts}^*V_{tb} + \mathcal{A}(m_c)V_{cs}^*V_{cb} + \mathcal{A}(m_u)V_{us}^*V_{ub}|^2. \quad (2.104)$$

After averaging over the Z^0 spin,

$$\overline{|\mathcal{M}|^2} = \left[\frac{g^3}{(4\pi)^2}\right]^2 8(p_b^\alpha p_s^\beta + p_s^\alpha p_b^\beta - g^{\alpha\beta}p_b \cdot p_s)\frac{1}{3}\left(-g_{\alpha\beta} + \frac{P_{Z\alpha}P_{Z\beta}}{M_Z^2}\right)$$
$$\times |\mathcal{A}(m_t)V_{ts}^*V_{tb} + \mathcal{A}(m_c)V_{cs}^*V_{cb} + \mathcal{A}(m_u)V_{us}^*V_{ub}|^2. \quad (2.105)$$

Multiplying by the phase space and integrating yields for the partial width

$$\Gamma(Z^0 \to b\bar{s} + s\bar{b}) = 2 \times 3 \frac{1}{2M_Z} \int \frac{d^3p_b}{(2\pi)^3 2E_b} \frac{d^3p_s}{(2\pi)^3 2E_s} (2\pi)^4 \delta^4(P_Z - p_b - p_s)\overline{|\mathcal{M}|^2}.$$

(2.106)
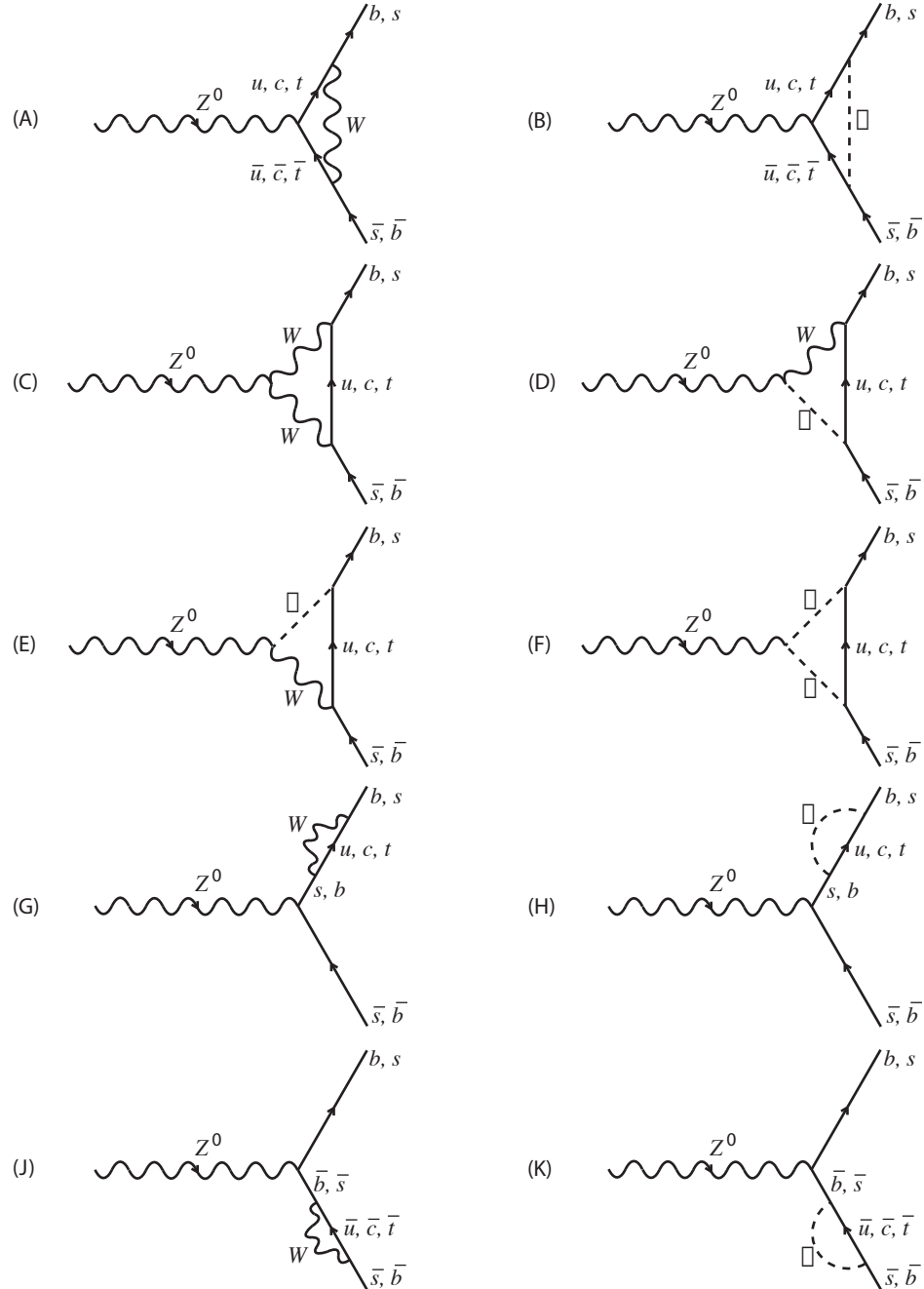
FIGURE 1. Feynman diagrams which contribute to $Z^0 \to b\bar{s} + s\bar{b}$ in the 't Hooft-Feynman gauge.

We used in the calculation the following values for the mixing angle and masses [15]:

$$\sin^2 \theta_W = 0.23113 \tag{2.107}$$

$$M_W = 80.4251 \text{ GeV} \tag{2.108}$$

$$M_Z = 91.1876 \text{ GeV} \tag{2.109}$$

$$m_t = 174.3 \text{ GeV} \tag{2.110}$$

$$m_c = 1.25 \text{ GeV} \tag{2.111}$$

$$m_u = 0.00325 \text{ GeV.} \tag{2.112}$$

$\mathcal{A}(m_j)$ is a cumbersome expression for arbitrary m_j: Numerical values for $\mathcal{A}(m_j)$ corresponding to m_t, m_c, and m_u are

$$\mathcal{A}(m_t) = -0.74 \tag{2.113}$$

$$\mathcal{A}(m_c) = -0.18 - 0.21i \tag{2.114}$$

$$\mathcal{A}(m_u) = -0.18 - 0.21i. \tag{2.115}$$

The constant g was as usual

$$g = \frac{\sqrt{4\pi\alpha}}{\sin \theta_W} \tag{2.116}$$

where $\alpha^{-1} \rightarrow \alpha(M_Z)^{-1} = 127.922$ [15].

The elements of the CKM matrix were calculated from the Wolfenstein parameterization as follows [16]:

$$V_{CKM} = \begin{pmatrix} 1 - \frac{\lambda^2}{2} & \lambda & A\lambda^3(\rho - i\eta) \\ -\lambda & 1 - \frac{\lambda^2}{2} & A\lambda^2 \\ A\lambda^3(1 - \rho - i\eta) & -A\lambda^2 & 1 \end{pmatrix} \tag{2.117}$$

$$\tag{2.118}$$

where

$$\lambda = |V_{us}| \tag{2.119}$$

$$A = \frac{|V_{cb}|}{|V_{us}|^2} \tag{2.120}$$

$$\rho = 1 - \frac{|V_{td}| \cos \beta}{|V_{us}||V_{cb}|} \tag{2.121}$$

$$\eta = \frac{|V_{td}| \sin \beta}{|V_{us}||V_{cb}|} \tag{2.122}$$

and where [15]

$$|V_{us}| = 0.2225 \tag{2.123}$$

$$|V_{cb}| = 0.04 \tag{2.124}$$

$$|V_{td}| = 0.009 \tag{2.125}$$

$$\sin 2\beta = 0.78. \tag{2.126}$$

Performing the Integration over phase space, the partial width is

$$\Gamma(Z^0 \to b\bar{s} + s\bar{b}) = 1.0 \times 10^{-7} \text{ GeV.} \tag{2.127}$$

Taking $\Gamma(Z^0 \to \text{hadrons}) = 1.7422$ GeV [15],

$$R_{bs} \quad = \quad \frac{\Gamma(Z^0 \to b\bar{s} + s\bar{b})}{\Gamma(Z^0 \to \text{hadrons})} = 5.8 \times 10^{-8}. \tag{2.128}$$

2.6 R_b and R_c in the Standard Model

The quantities $R_b = \frac{\Gamma(Z^0 \to b\bar{b})}{\Gamma(Z^0 \to \text{hadrons})}$ and $R_c = \frac{\Gamma(Z^0 \to c\bar{c})}{\Gamma(Z^0 \to \text{hadrons})}$ provide excellent tests of the Standard Model. Because R_b and R_c are ratios between two hadronic rates, propagator (oblique), radiative, and QCD corrections which affect all quark flavors largely cancel [17]. And R_b and R_c are insensitive to the as yet unknown Higgs mass [18].

The $Z^0 \to b\bar{b}$ vertex in particular is unique in that it receives relatively large radiative corrections from one-loop Feynman diagrams involving the t quark. This is due both to the t quark's large mass and to $|V_{tb}|$ being ≈ 1. The quantity R_b may thus be used to observe vertex corrections directly resulting from the presence of the t quark [17, 19].

The tree level contribution (diagram (A) in Figure 2) to R_q is, it turns out, fairly easy to work out. First recall from equations 2.75 and 2.76 that the vector coupling g_V and axial vector coupling g_A were defined as

$$g_V \quad = \quad I_3^W - 2q \sin^2 \theta_W \tag{2.129}$$

$$g_A \quad = \quad I_3^W \tag{2.130}$$

meaning that g_V and g_A depend on the charge q and weak isospin I_3^W of the quark in question. A slight change of notation would therefore be helpful: Thus by g_{qV} and g_{qA} we mean the vector and axial vector couplings, respectively, for a specific quark flavor q. The matrix element may be read off from the Lagrangian in equation 2.77:

$$\mathcal{M} \;=\; -\frac{g}{2\cos\theta_W}\overline{u}(p_{\overline{q}})\displaystyle{\not}\epsilon(g_{qV} - g_{qA}\gamma^5)v(p_q) \tag{2.131}$$

Summing over the spins of q and $\overline{q}$ gives

$$\sum_{\text{spins}} |\mathcal{M}|^2 \;=\; \left[\frac{g}{2\cos\theta_W}\right]^2 8(p_{\overline{q}}^\alpha p_q^\beta + p_q^\alpha p_{\overline{q}}^\beta - g^{\alpha\beta}p_{\overline{q}}\cdot p_q)\epsilon_\alpha\epsilon_\beta^*(g_{qV}^2 + g_{qA}^2). \tag{2.132}$$

After averaging over the Z^0 spin,

$$\overline{|\mathcal{M}|^2} \;=\; \left[\frac{g}{2\cos\theta_W}\right]^2 8(p_{\overline{q}}^\alpha p_q^\beta + p_q^\alpha p_{\overline{q}}^\beta - g^{\alpha\beta}p_{\overline{q}}\cdot p_q)\frac{1}{3}\left(-g_{\alpha\beta} + \frac{P_{Z\alpha}P_{Z\beta}}{M_Z^2}\right)$$
$$\times(g_{qV}^2 + g_{qA}^2). \tag{2.133}$$

Multiplying by the phase space and integrating yields for the partial width

$$\Gamma(Z^0 \to q\overline{q}) \;=\; 3\frac{1}{2M_Z}\int \frac{d^3p_{\overline{q}}}{(2\pi)^3 2E_{\overline{q}}}\frac{d^3p_q}{(2\pi)^3 2E_q}(2\pi)^4\delta^4(P_Z - p_{\overline{q}} - p_q)\overline{|\mathcal{M}|^2}. \tag{2.134}$$

Only the factor $(g_{qV}^2 + g_{qA}^2)$ in equations 2.134 and 2.133 is dependent on quark flavor; all other factors in the matrix element and the integral over phase space

are the same for all quark flavors. In the ratio $R_q = \frac{\Gamma(Z^0 \to q\bar{q})}{\sum_q \Gamma(Z^0 \to q\bar{q})}$, all other factors cancel leaving only

$$R_b = \frac{g_{bV}^2 + g_{bA}^2}{\sum_q (g_{qV}^2 + g_{qA}^2)} \tag{2.135}$$

$$R_c = \frac{g_{cV}^2 + g_{cA}^2}{\sum_q (g_{qV}^2 + g_{qA}^2)}. \tag{2.136}$$

The loop order computation has been worked out by Bryan Lynn and Robin Stuart [19] among others. The loop-order Feynman diagrams which contribute to, in this case, the $Z^0 \to b\bar{b}$ vertex are shown in Figure 2. Diagrams for $Z^0 \to c\bar{c}$ are identical apart from replacing $q = +\frac{2}{3}$, $I_3^W = +\frac{1}{2}$ quarks with $q = -\frac{1}{3}$, $I_3^W = -\frac{1}{2}$ quarks, and vice versa.

The Standard Model gives the following values for R_b and R_c [15]:

$$R_b^{SM} = 0.21569 \pm 0.00016 \tag{2.137}$$

$$R_c^{SM} = 0.17230 \pm 0.00007. \tag{2.138}$$

Although this analysis presents measurements of R_b and R_c which agree well with the Standard Model, the present harmony between theory and experiment has not always attained. Figures 3 and 4 [20, 21, 22, 23, 24, 15] compare theoretical calculations with experimental measurements of R_b and R_c over the past decade. In 1995 in particular, the agreement between theory and experiment was at an all time low – bad enough in fact to precipitate what came to be known as the "R_b-R_c crisis". Figures 5 and 6 [25] show the state of the experimental measurements of R_b and R_c respectively at that time. Figure 7 [25] shows that experimental
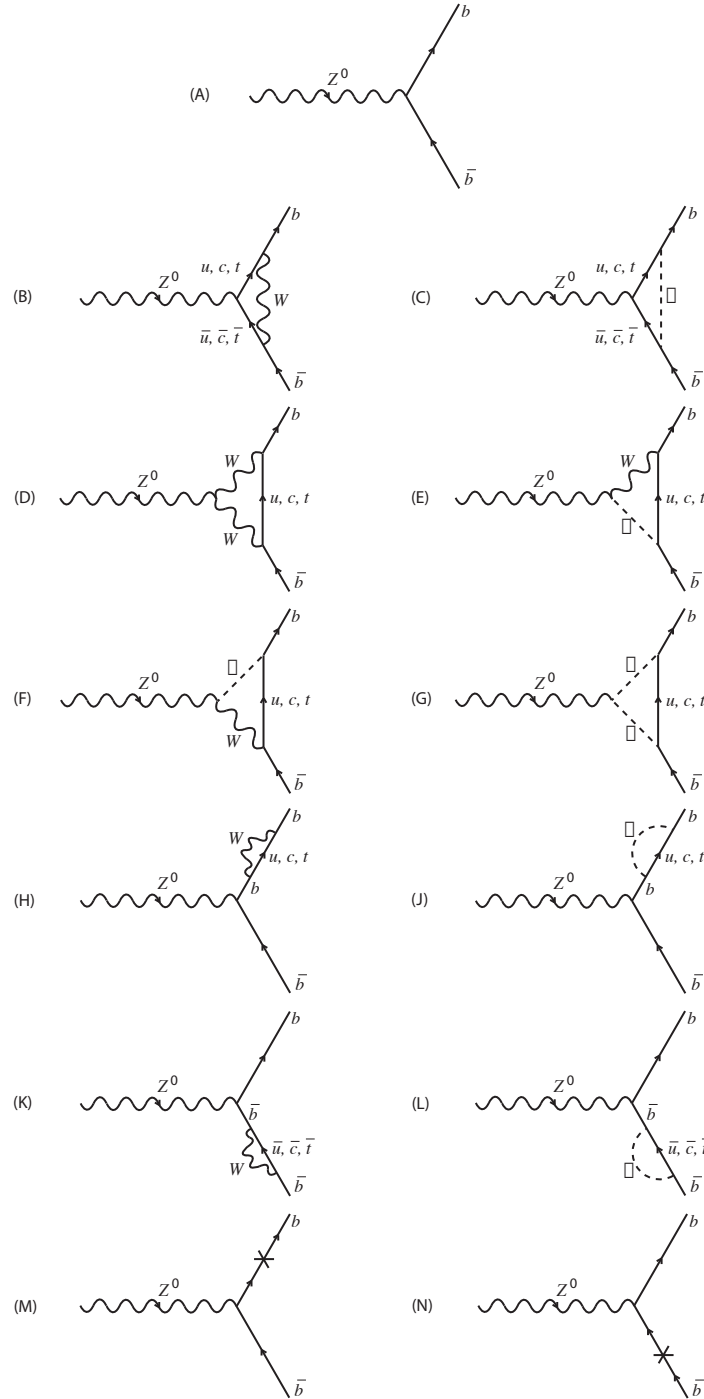
FIGURE 2. Feynman diagrams which contribute to $Z^0 \to b\bar{b}$ in the 't Hooft-Feynman gauge. Diagrams for $Z^0 \to c\bar{c}$ are identical apart from replacing $q = +\frac{2}{3}$, $I_3^W = +\frac{1}{2}$ quarks with $q = -\frac{1}{3}$, $I_3^W = -\frac{1}{2}$ quarks, and vice versa.

History of R_b (From Reviews of Particle Physics, 1992 - 2002)
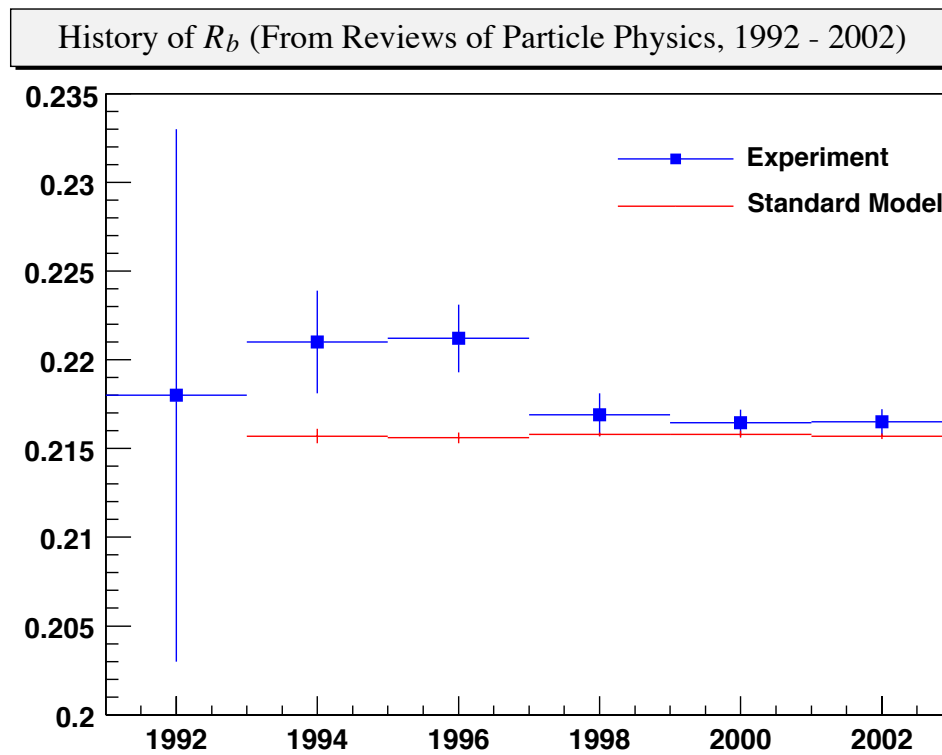
FIGURE 3. History of the R_b measurement over the past decade. The sudden shift of the measured value toward the Standard Model prediction after 1996 coincided with SLD's first measurement of R_b.
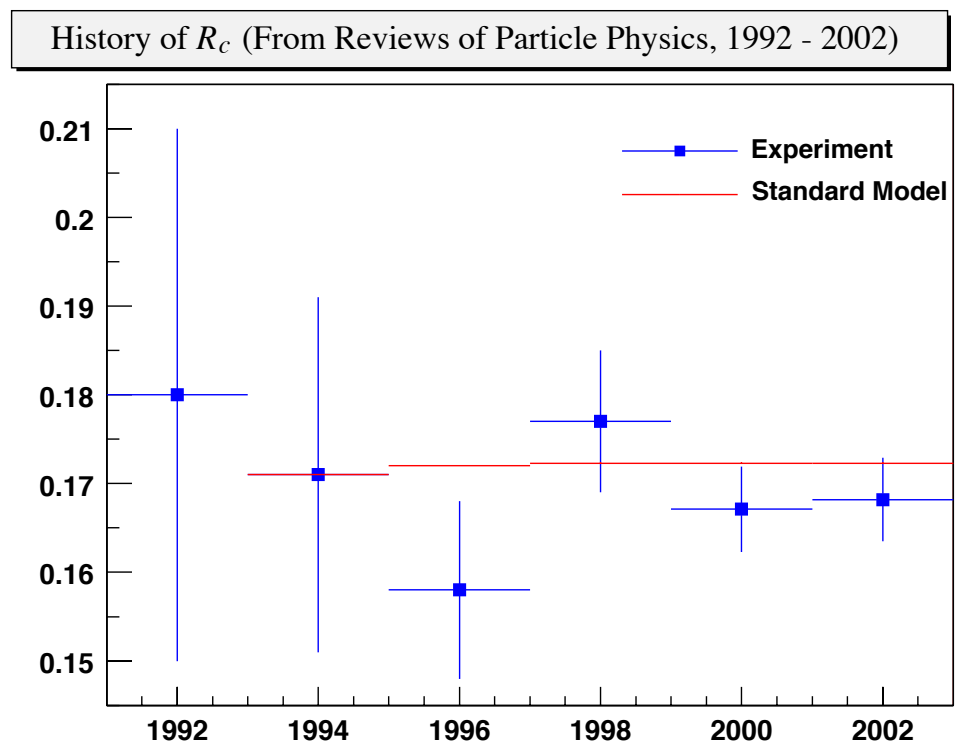
FIGURE 4. History of the R_c measurement over the past decade.

measurements at the time ruled out the Standard Model at better than the 99.9% confidence level for a t quark mass of 175 GeV.

Several issues contributed to the R_b crisis: Measurements from DELPHI underestimated the detector resolution systematic uncertainty; the OPAL measurement miscalculated the hemisphere correlation and the Monte Carlo statistical uncertainty [26, 27].

2.7 $Z^0 \rightarrow bs$ in Models Beyond the Standard Model

Secretary of Defense Donald Rumsfeld once famously remarked that "as we know, there are known knowns; there are things we know we know. We also know there are known unknowns; that is to say we know there are some things we do not know. But there are also unknown unknowns – the ones we don't know we don't know. And if one looks throughout history..., it is the latter category that tend to be the difficult ones" [28]. Experimentally, the Standard Model is in very good shape: All the fermions of three families of quarks, leptons, and neutrinos have been seen, and the Standard Model is consistent with high precision electroweak measurements. We know the answers to most of the questions: They are, increasingly, what Rumsfeld would call "known knowns." There are numerous other models which build on the success of the Standard Model, but with far less empirical support and with predictions that remain to be tested experimentally. We know some of the questions to ask, but we do not yet know the answers. Such models constitute Rumsfeld's "known unknowns." Implicit in any search for what is ostensibly a forbidden process is a latent hope that something new will be found,

R_b results

ALEPH (92)	**lifetime**	
0.2192±0.0022±0.0026		
DELPHI (92+93 prel)	**lifetime**	
0.2216±0.0017±0.0027		
DELPHI (92+93 prel)	**mixed**	
0.2231±0.0029±0.0035		
DELPHI (92+93 prel)	**multivariate**	
0.2186±0.0032±0.0022		
OPAL (92-94 prel)	**lifetime + lepton**	
0.2197±0.0014±0.0022		
ALEPH (90+91)	**event shape**	
0.228±0.005±0.005		
L3 (91)	**event shape**	
0.222±0.003±0.007		
LEP	**lepton fits**	
0.2219±0.0039		
SLD (93+94 prel)	**lifetime**	
0.2171±0.0040±0.0037		
Average	**SM=0.2155**	
0.2205±0.0016		

R_c = 0.172 (fixed)

0.2   0.21   0.22   0.23   0.24

R_b

FIGURE 5. Measurements of R_b during the "R_b-R_c crisis" in 1995, as shown at EPS-HEP 95.
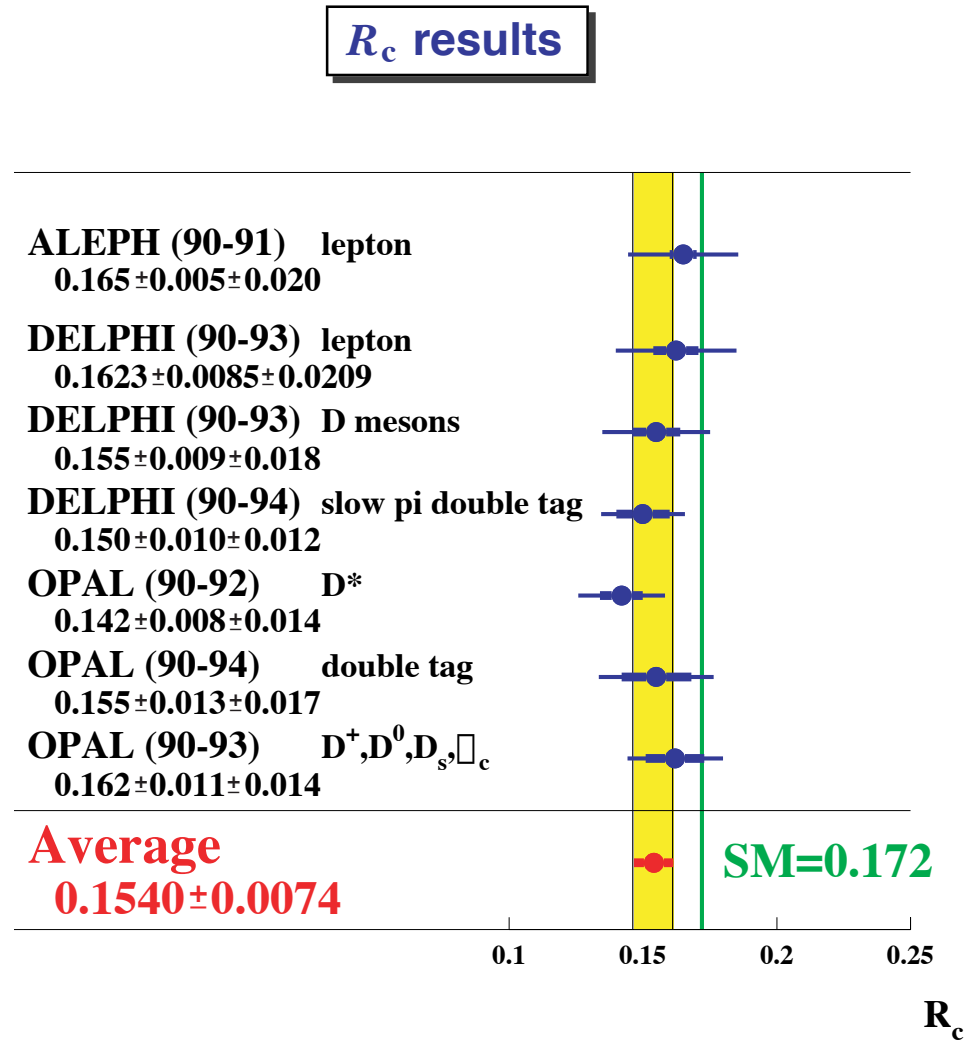
FIGURE 6. Measurements of R_c during the "R_b-R_c crisis" in 1995, as shown at EPS-HEP 95.
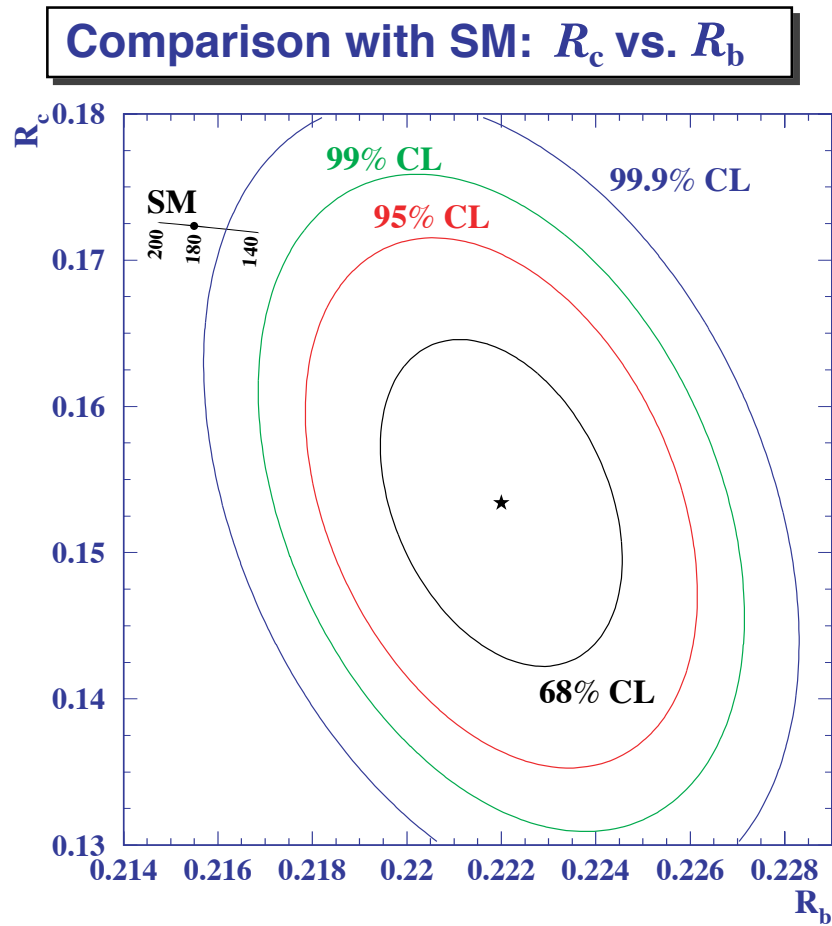
FIGURE 7. Measurements of R_b and R_c had ruled out the Standard Model with a t quark mass of 175 GeV at better than 99.9% C.L. during the "R_b-R_c crisis" in 1995, as shown at EPS-HEP 95.

that new questions will have to be asked, and that one of Rumsfeld's "unknown unknowns" will cease to be so, giving the field of physics a new "known unknown" to pursue. But it is to some of the existing "known unknowns" – models that build on the success of the Standard Model – that we now turn.

The most model independent and general flavor changing neutral current Lagrangian may be written

$$\mathcal{L} = -\frac{g}{2\cos\theta_W}\bar{b}\left[\gamma^\mu\left(g_V - g_A\gamma^5\right) + \frac{i\sigma^{\mu\nu}q_\nu}{m_b + m_s}\left(\kappa - \tilde{\kappa}\gamma^5\right)\right]Z^0_\mu s. \quad (2.139)$$

The first term in square brackets is probed by $B \to X_s l^+ l^-$. The second term is probed by $Z^0 \to bs$ and is not constrained elsewhere [29].

What follows is a survey (which is by no means exhaustive) of some of the models which go beyond the Standard Model and a speculative discussion of their respective effects on flavor changing neutral currents.

– The two Higgs doublet extension of the Standard Model, under most theoretical assumptions, produces an enhancement in R_{bs}. Figure 8 illustrates the additional Feynman diagrams which contribute to $Z^0 \to bs$. Most models of this type attempt to eliminate flavor changing neutral Higgs boson exchange, but contributions from the charged Higgs boson in particular – which emerges from the extra Higgs doublet – may nonetheless increase R_{bs} significantly [30]. And in models which do not *a priori* eliminate flavor changing neutral Higgs couplings, the branching ratio $\mathcal{B}(Z^0 \to bs)$ may be as high as $\sim 10^{-6}$ [31].
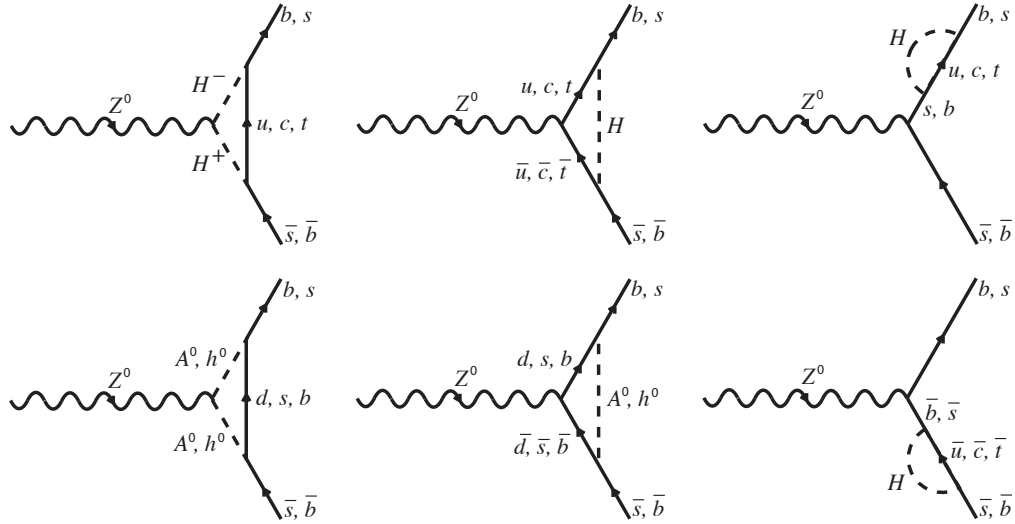
FIGURE 8. Additional Feynman diagrams in two Higgs doublet models which contribute to $Z^0 \to bs$.

– Gluino exchange in minimal supersymmetry provides only a small contribution to R_{bs} compared to the contribution from the Standard Model [32].

– Left-right symmetric models include additional gauge fields analogous to the $W_{a\mu}$ fields from the $SU(2)_L$ gauge group in the Standard Model. These additional gauge fields – call them $X_{a\mu}$ – come from the new $SU(2)_R$ gauge group. These new gauge fields have additional Feynman diagrams analogous to those in Figure 1 with the W propagators replaced by X propagators [33]. However, left-right symmetric models still predict values for R_{bs} that are not too different from the Standard Model [34].

– Models which attempt to give masses to the quarks through the analogue of the seesaw mechanism for neutrino masses require additional left-right sym-

metric singlet quarks which can give rise to flavor changing neutral currents through their mixing with the conventional quarks [35].

– Models with extra down-type quark singlets that arise naturally in string compactified gauge groups like E_6 would require a larger Yukawa matrix for the down type quarks. The CKM matrix would therefore no longer be unitary, allowing tree level flavor changing neutral currents [36, 33] and may be expected to enhance R_{bs} by approximately an order of magnitude above that predicted in the Standard Model [34].

– Models with dynamical electroweak symmetry breaking are motivated chiefly by the ongoing failure to detect the Higgs boson experimentally. One of the key questions of electroweak symmetry breaking is whether the Goldstone bosons of the Higgs mechanism are composite or elementary. Such questions concerning compositeness must always be related to some momentum or distance scale, q_ν in the Lagrangian above, since systems which appear to be elementary at some scale may in fact be composite when viewed at some higher momentum (shorter distance) scale. In other words, it may turn out that there are no elementary scalars, and that their effects are replaced by the dynamics of fermions. This usually implies the existence of new fermions and some kind of new strong interaction between them in order for a composite fermion-antifermion bound state to be formed which can play the role of the Higgs scalar fields. Technicolor is the simplest new strong confining gauge force. However, technicolor models have difficulty generating fermion masses without generating large flavor-changing neutral currents beyond what is seen empirically [37].

– Strong supersymmetric electroweak symmetry breaking, so called "S-color," where the "S" stands for "super" or "scalar," can be thought of as the superpartner to the technicolor mechanism. In these models, the Goldstone bosons of the Higgs mechanism are composites of scalars. Such models have no problem with fermion masses, which arise from ordinary Yukawa couplings, because they contain an elementary Higgs multiplet that gets a vacuum expectation value by mixing with the composite fields of the S-color sector. Moreover, flavor changing neutral currents are naturally suppressed in the usual way [38].

CHAPTER III

THE SLD DETECTOR

3.1 Overview

Proposed in 1984 and installed in 1991, the SLAC Large Detector (SLD) replaced the less sophisticated Mark II detector at the interaction point (IP) of the SLAC Linear Collider (SLC). A brief engineering run in 1991 was followed by physics data taking the next year when 10,000 Z^0 decays were recorded. By 1993, improvements in the operation of the SLC resulted in increased luminosity and over 50,000 Z^0 decays logged. For the 1994-95 run, further improvements in SLC hardware and operation yielded over 100,000 Z^0 decays recorded. The SLD vertex detector was upgraded for the 1996 run, but because of scheduling constraints, budget cuts, and a fire in the North Damping Ring of the SLC, the run lasted only two and a half months. Against these odds, however, the SLC still managed to deliver 50,000 Z^0 decays. The final SLD run began in mid 1997 and continued until mid 1998, but ended abruptly one week early because of a vacuum leak in the SLC positron source. A total of over 350,000 Z^0 decays were recorded [39]. This history is summarized in Figure 9.

The SLD was a general purpose particle physics detector with almost complete solid angle coverage. The layout of the detector was similar to an onion,
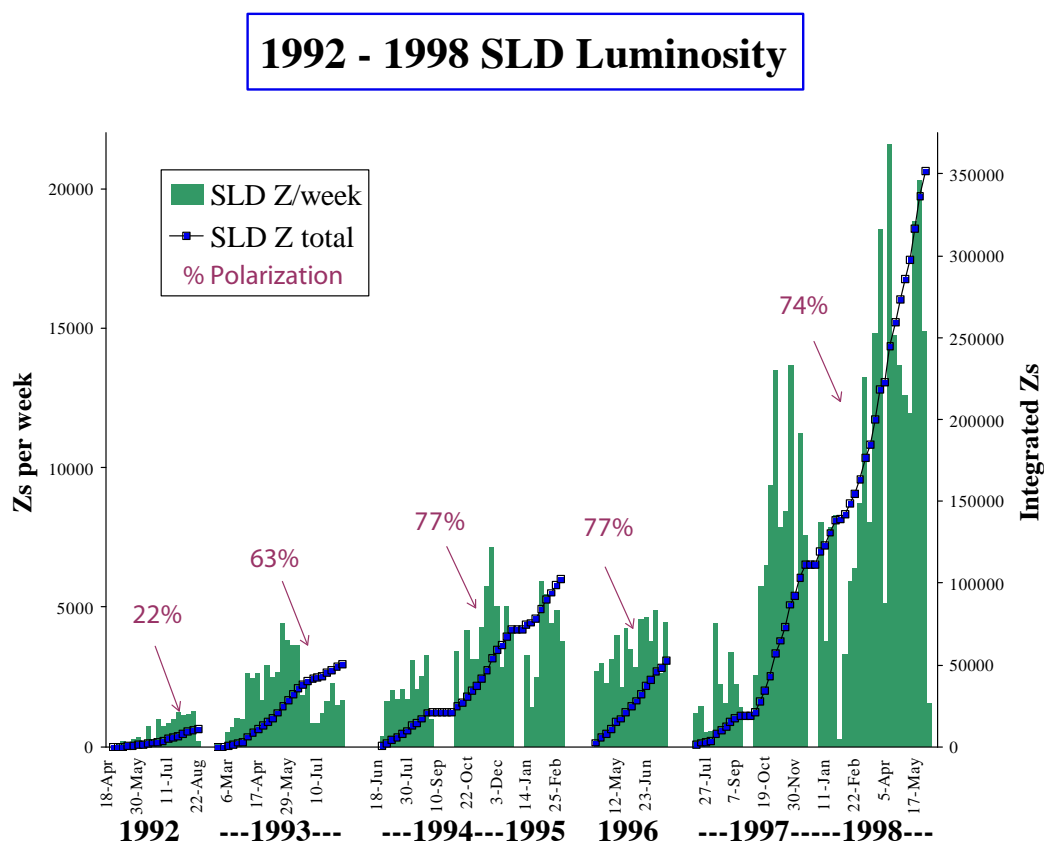
FIGURE 9. SLD luminosity showing the performance improvements over the years from 1992-1998. The bars show luminosity delivered per week and the squares show integrated luminosity for each run. The numbers give the average polarization for the run.
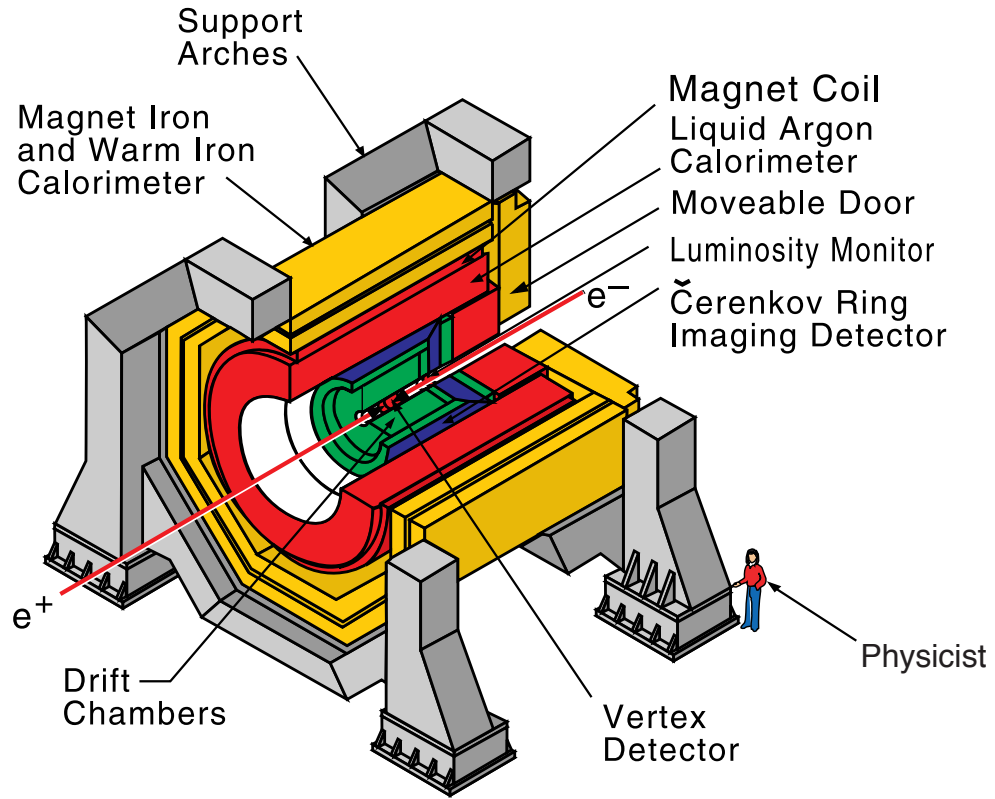
FIGURE 10. Cutaway of the SLD detector.

with multiple layers where each different layer was intended to measure different aspects of a Z^0 decay. The detector consisted of a cylindrical barrel with endcaps on each end. In this analysis, only events which were well contained within the barrel region of the detector were considered. The detector is illustrated in Figure 10.

Particle tracking and momentum measurements were provided by a CCD vertex detector and a high resolution central drift chamber (CDC) all in a 0.6 Tesla magnetic field provided by a conventional aluminum solenoid. Particle identification was provided by a Cherenkov ring imaging detector (CRID) in which

Cherenkov light from a charged particle was optically focused onto a detector in such a way that the Cherenkov angle and in turn the velocity of the particle could be measured. The calorimeter consisted of two parts: a liquid argon calorimeter (LAC) with lead radiators was located inside the solenoid, and the laminated iron of the magnetic flux return was instrumented with limited-streamer-mode tubes to complete the energy measurement. The streamer tubes of this warm iron calorimeter (WIC) were instrumented with strip readout to provide muon tracking in addition to calorimetric data. A cross section of the detector is illustrated in Figure 11.

3.2 Luminosity Monitor (LUM)

The Luminosity Monitor Small Angle Trigger (LMSAT), or more often simply the luminosity monitor (LUM) was used to measure the luminosity delivered by the SLC. It worked by measuring the rate of small-angle Bhabha scattering events, $e^+e^- \rightarrow e^+e^-$. This process was ideal for measuring the luminosity because of the large event rate and the dominance of the QED t-channel photon exchange, which could be precisely calculated in QED. The LUM covered the angular region between 28 and 65 milliradians: The cross section for $e^+e^- \rightarrow e^+e^-$ into this region was approximately 120 nanobarns, and was four times the hadronic Z^0 cross section at the Z^0 peak [40].

Designed and built at the University of Oregon in collaboration with the University of Tennessee, the LUM was a finely-segmented silicon-tungsten sampling calorimeter which pioneered the use of silicon calorimetry. Indeed, it proved to be
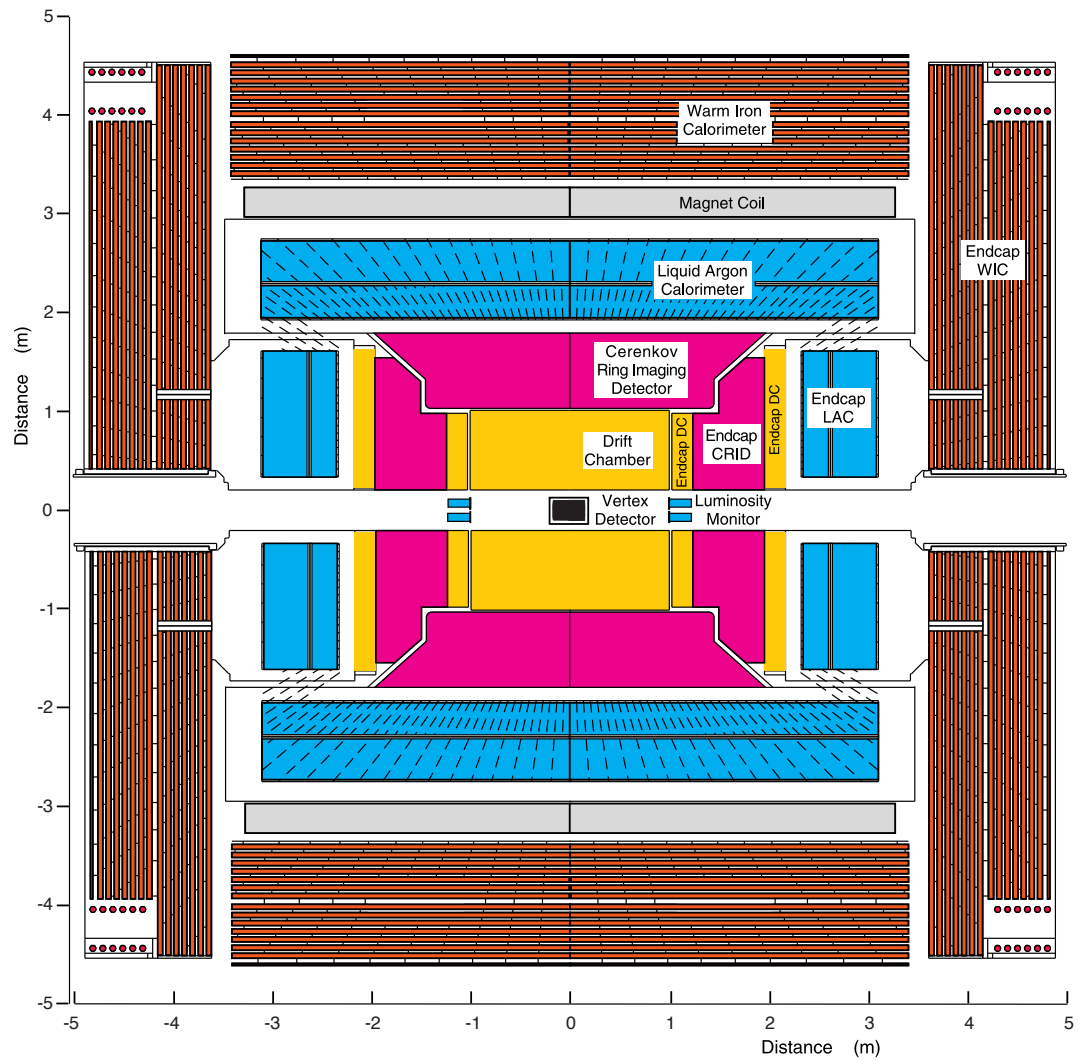
FIGURE 11. Cross section of the SLD detector along the beamline.
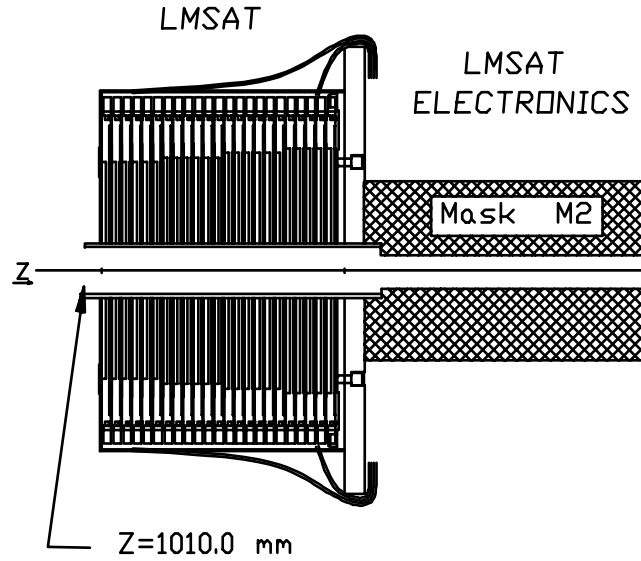
FIGURE 12. Luminosity Monitor.

such a successful design that two of the four LEP experiments (OPAL and ALEPH) subsequently replaced their luminosity monitors with silicon-tungsten calorimeters similar to the LUM [41].

Consisting of 23 layers of alternating tungsten radiator plates and highly segmented silicon detectors, the LUM was located about 1 meter downstream from the IP [41, 42, 43, 44]. Electromagnetic showers developed in the tungsten radiator plates and the ionization signal was detected in the silicon detectors with an energy resolution of about $\pm 3\%$ at 50 GeV. The LUM is illustrated in Figures 12, 13, and 14.

Beyond measuring luminosity, the LUM also performed a critical function when tuning the SLC for collisions. Virtually any campaign to reduce beam in-duced backgrounds necessarily started with the north and south LUMs (for the
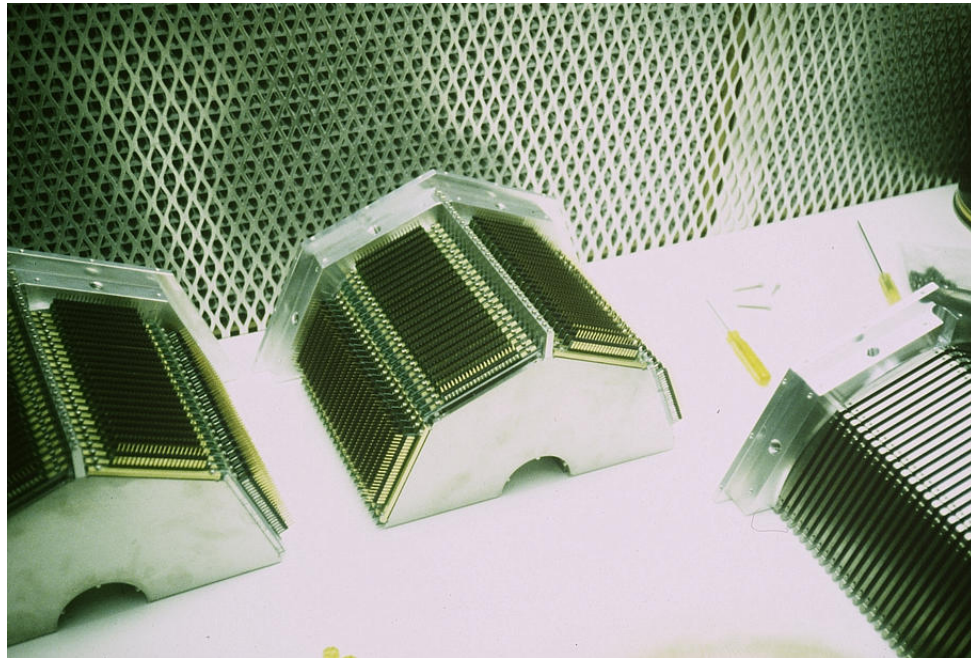
FIGURE 13. Photograph of three of the four luminosity monitor modules during construction.
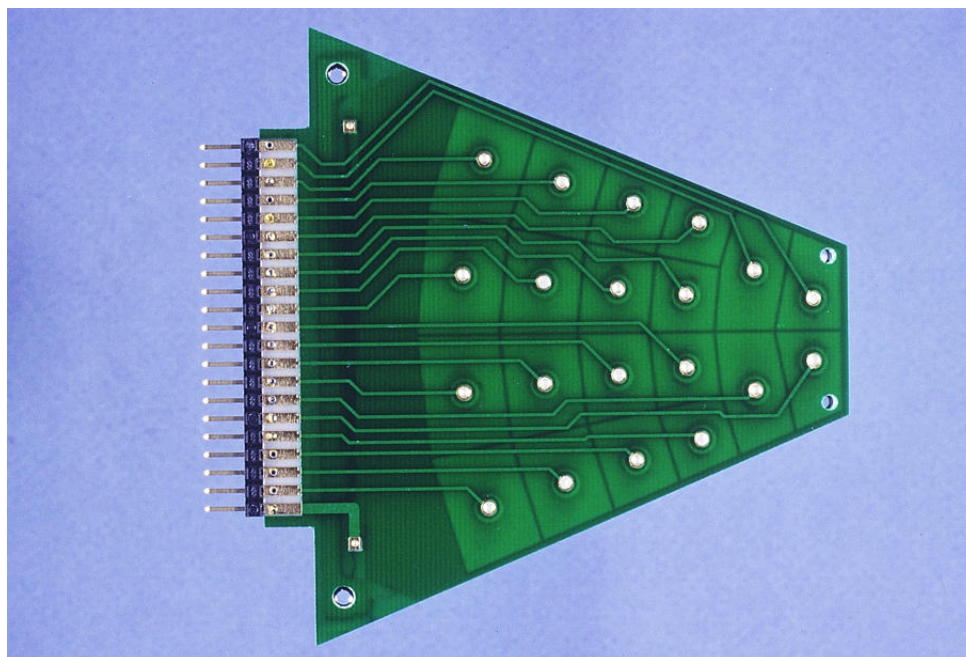
FIGURE 14. Photograph of one octant of one layer of the the luminosity monitor silicon detector. The silicon pads are visible through the G10 motherboard.

positron and electron beams respectively) because when backgrounds were high, other SLD detector subsystems could not be activated without risking damage.

3.3 Vertex Detector (VXD3)

Starting at the interaction point and moving radially outward, the first onion-like layer of the SLD was the vertex detector (VXD). The purpose of the VXD was to measure the trajectories of charged tracks in a Z^0 decay event with sufficient precision that by extrapolating the tracks back to the interaction region (IR), it was possible to distinguish between tracks coming from the primary vertex (PV) located at the interaction point (IP), and tracks coming from any secondary or tertiary vertices associated with the decays of particles containing heavy quarks. Indeed, as will be explained elsewhere, this was the entire basis of heavy-flavor quark tagging.

The VXD employed in SLD utilized silicon pixel charged coupled devices (CCDs) as the medium to detect the ionization deposited by charged particles, and was the first such use of CCDs in a colliding beam environment. The linear collider environment made the use of a vertex detector based on CCD technology appealing for the following reasons [45]:

1. very small beam spot producing a well defined primary vertex.

2. small diameter beam pipe compatible with the limited area coverage practical with CCD detectors.

3. long interval between beam crossings. While this interval was not sufficient for complete readout, the background integrated during readout would be

only ~ 10 beam crossings as opposed to $\sim 10^5$ beam crossings for a typical storage ring.

Over the years, SLD collected physics data using two different CCD technology based vertex detectors. After tests with a prototype detector VXD1 consisting of a few ladders, the 120 Mpixel VXD2 was installed for physics runs from 1992-95. In 1996 an improved vertex detector, VXD3 [45], was installed. VXD3 was made possible by advances in CCD technology, and with 307.2 Mpixels was an evolutionary improvement over VXD2 both in terms of the solid angle coverage and impact parameter resolution. Because this analysis used only the data collected from 1996-98, VXD2 will not be described here. The VXD3 detector is illustrated in Figures 15 and 16. Figure 17 shows the position of VXD3 relative to other components in the beam line near the interaction point of the SLC.

VXD3 used 96 CCDs [46] each with an active area measuring 80×16 mm^2 (see Figure 21). Two CCDs were mounted on a beryllium substrate to form a ladder, as shown in Figure 18. The two CCDs overlapped by ≈ 1 mm to allow their relative alignment using charged tracks. These ladders were mounted onto a series of three concentric beryllium annuli in a shingled arrangement, so that complete azimuthal coverage was attained, with ≈ 500 μm overlap between adjacent ladders for alignment purposes. This is shown in Figure 19 and 20. VXD3 was designed with a small inner layer of mean radius 28 mm, with the radii of the two outer layers considerably larger to allow for a long lever arm for precise extrapolation back to the IR: The mean radii of the middle and outer layers by comparison were 38.2 mm and 48.3 mm respectively.
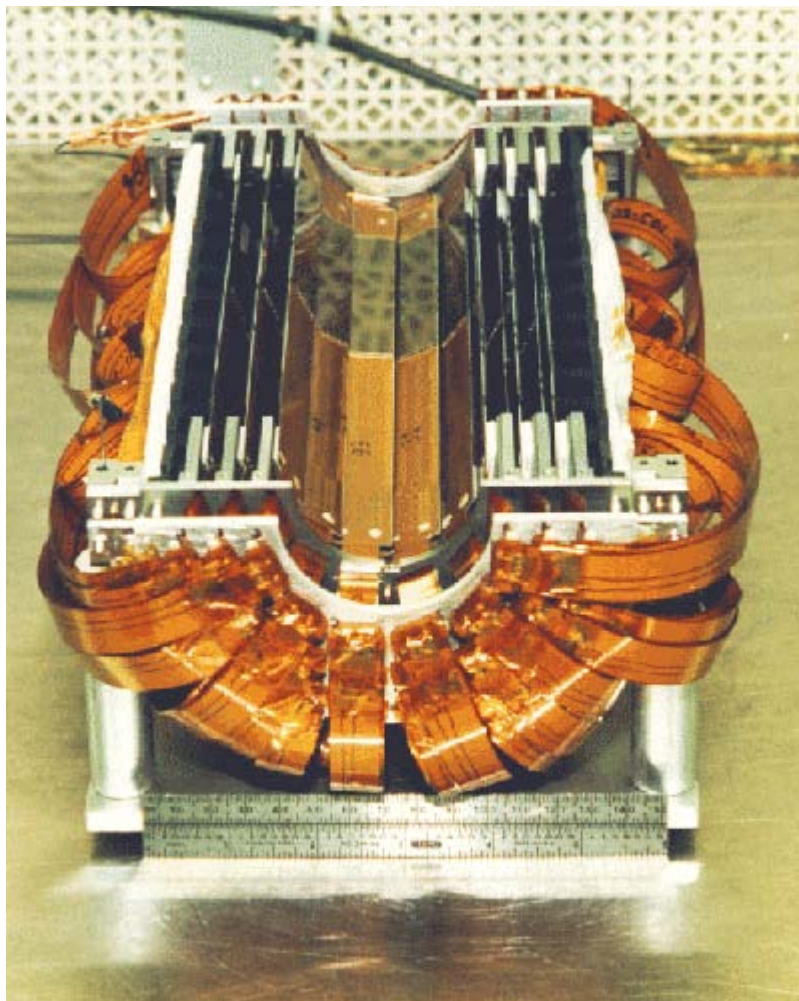
FIGURE 15. Photograph of one half of the VXD3 vertex detector before installation at the interaction point. (Photographer: J. Brau.)
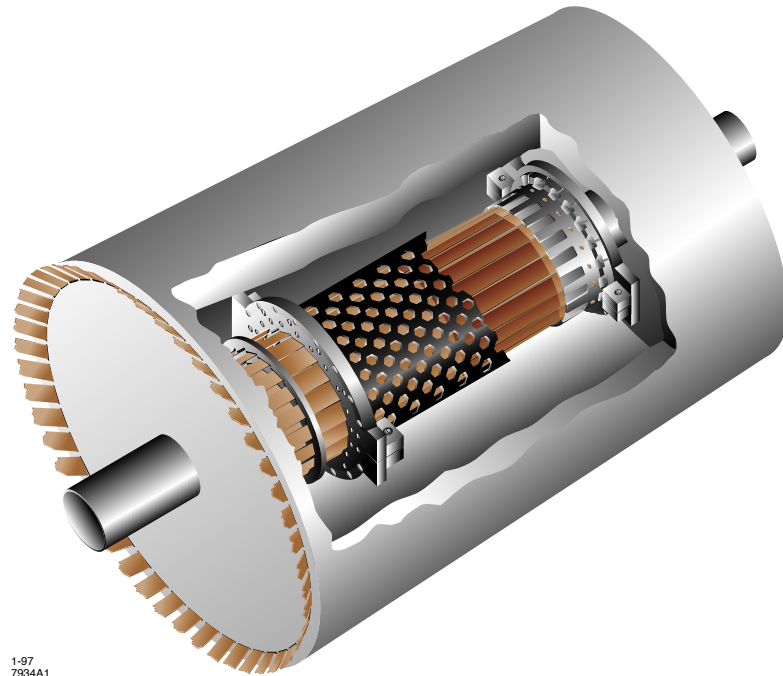
FIGURE 16. Cut-away isometric drawing of the VXD3 vertex detector.
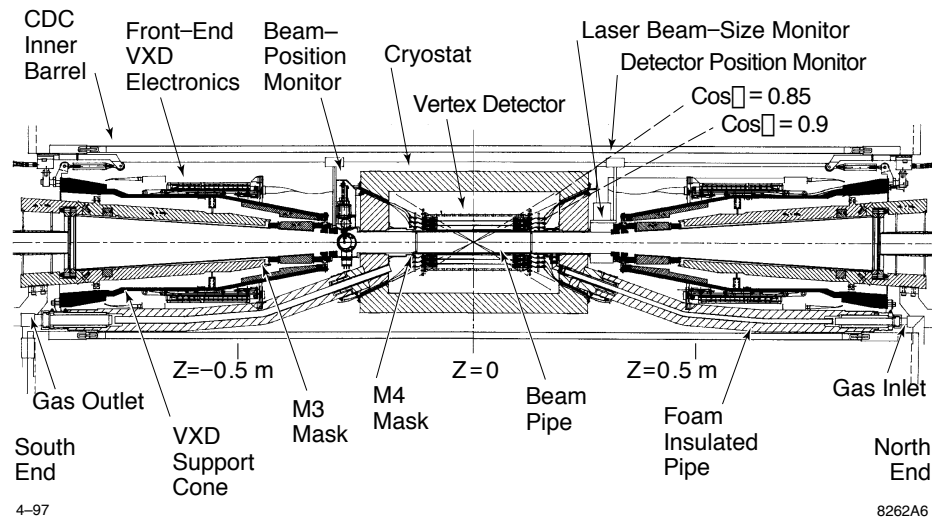
FIGURE 17. The SLC beam line area extending one meter on either side of the SLD IP. The VXD3 is in the center, within its cryostat.

CCD Fiducials   Flex-Circuit
Fiducials

Outer CCD

Pigtail
(Kapton/
Copper
stripline)

Inner CCD

Beryllium
substrate

North End   South End

4–97   8262A11
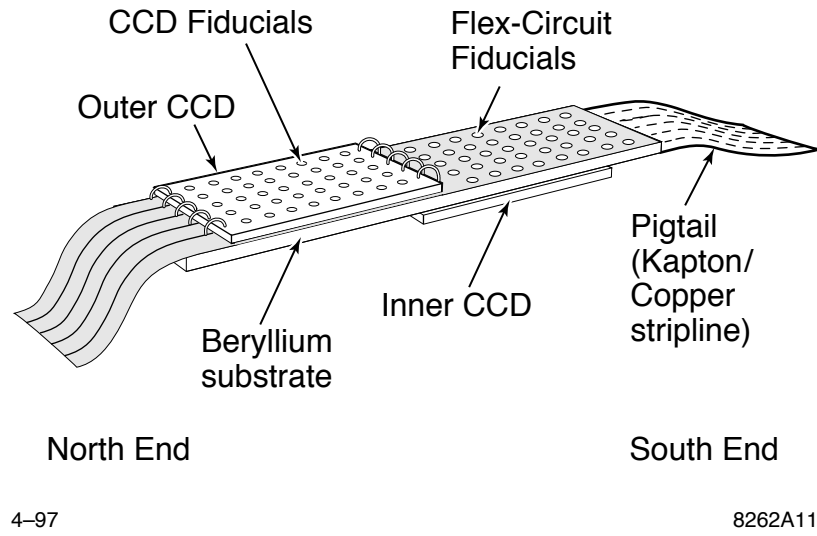
FIGURE 18. Basic CCD ladder design used for VXD3. Active length = 16 cm

Support Shell   Beam–Pipe

Gas Shell

Y

X

5–97
8262A4   Ladder
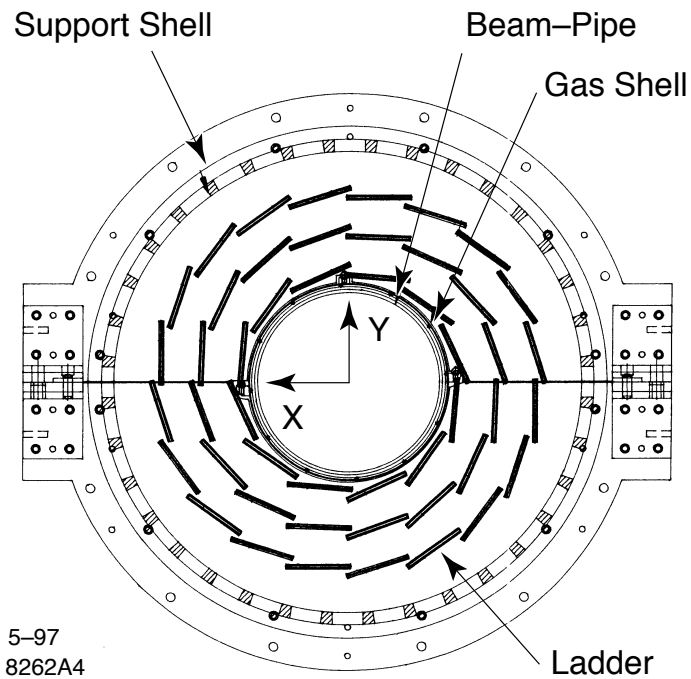
FIGURE 19. Schematic layout of VXD3 in the $r\phi$ view.

Striplines
Support Shell
Cryostat
M4
Mask
3 Barrels
Cosθ = 0.85
Cosθ = 0.9

Gas
Exit
Faraday
Cage
Beam–Pipe
& Gas Shell
Gas Inlet
Micro–Connectors

South End
North End

0   5   10
cm

4–97
8262A3
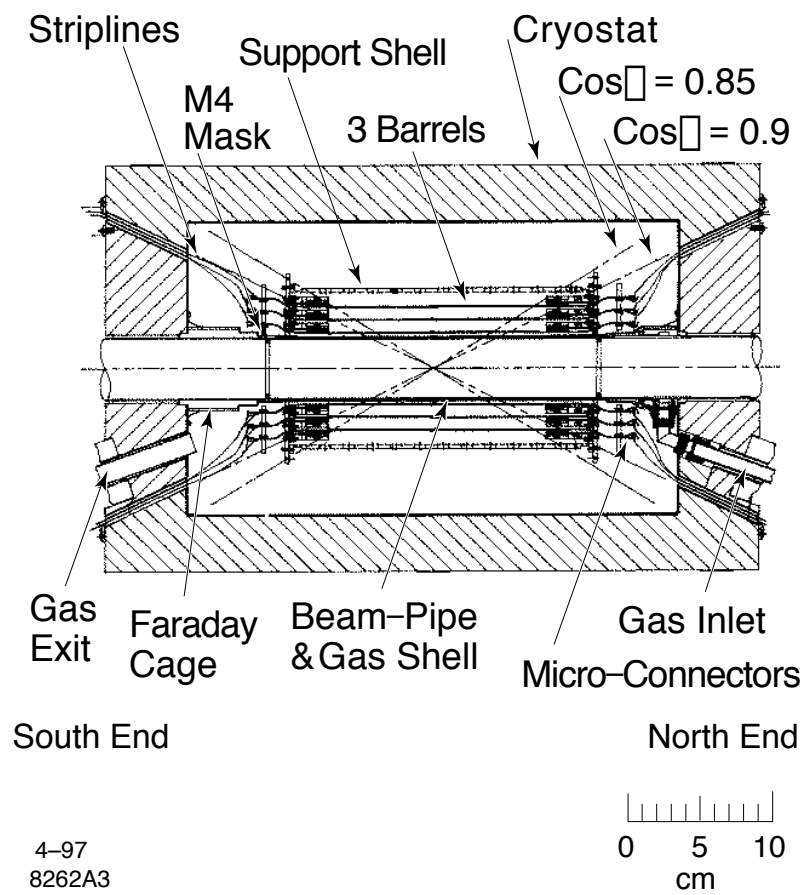
FIGURE 20. Schematic layout of VXD3 in the rz view.

80 x 16 mm^2 Active area

1 of 4
Output
nodes

≤ 300 μm

Bond pads
(2mm from
long edges)

5–97

8262A12
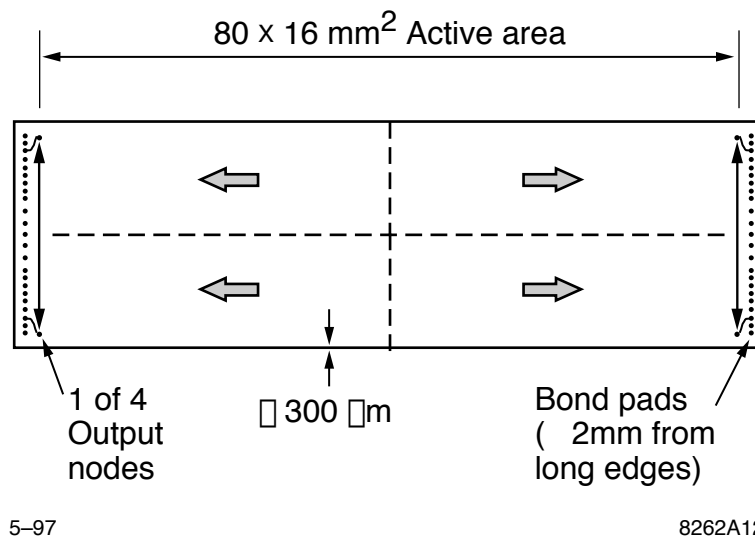
FIGURE 21. Basic architecture of the CCDs used in VXD3. The parallel register (I register,) shifts signal charge packets to each end of the device. A serial register (R register) at each end shifts charge packets to a pair of output circuits. The I clock runs at 100 kHz while the R clock runs at 5 MHz.

Each individual pixel was $20 \times 20 \times 20$ μm^3. Each CCD had a total of 4000×800 pixels and was divided into four quadrants, with one output amplifier for each quadrant located at the four corners of the CCD. Readout was accomplished as follows: The I clock caused rows of signal charge packets in the parallel register (I register) to shift towards the two shorter sides of the CCD, where the serial register (R register) was located. Once a row had been loaded into the R register, the R clock successively moved each signal charge packet in the register to the output amplifier. The I clock ran at 100 kHz while the R clock ran at 5 MHz. This is illustrated in Figure 21. To read out the entire dectector took 0.2 seconds, or 24 beam crossings at 120 Hz. Because the pixel occupancy was $< 10^{-4}$, rejecting the background pileup hits was not difficult.

VXD3 was mounted in a nitrogen gas cryostat (see Figure 20) and maintained at a temperature of about 185 K. It was necessary to operate the detector at low temperatures to reduce lattice defects caused by radiation damage, which could cause trapping centers to develop in the silicon. Because CCDs are read out serially, a trapping center affected not just nearby pixels, but could impact the charge transfer out of all pixels behind it in that column.

For VXD3 to reach it's full potential, the CCDs had to be aligned with respect to one another and with respect to the rest of the SLD to a very high degree of precision. The alignment procedure was done in two stages: An optical survey of all ladders and all barrels was performed in order to determine the internal geometry of the detector to a degree of accuracy sufficient for the second stage in which beam-related tracks were used for the final alignment. The ladder survey determined the geometry of each CCD surface and the relation of the two CCDs to each other, while the barrel survey fixed the relative positions of the ladders to each other. The optical survey determined the global geometry to within < 20 μm (< 1 pixel) rms. A secondary goal of this optical survey was to measure aspects of the geometry which would be difficult to determine from tracks, such as the complex shapes of the CCDs themselves, the gravitational sag of the ladders, and temperature scaling corrections. These three aspects were important factors in achieving the 4 μm precision.

The optical survey was followed by a track-based internal alignment [47]. VXD vectors were forced to go through two track hits precisely, with the track curvature measured by the central drift chamber (CDC). The residual of a third

hit or other constraint to this fixed vector was then measured. Several types of hit vectors from tracks were used for this process:

1. Doublets – tracks with momentum greater than 1 GeV from hadronic Z^0 decays which passed through the overlapping region (z) of two CCDs on the same ladder.

2. Shingles – tracks with momentum greater than 1 GeV from hadronic Z^0 decays which passed through the overlapping region ($r\phi$) of two ladders in the same layer.

3. Triplets – tracks with momentum greater than 1 GeV from hadronic Z^0 decays and with hits in all three layers.

4. Pairs – back to back tracks from $Z^0 \rightarrow \mu^+\mu^-$ or $Z^0 \rightarrow e^+e^-$ events, with the residuals being measured as the mis-distance between the two tracks at the IP.

5. VXD3 vs. CDC track angle matching – tracks from the $Z^0 \rightarrow \mu^+\mu^-$ or $Z^0 \rightarrow e^+e^-$ events measured by the CDC were compared with the angle measured from the hits in layers 1 and 3 of VXD3. The residual angle was converted into a residual distance on the reference CCD.

6. IP constraint – tracks from light flavor selected hadronic Z^0 decays with momentum greater than 7 GeV and with hits in layers 1 and 3. On average, such tracks should project back to the SLC interation point.

These different residual types are illustrated in Figure 22. The doublets constrained the relative locations of two CCDs on the same ladder; the shingles provided direct

connections between different ladders within a layer; the triplets related ladders on different layers; pairs related opposite regions of the detector; and the IP constraint added two further residuals for the offset of the IP from the nominal location of the event IP.

The detailed internal alignment yielded a single hit resolution of 3.8 μm (see Figure 23) and an impact parameter resolution (as a function of momentum and angle) of [48]

$$\sigma_{r\phi} = 7.8 \oplus \frac{33}{p\sin^{3/2}\theta} \; \mu\text{m} \tag{3.1}$$

$$\sigma_{rz} = 9.7 \oplus \frac{33}{p\sin^{3/2}\theta} \; \mu\text{m} \tag{3.2}$$

as explained in Figure 24.

3.4 Central Drift Chamber (CDC)

Moving radially outward away from the interaction point past the vertex detector, the next onion-like layer of the SLD was the central drift chamber (CDC). The purpose of the CDC was to measure the positions and momenta of charged particles, and was the primary tracking system for the entire SLD detector.

The CDC [49] was comprised of a cylindrical annulus of length 2 m with an inner radius of 20 cm and an outer radius 1 m. Inner and outer low-mass cylinders made from an aluminum and Hexcel fiberboard laminate surrounded an annular region containing wires strung between two dished aluminum endplates. The CDC contained 80 layers of sense wires arranged in ten staggered superlayers of eight
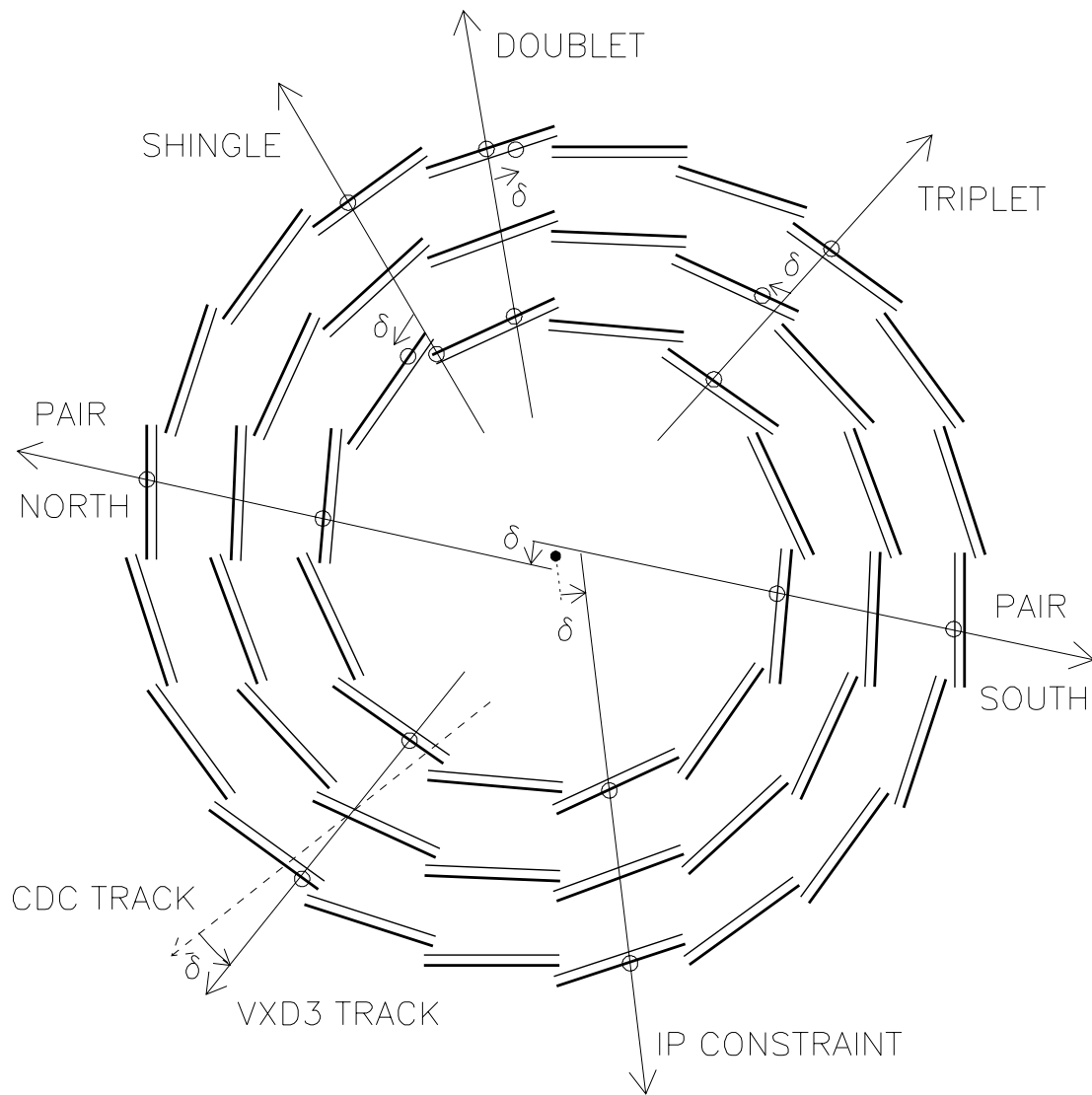
FIGURE 22. Construction of the VXD3 residual types. The thick and thin lines represent the North and South CCDs respectively.
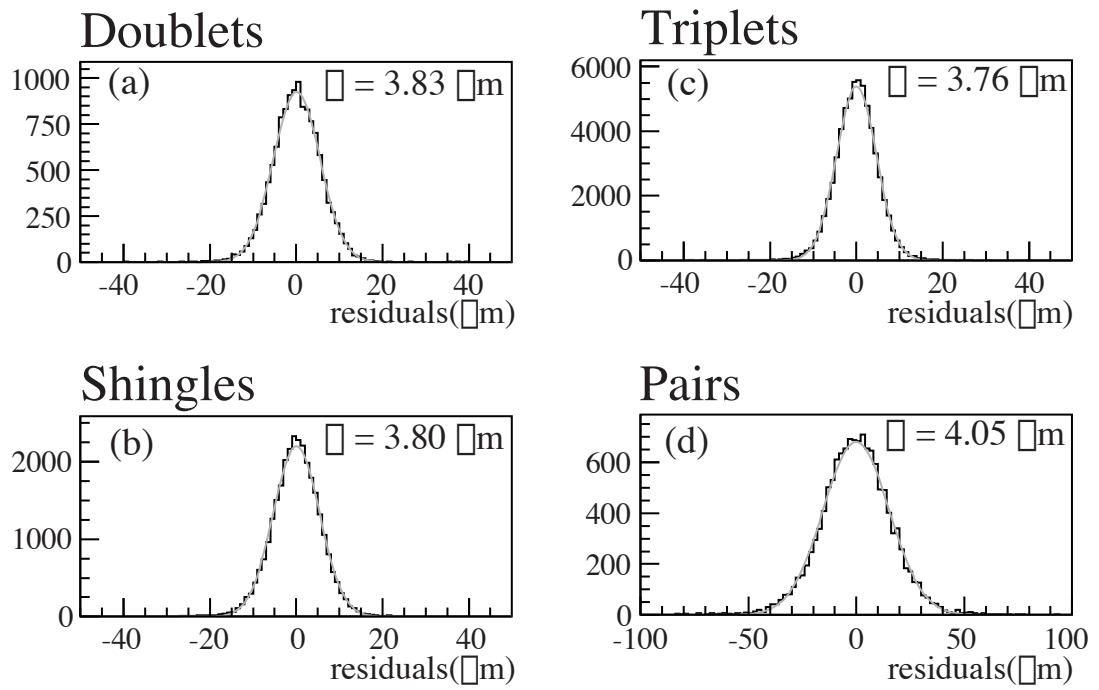
FIGURE 23. Residual distributions for (a) doublets, (b) shingles, (c) triplets, and (d) pairs. Fitting a Gaussian curve to each of these figures yields a width of 5.42 μm, 5.37 μm, 4.61 μm, and 15.27 μm, respectively, corresponding to spacial resolutions of 3.83 μm, 3.80 μm, 3.76 μm and 4.05 μm. The single hit resolution was consistently $\sim$ 3.8 μm.
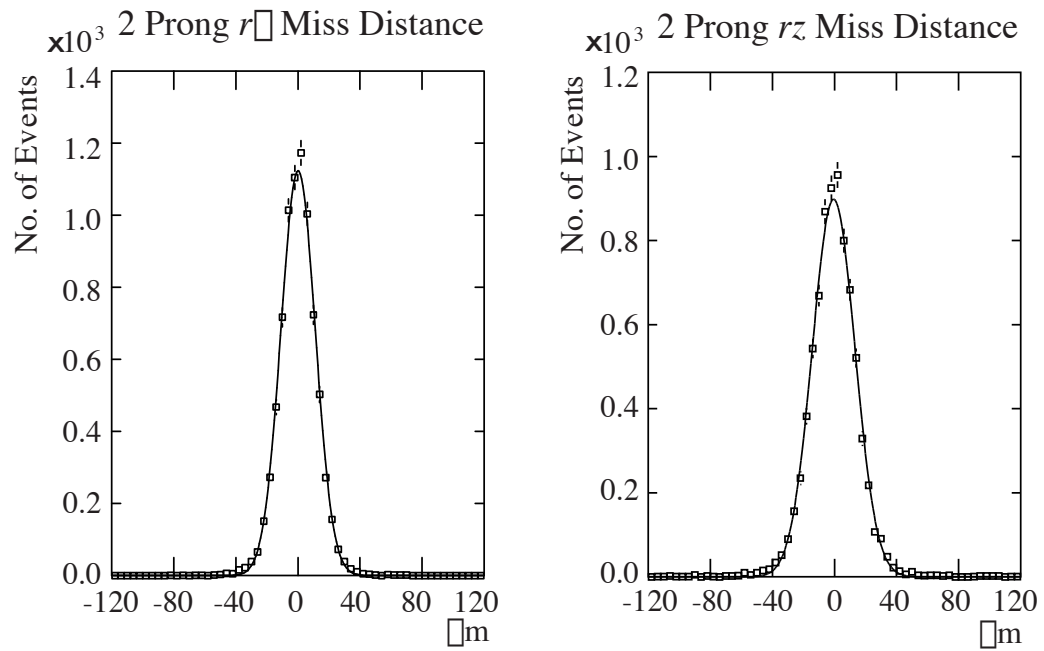
FIGURE 24. μ-pair miss distances in $r\phi$ and rz projections. Fitting a Gaussian curve to each figure yields a width of 11.0 μm and 13.7 μm for $r\phi$ and rz projections respectively. These numbers are divided by the geometric factor $\sqrt{2}$ to obtain impact parameter resolutions of 7.8 μm and 9.7 μm respecctively.

wires each. Six superlayers had a 41 mrad stereo angle with respect to the beam axis. This is illustrated in Figure 25. Each cell measured about 6 cm in ϕ by 5 cm in r and was composed of eight sense wires, 18 inner field wires held at a potential of -3027 V which focused the electric field lines to produce a charge amplification of about 10^5 in the region near the sense wires, 23 high voltage outer field wires held at a potential of -5300 V, and 2 guard wires which ran at an intermediate voltage to grade the field between the sense wires and the inner and outer field wires [50], as shown in Figure 26. The sense wires were of 25 μm gold plated tungsten while the guard wires and inner and outer field wires were of 150 μm gold plated aluminum. The CDC had a total of 5,120 sense wires in 640 cells, for a grand total of 32,640 wires.

When a charged particle transited the central drift chamber, gas molecules along the particle track were ionized. Electric fields directed the free electrons toward the sense wires (see Figure 27). Through the phenomenon of gas multiplication, the charge represented by these ion pairs was amplified by a factor of 10^4-10^5 at the sense wire. The charge incident on a sense wire served as the basis of the electrical signal developed by the drift chamber.

The gas mix was comprised of a 75% CO_2, 21% Ar, 4% isobutane, and 0.2% H_2O, yielding a drift velocity v_d of 7.9 μm/ns in the average field of 0.9 kV/cm.

The trajectory of a charged particle in $r\phi$ was determined by the addresses of the sense wires which collected ionization current. Additionally, the timing of the leading edges of the pulses was used to estimate the precise distances of the wires from the track. The position in z was determined from the ratio of the pulse heights at the two ends of the wire, and was accurate to within about 5 cm.
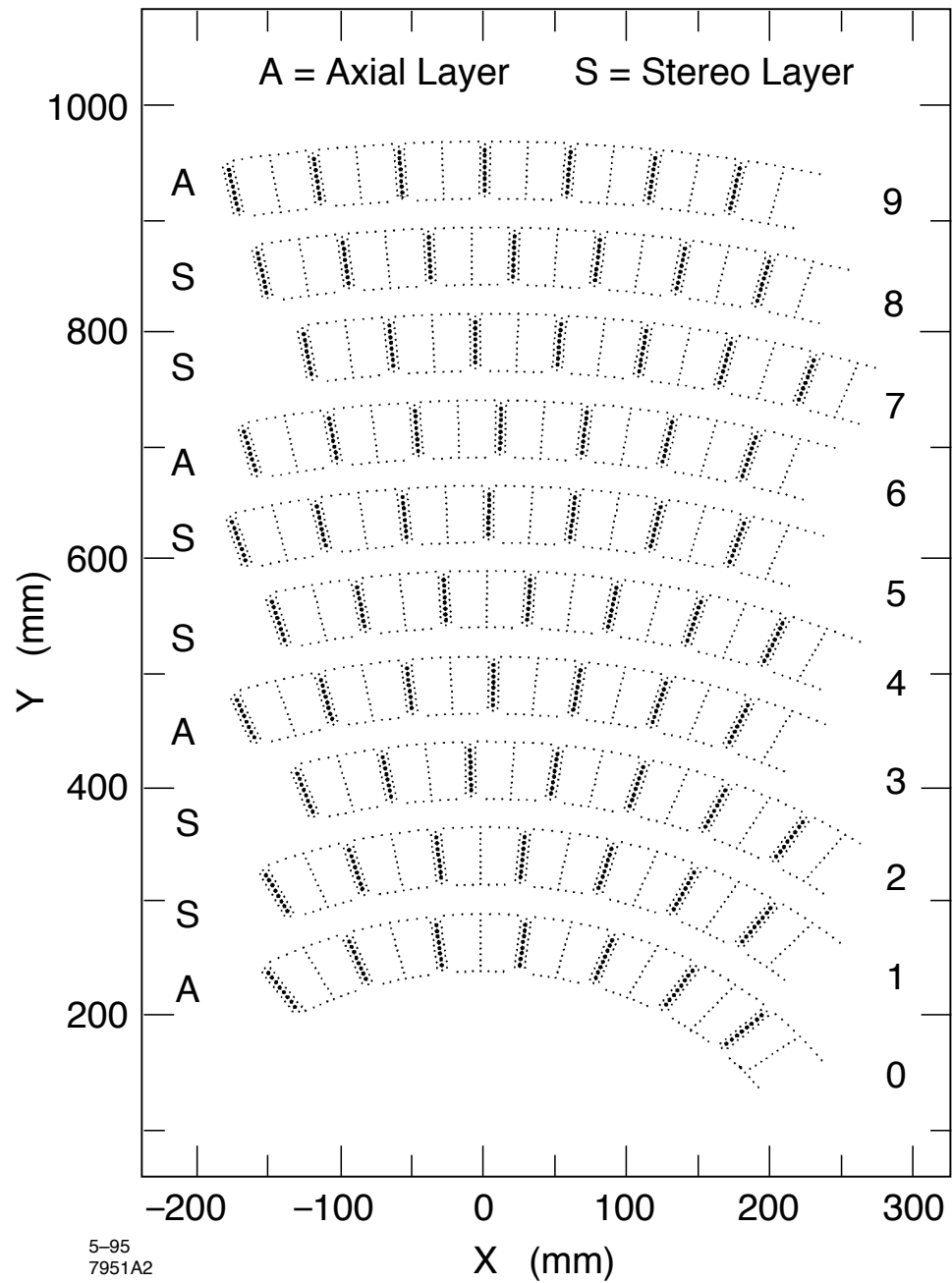
FIGURE 25. Partial view of the CDC endplate showing the 10 superlayers. Axial superlayers are labeled 'A', while the stereo superlayers are labeled 'S'.
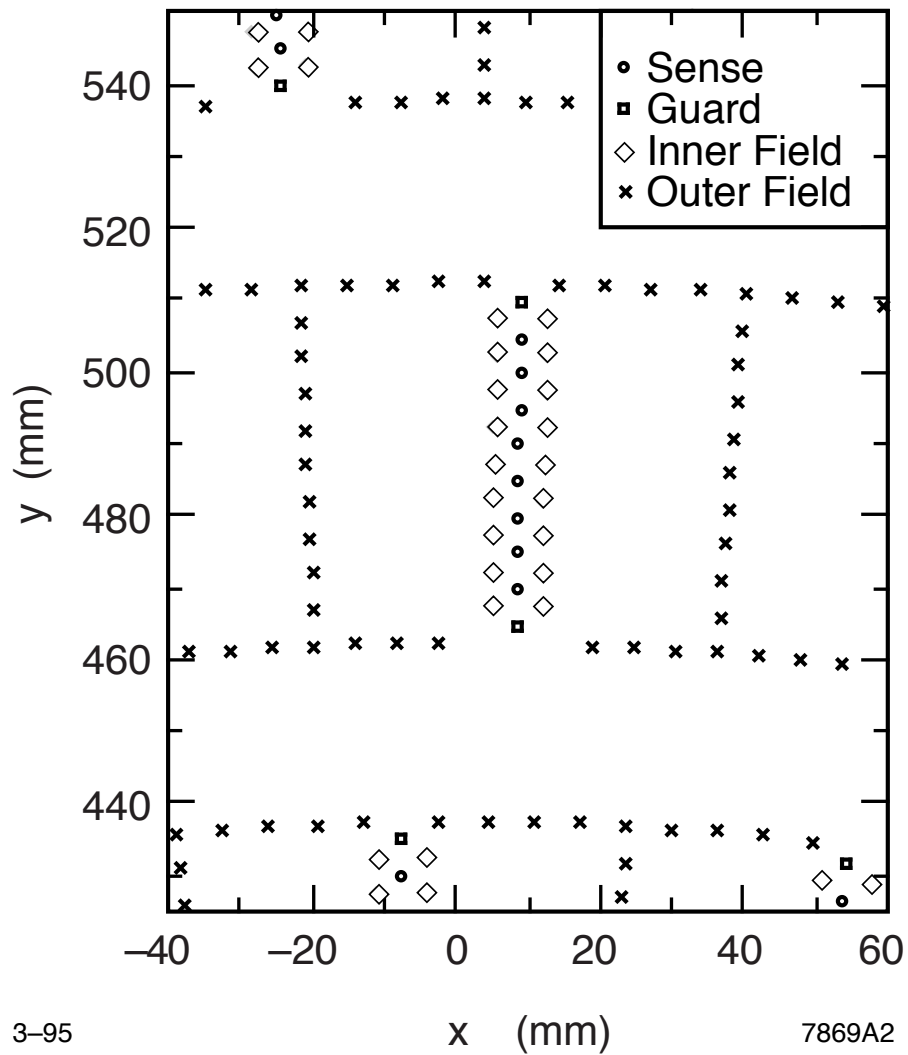
FIGURE 26. Wire layout of a single cell in an axial layer of the SLD drift chamber.The 8 sense wires (circles) are surrounded by a grid of 18 inner field-shaping wires (diamonds) and two guard wires (squares). The outer field-shaping wires are shown as x's..
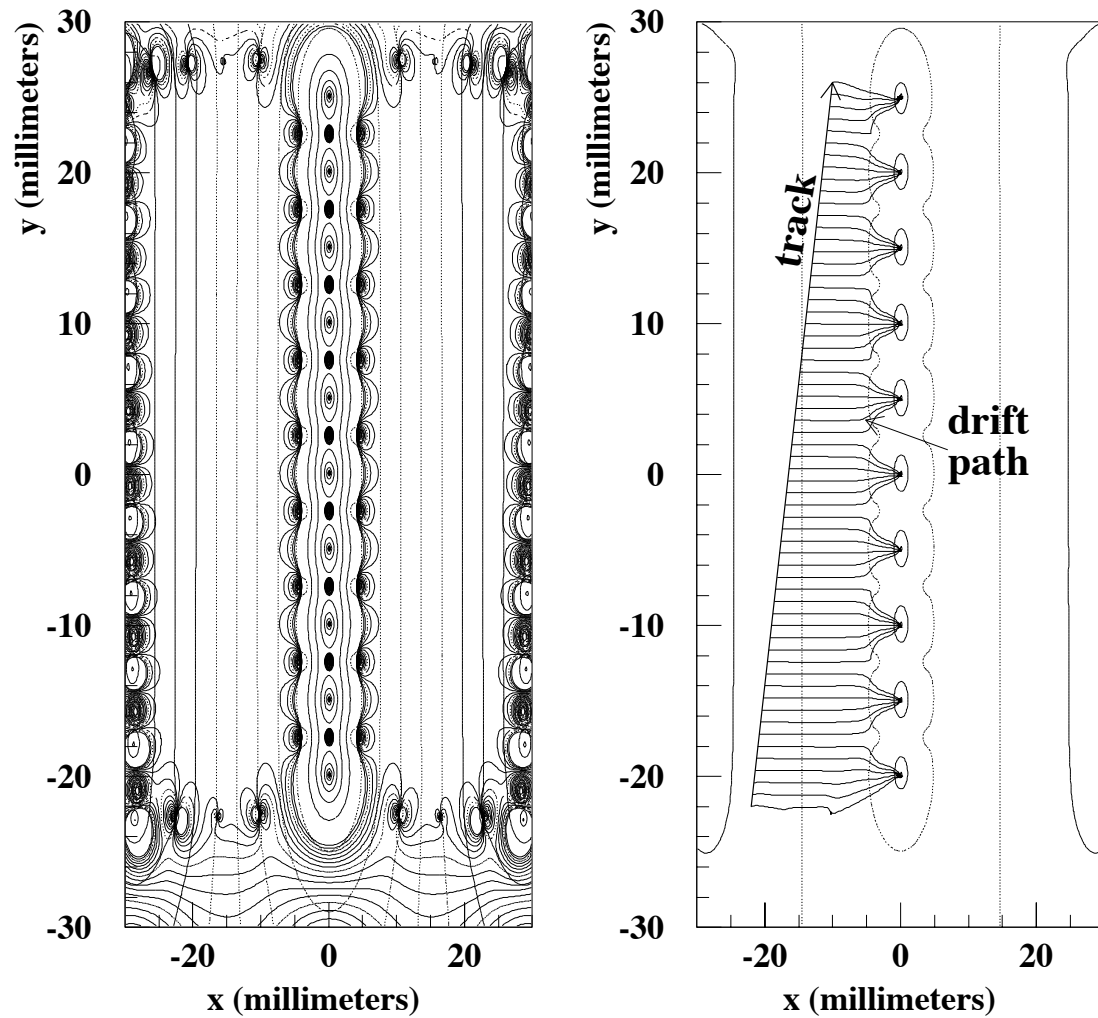
FIGURE 27. The field configuration for a CDC cell (left) and the drift paths of liberated electrons from the passage of a charged particle (right).

The hits within a cell were then combined into a vector, which was the basic element for track finding. A pattern recognition program combined the vectors from adjacent cells into track candidates: The algorithm found circular segments in $r\phi$ consistent with at least two axial superlayer vectors, and combined this with VXD hits and stereo vectors to determine the track angle in rz. A detailed fit was then performed on these track candidates taking into account electric and magnetic field variations and energy loss in the detector materials. The vectors assigned to the track were then removed and the algorithm was iterated until no more tracks were found.

The momentum resolution function of the CDC was measured using both mono-energetic $Z^0 \rightarrow \mu^+\mu^-$ events and cosmic ray events. In the case of the cosmic ray events, the upper and lower halves of each track were considered as two separate tracks, and the two measured momenta were compared. The momentum resolution function was determined to be

$$\frac{\sigma(p_\perp)}{p_\perp^2} \;=\; 0.0050 \oplus \frac{0.010}{p_\perp^2} \tag{3.3}$$

The first term represents the effect of measurement uncertainty and the second term takes into account multiple scattering.

3.5 Cherenkov Ring Imaging Detector (CRID)

The next onion-like layer of the SLD was the Cherenkov ring imagining detector (CRID) which provided the SLD with a particle identification capability crucial to this analysis. The CRID consisted of a barrel system and two endcaps, as illustrated in Figure 11.

Charged particles emit Cherenkov light whenever they pass through a medium at a velocity greater than the speed of light in that medium, i.e. such that

$$\beta n \; > \; 1 \tag{3.4}$$

where β is the ratio of the velocity of the charged particle to that of light in a vacuum, and n is the index of refraction of the material. The yield of Cherenkov photons per unit wavelength λ is proportional to $1/\lambda^2$ and the emission is therefore concentrated in the short-wavelength region of the spectrum [51]. The light is emitted continuously in conical sheets with angle θ_C to the trajectory of the charged particle:

$$\cos\theta_C \; = \; \frac{1}{\beta n}. \tag{3.5}$$

The Cherenkov ring imaging detector measureed this angle thereby giving information on the velocity of the particle. When this information was combined with knowledge of the momentum of the particle (obtained, for example, from the central drift chamber), the particle's mass could be calculated, and the identity of the particle deduced [52].

By using media of different indices of refraction, discrimination between e, $\pi^{\pm}$, $K^{\pm}$, and p over a large momentum range could be obtained. Indeed, as will be explained elsewhere, this was the basis of $K^{\pm}$ tagging in this analysis. In the SLD CRID, two different radiator materials were used: Liquid C_6F_{14} having an index of refraction of $n_{liquid} = 1.277$ and a gaseous mix of C_5F_{12} and N_2 having an index of refraction of $n_{gas} = 1.001725$. These media were chosen to provide particle identification coverage with a minimum momentum gap between the two with the liquid radiator most effective in the low momentum range and the gaseous radiator most effective in the high momentum range. Figure 28 illustrates the Cherenkov angle curves for $\pi^{\pm}$, $K^{\pm}$, and p as a function of momentum for the two radiators. Both media also had good transmission in the relevant UV wavelengths with relatively low chromatic dispersion.

Charged particles passed first through the 1 cm thick liquid radiator and the Cherenkov photons were allowed to propagate some distance before encountering the photon detector forming a "proximity focused" image at the detector. After passing through the photon detector unimpeded, the charged particles then passed through the 45 cm thick gas radiator and these Cherenkov photons were optically focused by spherical mirrors onto the opposite side of the photon detector. The Cherenkov photons, whether from the liquid or gas radiators, passed through quartz windows on the front and back of the photon detector box and photo-ionized gaseous Tetrakis Dimethyl Amino Ethylene (TMAE). An electric field drifted the photoelectrons at a constant velocity axially along the detector box to a picket fence of proportional wires where they were read out. Three coordinates gave the origin of the photoelectron: The drift time of the electron gave the
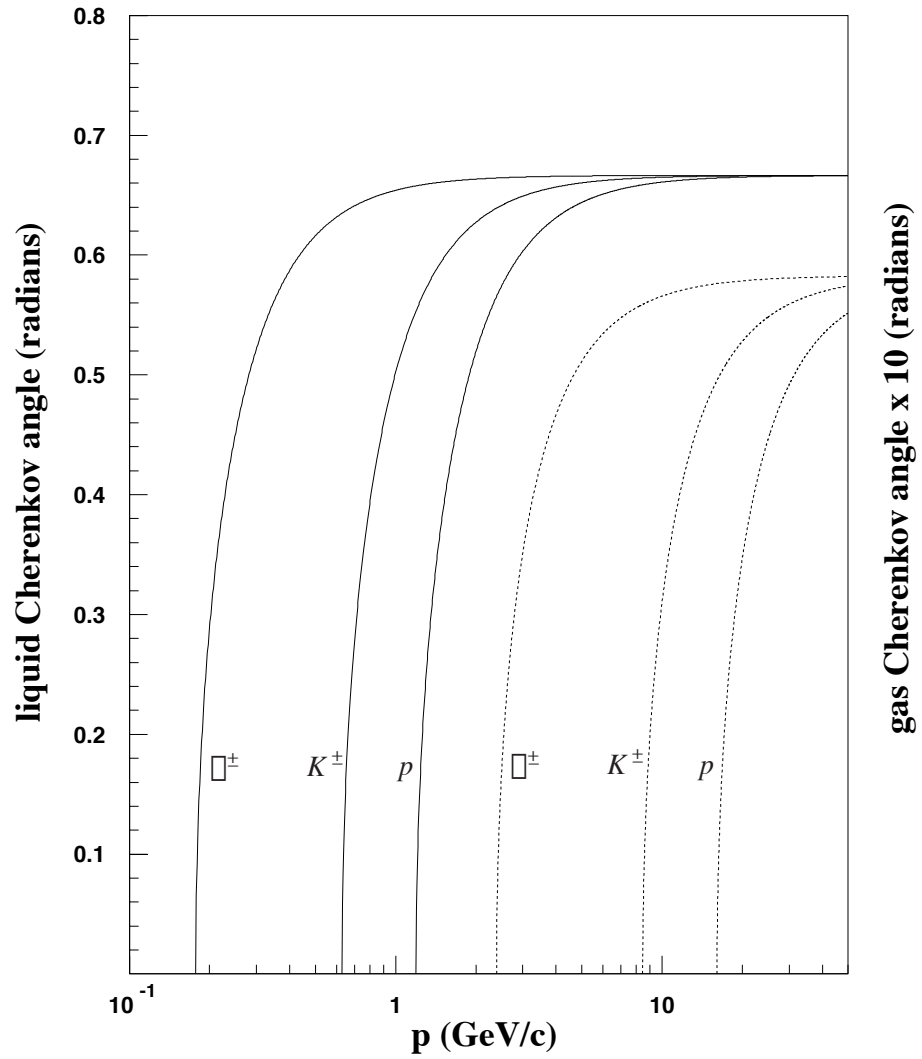
FIGURE 28. The Cherenkov angle for the liquid (solid line) and gas (dotted line) radiators in the barrel CRID as a function of momentum for three long-lived hadronic particle species.

axial coordinate, the wire address where it was counted gave the lateral coordinate, and charge division on the proportional wire gave the conversion depth [53]. This is explained schematically in Figure 29.

The angles θ_C and ϕ_C, where θ_C is the Cherenkov angle and ϕ_C is the azimuthal angle in the plane perpendicular to the track, were reconstructed from all relevant hits in the CRID for each charged track extrapolated from the SLD central drift chamber. Figure 30 shows plots for isolated gas rings in hadronic events. The angular resolution and number of photons were found by a fitting procedure.

The average reconstructed θ_C for $\beta = 1$ tracks was 675 mrad in the liquid radiator and 58.6 mrad in the gas radiator. The average number of detected photons per $\beta = 1$ track in μ-pair events was 16.1 for the liquid radiator and 10.0 for the gas radiator [54].

3.6 Liquid Argon Calorimeter (LAC)

The liquid argon calorimeter (LAC) was the second to last onion-like layer of the SLD detector and was the last of the detector subsystems to reside inside the SLD magnet coil.

Calorimetry in this context refers to the destructive measurement of the energy of a particle, i.e. the original particle enters the calorimeter and interacts, but does not transit the detector. The interaction can be either electromagnetic if it is initiated by photons and electrons, or hadronic if it is initiated by the inelastic scattering of hadrons. These interactions, when sufficiently high in energy, develop into showers – literally streams of particles produced or knocked out by a sequence

Gas Radiator
$(C_5 F_{12} / N_2$ Mix)
$n = 1.001725$

Mirror
Array

External
Field Cage

Drift Box

e^-

$C_2 H_6$ + TMAE

Liquid Radiator
$(C_6 F_{14})$
$n = 1.277$

Charged Track

e^+ e^-

CATHODE

ANODE WIRE
PLANE

PHOTONS FROM
GAS RADIATOR

e^-

y

z

x

WIRE
ADDRESS

TIME

CHARGE DIVISION
THIRD COORDINATE
READOUT

PHOTONS FROM
LIQUID RADIATOR
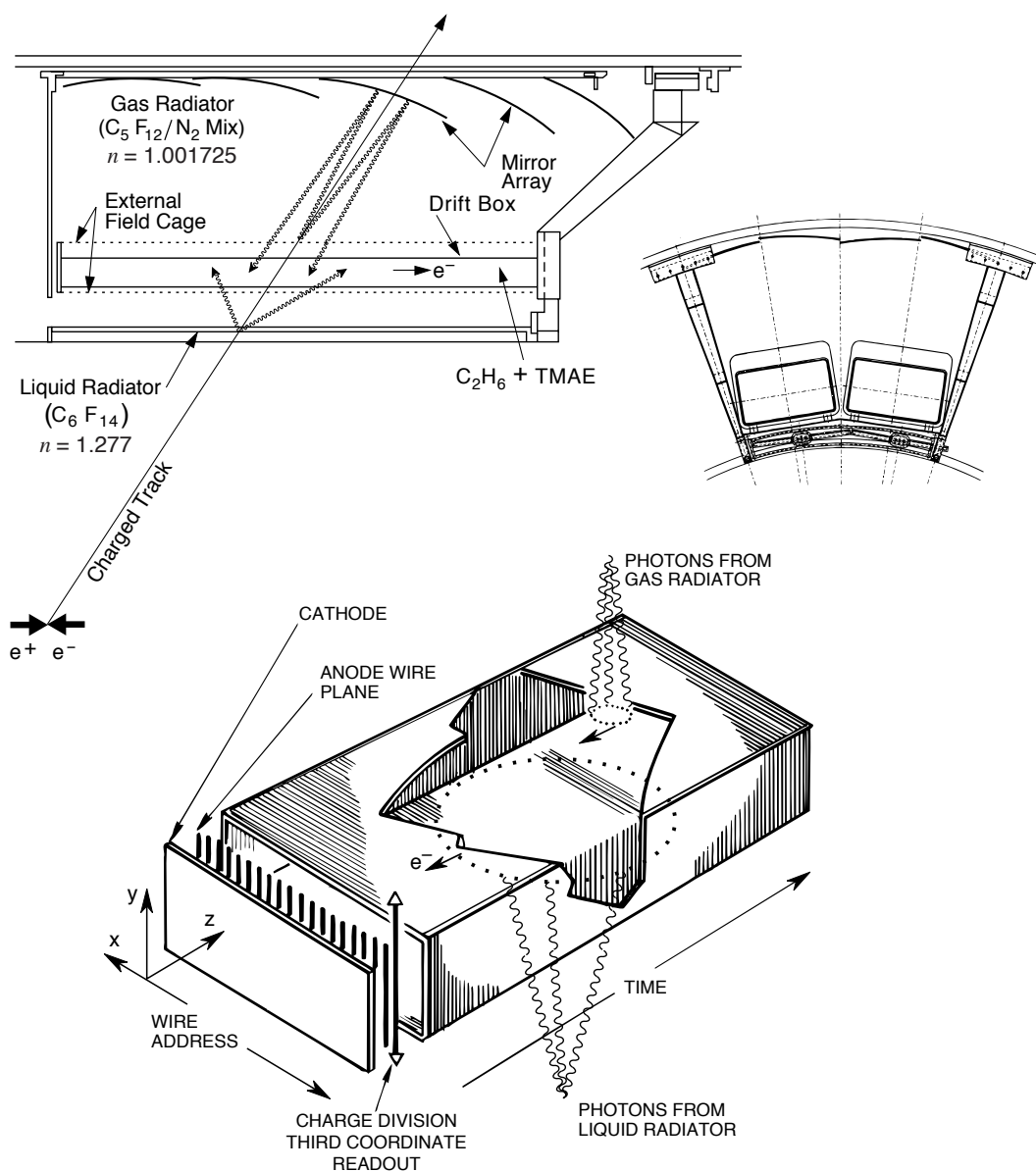
FIGURE 29. The barrel CRID showing one sector in both the transverse (top left) and axial (top right) views. At bottom is a view of the CRID photon detector box. Cherenkov photons from the liquid radiator are proximity focused on one side of the box while Cherenkov photons from the gas radiator are focused using an array of spherical mirrors onto the other side of the box. Gaseous TMAE is used to convert the Cherenkov photons into photoelectrons which drift onto a picket fence of proportional wires. The origins of the photoelectrons are determined from the drift time, the wire address, and charge division on the proportional wire.
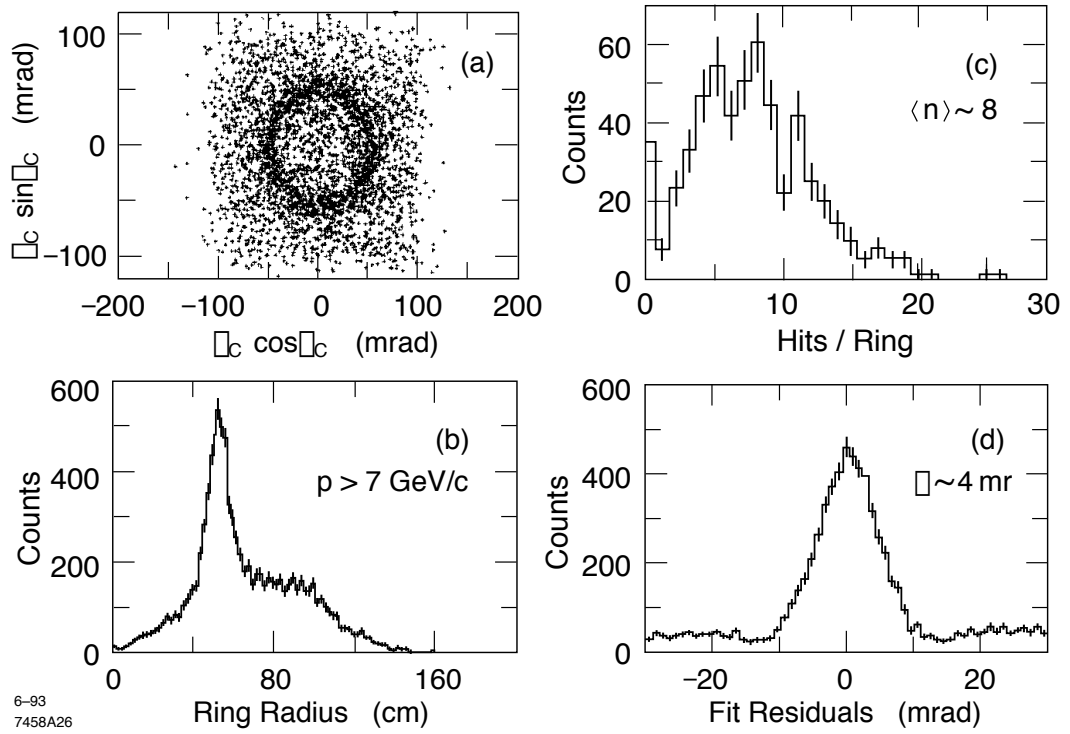
FIGURE 30. (a) Gas ring photons integrated over many hadronic events, (b) projection of (a) in Cherenkov angle, (c) number per ring derived from fits, and (d) the residuals with respect to the fitted Cherenkov ring angle, from which the local resolution is extracted.

of interactions. In general, a calorimeter detects the remnants of the interaction by measuring the ionization signature from the shower [55].

The canonical layout of a sampling calorimeter is a sandwich of high-Z passive absorber material to catalyze shower development and active material where ionization is detected. The LAC was a lead-liquid argon sampling calorimeter consisting of planes of lead absorbers, arranged in stacks of plates held alternately at ground and -2 kV and separated by several millimeters of pure liquid argon. The LAC worked as an ion chamber by collecting the charge deposited in the argon gap by electromagnetic or hadronic showers originating predominantly in the lead plates. SLD was originally conceived with a uranium-liquid argon calorimeter. Strictly speaking, when the ratio of the electromagnetic to the hadronic response of a calorimeter to particles of equal incident kinetic energy is 1, the calorimeter is said to be "compensating" [56, 57]. This is ideally achieved by making the active medium sensitive to nuclear fragments so as to, in effect, replace some of the energy normally lost to nuclear breakup. Early studies by Brau and Gabriel [58] to understand compensation in uranium calorimeters and to optimize the SLD calorimeter revealed that the uranium-liquid argon calorimeter was unlikely to achieve compensation through this mechanism, although the suppressed electromagnetic response did tend to reduce the ratio of the electromagnetic to the hadronic response toward 1. However, the advantages of uranium absorbers were modest and did not produce a sufficient improvement over a pure lead-liquid argon calorimeter to justify the added cost. When these predictions were supported by beam tests, the present lead-liquid argon design was adopted.

Two types of calorimeter modules were employed in the SLD barrel LAC: Electromagnetic (EM) modules and hadronic (HAD) modules. The EM modules consisted of stacks of 2 mm thick lead plates separated by 2.75 mm gaps of liquid argon for a total of 21 radiation lengths; the HAD modules consisted of 6 mm thick lead plates again separated by 2.75 mm gaps of liquid argon for a total of 2 absorption lengths [17]. The calorimeter stacks were divided into readout towers that projected back to the beam interaction point. Tower sizes were chosen to provide the best possible efficiency for isolating electrons from b quark jets, the lowest possible π/γ overlap background, and the best position resolution, subject to the constraints of economy. At $z = 0$, the θ angle subtended at the tower entrance was 36 mrad for the EM section, and 72 mrad for the HAD section. The inner section of the EM module contained 70 segments along the z direction while the outer section contained 68. The inner section of the HAD module contained 32 segments along the z direction while the outer section contained 30. In azimuth, there were 192 EM segments and 96 HAD segments. This gave a total of 32,448 channels in the barrel LAC. The EM and HAD modules are illustrated in Figure 31.

These modules were arranged in an annular configuration with an inner radius of 1.77 meters and an outer radius of 2.91 meters. The barrel LAC was longitudinally segmented into three compartments by two aluminum washers welded to the inner wall of the dewar. In each of the three compartments, 48 EM modules occupied the inner portion of the annulus and 48 HAD modules occupied the outer portion for a total of 288 individual modules.
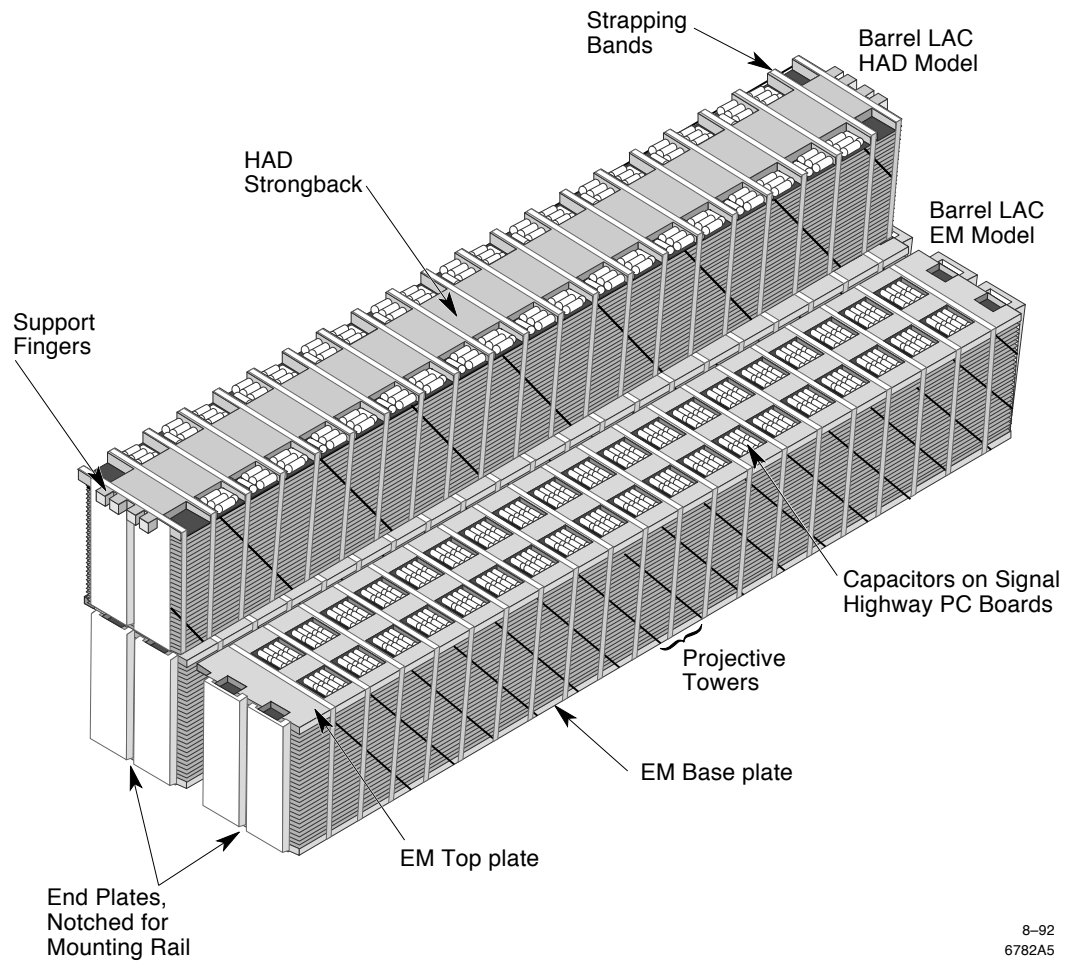
FIGURE 31. Isometric view of two electromagnetic (EM) and one hadronic (HAD) stack modules of the barrel LAC.

For showers of energy E, the energy resolution of the LAC was measured to be $\sigma/E = 15\%/\sqrt{E}$ for electromagnetic showers and $\sigma/E = 60\%/\sqrt{E}$ for hadronic showers.

The LAC was important in this analysis because, as will be explained elsewhere, it was the basis for the hadronic event trigger, and was also used in the determination of the thrust axis.

3.7 Magnet Coil

The magnet coil was made of 10 km of 5 cm × 7 cm rectangular Al conductor wound in four 127 turn layers to give an 80 ton cylinder 5.9 m in diameter, 6.4 m long, and 29 cm thick. It produced a uniform solenoidal field of strength 0.6 Tesla in a volume of 175 m^3. An electric current of 6,600 amps at a potential difference of 750 V flowed through the magnet coil to produce the magnetic field. This produced 5 MW of heat which had to be removed. A one inch diameter hole ran longitudinally through the rectangular conductors for cooling water to flow: The total flow rate for the entire solenoid was approximately 50 liters per second [53].

3.8 Warm Iron Calorimeter (WIC)

The final onion-like layer of the SLD was the warm iron calorimeter (WIC), and was the only detector subsystem (notwithstanding the Compton polarimeter and the WISRD, both discussed in the next chapter) to reside outside the magnet coil.

The barrel WIC was an octagonal cylinder surrounding the magnet coil and was composed of 14 layers of 5 cm thick steel plates separated by 3.2 cm gaps. The steel in the barrel provided the flux return path for the magnetic field. Detector elements placed in the gaps converted this passive flux return into a calorimeter with the steel plates doubling as absorber elements.

The detector elements consisted of long, retangular tubes similar to those developed by the Iarocci group in Frascati for the Mont Blanc proton decay experiment. They had an active section of 9 mm × 9 mm, and were constructed in groups of eight tubes from 1 mm thick extruded PVC. At the center of each tube was a 100 μm Be-Cu wire. The tubes were filled with 88% CO_2, 9.5% isobutane, and 2.5% Ar. The barrel section contained approximately 40,000 of these tubes.

In addition to the Iarocci type tubes were strips – both transverse and logitudinal, and pads. The strips were made from 1.6 mm thick Glasteel sheet laminated with 25 μm Cu on both sides. On the top side, the actual strip electrodes were made by removing lines of Cu 2 mm wide, with the strip electrodes located under the active regions of the tubes. The Cu on the opposite side of the Glasteel sheet formed the ground plane. The pads were likewise made using Glasteel sheets laminated with Cu on one side, with Cu removed to form the individual pads [53]. The general layout of the barrel WIC is shown in Figure 32.

Double Layer
for Muon Tracking

Detail of Single Layer

Fe

Pads

Wire

Plastic 8-Tube Container

Graphite Coated Comb Structure

Fe

Longitudinal Strips

100 cm

Fe

Pads

Transverse Strips

Ground Plane

Transverse Strips

Fe

Longitudinal Strips

Fe Typical

Single Layer Typical

Detail of Double Layer

100 cm

1-95

5996A5
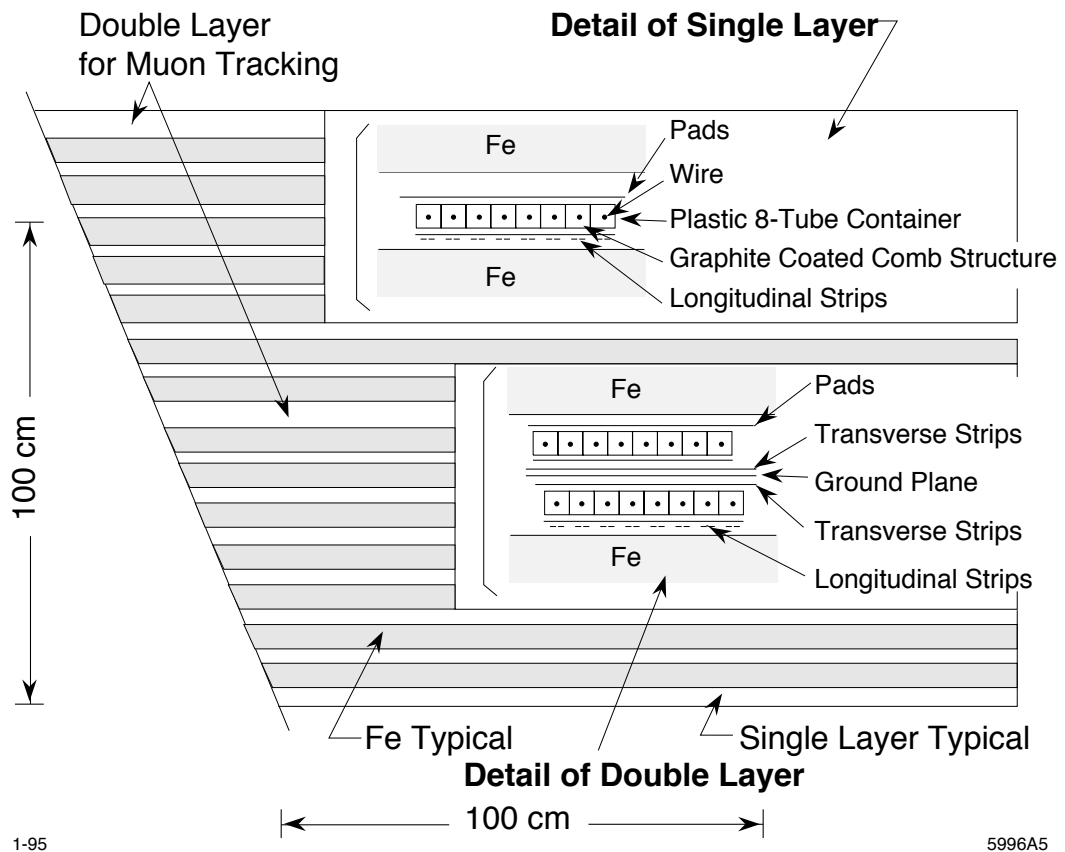
FIGURE 32. Cutaway view of a barrel WIC section showing details of the layer construction.

3.9 Simulation Tools

Simulated data generated using Monte Carlo techniques are de rigueur in most particle physics experiments. The Monte Carlo simulation is, in effect, the physicists' chance to play God, for only in simulated data can all the physical parameters associated with a particle or event be known with absolute certainty and adjusted with impunity. Underlying physical processes and the response of the detector to them can be studied, and background rates, biases, and acceptances that are impossible to determine from the data can be reasonably estimated.

The measurements presented in this analysis relied on a Monte Carlo simulation based on the JETSET 7.4 event generator, which was intimately connected with string fragmentation in the form of the time-honoured "LUND model." Finally, a detailed simulation of the detector was performed with GEANT 3.210.

In some semblance of a time order, the evolution of a typical simulated SLD event proceeded as follows [59, 60]:

1. Initially two beam particles were coming in towards each other.

2. The incoming particles entered a hard process, where then a number of outgoing partons – usually two – were produced. It was the nature of this process that determineed the main characteristics of the event.

3. The hard process often produced a short-lived resonance – specifically a Z^0 gauge boson – whose decay to normal partons had to be considered in close association with the hard process itself.

4. The outgoing partons branched to build up final-state showers.

5. The QCD confinement mechanism ensured that the outgoing quarks and gluons were not observable, but instead fragmented to color neutral hadrons. In the LUND string fragmentation model, the long-range confinement forces were allowed to distribute the energies and flavors of a parton configuration among a collection of primary hadrons [59]. The LUND parameters were specifically tuned to hadronic e^+e^- annihilation data [61]. However, charm and bottom data indicated the need for a harder fragmentation function: Fragmentation functions for b and c quarks were according to Peterson *et al.* [62].

6. Many of the produced hadrons were unstable and decayed further. For the B meson decay simulation, the CLEO QQ generator [63] was adopted, with adjustments to improve the agreement with inclusive particle production measurements from ARGUS and CLEO [64]. Semileptonic decays followed the Isgur-Scora-Grinstein-Wise (ISGW) form factor model [65] with the inclusion of D** production.

7. The detector's response to charged and neutral particles was modeled using GEANT 3.210 [66], with a detailed geometric description of the SLD.

Beyond the orthodox SLD Monte Carlo, two non-standard simulations were run. One simulation varied the b quark mass in JETSET to study the running b mass effect. Another simulation demanded that the the Z^0 decay to a b quark and

an $\bar{s}$ quark in one instance, and to an s quark and a $\bar{b}$ quark in another [67] in order to have simulated flavor changing neutral current events for training neural networks, tuning cuts, and so forth.

CHAPTER IV

THE SLC

4.1 Introduction

Over the past 40 years, accelerators have become the main tool for exploring the fundamental particles and forces of nature. SLAC was the first large-scale electron accelerator and began operation in the mid 1960s. This was followed by the evolution of electron-positron storage rings starting with the early ADONE and SPEAR rings at Frascati and SLAC respectively having center of mass energies of a few GeV, and culminating most recently with the LEP collider at CERN having a center of mass energy of over 200 GeV. The evolution of both hadron and e^+e^- colliders is shown in Figure 33 [68].

Because of energy losses to synchrotron radiation, the bending radius of an electron storage ring must increase approximately as the square of the energy, and thus the size and cost must also increase as the square of the energy, while the size and cost of a linear collider scale approximately linearly with energy. The LEP ring is already 27 km in circumference making even modest increases in energy impractical.

M. Tigner, in 1965, proposed the original "apparatus for electron clashing-beam experiments," although beam spot size appeared to motivate his ideas rather
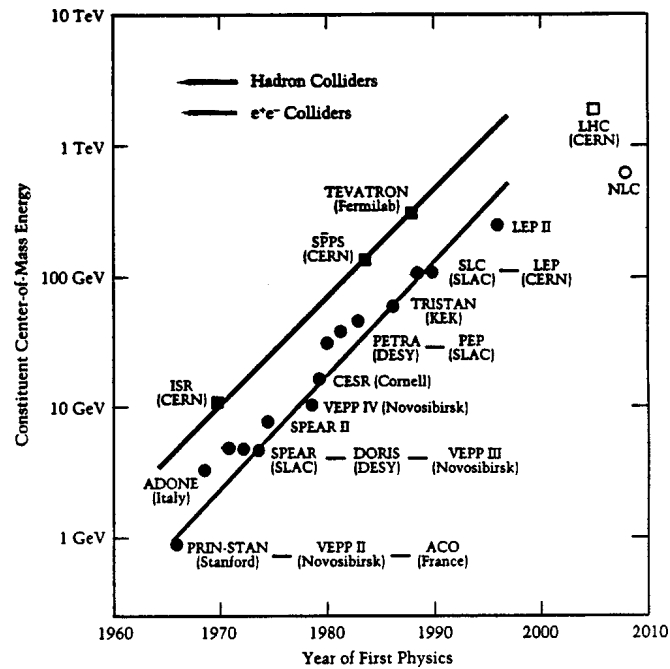
FIGURE 33. The energy in the constituent frame of electron-positron (circles) and hadron (squares) colliders: Filled circles and squares refer to machines which have been constructed; the open circle and square are planned machines. The energies of hadron colliders have been derated by factors of 6-10 in this plot in accordance with the fact that the proton's incident energy is shared among its quark and gluon constituents. (From W. K. H. Panofsky and M. Breidenbach, Rev. Mod. Phys. 71, 1999.)

than limiting energy losses to synchrotron radiation: "In order to be useful for clashing-beam work an acceleration device must produce beams of small-cross section or high enough quality that they may be focused to a small spot in the interaction region or regions. Such beams are well known to be produced by linear radio-frequency accelerators" [69].

The SLAC Linear Accelerator (linac), upon which the SLC is built, is a particle accelerator in which electrons (and positrons) are accelerated in a straight line by means of radio frequency electric fields (RF), as illustrated in Figure 34. The passage of the electrons are synchronized with the phase of the accelerating fields. The SLAC linac is a three kilometer long disc-loaded copper wave guide placed on concrete girders in a tunnel about 25 feet underground, and is fed by approximately 240 65 MW S-band klystrons spaced at 40 foot intervals. A klystron is a microwave generator consisting of an electron tube wherein a beam of electrons from a hot cathode is passed through a resonant cavity where it is modulated by high frequency radio waves. The electrons are bunched as they pass through a final cavity, where they induce RF with a higher gain. The RF from the klystrons is transmitted by rectangular waveguides to the disc-loaded wave guide of the linac.

Figure 35 illustrates the layout of the SLC including linac, damping rings, positron source, positron return line, arcs, and beam dumps. Nan Phinney describes the SLC [70]:

"Built on the existing SLAC Linac, the SLC is a 'folded' version of a linear collider where both electron and positron bunches are accelerated in the same beam pipe to about 50 GeV. The SLC cycle begins

Disc-Loaded Wave Guide

Electric Field Lines
Magnetic Field Lines
Particle Bunch
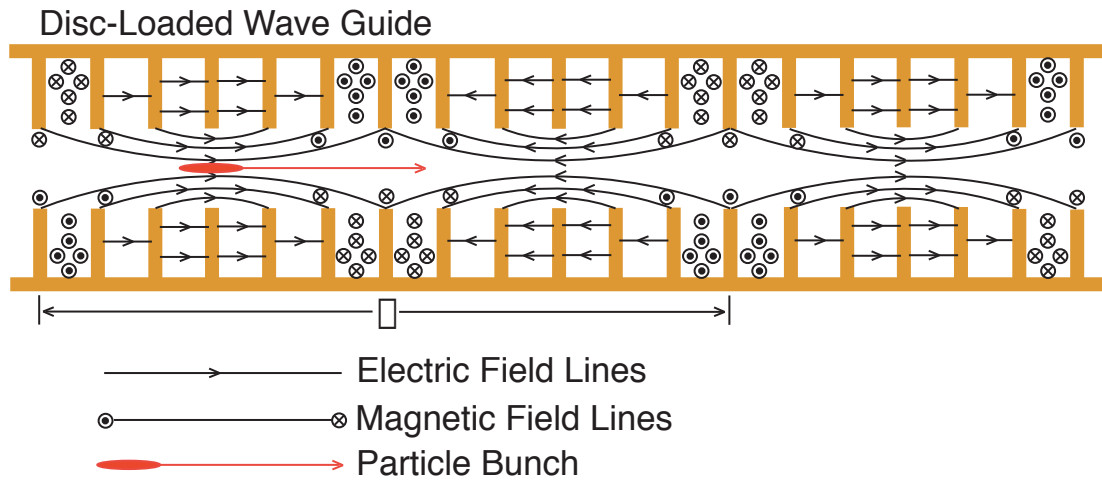
FIGURE 34. Formation of an accelerating wave in an RF linear accelerator.
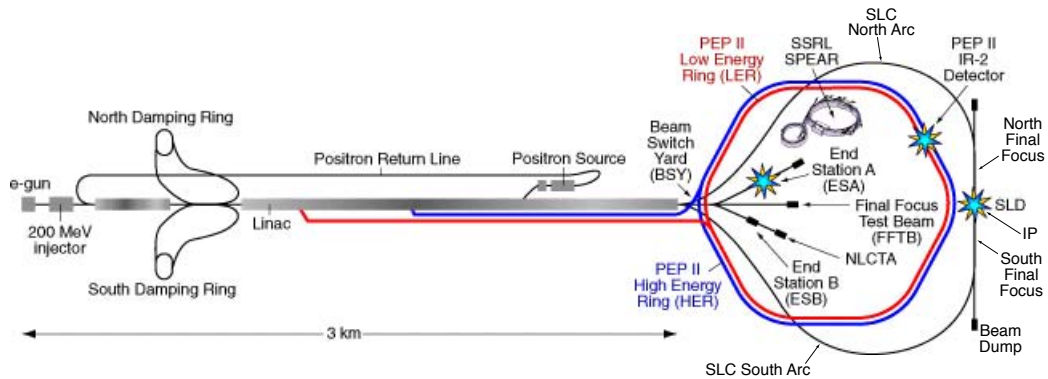
FIGURE 35. The Stanford Linear Accelerator Center (SLAC).

with two electron bunches stored in the north damping ring and two positron bunches stored in the south damping ring. On each pulse, one positron bunch followed by both electron bunches are accelerated in the linac. The second positron bunch remains in the damping ring for an additional damping cycle to reduce the large incoming emittance. Two thirds of the way along the Linac, the second electron bunch is extracted onto a target to produce a new pulse of positrons. The leading positron and electron bunches are separated by a bend magnet at the end of the Linac, bent around two roughly circular transport lines, the Arcs, and brought into collision at the Interaction Point (IP). In the last 150 meters of beam line, the Final Focus, the beams are focused to micron size for collision. They then travel back through the opposite Final Focus and are extracted onto high power beam dumps. At the same time, two new bunches of electrons are produced by the polarized source and accelerated to 1.19 GeV into the north damping ring. The new positrons are transported back to the beginning of the linac where they are coaccelerated with the electrons and injected into the south damping ring, joining the positron bunch from the previous pulse. This cycle repeats 120 times a second."

4.2 Polarized Electron Source

The electron bunches accelerated by the SLC were longitudinally polarized. Electrons were produced from a photoemission electron gun which utilized a semiconductor cathode. Optical pulses from a Nd:YAG-pumped Ti:sapphire laser were chopped by a Pockels cell optical pulse chopper to produce the short optical pulses required, and then circularly polarized by a pulsed Pockels cell optical retarder. This circular polarization, necessary for the production of longitudinally polarized electrons, was reversed randomly on a pulse-to-pulse basis. These short, circularly polarized optical pulses excited electrons from the valence to the conduction band of the GaAs photocathode, the surface of which was treated with cesium and NF_3 to attain a negative electron affinity which allowed the excited electrons to escape the photocathode with a quantum efficiency of about 0.1%. The SLC polarized source is illustrated schematically in Figure 36.

Space-charge and transient phenomena make the bunching and capture of short duration electron pulses problematic: However these difficulties decrease significantly in bunches having a longer duration. A subharmonic buncher consisting of two cavities located between the electron gun and the S-band linac was used to shorten the two-nanosecond duration polarized electron pulses from the gun down to 100 picoseconds in duration. A 10-cm traveling wave buncher further reduced the duration of the electron pulses to 20 ps, and a standard 3-meter accelerator section prepared the pulses for injection into the main linac [71].

Although the electrons started off circularly polarized, they got horizontally polarized by the bending magnets in the transfer line which sent the electrons to the north damping ring – the so called "linac-to-ring" (LTR). A solenoid spin
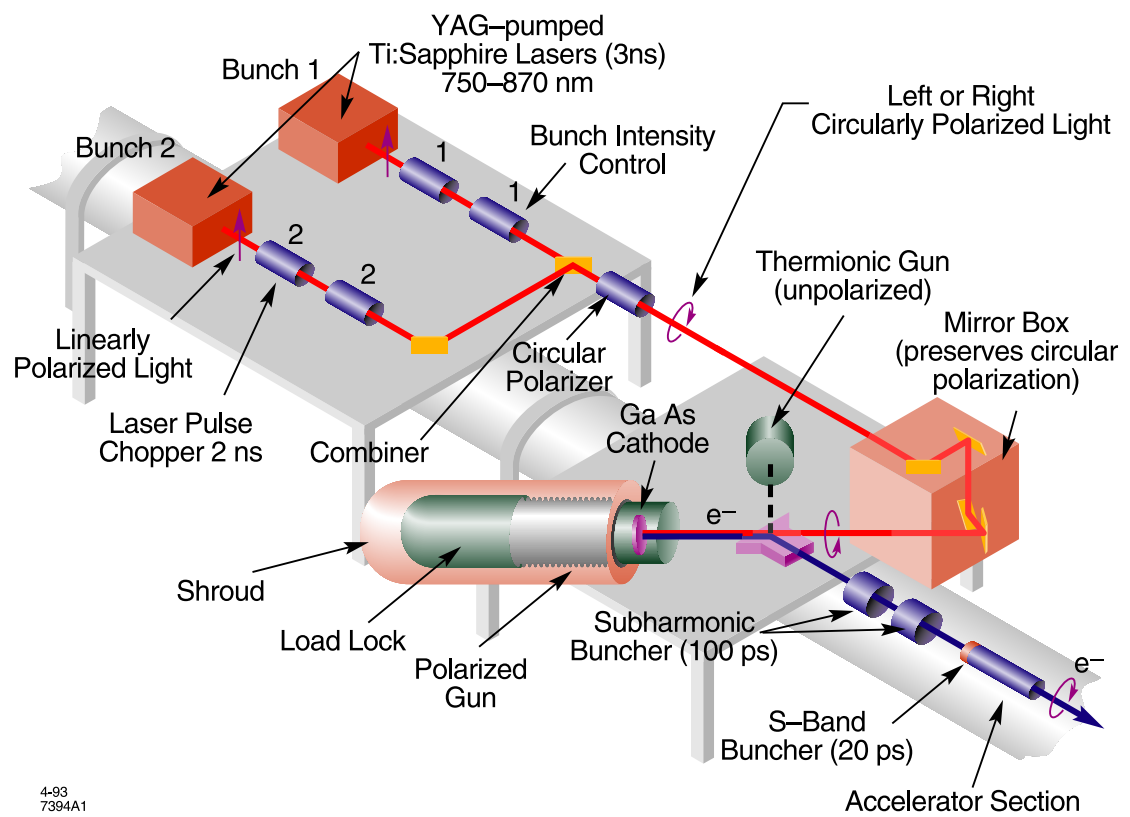
FIGURE 36. The SLC polarized source.

rotator then vertically polarized the electrons, and this vertical spin was preserved during the 8.3 μs store in the north damping ring. Two additional spin rotators were installed, one in the ring-to-linac (RTL) transfer line and one at the entrance to the linac, and coupled with the rotation induced by the transfer line, these allowed the spin to be oriented in an arbitrary direction at injection to the linac. In practice however, these two additional spin rotators were not used because the solenoids would have coupled the horizontal and vertical emittances and prevented operation with "flat beams." The orientation of the spin was preserved in the linac, and then precessed through the bending magnets of the north arc. It turns out that the spin orientation is extremely sensitive to minor orbit changes through the arc due to a resonance between the precession of the spin and the betatron oscillations induced by the north arc lattice. This feature was quickly turned to an advantage, and since 1993, "spin-bumps" in the orbit through the north arc have been used to orient the spin direction as desired. Nominally, the electrons arrived at the IP longitudinally polarized [70]. Figure 9 shows the average polarization attained during each run period.

4.3 Measuring the e^- Polarization

The polarization of the SLC electron beam was measured using the asymmetry in the Compton scattering cross sections for the $J_z = 3/2$ and $J_z = 1/2$ combinations of circularly polarized light and the longitudinally polarized electron beam. The longitudinal component of the electron polarization P_e can be extracted

from the measurement of this asymmetry as follows:

$$A_{measured} \quad = \quad \frac{\sigma_{J_z=\frac{3}{2}} - \sigma_{J_z=\frac{1}{2}}}{\sigma_{J_z=\frac{3}{2}} + \sigma_{J_z=\frac{1}{2}}} = a_d P_e P_\gamma A_C(E) \tag{4.1}$$

where a_d is the measured analyzing power of the detector, P_γ is the measured longitudinal component of the laser polarization, and A_C is the Compton scattering asymmetry as a function of energy which is calculable from QED.

The SLC polarimetry system is shown in Figure 37. Circularly polarized photons of energy 2.33 eV from a frequency-doubled YAG laser collided with the electron beam at a point 33 m downstream from the SLC interaction point. The backscattered electrons were then separated from the main beam by a dipole bend magnet and aimed into a Cherenkov detector. This detector used an array of propane radiators coupled to PMT readouts to measure the energy spectrum of the scattered electrons in the range 17 to 30 GeV. The energy corresponding to each channel of the detector was determined by the channel's distance from the beam line.

Two other detectors, the polarized gamma counter (PGC) and the quartz fiber calorimeter (QFC), made additional measurements of the beam polarization. Both worked by observing the scattered photons rather than the electrons, as shown in Figure 37. Both detectors provided consistency checks of the Compton Polarimeter result with a precision of better than 1%.

This analysis was not, however, dependent on the polarization measurement.
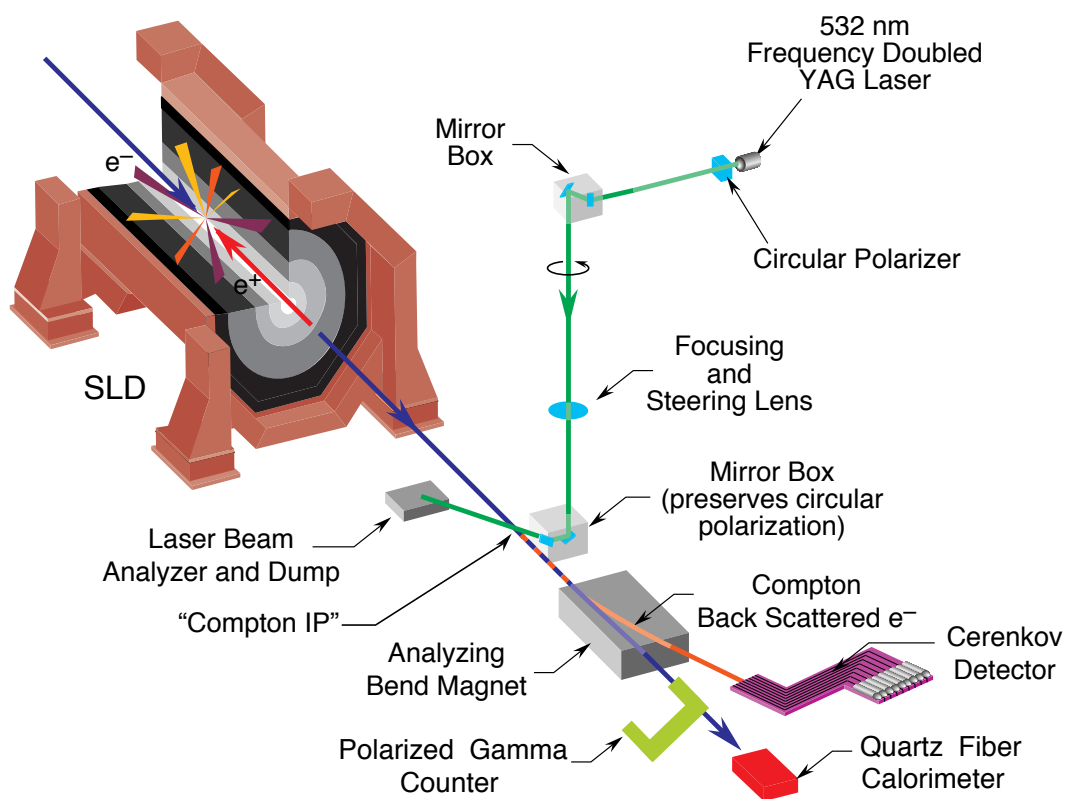
FIGURE 37. Schematic diagram of the Compton Polarimeter.
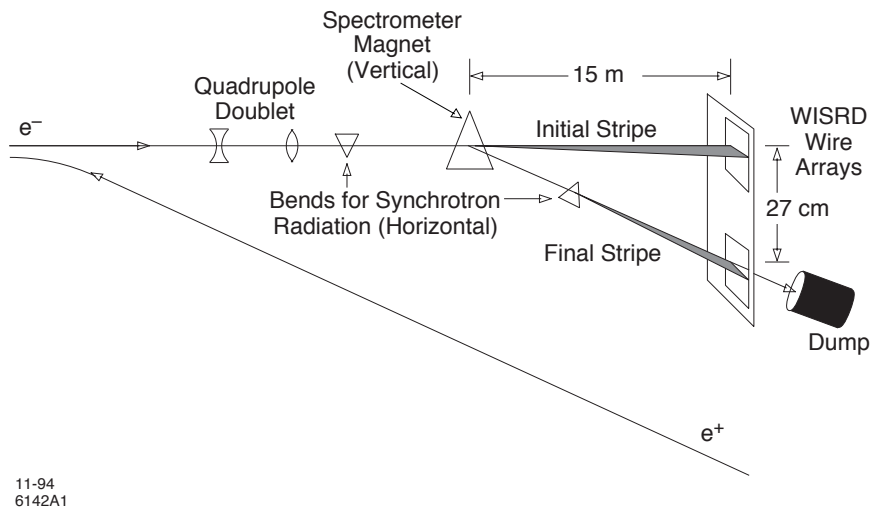
FIGURE 38. Schematic diagram of the WISRD.

4.4 Beam Energy Measurement

Both the electron and positron beams passed through extraction-line spectrometers installed approximately 150 m downstream from the IP before ultimately reaching their respective beam dumps. In each spectrometer, the $e^{\pm}$ bunches traveled through three dipole magnets: The second magnet was a spectrometer magnet which bent the beam; the first and third magnets bent the beam perpendicular to the bend direction of the spectrometer magnet and caused the beam to emit two stripes of synchrotron radiation. A quadrupole doublet upstream of the bending magnets focused the $e^{\pm}$ and synchrotron stripes approximately 15 m downstream of the spectrometer magnet. Synchrotron radiation detectors located at this focal

point measured the distance (approximately 27 cm) and thus the angle between these two stripes, which allowed a determination of the beam energy [72].

The synchrotron radiation detectors consisted of arrays of 75 μm diameter copper wires spaced 100 μm apart. Incident synchrotron radiation ejected electrons from the wires via Compton scattering. These were known as wire imaging synchrotron radiation detectors (WISRDs).

The precision of the WISRD, based on magnetic measurements done on the bench in 1988 and *in situ* surveys done about once per SLD run indicated an uncertainty on E_{cm} of about ±20 MeV. However, a Z^0 peak scan was performed during the 1997-98 SLD run which allowed the WISRD energy spectrometer to be calibrated against the precise Z^0 mass measurement obtained at LEP. From this, the total uncertainty on E_{cm} was found to be ±29 MeV [73].

4.5 Emittance Preservation

The SLC is likely the most difficult accelerator ever operated: Linear colliders are inherently less stable than storage rings, and each pulse is an injected pulse. Emittance preservation is the key to high luminosity with low detector backgrounds in a linear collider.

In a linear colider, the luminosity depends on the beam intensities, transverse beam size, and repetition rate:

$$L \;=\; \frac{fN^+N^-}{4\pi\sigma_x\sigma_y}H_d \tag{4.2}$$

where f is the repition rate and $N^{\pm}$ are the numbers of particles per bunch for electrons and positrons. The $\sigma_{x,y}$ are the horizontal and vertical beam sizes. For small, intense, oppositely charged beams, there is an additional enhancement from the attractive forces between the bunches which causes each beam to be focused by the field of the other: H_d takes into account this disruption enhancement or pinch effect. During the 1997-98 run, the number of positrons and electrons per bunch was typically around $N^{\pm} \approx 4 \times 10^{10}$; horizontal and vertical beam sizes as low as $\sigma_x = 1.5$ μm and $\sigma_y = 0.65$ μm respectively were achieved; the repetition rate was $f = 120$ Hz; and the disruption enhancement got as high as $H_d = 2.0$. [39]

Emittance ε is a phase-space measurement of the quality of a beam with regard to the spacial spread and uniformity of the momenta of its individual particles, and is the area in phase space of the ellipse enclosing the particles within one σ [74]. Emittance is defined as the product of the beam size $\sigma_{x,y}$ and angular divergence $\Theta_{x,y}$ [75],

$$\varepsilon_{x,y} = \sigma_{x,y}\Theta_{x,y}. \tag{4.3}$$

Using the definition of emittance, one may re-express the luminosity as

$$L \propto \frac{\Theta_x \Theta_y}{\varepsilon_x \varepsilon_y} H_d. \tag{4.4}$$

Emittance is the key to the successful operation of a linear collider: The basic strategy is to decrease the emittances and increase the angular divergences to the extent possible.

Location		ε_x (m·Rad)	ε_y (m·Rad)
Injection	e^-	2×10^{-4}	2×10^{-4}
	e^+	1×10^{-3}	1×10^{-3}
Extraction		3.0×10^{-5}	0.3×10^{-5}
Sector 28		4.0×10^{-5}	0.6×10^{-5}
Final Focus		5.5×10^{-5}	1.0×10^{-5}

TABLE 1. Typical horizontal and vertical emittances, $\varepsilon_{x,y}$, achieved during the 1997-98 run. The numbers represent emittances measured at different locations throughout the SLC: Injection into the damping ring, extraction from the damping ring, close to the end of the linac (sector 28), and in the final focus.

A damping ring is essentially a small storage ring the purpose of which is to reduce the emittance of a beam. Because of synchrotron radiation, the beam loses energy as it travels around the damping ring. The lost energy is replaced by an RF source, but only the longitudinal component is replaced. Thus the tranverse emittance is reduced, or "damped." A damping ring is illustrated in Figure 39. A schematic of the north damping ring is shown in Figure 40. The beam emittance is plotted as a function of damping ring store time in Figure 41 [76].

At the SLC, the damping rings were located quite near the front end of the accelerator such that the emittances of the electron and positron beams were as small as possible as they propagated through the rest of the machine. The goal in SLC operation then became to preserve – to the extent possible – whatever emittances were achieved after extraction from the damping rings. Table 1 shows typical values for the beam emittances at various locations in the SLC which were achieved during the 1997-98 run [39, 77, 78].

One of the most important sources of emittance growth in the SLC occured early in the accelerator where there was a mismatch between the incoming beam and the optics of the beam line lattice. If the beam was not matched to the lattice
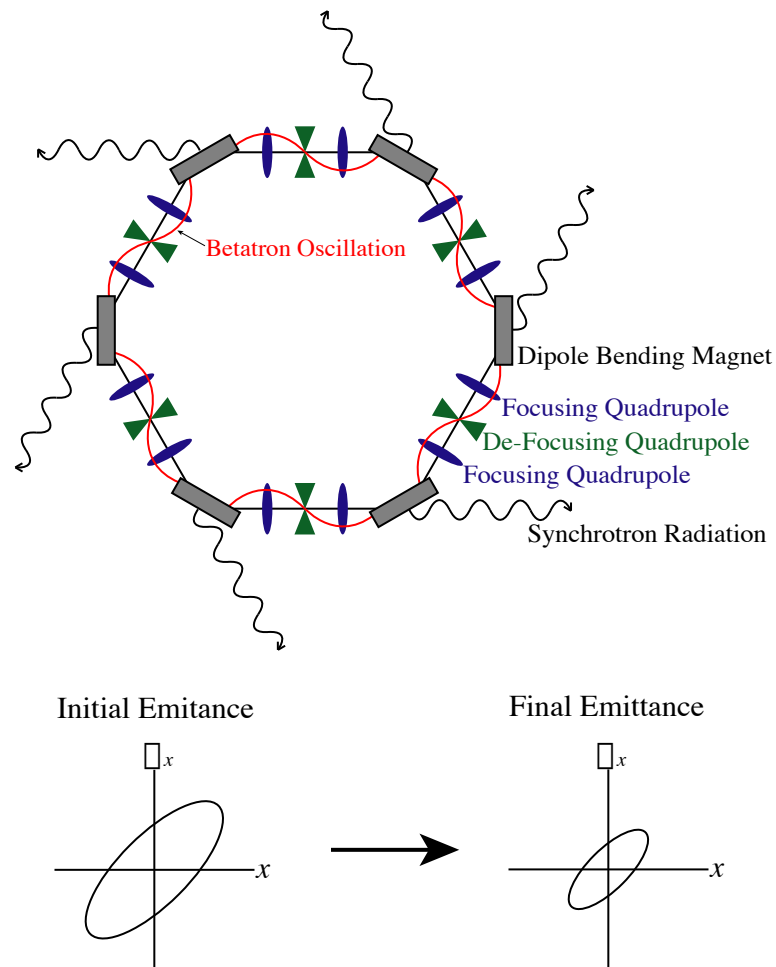
FIGURE 39. Because of energy losses to synchrotron radiation, the phase space occupied by a charged particle beam – the emittance – decreases in a damping ring. The lost energy is replaced by an RF source, but only the longitudinal component is replaced. Thus the tranverse emittance is reduced, or "damped." Note that Liouville's Theorem doesn't apply to the damping ring because it is disapative.
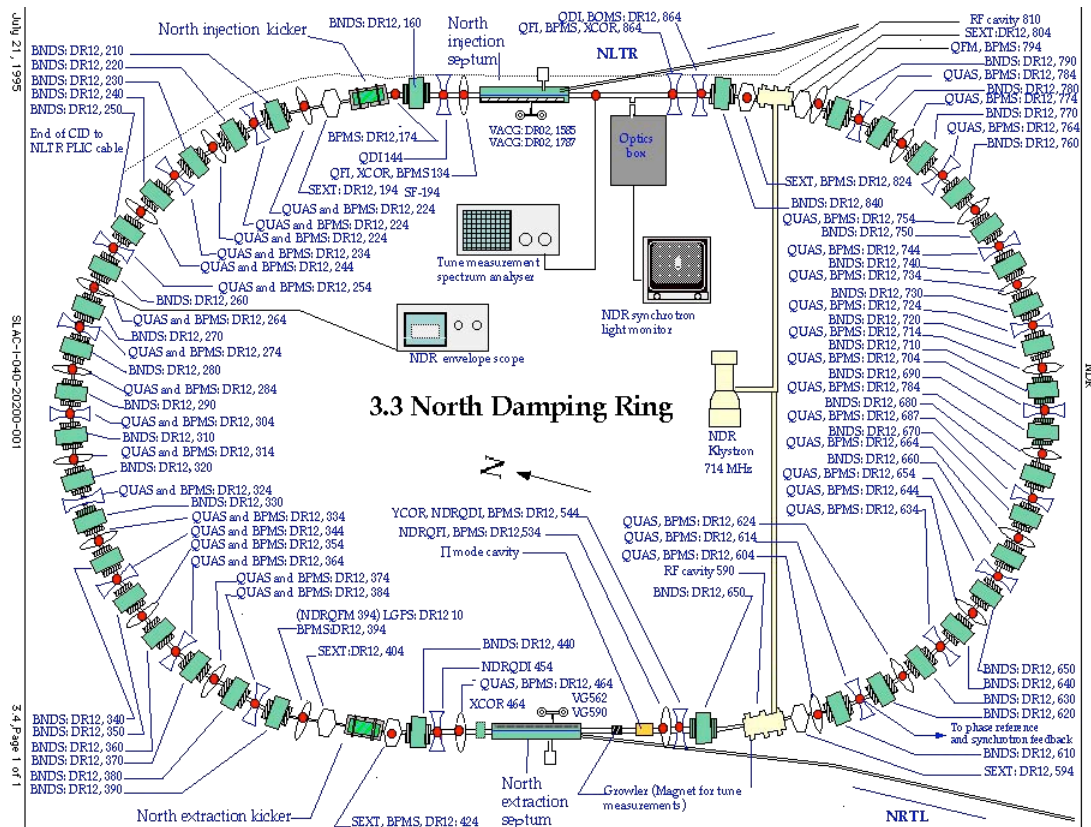
FIGURE 40. Schematic of the North Damping Ring of the SLC showing the latice of dipole bend and quadrupole focusing/defocusing magnets, the NDR klystron, and the injection and extraction septums.
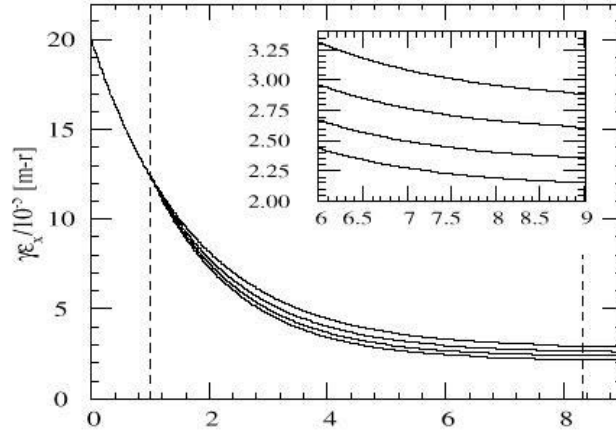
FIGURE 41. Beam emittance in m·Rad plotted as a function of store time in msec. (The different lines in the plot represent variations in the mid-store frequency shift of between 25 and 150 kHz.) (From P. Ramondi *et al.,* Luminosity Upgrades for the SLC, PAC99, 1999.)

at the entrance of the linac, dispersion resulting from the beam passing off-axis through the quadrupole magnets would interact with the correlated energy spread along the beam resulting in a larger final transverse emittance. [70]

Wire scanners are beam profile monitors which provide measurements of beam size and position in all three planes (vertical, horizontal and longitudinal). They consist of a wire capable of being moved precisely through the path of a beam and a detector which measures the amount of charge striking the wire. The wire is scanned across the path of a beam, and the wire's position is compared to the beam's intensity in order to measure the beam profile. It takes four wire scanners, separated in betatron phase but otherwise near to each other in the machine, to provide the measurement of the beam emittance at a particular region of the SLC. Over 60 wire scanners distributed throughout the SLC from the injector to the

final focus were used to measure the beam emittances at different locations, and were essential for correctly matching the beam to the lattice.

Short time-scale variations in the beam properties were another source of emittance growth. These were caused by a variety of sources such as collective instabilities in the damping rings, mechanical vibration, or power supply regulation. Over the years, techniques were developed to correlate these pulse-to-pulse fluctuations throughout the machine and track them back to their sources. [70]

Wakefields were also a source of emittance growth. A wakefield is the field created by the bunch as it passes through the beam pipe. The charges induced in the wall of a beam pipe by the leading edge of the bunch have an effect (usually bad) on the tail of the bunch. If the beam is centered, wakefields will cancel each other by symmetry, but if the beam is closer to one wall, the tail will be attracted to this wall resulting in a 'banana' shaped bunch.

A technique suggested by Balakin, Novokhatsky and Smirnov, called BNS damping [79], was successfully used to reduce the sensitivity to wakefields at the SLC. By running the bunch a little behind the peak in the RF phase, a longitudinal energy spread was introduced into the beam at the beginning of the linac such that the tail of the bunch had a lower energy than the head. The wakefield of the head of an off-axis bunch, being asymmetrical, would produce a kick on the tail. But because the tail had lower energy, it was overfocused by the lattice, counteracting the effects of the wakefield kick and reducing trajectory oscilations. In addition, without BNS damping, the long range wakefields from the leading positron bunch could resonantly amplify the trajectory oscillations in the following electron bunch. Even with BNS damping, pulse-to-pulse jitter remained a problem in the SLC. [70]

4.6 Detector Backgrounds

The most serious backgrounds in the SLD appeared in the liquid argon calorimeter (LAC), the central drift chamber (CDC), and the Compton polarimeter. Other subsystems had their own background problems – the Cherenkov Ring Imaging Detector (CRID) for example – but if these first three had low background levels, the rest were generally clean.

In terms of tuning backgrounds, it was important to first control the backgrounds in the LAC since it figured prominently in the SLD trigger and thus determined how many events per second were written to tape. The CDC usually posed the toughest background tuning problem. Because of its sensitivity, the CDC could be turned on only when the backgrounds were suffiently under control already as determined by the north and south luminosity monitors (LUMs). If both LUMs were relatively background free, the CDC high voltage could be ramped up to 80%. Only when the backgrounds in the CDC at 80% voltage were brought under control could the high voltage be raised to 100% and the final backgrounds tuning be done.

Collimators – sometimes called "slits" – were installed at many locations along the beam line to reduce the aperture. SLC collimators were either fixed or had movable "jaws." A betatron oscillation is the transverse oscillation of a beam. The restoring force for the betatron oscillations is provided by the quadrupole magnets which focus the beam in one plane and defocus it in the orthogonal plane. There are therefore both horizontal and vertical betatron oscillations. Dispersion is a correlation of transverse position with longitudinal momentum, and occurs when

the beam is bent by a magnetic field: Charged particles with less energy bend more and particles with more energy bend less. Therefore collimators placed at the appropriate locations in betatron phase can be used to remove both geometric beam tails and – thanks to dispersion – off-energy tails.

A high energy beam of electrons interacting with a collimator produces an electromagnetic shower consisting of lots of electrons and positrons, not to mention muons, all with a broad energy spectrum which can then propagate down the beam line and cause all sorts of backgrounds. In other words, collimators can easily make the backgrounds worse, not better.

Emittances and luminosity were optimized before attempting to reduce the backgrounds with collimation. But once these were optimized, adjusting the movable jaws was nominally the most significant part of background tuning. The primary source of backgrounds in the CDC were off-energy particles going through the final focus triplets geometrically off-axis, creating a large amount of synchrotron radiation which hit the M4 and M5 masks and sent electromagnetic showers into the CDC, as illustrated in Figure 42. The objective was to use the collimators to remove these off-energy particles. However, because high backgrounds in the LAC were caused by muons created in the final focus – usually when a collimator cut into the beam – the primary collimation was always done as far upstream as possible – usually at the end of the linac. The final focus collimators were just used to finish the clean up from the upstream collimation and catch the few remaining
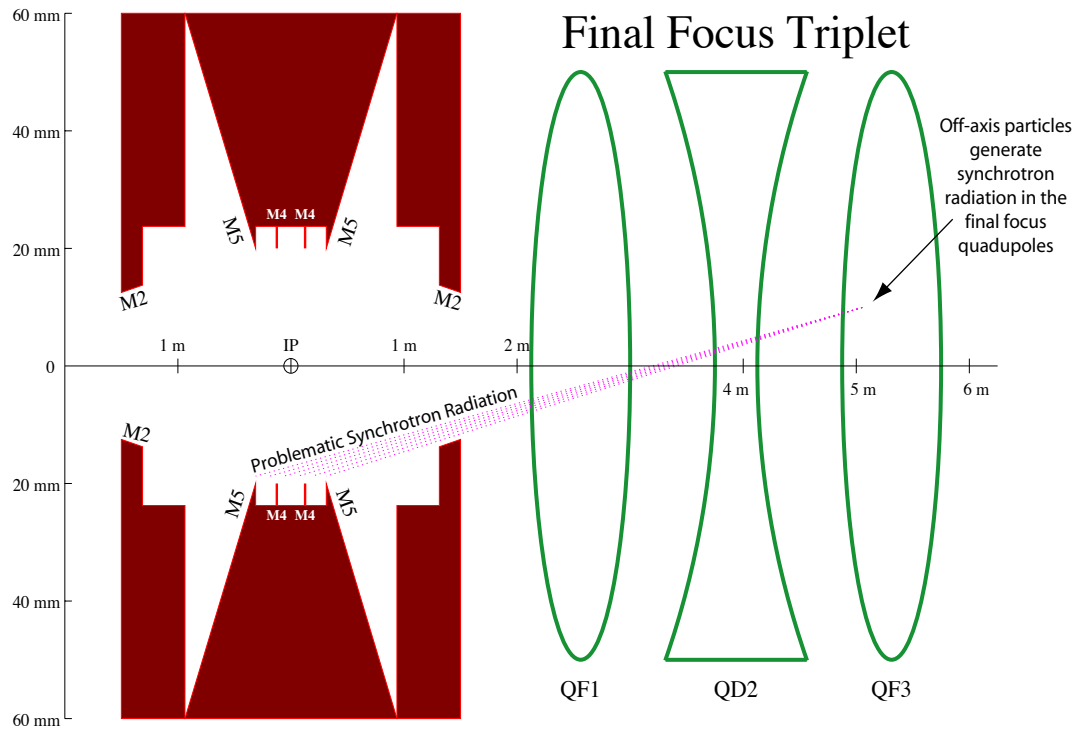
FIGURE 42. Backgrounds in the CDC were caused predominantly by off-axis particles going through the strong field regions of the final focus quadrupole magnets, particularly QD2 and QF3, and generating synchrotron radiation which would go on to hit the M4 and M5 masks, sending electromagnetic showers into the CDC. To hit the beam pipe region in the detector where the M4 and M5 masks are located, synchrotron radiation generated in QF3 at a radius of 10 mm must fall within an angular region of between 5.9 and 6.7 mrad.

off-energy particles that managed to slip through. Balancing the backgrounds in the CDC and the LAC to minimize both was usually tricky.

Regardless of where a moveable jaw was located, it was important not to let it cut into the beam too much as this would generally make the backgrounds worse, not better. Ionization Chambers located near the moveable jaws in the final focus were used for detecting the ionizing radiation caused by the beam hitting a jaw. These ion chambers consisted of two high-voltage electrodes in a gas-filled chamber. Current passing between these electrodes through the ionized gas was proportional to the level of radiation. If backgrounds were bad and a hot ion chamber could be found, many times the backgrounds would improve by backing the corresponding jaw out slightly. A Panofsky long ion chamber (PLIC) is a particular type of ion chamber consisting of a gas filled cable running along the beam line. The point where the beam was lost was determined from the time of arrival of the ion shower that the lost beam sprayed into the cable-chamber [80]. The PLIC was used during backgrounds tuning to detect beams hitting the collimators in the end of the linac or in the arcs. Scope traces from the PLIC are illustrated in Figure 43.

When tuning backgrounds, other important issues to watch for included phase ramp, DALEC thresholds, LEM, angular divergences, and beam crossing angles.

"Phase ramp" was used to change the phase of the arrival at the beginning of the linac of the beam extracted from the damping rings by changing the phase of the damping ring RF relative to that of the compressor and linac. It had the effect of adjusting the beam spectrum and energy at the end of the linac, and as such played an important role with respect to both luminosity and backgrounds.
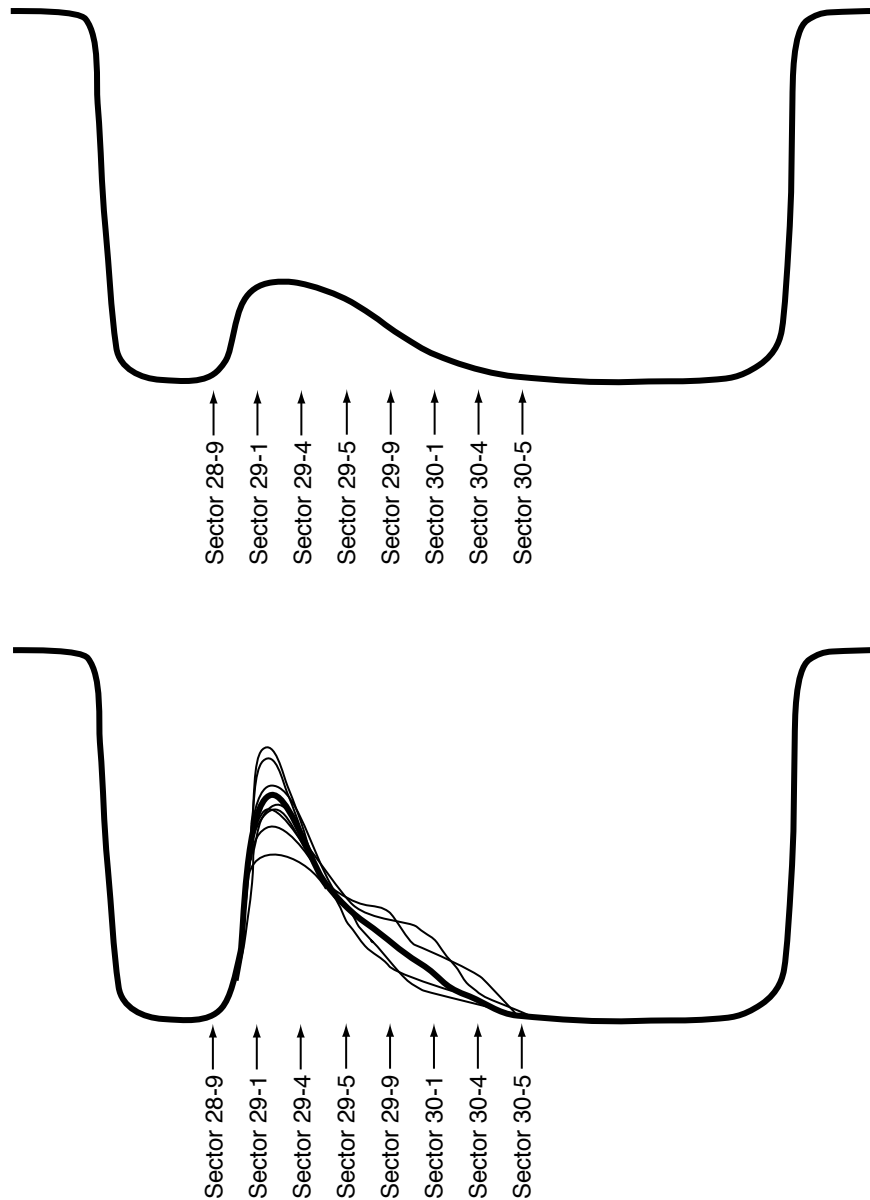
FIGURE 43. Scope traces from the Panofsky long ion chamber (PLIC) at the end of the linac (end of sector 28, sector 29, and most of sector 30) Top: Good PLIC. Bottom: Bad PLIC indicating too much beam is being lost either because a collimator jaw is misplaced or more likely because the orbit trajectory of the beam is mis-steered. The solid line is meant to represent the average position of the scope trace, and the smaller lines are the wild fluctuations about the average position.

The current of a stored beam in the damping ring was easy to measure, and could predict an energy problem down the line at the other end of the linac. If something went wrong at the electron source and the beam current ended up being low, there would not be enough beam loading and the energy of the pulse would be too high by the end of the linac [81]. "DALEC," which stood for "Dump All Low Extracted Currents," an homage to the British science fiction series "Dr. Who," was a system which sensed the current in the Damping Ring before extraction and stopped the extracted beam in the Beam Switch Yard if the current was below a specified threshold. This prevented most off-energy pulses from reaching the SLD detector and showering particularly the CDC with high backgrounds. If CDC trip-offs were frequent, raising the DALEC threshold could sometimes alleviate the problem.

"Linac Energy Management" (LEM) was a procedure used to adjust the linac quadrupole focusing strengths to match the beam energy profile if it had changed slightly. The beam energy tended to vary slightly as klystrons tripped on or off or their phases were changed. The computer would ascertain the beam energy at each quadrupole from the phases of the klystrons to that point, and then adjust the current in each quadrupole for that calculated energy.

Angular divergences were typically $\Theta_x = 450$ μrad and $\Theta_y = 250$ μrad. However, from time to time, the angular divergences were increased in an effort to increase the luminosity, usually at the expense of backgrounds, which tended to dictate that the angular divergences be $\Theta_x < 500$ μrad and $\Theta_y < 300$ μrad.

It was important for backgrounds that the beam crossing angle through the IP be nearly zero. A non-zero crossing angle meant that the beams were going

through the final focus quadrupoles off axis and through the strong field regions, and thus generating background-causing synchrotron radiation.

The source of backgrounds in the Compton Polarimeter was fundamentally different from the sources of backgrounds in the rest of the SLD detector. The attractive forces between small, intense, oppositely charged beams caused each beam to be focused by the field of the other, and the outgoing bunches tended to blow up as a result. Because the Compton polarimeter measured the polarization of the electron beam on the way out of the IP, backgrounds were generally caused by beam disruption. As such, the backgrounds in the polarimeter tended to deteriorate as luminosity increased. The collimator in the south final focus nearest to the IP could sometimes be used to shield the Compton polarimeter to some degree. But increases in luminosity go hand in hand with higher degrees of beam disruption at a linear collider, and as the luminosity approached its maximum late in the 1997-98 run, ultimately the only way to get an accurate measurement of the polarization was to periodically dump the positron beam at the beam switch yard and allow the Compton polarimeter to measure the polarization of the undisrupted electron beam.

CHAPTER V

INITIAL EVENT CHARACTERISTICS

5.1 Event Selection

In order to make measurements of R_{bs}, R_b, and R_c, a sample of hadronic Z^0 decays had to be isolated. The selection of events was done in several stages: First, various "triggers" were employed by the SLD data acquisition system to initiate a readout of the detector and write an event to tape. Second were a series of filters which constituted a first pass through the raw data with a loose set of selection criteria designed to select Z^0 decay events with maximum efficiency while reducing the number of background triggers passed to the reconstruction and analysis stages, and to separate hadronic Z^0 decays from leptonic decays and accelerator-induced backgrounds. And finally, a hadronic event selection algorithm was employed to select hadronic Z^0 decay candidates with well measured tracks and well contained within the fiducial volume of the detector.

At only 120 Hz, the SLC beam crossing rate made the design of the trigger to decide if data should be recorded to tape fairly simple. The data acquisition at the SLD assembled complete data events by combining the data from all the detector

sub-systems, and all sub-systems were written out when a trigger occurred. The three triggers which were used for identifying the hadronic events important for this analysis were as follows [82]:

- Energy trigger: Required at least 8 GeV of total deposited energy in the EM and/or HAD calorimeter towers in the LAC. Only EM towers above the threshold of 246 MeV and HAD towers above the threshold of 1.298 GeV contributed.

- Tracking trigger: Required at least two charged tracks, separated by at least 120°, which passed through at least 9 superlayers of the CDC. In addition, the pattern of CDC cells hit by each of those tracks had to match the configuration of one of the pre-calculated CDC cell pattern maps which collectively accounted for all possible trajectories of charged tracks with momentum transverse to the beam direction above $p_\perp > 250$ MeV. A CDC cell hit was recorded if at least 6 of the 8 sense wires recorded pulses above a certain threshold.

- Hadron Trigger: Required at least 4 GeV of total deposited energy in the EM and/or HAD calorimeter towers in the LAC, and at least one charged track which passed through at least 9 superlayers of the CDC. Only EM towers above the threshold of 246 MeV and HAD towers above the threshold of 1.298 GeV contributed. The pattern of CDC cells hit by the track had to match the configuration of one of the pre-calculated CDC cell pattern maps

TABLE 2. SLD Filters

EIT Pass 1	$N_{high}^{EM} > 0$ for both detector hemispheres
	$N_{high}^{EM} \geq 10$
	$E_{low}^{EM} + E_{low}^{HAD} < 140$ GeV
	$E_{high}^{EM} + E_{high}^{HAD} > 15$ GeV
	$E_{high}^{EM} + E_{high}^{HAD} > \frac{3}{2}(E_{low}^{EM} + E_{low}^{HAD} - 70)$ GeV
Track Trigger	≥ 1 track with $p > 1$ GeV

which collectively accounted for all possible trajectories of charged tracks with momentum transverse to the beam direction above $p_\perp > 250$ MeV.

The combination of these three hadronic triggers yielded an estimated 96% efficiency for hadronic Z^0 decays [83].

The second stage of event selection consisted of filters, evaluated offline, to process the information from the calorimetry and tracking (LAC and CDC) to reject beam-induced backgrounds, especially beam-gas events, and to remove events with large numbers of muons generated upstream in the SLC final focus, for example from beam-collimator interactions. The hadronic filters important for this analysis were the energy imbalance trigger (EIT) [84] and the track trigger (note that the term "trigger" here is perhaps misleading because these "filters" happened offline), described in Table 2. Events had to pass either of these filters. In Table 2, N_{high}^{EM} is the number of EM towers above the high threshold of 246 MeV, E_{high}^{EM} is the energy sum of EM towers above the high threshold of 246 MeV, E_{low}^{EM} is the energy sum of EM towers above the low threshold of 32.8 MeV, E_{high}^{HAD} is the energy sum of HAD towers above the high threshold of 1.298 GeV, and E_{low}^{HAD} is the energy sum of HAD towers above the low threshold of 129.8 MeV.

The EIT Pass 1 filter rejected an estimated 97% of the background events which were read out by the SLD trigger system and written to tape, and the

combination of the SLD triggers and the EIT Pass 1 filter yielded an estimated 92% efficiency for hadronic Z^0 decays [83]. Events surviving the EIT Pass 1 filter were then categorized by the EIT Pass 2 filter as either hadronic, μ-pair, or wide-angle Bhabha candidates. These filtered events were then processed by the detector reconstruction algorithm and written out to data summary tapes (DST) on which physics analyses were run.

The hadronic event candidates which passed the filtering process above were then evaluated by the hadronic event selection algorithm to select only events contained within the fiducial volume of the detector and possessing well-measured tracks. At least seven CDC tracks were required per event, where a well-measured track had momentum transverse to the beam direction $p_\perp > 0.2$ GeV and passed within 5 cm of the IP along the z axis at the point of closest approach to the beam axis, i.e. $|z_{track} - z_{IP}| < 5$ cm. At least three CDC tracks with hits in the vertex detector were required. This was done to facilitate the flavor-tagging techniques applied later in the analysis. The total energy measured using CDC tracks, E^{CDC}, was required to exceed 18 GeV. This was calculated using the 3-momentum measurement in the CDC with the IP taken as the origin and assuming that each track's mass was that of the charged pion, $m_{\pi^\pm} = 139.57$ GeV:

$$E^{CDC} \quad = \quad \sum_{tracks} \sqrt{p_i^2 + m_{\pi^\pm}^2} > 18 \text{ GeV} \tag{5.1}$$

Detector acceptance was considered by evaluating the event thrust axis, $\hat{t}$, which provided information about the direction of the energy flow of the event. The

TABLE 3. Hadronic Event Selection

1.	EIT pass 1 filter passed
2.	Precisely determined IP
3.	> 7 CDC tracks with $p_\perp > 0.2$ GeV and $|z_{track} - z_{IP}| < 5$ cm
4.	> 3 CDC tracks each having > 2 associated VXD hits
5.	$E^{CDC} > 18$ GeV
6.	$|\cos\theta_{thrust}| < 0.71$
7.	≥ 1 track in CDC layers 0 and 1

TABLE 4. Selected hadronic event samples for the 1996 and 1997-98 run periods.

Run Period	Reconstruction	Hadronic Events
1996	R17 Monte Carlo	154,724
1996	R17 Data	33,768
1997-98	R17 Monte Carlo	927,470
1997-98	R17 Data	213,508

thrust axis was determined by maximizing the quantity T, defined as

$$T \;=\; \frac{\sum_{\text{LAC Clusters}} |\vec{p_i} \cdot \hat{t}|}{\sum_{\text{LAC Clusters}} |\vec{p_i}|} \tag{5.2}$$

where the 3-momentum, $\vec{p}$, of the energy cluster was calculated with the IP taken as the origin and assuming $m_{\pi^\pm}$ for the mass of the particle causing the energy deposition. The thrust axis polar angle θ_{thrust} was measured with respect to the e^+ beam direction, and the requirement $|\cos\theta_{thrust}| < 0.71$ was imposed to ensure that the event was contained within the barrel portion of the SLD detector. To remove CDC high voltage trips, events without tracks starting below $r_{xy} = 37.5$ cm in the CDC – layers 0 and 1 – were eliminated. The hadronic event selection is summarized in Table 3. Table 4 summarizes the selected hadronic events statistics for the two run periods.

5.2 Interaction Point Determination

A precise and accurate determination of the location of the the primary Z^0 decay vertex was critical, most notably for heavy-quark identification which relied on distinguishing secondary B- or D-meson decay vertices from this primary vertex (PV). By 1998, the transverse dimensions of the beam spot had reached 1.5 μm × 0.65 μm, and the beam feedback system used to keep the beams in collision provided a stable beam spot to within less than 6 μm. If all the tracks in a single hadronic event which were consistent with having come from the Z^0 decay were fitted to a common vertex in the plane transverse to the beam (xy plane), the fit uncertainty ellipse was large by comparison – typically on the order of 100 μm × 15 μm. Given the small and stable SLC interaction region, the best estimate of the PV in the xy plane was the average SLC interaction point, $\langle$IP$\rangle$. A precise estimate of $\langle$IP$\rangle$ was obtained by averaging over a set of 30 sequential hadronic events: A trial IP location was chosen, and all tracks with VXD hits within 3σ of the trial IP were fitted to a common vertex. This fitted vertex position was taken as the new trial IP and the procedure was repeated until it converged. This technique reduced biases from tracks associated with secondary displaced vertices of heavy hadron decays (which can and do sometimes make it into the fit and don't in general point back to the IP) and removed any thrust axis dependencies.

The resolution of this method was checked in the data using Z^0 decays into muon pairs. Both muon tracks were extrapolated back to the IP: The width of the distribution of the impact parameter with respect to the IP was 8.2 μm, as shown in Figure 44. This uncertainty was the convolution of the IP uncertainty with the impact parameter resolution, found to be 7.55 μm. The IP resolution
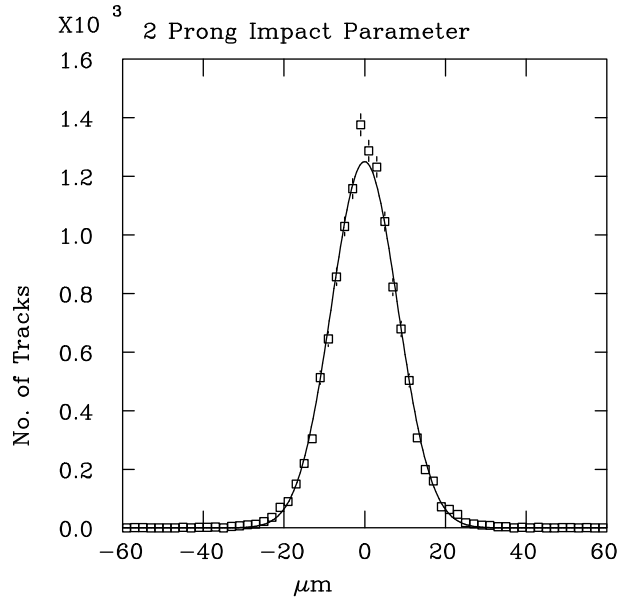
FIGURE 44. Distribution of track impact parameters in $\mu^+\mu^-$ events with respect to the IP in the xy projection. Fitting a Gaussian to this distribution yields a width of 8.2 μm.

in the xy projection could then be estimated as $\sigma_{IP} = \sqrt{8.2^2 - 7.55^2} = 3.2$ μm. However, both of these numbers have a fair amount of statistical and systematic uncertainty, and the quadrature difference of the two numbers likely has a significant uncertainty as well: The IP resolution in the xy projection could easily be 4 μm [26].

The procedure mentioned above for finding the $\langle \text{IP} \rangle$ also minimized the effects of large beam motions within each set of 30 events, but it was still possible that a set could contain a few events which occured far from the $\langle \text{IP} \rangle$. The same distributions which were used to measure σ_{IP} were examined for evidence of non-Gaussian tails. The $\mu^+\mu^-$ impact parameter distribution showed no evidence for non-Gaussian tails, but because $\Gamma(Z^0 \to \mu^+\mu^-) \ll \Gamma(Z^0 \to \text{hadrons})$ (84 MeV vs. 1744 MeV

[15]), this in itself could not conclusively rule out the presence of non-Gaussian tails on $\langle IP \rangle$. In the far more numerous hadronic events, the quantity Y_T also contains information on σ_{IP}: All the quality tracks in a two-jet event were fitted, using a χ^2 fit, to a common vertex; Y_T was the component perpendicular to the event thrust axis $\hat{t}$ of the vector $\vec{Y}$ pointing from the fitted primary vertex (PV) to $\langle IP \rangle$ in the xy-plane, as explained in Figure 45. In the case of the hemisphere Y_T, those tracks with $\vec{p}_{track} \cdot \hat{t} > 0$ were fitted to one vertex, and those tracks with $\vec{p}_{track} \cdot \hat{t} < 0$ were fitted to a second vertex. The sign was then determined by $\text{sign}(\vec{Y_T}) = \text{sign}(\vec{Y} \times \vec{J})$ where $\vec{J}$ was the jet axis. In the positive thrust hemisphere, the jet axis was taken as $\vec{J} = \hat{t}$, and in the negative thrust hemisphere, the jet axis was taken as $\vec{J} = -\hat{t}$. The probability of the χ^2 fit was required to have $P > 0.0001$ to eliminate events with secondary vertices – particularly heavy quark decays – where

$$ P = \int_{\chi^2}^{\infty} f(z, n_d) dz, \tag{5.3} $$

$f(z, n_d)$ is the χ^2 distribution function, and $n_d = 2n_{track} - 3$ is the number of degrees of freedom. The requirement that $P > 0.0001$ produced a purity of light flavored (uds) events of 95%, with charm events constituting the overwhelming majority of heavy flavor contamination (see Figure 47, right side plots).

In the past, the Y_T distribution for the data had shown evidence of non-Gaussian tails on $\langle IP \rangle$. Based on an old study using VXD2 data from the 1992-93 run, these tails were conservatively represented by a second Gaussian IP spread with a $\sigma = 100$ μm for 0.5% of the events.

In the most most recent study using the VXD3 1996 and 1997-98 data, the quanitiy $Y_T(+) + Y_T(-)$ was calculated, where $Y_T(+)$ refered to Y_T in the positive
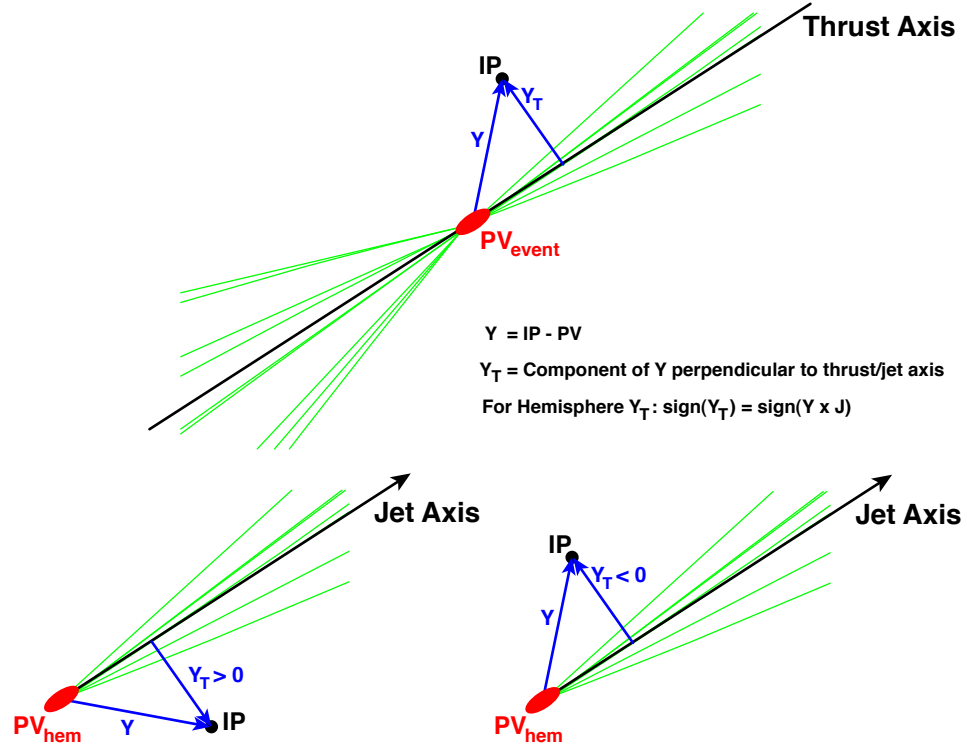
FIGURE 45. Event Y_T (top) and signed hemisphere Y_T. Y_T is the component in the xy-plane perpendicular to the event thrust axis of the vector pointing from the fitted primary vertex (PV) to the 30 event averaged IP. In the event Y_T, all the quality tracks in a 2-jet event were fitted, using a χ^2 fit, to a common vertex, the PV. In the case of the hemisphere Y_T, those tracks with $\vec{p}_{track} \cdot \hat{t} > 0$ were fitted to one vertex, and those tracks with $\vec{p}_{track} \cdot \hat{t} < 0$ were fitted to a second vertex. The sign was then determined by $\text{sign}(Y_T) = \text{sign}(\vec{Y} \times \vec{J})$ where $\vec{J}$ was the jet axis. In the positive thrust hemisphere, the jet axis was taken as $\vec{J} = \hat{t}$, and in the negative thrust hemisphere, the jet axis was taken as $\vec{J} = -\hat{t}$.

thrust hemisphere and $Y_T(-)$ refered to Y_T in the negative thrust hemisphere. This sum canceled out the position of the IP, analogous to the μ-pair miss distance, in order to measure the Y_T resolution independent of any uncertainties associated with the location of the IP. Figure 46 right side plots show that the resolution of the Monte Carlo was slightly better than the resolution of the data, but that on the whole agreement was reasonable. Furthermore, the width of the $Y_T(+) + Y_T(-)$ distribution was comparable to the width of the μ-pair impact parameter distribution in Figure 44.

There was evidence of a non-Gaussian tail in the 1996 data (Figure 47, lower left). As has been done in the past, the tail was represented by a second Gaussian IP spread with a $\sigma = 100\ \mu$m for 0.5% of the events. This was achieved by smearing the $\langle$IP$\rangle$ of the entire Monte Carlo sample to a Gaussian with $\sigma = 100\ \mu$m, and then recombining this smeared sample with an event weight of 0.5% with the unsmeared sample with an event weight of 99.5%. With IP smearing, the agreement between data and Monte Carlo is clearly quite good (see Figure 47, lower left).

The 1997-98 data on the other hand showed virtually no evidence of any non-Gaussian tails (Figure 47, upper left). Any deviation of the Monte Carlo distribution from that of the data can easily be attibuted to the slightly lower resolution of the data, as shown in the plots on the right side of Figure 46. This absence of non-Gaussian tails can be attibuted to the enormous progress in the performance of the SLC leading into the final 1997-98 run.

The longitudinal dimension of the SLC luminous region was larger than the transverse dimension, and the z position of the IP had to be found event-by-event. Tracks with hits in the vertex detector were extrapolated to their point of
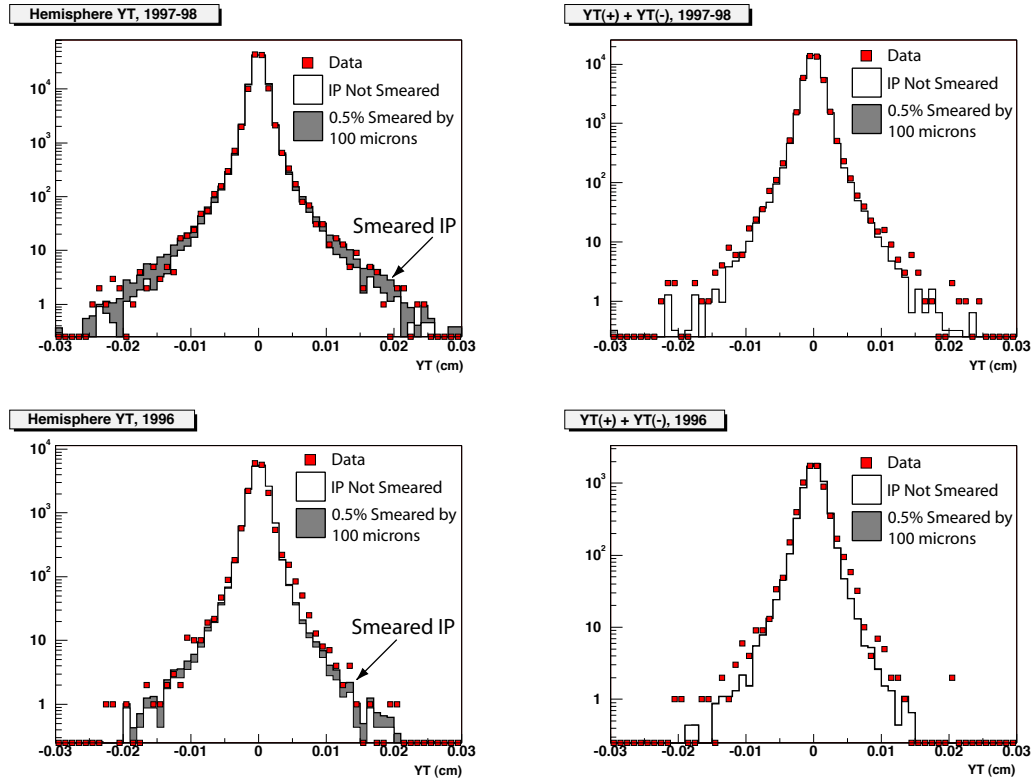
FIGURE 46. Hemisphere Y_T comparison of data with IP-smeared and IP-unsmeared Monte Carlo for the 1997-98 and 1996 runs. In order to eliminate events with secondary vertices – i.e. heavy flavor events – only 2-jet events with a vertex fit probability $P > 0.0001$ were considered. The plots on the right add the hemisphere Y_T for the positive and negative hemispheres in order to remove any effects associated with the IP to better compare the vertex fitting resolution of data and Monte Carlo. Note that the IP-smeared Monte Carlo completely disappears under the IP-unsmeared Monte Carlo, confirming that all IP effects have been completely removed. Not surprisingly, the Monte Carlo had a slightly better resolution than the data, but on the whole, agreement was reasonable.
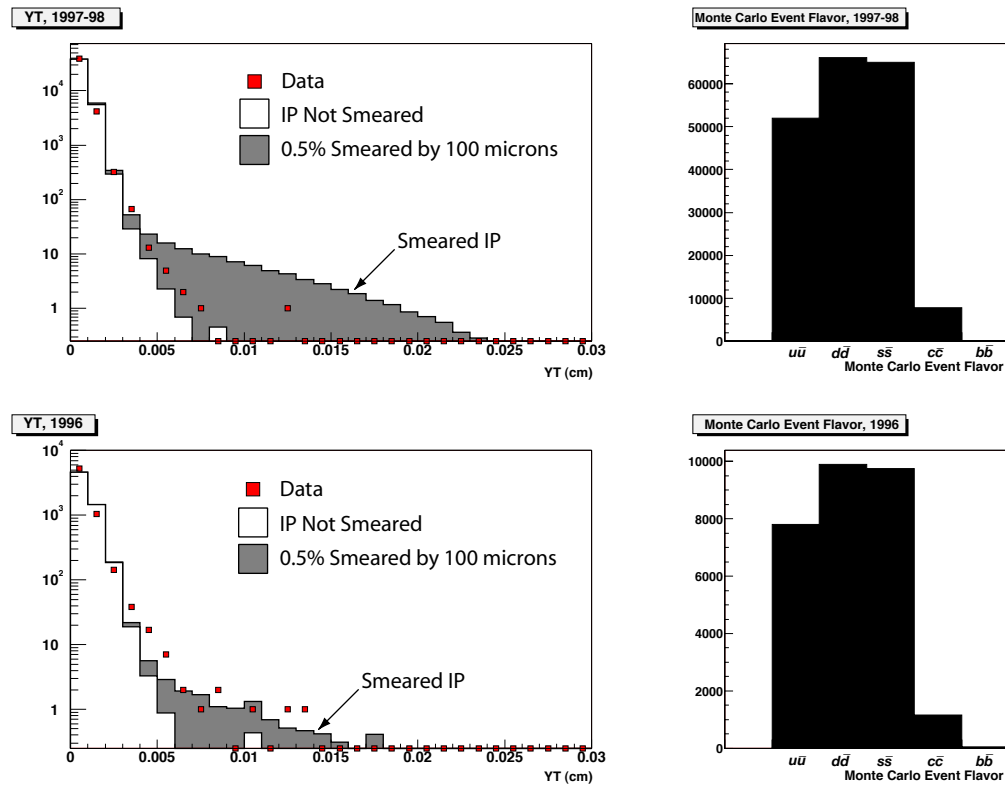
FIGURE 47. Event Y_T comparison of data with IP-smeared and IP-unsmeared Monte Carlo for the 1997-98 and 1996 runs. In order to eliminate events with secondary vertices – i.e. heavy flavor events – only 2-jet events with a vertex fit probability $P > 0.0001$ were considered. The histograms on the right show the distribution of Monte Carlo event flavors which result from the $P > 0.0001$ cut. Purity of light flavored (uds) events is 95%.

closest approach to the transverse (xy) IP position, excluding tracks having impact parameters > 500 μm or $> 3\sigma$ from the transverse IP. The median z coordinate of the positions of closest approach of the remaining tracks was taken as the z position of the IP. The resolution of this method was estimated from the Monte Carlo simulation to be approximately 10 μm for light flavor events, 11 μm for charm events, and 17 μm for bottom events.

5.3 Track Efficiency Correction

Track efficiency is defined as the fraction of charged particles which are reconstructed as tracks in the detector. A comparison of the track efficiency of the actual detector with that in the Monte Carlo simulation was made by comparing the fraction of CDC tracks which had associated VXD hits – called "linking efficiency" – between data and Monte Carlo. The CDC tracks were required to point back approximately towards the IP to reduce the number of K_S^0 and Λ decay products as well as detector interaction products, none of which should have had any hits in the VXD. Comparing the linking efficiency avoided uncertainties associated with the number of charged particles generated in the Monte Carlo simulation as compared to the data, and was thus a test of the detector modeling alone.

For the 1997-98 run, the overall linking efficiency in the Monte Carlo simulation was 1.5% higher than in the data. The linking efficiency was binned in $\cos\theta$, ϕ, and transverse momentum p_T, and a correction matched the simulation to the data bin by bin by removing a few tracks from the simulation. For 1996, there was actually a 1% discrepancy in favor of the data, so no correction was applied.

5.4 Track Resolution Correction

The exact positions and orientations of each of the CCD ladders in the VXD had been determined by the alignment procedure described in [47]. However, residual misalignment remained and affected especially the track impact parameter distributions.

The simulation was adjusted slightly in order to mimic this misalignment. The positions of the tracks were shifted in space – in bins of ϕ and $\cos\theta$ – to reproduce the impact parameter distribution seen in the data.

CHAPTER VI

METHOD

Because the mass of the Z^0 is substantially greater than the mass of the quarks it can decay into, events can be divided into two thrust hemispheres. The philosophy adopted here is thus to divide each event into two hemispheres, and then attempt to identify the flavor of the primary quark in each hemisphere. This method for determining R_{bs} evolved from a method called the "double-tag measurement" which has commonly been used to measure R_b and R_c. Consider the example of measuring R_b: In the double-tag measurement, the number of hadronic events N_{had} is known, but the number of specific $b\bar{b}$ events, N_{bb}, is not. A method of identifying the b quarks based on parameters measured with the detector is devised. Each event is separated into two thrust hemispheres. The number of identified b-hemispheres is H_b and the number of events with both b-hemispheres identified is E_{bb}:

$$H_b = 2\epsilon_b N_{bb} + \sum_{q \neq b} 2\mu_{qb} N_{qq} \qquad (6.1)$$

$$E_{bb} = C_{bb}\epsilon_b^2 N_{bb} + \sum_{q \neq b} \mu_{qb}^2 N_{qq} \qquad (6.2)$$

where ϵ_b is the tagging efficiency for b quarks, and μ_{qb} are the efficiencies to mistag non-b quarks as b quarks. C_{bb} accounts for any correlations between the two hemispheres in an event. Mistagged hemispheres were taken to be uncorrelated (i.e.

$C_{qb,q\neq b} = 1$). $R_b = N_{bb}/N_{had}$:

$$\frac{H_b}{2N_{had}} = \epsilon_b R_b + \sum_{q\neq b} \mu_{qb} R_q \qquad (6.3)$$

$$\frac{E_{bb}}{N_{had}} = C_{bb}\epsilon_b^2 R_b + \sum_{q\neq b} \mu_{qb}^2 R_q \qquad (6.4)$$

Neglecting backgrounds and correlations, i.e. $\epsilon_b \gg \mu_{qb}$ and $C_{bb} \approx 1$,

$$\epsilon_b \approx \frac{2E_{bb}}{H_b} \qquad (6.5)$$

$$R_b \approx \frac{H_b^2}{4E_{bb}N_{had}} \qquad (6.6)$$

The double tag method has the advantage that the tagging efficiency is measured directly from the data thus reducing the systematic uncertainty in the measurement. This method can be extended to make a joint measurement of R_b and R_c by considering H_b, H_c, E_{bb}, and E_{cc}.

The present analysis takes this several steps further, and specifically allows for events containing a primary b quark and a primary s quark. We took to heart one of the canons of experimental particle physics: "When possible, use data rather than Monte Carlo events to measure efficiencies and background levels" [85].

Thus the number of b-tagged hemispheres is

$$H_b = 2\epsilon_b N_{bb} + 2\mu_{cb}N_{cc} + 2\mu_{sb}N_{ss} + 2\mu_{db}N_{dd} + 2\mu_{ub}N_{uu} + (\epsilon_b + \mu_{sb})N_{bs}$$
$$H_b = 2N_{had}\left[\epsilon_b\frac{N_{bb}}{N_{had}} + \mu_{cb}\frac{N_{cc}}{N_{had}}\right.$$
$$\left. +\mu_{sb}\frac{N_{ss}}{N_{had}} + \mu_{db}\frac{N_{dd}}{N_{had}} + \mu_{ub}\frac{N_{uu}}{N_{had}} + \frac{1}{2}(\epsilon_b + \mu_{sb})\frac{N_{bs}}{N_{had}}\right].$$

Now, $N_{had} = N_{bb} + N_{cc} + N_{ss} + N_{dd} + N_{uu} + N_{bs}$, and therefore $N_{uu} = N_{had} - N_{bb} - N_{cc} - N_{ss} - N_{dd} - N_{bs}$.

$$H_b = 2N_{had}\left[\epsilon_b \frac{N_{bb}}{N_{had}} + \mu_{cb}\frac{N_{cc}}{N_{had}} + \mu_{sb}\frac{N_{ss}}{N_{had}} + \mu_{db}\frac{N_{dd}}{N_{had}}\right.$$
$$\left. + \mu_{ub}\frac{N_{had} - N_{bb} - N_{cc} - N_{ss} - N_{dd} - N_{bs}}{N_{had}} + \frac{1}{2}(\epsilon_b + \mu_{sb})\frac{N_{bs}}{N_{had}}\right].$$

The fraction of b-tagged hemispheres is

$$F_b = \epsilon_b R_b + \mu_{cb} R_c + \mu_{sb} R_s + \mu_{db} R_d$$
$$+ \mu_{ub}(1 - R_b - R_c - R_s - R_d - R_{bs}) + \frac{1}{2}(\epsilon_b + \mu_{sb})R_{bs}. \qquad (6.7)$$

The number of double b-tagged events is

$$E_{bb} = C_{bb}\epsilon_b^2 N_{bb} + \mu_{cb}^2 N_{cc} + \mu_{sb}^2 N_{ss} + \mu_{db}^2 N_{dd} + \mu_{ub}^2 N_{uu} + \epsilon_b \mu_{sb} N_{bs}$$
$$E_{bb} = N_{had}\left[C_{bb}\epsilon_b^2 \frac{N_{bb}}{N_{had}} + \mu_{cb}^2 \frac{N_{cc}}{N_{had}} + \right.$$
$$\left. \mu_{sb}^2 \frac{N_{ss}}{N_{had}} + \mu_{db}^2 \frac{N_{dd}}{N_{had}} + \mu_{ub}^2 \frac{N_{uu}}{N_{had}} + \epsilon_b \mu_{sb}\frac{N_{bs}}{N_{had}}\right].$$

Again, $N_{uu} = N_{had} - N_{bb} - N_{cc} - N_{ss} - N_{dd} - N_{bs}$.

$$E_{bb} = N_{had}\left[C_{bb}\epsilon_b^2 \frac{N_{bb}}{N_{had}} + \mu_{cb}^2 \frac{N_{cc}}{N_{had}} + \mu_{sb}^2 \frac{N_{ss}}{N_{had}} + \mu_{db}^2 \frac{N_{bb}}{N_{had}} + \right.$$
$$\left. \mu_{ub}^2 \frac{N_{had} - N_{bb} - N_{cc} - N_{ss} - N_{dd} - N_{bs}}{N_{had}} + \epsilon_b \mu_{sb}\frac{N_{bs}}{N_{had}}\right].$$

The fraction of double b-tagged events is

$$F_{bb} = C_{bb}\epsilon_b^2 R_b + \mu_{cb}^2 R_c + \mu_{sb}^2 R_s + \mu_{db}^2 R_d +$$

$$\mu_{ub}^2(1 - R_b - R_c - R_s - R_d - R_{bs}) + \epsilon_b \mu_{sb} R_{bs}. \tag{6.8}$$

In a similar fashion, the fraction of c-tagged hemispheres is

$$
\begin{aligned}
F_c &= \mu_{bc} R_b + \epsilon_c R_c + \mu_{sc} R_s + \mu_{dc} R_d + \\
&\quad \mu_{uc}(1 - R_b - R_c - R_s - R_d - R_{bs}) + \frac{1}{2}(\mu_{bc} + \mu_{sc}) R_{bs}.
\end{aligned} \tag{6.9}
$$

The fraction of double c-tagged events is

$$
\begin{aligned}
F_{cc} &= \mu_{bc}^2 R_b + C_{cc} \epsilon_c^2 R_c + \mu_{sc}^2 R_s + \mu_{dc}^2 R_d + \\
&\quad \mu uc^2 (1 - R_b - R_c - R_s - R_d - R_{bs}) + \mu_{bc} \mu_{sc} R_{bs}.
\end{aligned} \tag{6.10}
$$

The fraction of s-tagged hemispheres is

$$
\begin{aligned}
F_s &= \mu_{bs} R_b + \mu_{cs} R_c + \epsilon_s R_s + \mu_{ds} R_d + \\
&\quad \mu_{us}(1 - R_b - R_c - R_s - R_d - R_{bs}) + \frac{1}{2}(\mu_{bs} + \epsilon_s) R_{bs}.
\end{aligned} \tag{6.11}
$$

The fraction of bs-tagged events is

$$
\begin{aligned}
F_{bs} &= 2 \left[\epsilon_b \mu_{bs} R_b + \mu_{cb} \mu_{cs} R_c + \epsilon_s \mu_{sb} R_s + \mu_{ds} \mu_{db} R_d + \right. \\
&\quad \left. \mu_{us} \mu_{ub}(1 - R_b - R_c - R_s - R_d - R_{bs}) \right] + (\epsilon_b \epsilon_s + \mu_{bs} \mu_{sb}) R_{bs}.
\end{aligned} \tag{6.12}
$$

The fraction of cs-tagged events is

$$
\begin{aligned}
F_{cs} &= 2 \left[\mu_{bc} \mu_{bs} R_b + \epsilon_c \mu_{cs} R_c + \mu_{sc} \epsilon_s R_s + \mu_{dc} \mu_{ds} R_d + \right. \\
&\quad \left. \mu_{uc} \mu_{us}(1 - R_b - R_c - R_s - R_d - R_{bs}) \right] + (\mu_{bc} \epsilon_s + \mu_{sc} \mu_{bs}) R_{bs}.
\end{aligned} \tag{6.13}
$$

The fraction of bc-tagged events is

$$
\begin{aligned}
F_{bc} &= 2\left[\epsilon_b\mu_{bc}R_b + \epsilon_c\mu_{cb}R_c + \mu_{sb}\mu_{sc}R_s + \mu_{db}\mu_{dc}R_d + \right. \\
&\quad \left. \mu_{ub}\mu_{uc}(1 - R_b - R_c - R_s - R_d - R_{bs})\right] + (\epsilon_b\mu_{sc} + \mu_{bc}\mu_{sb})R_{bs}. \quad (6.14)
\end{aligned}
$$

These equations are solved iteratively.

From these eight equations, we can determine eight unknowns: The tagging efficiencies ϵ_b, ϵ_c, and ϵ_s; the mistag efficiencies μ_{cs} and μ_{bc}; and of course the ratios of partial widths R_b, R_c, and finally R_{bs}. Other mistag efficiencies and correlations are assumed to be the Monte Carlo values. Since R_b is a measured quantity, we take

$$
R_d = R_s = \frac{\Gamma^{SM}(Z^0 \to d\bar{d})}{\Gamma^{SM}(Z^0 \to b\bar{b})} R_b. \tag{6.15}
$$

At tree level, the three quarks d, s, and b corresponding to $I^W_{3,22} = -\frac{1}{2}$ all have the same ratios of partial widths; $R_d = R_s = R_b$. However, because the top quark mass is so large and $|V_{tb}| \cong 1$, to estimate R_d and R_s from R_b, we scale R_b by the ratio of partial widths calculated in the Standard Model [15]. The approximation that $R_d = R_s$ is reasonable since the radiative corrections to R_d and R_s are comparable.

Nominally, one might have hoped to determine the rate of b quarks mistagged as s quarks, μ_{bs}, from the data as well by considering the fraction of double s-tagged events, F_{ss}. However, μ_{bs} is very small and therefore has a significant statistical uncertainty relative to its size. The propagation of statistical uncertainties in a large system of nonlinear equations is complicated [86]. Determining μ_{bs} from the data turns out to be impractical and to greatly increase the statistical uncertainty

of R_{bs}. We were ultimately to abandon measuring μ_{bs} in favor of determining its value from the Monte Carlo, and come what may vis-a-vis systematic uncertainties.

It's not easy to tease out the skein of thrust hemisphere flavor. The methods used in this analysis for identifying primary b, c, and s quarks are detailed in the following sections.

CHAPTER VII

IDENTIFICATION OF HEAVY QUARKS

7.1 A Brief Introduction to Neural Networks

In high energy physics, neural networks have for some years now been used both in real-time and offline applications involving pattern classification. Most applications to date have utilized feed-forward neural networks trained with the standard back-propagation algorithm. Such neural nets are referred to as supervised networks, meaning they require a desired response to be trained: They learn how to transform input data from a set of event descriptors into a desired response in the form of a reduced set of output variables. They have been shown to approximate the performance of optimal statistical classifiers in difficult problems [87].

The basic constituents of such a neural network are units and links: The units are arranged in layers – an input layer I_i corresponding to the input variables, a hidden layer H_j, and an output layer O_k corresponding to the reduced set of variables upon which distinctions between signal and background may be defined, as illustrated in Figure 48; the links with weights ω_{ij} feed information from the
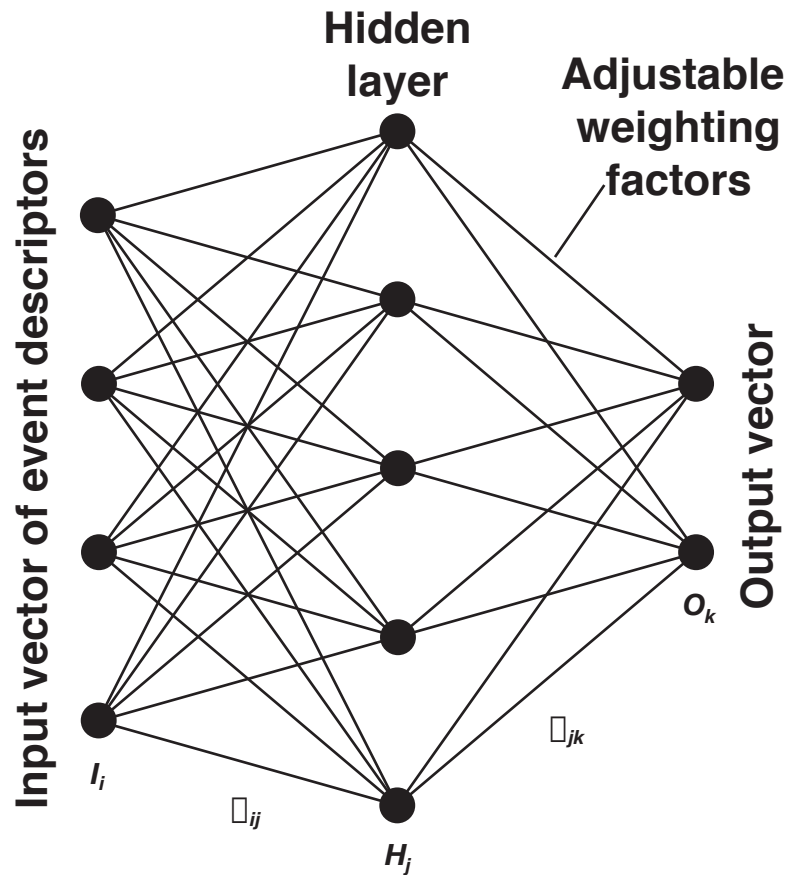
FIGURE 48. Schematic diagram for a typical feed-forward neural network of the type used in this analysis.

units in the input layer I_i to the units in the hidden layer H_j, and the links with

weights ω_{jk} feed information from the units in the hidden layer H_j to the units in

the output layer O_k.

A feed-forward network, as its name suggests, calculates the activation values

of the target units in a layer from the activation values of the source units in the

preceding layer. For classification problems, a sigmoid activation function is often

used. Thus, the activation values for the units in the hidden and output layers are

calculated

$$H_j \quad = \quad \frac{1}{1 + e^{-\sum_i \omega_{ij} I_i - \theta_j}} \tag{7.1}$$

$$O_k \quad = \quad \frac{1}{1 + e^{-\sum_j \omega_{jk} H_j - \theta_k}} \tag{7.2}$$

where θ is the bias corresponding to the unit in question and determines where the activation function has its steepest ascent [88].

The supervised networks often found in HEP applications acquire knowledge through a learning process that uses Monte Carlo data sets containing signal and background events. The knowledge is stored in the interneuron connection strengths or synaptic weights. To train a feed-forward neural network with the standard back-propagation algorithm, an input pattern is presented to the network which is fed forward in the usual manner to the output layer. The activation value for the target unit of the output layer O_k is then compared with its desired output or "teaching" value T_k (for example 1 corresponding to signal and 0 corresponding to background), and the difference is simply $\delta_k = T_k - O_k$. When no teaching values T_j exist, i.e. for the hidden layer, δ is calculated as $\delta_j = \sum_k \delta_k \omega_{jk}$. In either case, δ is used together with the activation value of the source unit in the previous layer to compute the necessary changes to the link's weight $\Delta\omega$:

$$\Delta\omega_{jk} \quad = \quad \eta H_j \delta_k \tag{7.3}$$

$$\Delta\omega_{ij} \quad = \quad \eta I_i \delta_j \tag{7.4}$$

where η is the learning rate – typically ~ 0.1.

In practice, networks with one hidden layer containing one more unit than the input layer are sufficient for most classification problems [89, 87].

In this analysis, neural networks are applied to secondary vertex reconstruction, to the problem of sorting out which tracks go with which vertices – so called vertex-track attachment, to separating c hemispheres from b hemispheres, and to separating b hemispheres from s hemispheres.

7.2 Secondary Vertex Reconstruction

The identification of heavy flavor quarks is crucial for this analysis. For $Z^0 \rightarrow b\bar{b}$ and $Z^0 \rightarrow c\bar{c}$, events, a heavy hadron decay can be expected in each hemisphere. These heavy hadrons tend to be created with significant momenta, and coupled with their relatively long lifetimes, they often propagate several millimeters before decaying: B mesons from Z^0 decays usually travel approximately 3 mm before decaying; D mesons go about half that far. Heavy hadron decays thus result in vertices which are significantly displaced from the event interaction point (IP).

The objective is then to identify these vertices and their corresponding tracks. Topological vertexing [90] utilizes the vertex detector to search for vertices in 3D coordinate space. This search is based on the function $V(\vec{r})$ which quantifies the relative probability of there being a vertex at location $\vec{r}$. The first step is to obtain from the relevant trajectory parameters for each track i a function $f_i(\vec{r})$ representing a Gaussian probability density tube for the track with a width equal to the uncertainty in the track position at $\vec{r}_0$, its position of closest approach to
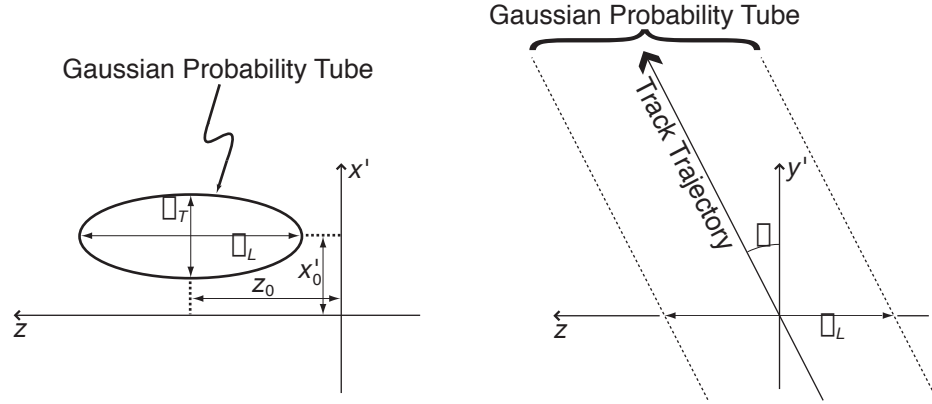
FIGURE 49. Construction of the Gaussian Probability Tube $f_i(\vec{r})$ for each track as viewed in the $x'z$ plane and in the $y'z$ plane.

the IP:

$$f_i(\vec{r}) \;=\; e^{-\frac{1}{2}\left[\left(\frac{x'-x'_0-\kappa y'^2}{\sigma_T}\right)^2 + \left(\frac{z-z_0-y'\tan\lambda}{\sigma_L}\right)^2\right]} \tag{7.5}$$

where the x and y coordinates have been transformed to x' and y' for each track such that the track momentum is parallel to the positive y' axis in the xy plane at $\vec{r}_0$. The third dimension z of the track's trajectory is taken into account via the helix parameter λ. The quantity σ_T is the measurement error for the track in the xy plane and σ_L the measurement error along z. See Figure 49.

$V(\vec{r})$ should be a smooth continuous function so that its maxima may be found. Additionally, it is desired that $V(\vec{r})$ reflect the multiplicity and degree of overlap of the track probability functions and thus measure the probability that at least some of the tracks originate at $\vec{r}$, therefore forming a vertex at that locale. However, it is important for $V(\vec{r}) \simeq 0$ in regions where $f_i(\vec{r})$ is significant for only
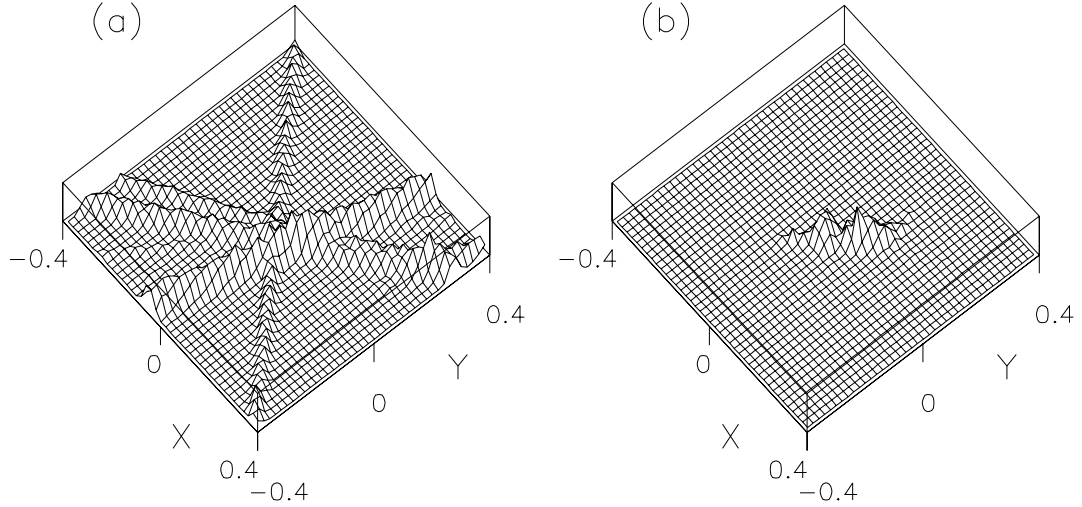
FIGURE 50. Track (a) and vertex (b) functions projected onto the xy plane for convenience.

one track. One functional form which meets these requirements is

$$V(\vec{r}) \;=\; \sum_{i=0}^{N} f_i(\vec{r}) - \frac{\sum_{i=0}^{N} [f_i(\vec{r})]^2}{\sum_{i=0}^{N} f_i(\vec{r})} \tag{7.6}$$

where N is the number of tracks. The first term reflects the degree of overlap, and the second ensures $V(\vec{r})$ is not dominated by a single track. The plots in Figure 50 show an example taken from a Monte Carlo $Z^0 \rightarrow b\bar{b}$ event of (a) $\sum_{i=0}^{N} f_i(\vec{r})$ and (b) $V(\vec{r})$. These plots were obtained by integrating the two functions over z within the limits ± 8 cm from the IP. The regions where vertices are probable can be seen from the distribution of $V(\vec{r})$ in Figure 50(b). In this case the topological

TABLE 5. Requirements for tracks used in secondary vertex reconstruction.

1.	≥ 3 VXD Hits
2.	$p_\perp > 0.250$ GeV
3.	3D impact parameter $b < 3$ mm
4.	Track not consistent with originating from γ, K_S^0, or Λ

vertexing algorithm resolved two vertices, the primary vertex at $x = y = 0$, and a secondary vertex to the right of the IP ~ 0.15 cm.

The event is first divided into two hemispheres perpendicular to the thrust axis. The tracks in each hemisphere, in order to be used in the secondary vertex reconstruction, must pass a set of loose requirements, as summarized in Table 5.

The vertices identified to this point must lie within 2.3 cm of the center of the beam pipe to remove false vertices associated with interactions of particles with the detector hardware. The vertex invariant mass must also not be close to the K_S^0 mass: $|M_{VTX} - M_{K_S^0}| > 15$ MeV. This helps to further remove K_S^0 decays that survived the track cuts listed in Table 5.

Despite the above cuts, there are still a few vertices falsely attributed to the decay of heavy quarks: The first of the many neural networks used throughout this analysis enhances the rejection of vertices from sources other than heavy flavor decays.

This neural network [89] is trained to separate vertices which contain only tracks from heavy hadron decays from vertices having tracks originating from other sources, including the IP or s hadron decays. It has three inputs: The distance from the IP, D; the normalized distance from the IP, D/σ_D; and the angle between the flight direction and vertex momentum, $p - D$ angle. These quantities are
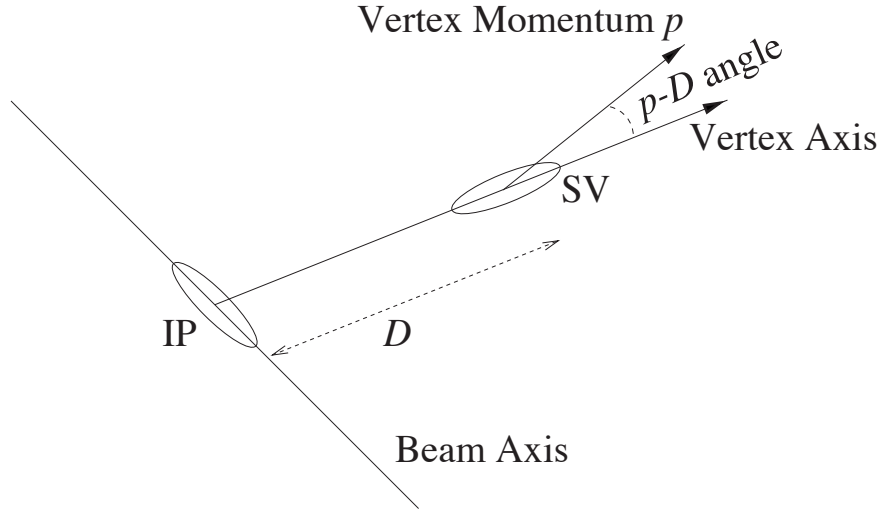
FIGURE 51. Schematic illustration of the quantities used in the vertex selection neural network.

illustrated schematically in Figure 51, and their distributions as well as the output of the neural network are shown in Figure 52.

Only vertices with a neural network output $NN_{vtx} > 0.7$ are retained, with 72.7% of b hemispheres, 28.2% of c hemispheres, and 0.41% of light flavor hemispheres passing this cut. Approximately 16% of b hemispheres contain multiple secondary vertices [89].

7.3 Vertex Track Attachment

The tracks in an event do not necessarily originate from the same vertex: To accurately identify heavy hadron decays, it is critical to correctly assign – "attach" – all the tracks in the event to the vertices they originate with. A second
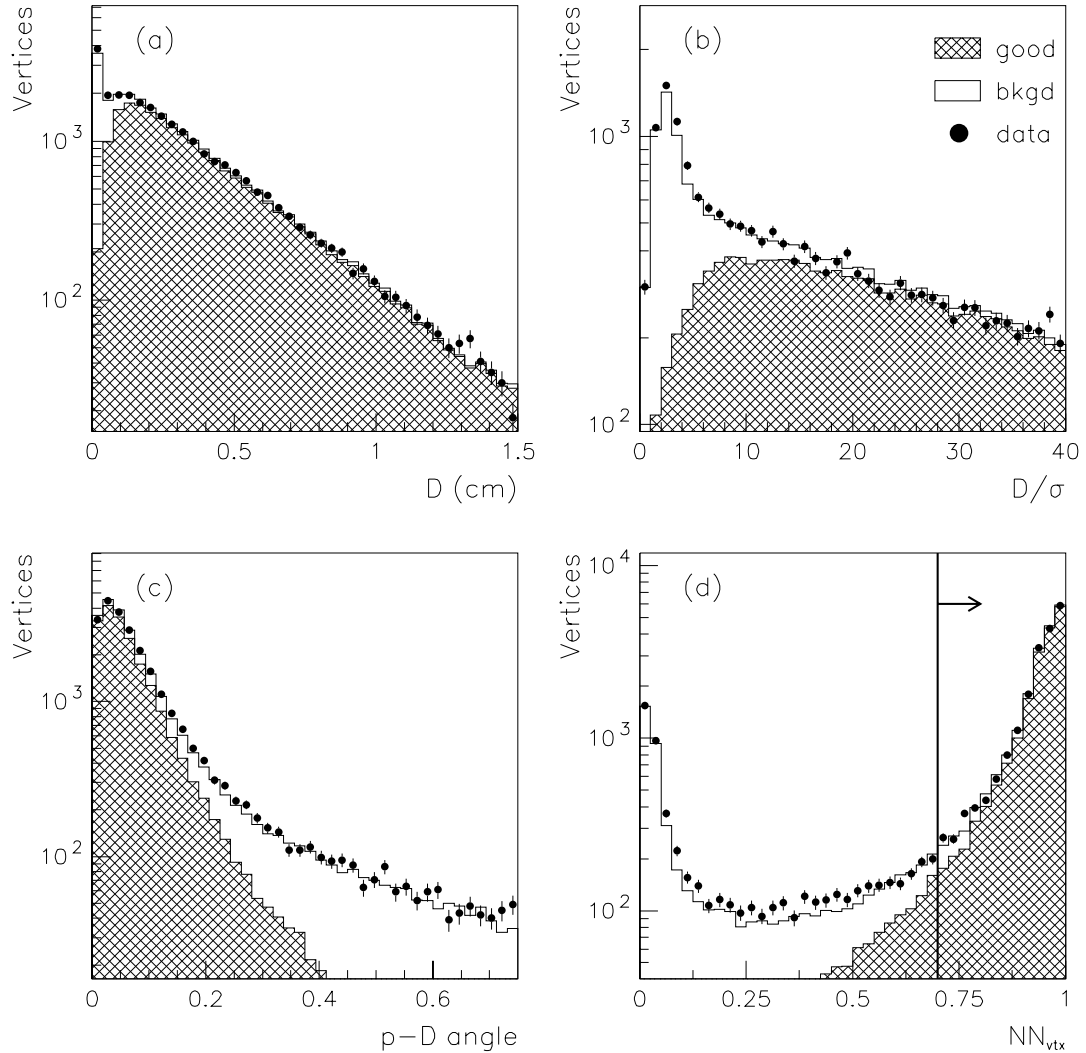
FIGURE 52. Distributions of vertex selection variables: (a) Distance from IP D; (b) normalized distance from IP D/σ_D; (c) angle between flight direction and vertex momentum, $p - D$ angle; (d) neural network output NN_{vtx}. In the plots, the histogram represents the Monte Carlo and the dots represent the data. A good vertex contains only heavy hadron decay tracks, and the region to the right of the line, indicated by the arrow, is the accepted region.

neural network is therefore used to attach tracks to their corresponding secondary vertices. This neural network [89] is trained to separate tracks originating with heavy hadron decays from tracks originating with other sources, including the IP and s hadron decays.

The first four of the total of five inputs of this neural network are defined at the point of closest approach of the track to the axis joining the secondary vertex (SV) to the IP (the so-called vertex axis): The transverse distance from the track to the vertex axis T, the distance from the IP along the vertex axis to the position of closest approach L, that distance divided by the flight distance of the SV from the IP L/D, and the angle of the track to the vertex axis α. The final input is the 3D impact parameter of the track to the IP normalized by its error b/σ_b. These inputs are illustrated schematically in Figure 53, and their distributions as well as the output of the neural network are shown in Figure 54.

Only tracks with a neural network output $NN_{trk} > 0.6$ are considered to originate from a heavy hadron decay.

7.4 Separating b Quarks from c Quarks

At this point, for each hemisphere containing a secondary vertex, there is a list of associated tracks. If no secondary vertex is found in the hemisphere, the list is empty. From this list of tracks, several parameters can be calculated to separate b quarks from c quarks and from light flavored quarks. The most important of these
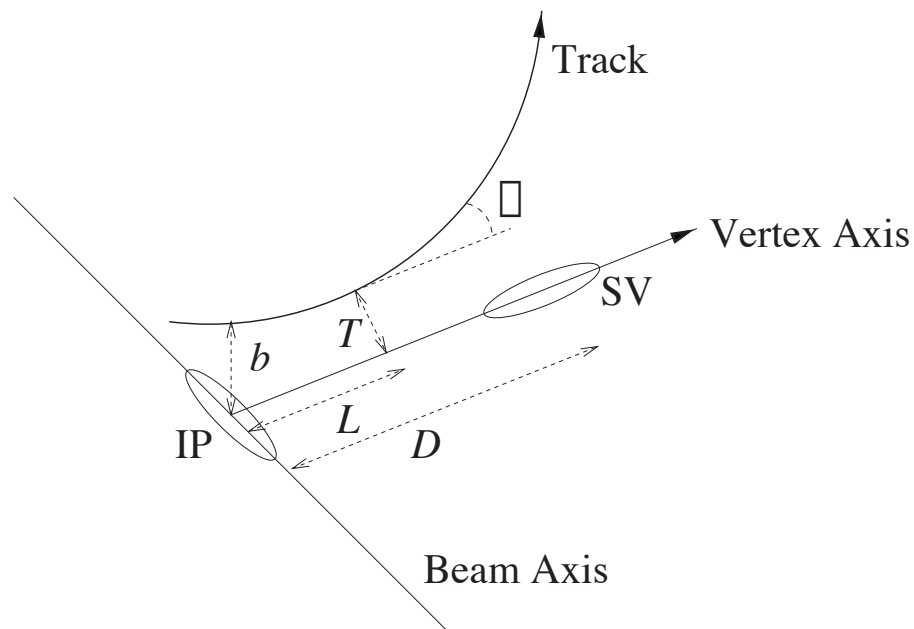
FIGURE 53. Schematic illustration of the quantities used in the track attachment neural network. The first four inputs are defined at the point of closest approach of the track to the vertex axis. They are the transverse distance from the track to the vertex axis T, the distance from the IP along the vertex axis to the position of closest approach L, that distance divided by the flight distance of the SV from the IP L/D, and the angle of the track to the vertex axis α. The last input is the 3D impact parameter of the track to the IP normalized by its error b/σ_b.
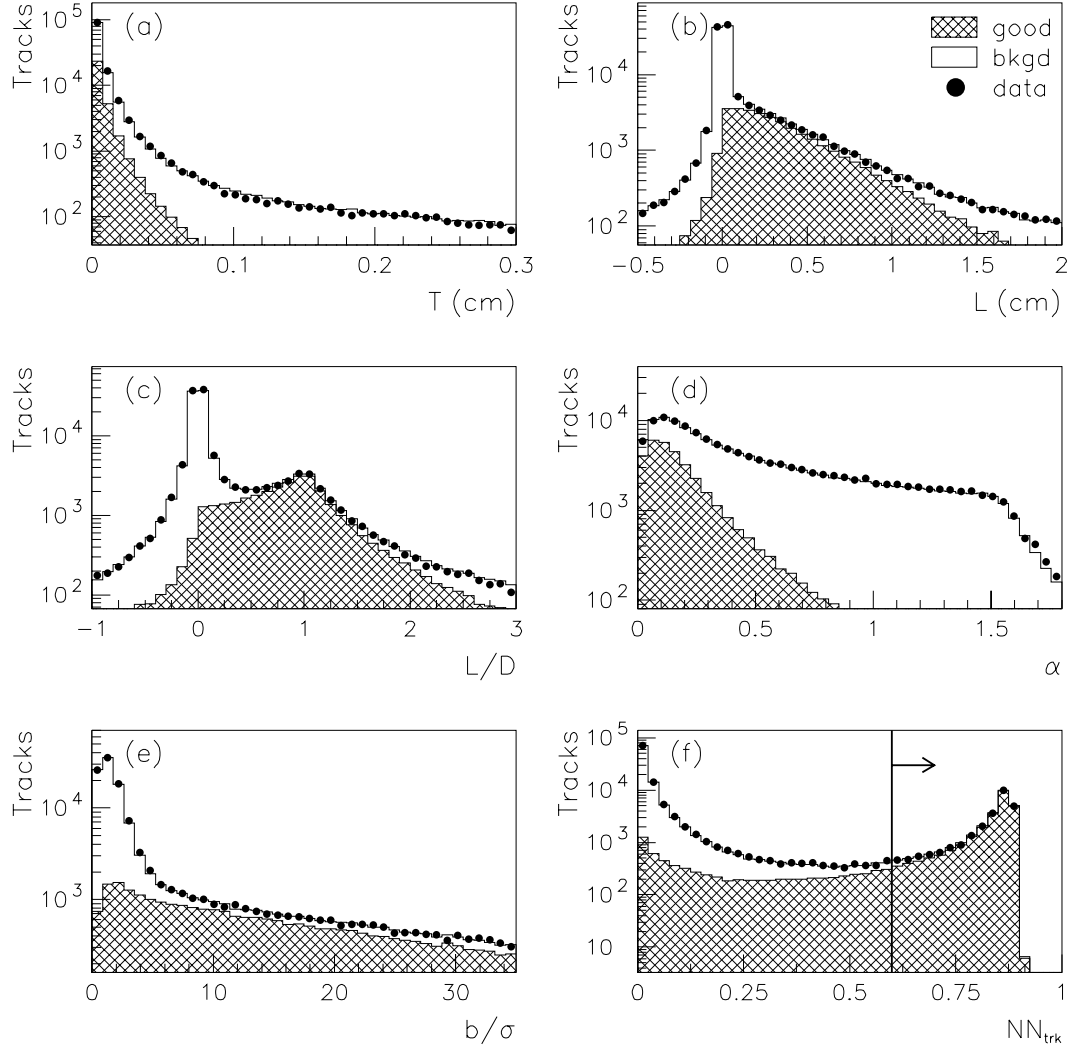
FIGURE 54. Distributions of cascade track selection variables: (a) Transverse distance from the track to the vertex axis T; (b) distance from the IP to the position of closest approach along the vertex axis L; (c) L divided by the flight distance of the SV from the IP L/D; (d) angle of the track to the vertex axis at the position of closet approach to the vertex axis α; and (e) 3D impact parameter of the track to the IP normalized by its error b/σ_b. The final plot (f) is the output of the track attachment neural network NN_{trk}. In the plots, the histogram represents the Monte Carlo and the dots represent the data. A good track is one which originates from a heavy hadron decay, and the region to the right of the line, indicated by the arrow, is the accepted region.

parameters is the invariant mass of the candidate heavy hadron decay vertex:

$$M_{raw} = \sqrt{\left(\sum_{tracks} E_i\right)^2 - \left(\sum_{tracks} \vec{p}_i\right)^2} \tag{7.7}$$

where M_{raw} is the invariant mass of the vertex considering only the charged tracks. For the purposes of calculating the invariant vertex mass, each of the charged tracks associated with the vertex is assumed to be a pion and assigned a mass of $m_\pi = 139.6$ MeV.

$$M_{raw} = \sqrt{\left(\sum_{tracks} \sqrt{p_i^2 + m_\pi^2}\right)^2 - \left(\sum_{tracks} \vec{p}_i\right)^2} \tag{7.8}$$

In truth, the vertex is comprised of more than just the charged tracks; there may also be some number of unseen neutral particles. The unknown contribution to the mass from these neutral particles can be partially taken into account by considering the alignment between the vertex momentum p_{VTX} and the vertex axis – the vector going from the interaction point to the vertex. The degree of misalignment depends on the momentum p_T transverse to the vertex axis (Figure 55). The problem is most easily considered by boosting to the frame of reference where the momentum sum of the charged tracks parallel to the vertex axis p_L equals zero.

The charged tracks thus have collectively zero longitudinal momentum p_L, but presumably still some amount of transverse momentum p_T. In order not to violate the law of conservation of momentum, there must be an exactly equal amount of transverse momentum associated with the unseen neutral particles – the missing p_T. In the case where the neutrals also have zero longitudinal momentum
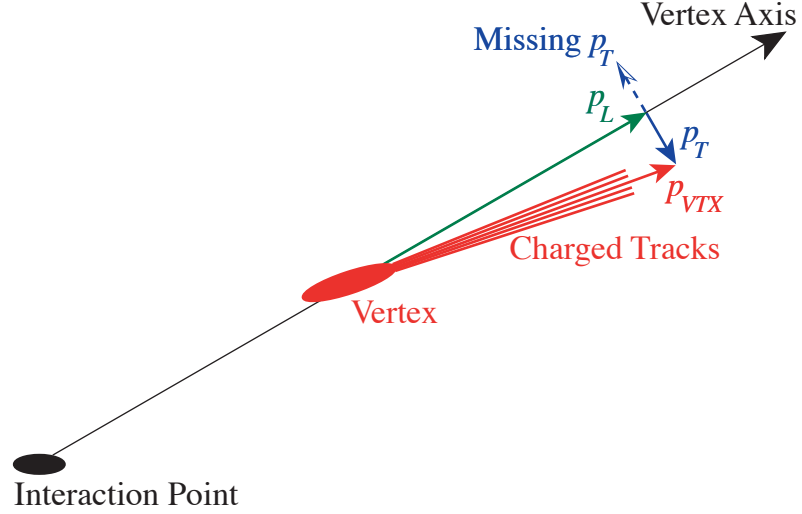
FIGURE 55. Vertex in the Lab Frame.

(the minimal assumption), the total vertex mass in this frame of reference is just the sum of the energies of the charged and neutral particles

$$M_{VTX} \quad = \quad E_{charged} + E_{neutral} \tag{7.9}$$

In this reference frame, $E_{charged}$ is simply

$$E_{charged} \quad = \quad \sqrt{M_{raw}^2 + p_T^2} \tag{7.10}$$

An assumption about the mass of the neutrals is required, and the minimal assumption is that they all have negligible mass.

$$E_{neutral} \quad = \quad \sqrt{0 + p_T^2} \tag{7.11}$$
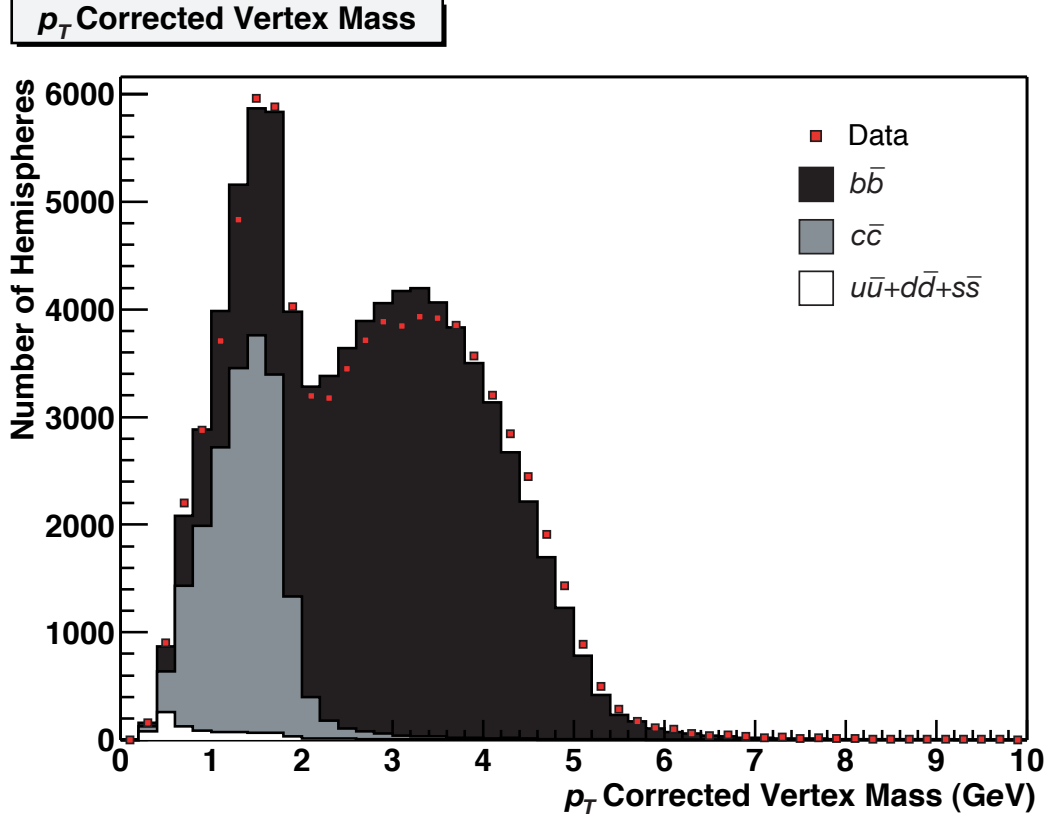
FIGURE 56. p_T Corrected Vertex Mass. In the plot, the histogram represents the Monte Carlo and the dots represent the data.

The p_T-corrected invariant vertex mass (really a lower limit on the actual vertex mass) is thus

$$M_{VTX} = \sqrt{M_{raw}^2 + p_T^2} + |\vec{p}_T| \qquad (7.12)$$

Figure 56 clearly shows that vertices with $M_{VTX} > 2$ GeV come almost entirely from b decays.

However, a third neural network is used to further enhance the discrimination between b and c decays. To the p_T corrected vertex mass M_{VTX} described above we
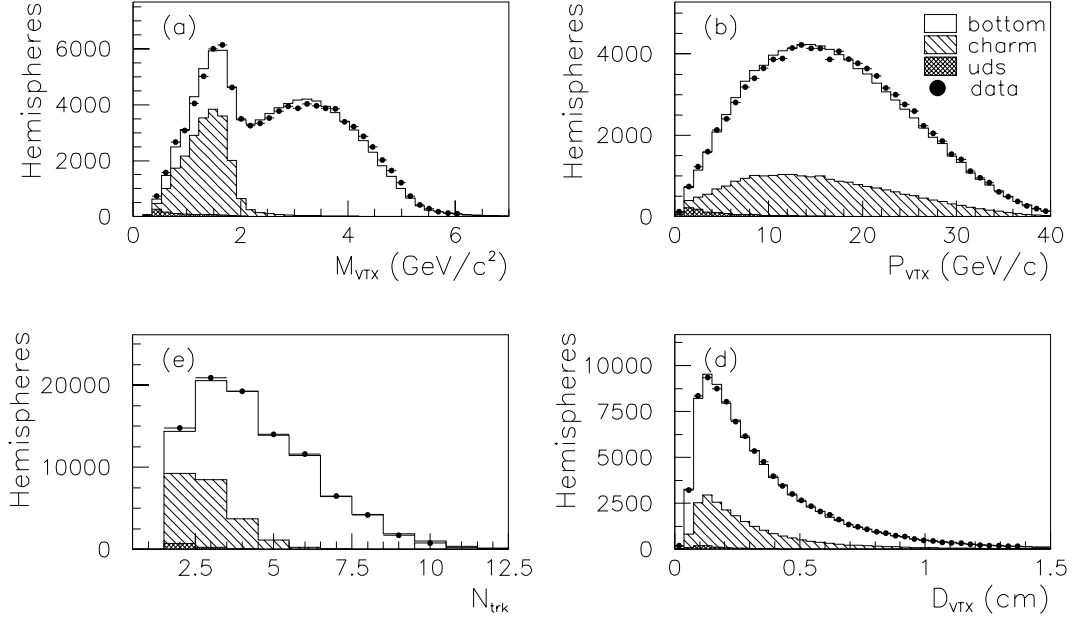
FIGURE 57. Several signatures can be computed to discriminate between bottom/charm/light event hemispheres. These are the corrected invariant mass of the selected tracks M_{hem}, the total momentum sum of the selected tracks P_{hem}, the distance from the IP to the vertex obtained by fitting all of the selected tracks D_{hem}, and the total number of selected tracks N_{hem}. These collectively are the c/b selection neural net input parameters. In the plots, the histogram represents the Monte Carlo and the dots represent the data.

add the total momentum sum of the selected tracks P_{VTX}, the IP to vertex flight distance D_{VTX}, and the track multiplicity N_{VTX} as inputs to this c/b selection neural network. The distributions of these inputs are shown in Figure 57.

The c/b selection neural network is trained such that for c quarks, the neural net output is near 0; for b quarks, the neural net output is near 1; and for light
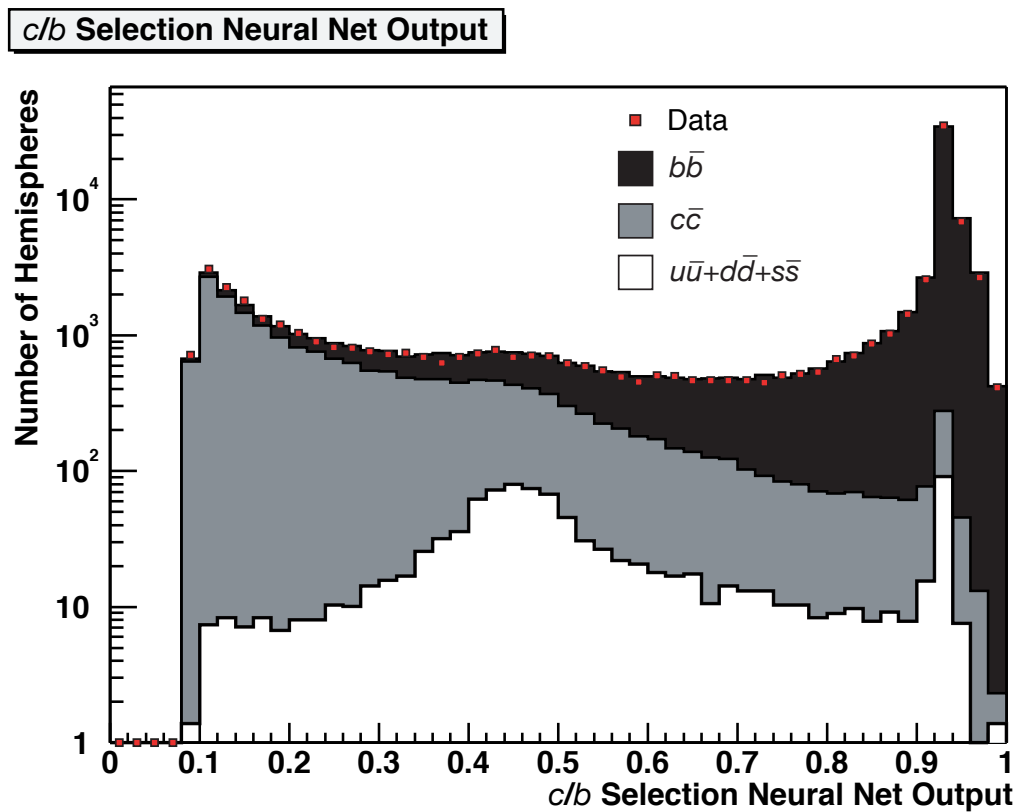
FIGURE 58. Output of c/b Selection Neural Net. In the plot, the histogram represents the Monte Carlo and the dots represent the data. The spike in identified b decays in Monte Carlo c and light flavor events located at 0.92 are due to gluon splitting, $g \rightarrow b\bar{b}$.
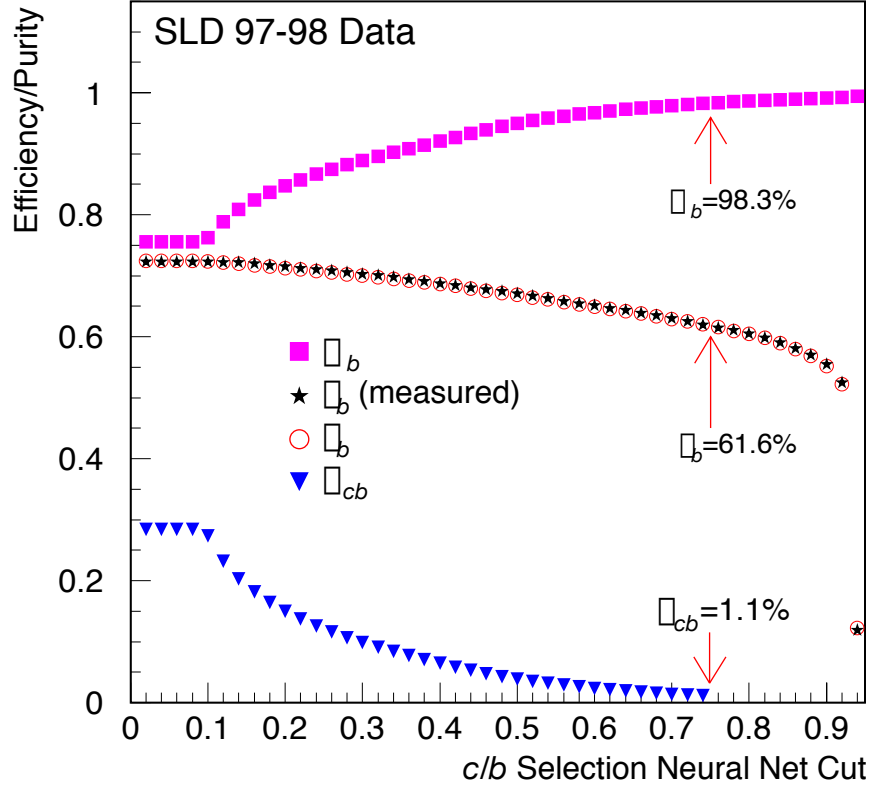
FIGURE 59. Bottom identification efficiency and purity vs. cut on c/b Selection Neural Net output.

flavor quarks, the neural net output is near 0.5. Figure 58 shows the distribution of the output of the c/b selection neural network.

Vertices with a c/b selection neural net output of > 0.75 are considered b decays. Figure 59 shows the relation of b identification efficiency and purity to the cut on the c/b selection neural net.

Vertices with a c/b selection neural net output of < 0.3 and a p_T corrected vertex mass $M_{VTX} > 0.6$ GeV to eliminate light flavor events (see Figure 56) are considered c decays. Figure 60 shows the relation of c identification efficiency and purity to the cut on the c/b selection neural net.
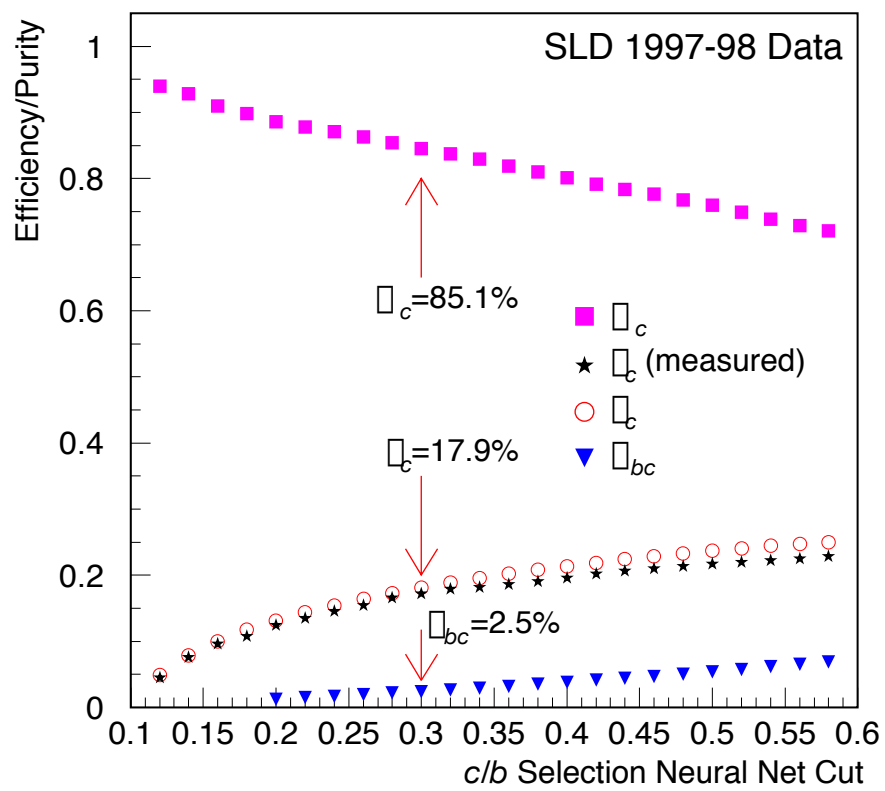
FIGURE 60. Charm identification efficiency and purity vs. cut on c/b Selection Neural Net output.

CHAPTER VIII

IDENTIFICATION OF STRANGE QUARKS

One component of this analysis is a search for flavor changing neutral currents in the form of a measurement of R_{bs}. This aspect of the analysis depends on identifying primary s quarks originating from the decay of the Z^0, as identified by the presence of high momentum strange particles [91]. Based on previous SLD experience [92], three species of strange particles can be identified: $K^{\pm}$, Λ, and K_S^0. Identification of primary s quarks proceeds in three stages:

1. Intial rejection of heavy flavors.

2. Identification of high momentum $K^{\pm}$, Λ, and K_S^0 particles; for those cases where more than one strange particle is found in the same hemisphere, only the highest momentum strange particle is considered as it is more likely to contain the primary s quark.

3. Three neural networks – one for each species of strange particle – are used to separate hemispheres containing primary s quarks from hemispheres containing an unseen b quark and an s quark originating from another source such as fragmentation or a heavy hadron decay.
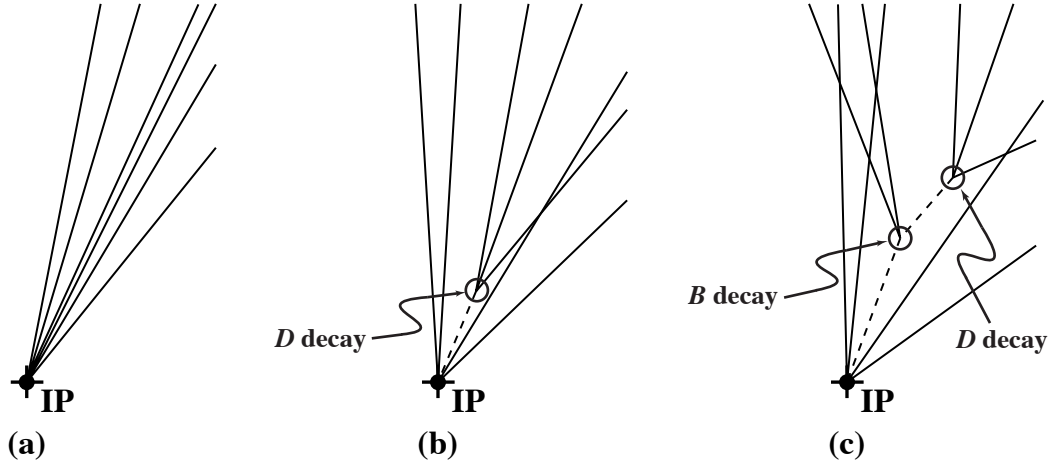
FIGURE 61. Comparison of hadronic Z^0 decay topologies: (a) $u\bar{u}$, $d\bar{d}$, or $s\bar{s}$ hemisphere; (b) $c\bar{c}$ hemisphere with a secondary D hadron decay; (c) $b\bar{b}$ hemisphere with secondary B hadron decay and tertiary D hadron decay.

8.1 Rejection of Heavy Flavors

Heavy hadrons created in $Z^0 \rightarrow b\bar{b}$ and $Z^0 \rightarrow c\bar{c}$ events usually propagate several millimeters before decaying. The displaced vertices associated with these B and D meson decays – coupled with their decay kinematics – produce particles with a significant impact parameter with respect to the IP. By contrast, hadrons created in $Z^0 \rightarrow u\bar{u}$, $Z^0 \rightarrow d\bar{d}$, and $Z^0 \rightarrow s\bar{s}$ events tend to lack a displaced vertex, with all tracks appearing to come directly from the IP. This is illustrated in Figure 61.

The charged tracks in each hemisphere which meet the requirements listed in Table 6 are termed "quality tracks". Because the tracking capabilities of the

TABLE 6. Requirements of a Quality Track

1.	≥ 40 CDC Hits
2.	CDC Fit Quality $\chi^2_{CDC}/d.o.f. < 5$
3.	First CDC Hit ≤ 39 cm radially from IP
4.	Extrapolate to within 1 cm of IP radially
5.	Extrapolate to within 1.5 cm of IP longitudinally
6.	≥ 1 VXD Hit
7.	CDC+VXD Fit Quality $\chi^2_{CDC+VXD}/d.o.f. < 5$
8.	2-dimensional impact parameter $b_{xy} < 3$ mm
9.	Uncertainty on impact parameter $\sigma_b < 250$ μm
10.	Reject pairs of oppositely charged tracks associated with candidate K^0, Λ, and $\gamma \to e^+e^-$ vertices

SLD are best in the xy-plane, the 2-dimensional impact parameters – normalized by their uncertainties – of the quality tracks are considered. An algebraic sign is associated with the impact parameter of each quality track to further enhance the effectiveness of separating light from heavy flavor hemispheres: Tracks which cross the jet axis in front of the IP are assigned a positive impact parameter, and those which cross behind are assigned a negative impact parameter. This convention is illustrated in Figure 62.

The distribution of the signed, normalized 2-dimensional impact parameter is plotted in Figure 63. A significant track is defined as a quality track with a signed, normalized 2-dimensional impact parameter $b_{xy}/\sigma_b > 3$. A high-purity sample of light flavor hemispheres can be obtained by requiring that the hemispheres contain zero significant tracks, as evidenced by Figure 64.

In addition, light flavor hemispheres are required to contain no b or c candidate vertices.
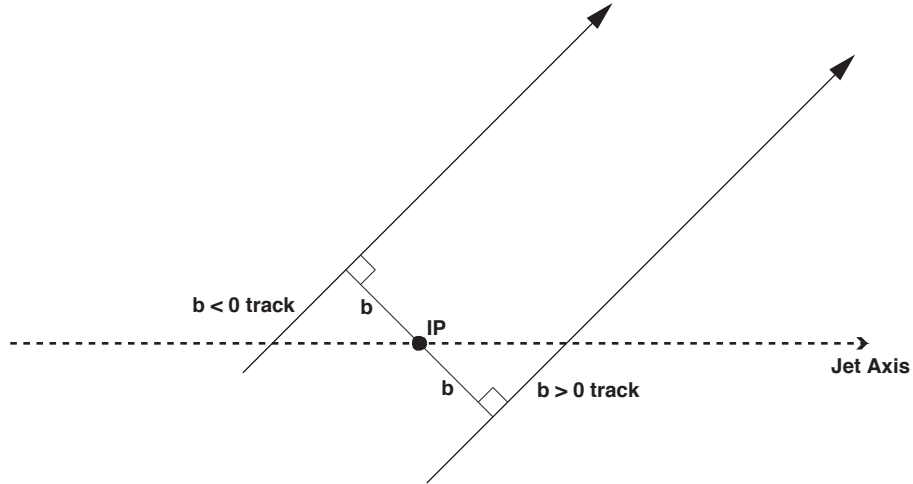
FIGURE 62. The sign convention for the signed impact parameter. The jet axis approximates the heavy-quark hadron flight direction.

8.2 $K^{\pm}$ Identification

$K^{\pm}$ can be separated from other charged tracks with the CRID over a wide momentum range. However, the CRID efficiency matrix (see Figure 65 [54], center plot) has a gap for $K^{\pm}$ with a momentum between 3 GeV $< p <$ 9 GeV due to the absence of overlap between the liquid and gas radiators [93, 94, 92]. Because only the high-momentum particles are important to this analysis, the CRID gas system is used to identify $K^{\pm}$ with a momentum above 9 GeV.

A charged track must be possessed of certain characteristics to be considered a $K^{\pm}$ candidate, as listed in Table 7.

Particle identification with the CRID uses the method of maximum likelihood. In broad strokes, the likelihood function $\mathcal{L}$ represents the joint probability distribution function for the data, evaluated with the data obtained in the experi-
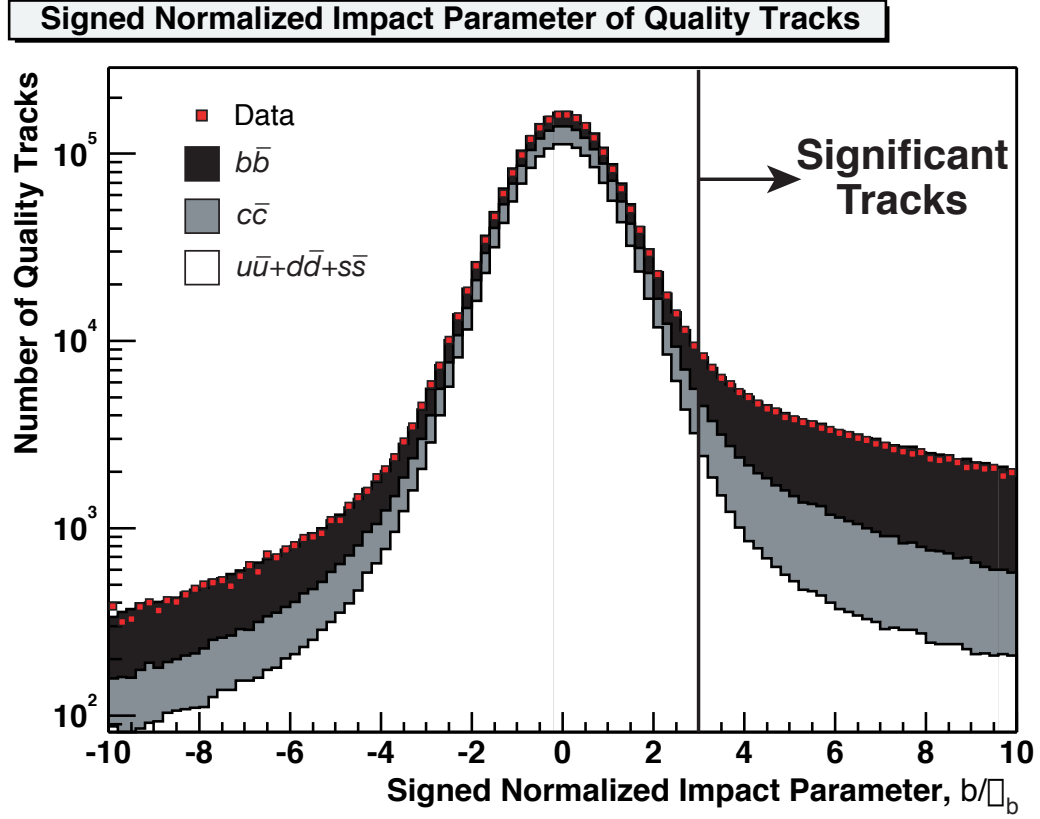
FIGURE 63. Distribution of the signed, normalized impact parameter. In the plot, the histogram represents the Monte Carlo and the dots represent the data.

TABLE 7. Requirements of $K^{\pm}$ Candidate Charged Tracks

1.	Track must extrapolate through an active region of the CRID gas radiator
2.	Track must extrapolate through a live TPC
3.	Within the CRID acceptance of $\cos\theta < 0.68$
4.	Distance of closest approach to the IP transverse to the beam < 1.0 mm
5.	Distance of closest approach to the IP along the beam < 5.0 mm
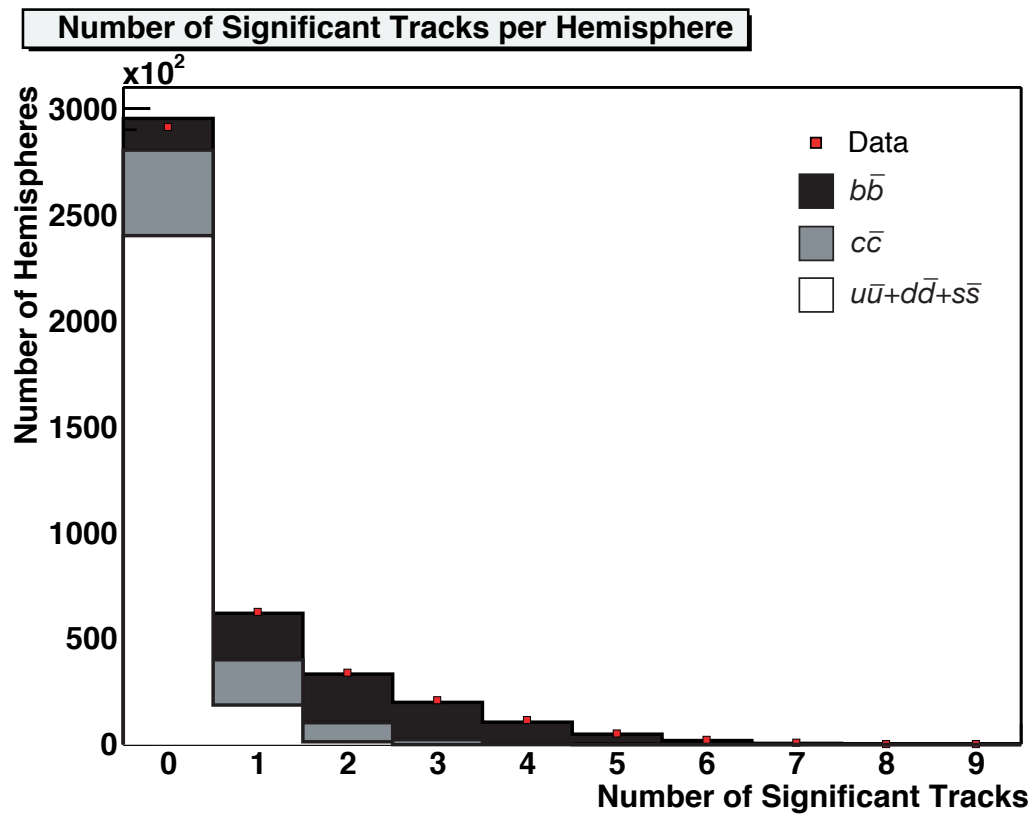
FIGURE 64. Number of significant tracks per hemisphere. In the plot, the histogram represents the Monte Carlo and the dots represent the data.
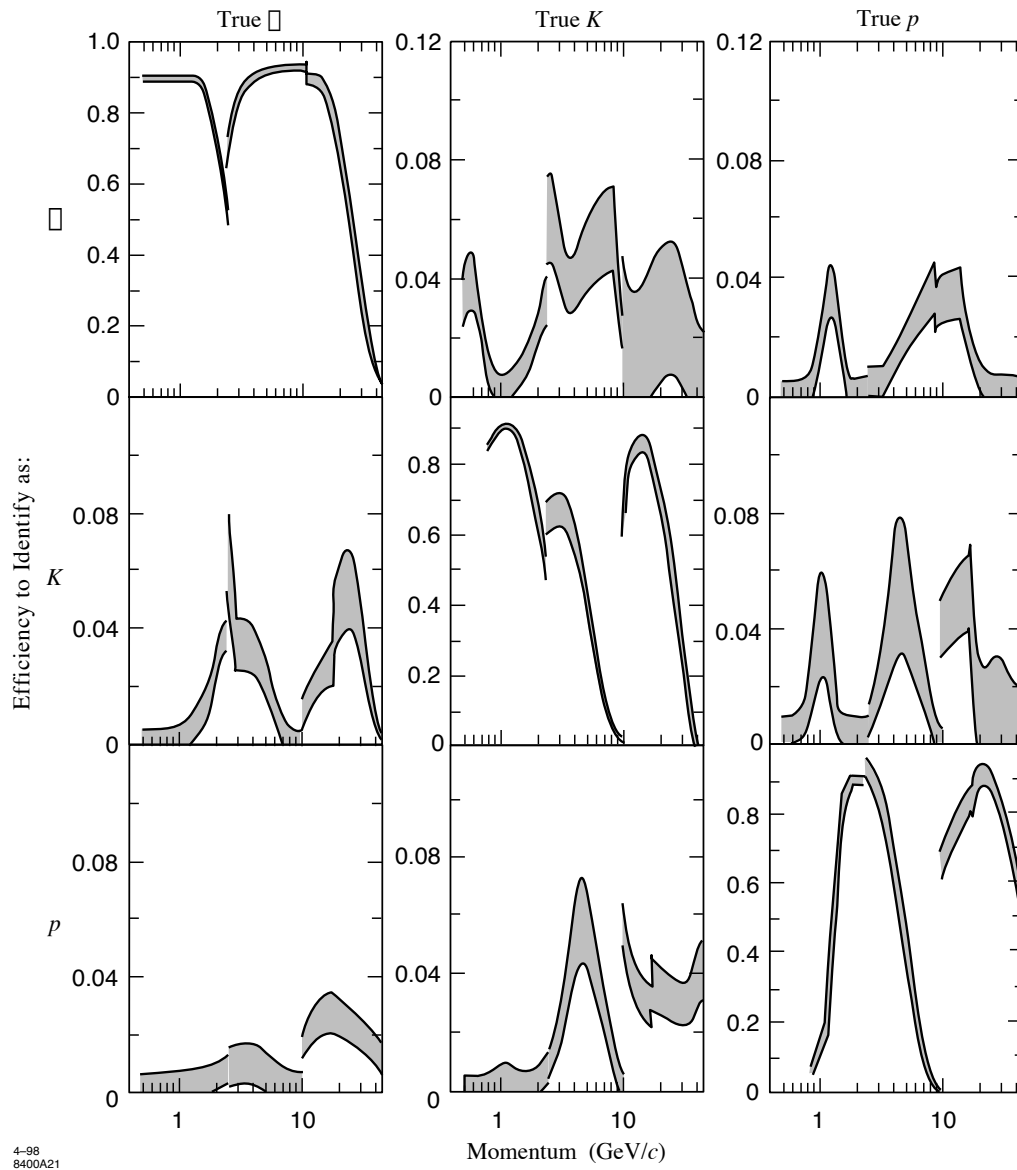
FIGURE 65. The matrix of hadronic particle identification efficiencies as a function of momentum as predicted from Monte Carlo simulation of the CRID. The efficiencies include both the liquid and gas radiators.

ment regarded as a function of whatever unknown parameters exist. The method of maximum likelihood estimates the unknown parameters to be those values which maximize the likelihood function $\mathcal{L}$. For the purpose of particle identification, the unknown parameters are the identities of the particles themselves. It is usually easier to work with $\ln \mathcal{L}$, and both are maximized for the same values of the unknown parameters. The set of hypothetical particle identities h_k (corresponding to the k observed charged tracks) which maximizes $\ln \mathcal{L}$ is desired, and can be found by solving the likelihood equations,

$$\frac{\partial \ln \mathcal{L}}{\partial h_k} = 0. \tag{8.1}$$

The CRID essentially generates photoelectrons when a charged particle passes through it, and the observed density of these photoelectrons in the detector depends on the type of the charged particle involved. The algorithm described here is discussed in more detail in K. Abe, et al. [95]. The probability to observe n photoelectrons if $\overline{n}$ are expected for a particular type of particle is given by Poisson statistics:

$$P_{(n|\overline{n})} = \frac{\overline{n}^n}{n!} e^{-\overline{n}}. \tag{8.2}$$

The probability of finding a certain photoelectron in a differential volume $d\mathbf{r}^3$ is $P(\mathbf{r})$, and $\overline{n}P(\mathbf{r})$ is the expected number of photoelectrons in $d\mathbf{r}^3$. The overall probability for there to be n photoelectrons, and for those photoelectrons to be distributed as they were found is the likelihood function $\mathcal{L}'$ which, taking into

account all the permutations, may be written as

$$\mathcal{L}' = n! P_{(n|\overline{n})} \prod_{i}^{n} P(\mathbf{r}_i) \tag{8.3}$$

$$= \overline{n}^n e^{-\overline{n}} \prod_{i=1}^{n} P(\mathbf{r}_i). \tag{8.4}$$

The density of photoelectrons under the assumption of a given set of hypotheses for the tracks, plus an assumed background model, is $\rho(\mathbf{r})$, such that

$$\overline{n} P(\mathbf{r}) = \rho(\mathbf{r}) d\mathbf{r}^3. \tag{8.5}$$

Since we are only interested in the likelihood ratios between $\mathcal{L}'$ for different hypotheses, it is convenient to remove all the awkward factors of $d\mathbf{r}^3$:

$$\mathcal{L} = e^{-\overline{n}} \prod_{i=1}^{n} \rho(\mathbf{r}_i) \tag{8.6}$$

where the index i runs over all the observed photoelectrons.

It is convenient to write $\rho(\mathbf{r})$ explicitly as two terms,

$$\rho(\mathbf{r}) = B(\mathbf{r}) + \sum_{k} \rho_{k,h_k}(\mathbf{r}) \tag{8.7}$$

where $B(\mathbf{r})$ is the expected background in the absence of Cherenkov photoelectrons, and $\rho_{k,h_k}(\mathbf{r})$ is the photoelectron density associated with track k and its assumed hypothetical particle identity h_k.

At present, $\mathcal{L}$ depends explicitly on the hypothetical identities of all the tracks – a combinatorial disaster. A reasonable compromise is to allow the hypothesis

h_k for track k to vary whilst keeping the hypotheses for the other tracks $j \neq k$ constant at h_j. Thus

$$\mathcal{L}_{k,h_k} \;\; = \;\; e^{-\overline{n}_{k,h_k}} \prod_{i=1}^{n} \left[B_k + \rho_{k,h_k}(\mathbf{r}_i) \right] \tag{8.8}$$

where the background B_k is defined as the density of photoelectrons minus those photoelectrons associated with track k under hypothetical identity h_k. B_k includes the photoelectrons from other tracks $j \neq k$:

$$B_k \;\; = \;\; B + \sum_{j \neq k} \rho_{j,h_j}. \tag{8.9}$$

Since we are only interested in the likelihood ratios, and since the B_k are independent of the hypothetical particle identities h_k, the likelihood can be written

$$\mathcal{L}_{k,h_k} \;\; = \;\; e^{-\overline{n}_{k,h_k}} \prod_{i=1}^{n} \left[1 + \frac{\rho_{k,h_k}(\mathbf{r}_i)}{B_k} \right] \tag{8.10}$$

and finally

$$\ln \mathcal{L}_{k,h_k} \;\; = \;\; -\overline{n}_{k,h_k} \sum_{i=1}^{n} \ln \left[1 + \frac{\rho_{k,h_k}(\mathbf{r}_i)}{B_k} \right]. \tag{8.11}$$

In practice, the computation of $\ln \mathcal{L}_{k,h_k}$ is iterative since the B_k are dependent on the hypothetical particle identities of the other tracks (the current best overall hypothesis is used, defaulting to $\pi^{\pm}$), but the procedure always converges quickly.

For $K^{\pm}$ identification, the $\ln \mathcal{L}_{k,h_k}$ of a charged track for the CRID gas radiator is calculated for each charged hadron hypothesis; $\pi^{\pm}$, $K^{\pm}$, and $p/\overline{p}$. A charged

TABLE 8. Requirements of Λ and K_S^0 Candidate V^0s

1.	Momentum transverse to the beam $p_{xy} > 150$ MeV for both tracks
2.	Both tracks within $\cos\theta < 0.9$
3.	Both tracks have ≥ 30 CDC Hits
4.	Both tracks have ≤ 1 VXD Hit
5.	Distance of closest approach of the two tracks < 15 mm
6.	χ^2 fit probability of two tracks to a common vertex $> 2\%$
7.	$p_{V^0} > 5$ GeV

track is identified as a $K^\pm$ if the following two requirements are met:

$$\ln \mathcal{L}_{K^\pm} - \ln \mathcal{L}_{\pi^\pm} \quad > \quad 3 \tag{8.12}$$

$$\ln \mathcal{L}_{K^\pm} - \ln \mathcal{L}_{p/\overline{p}} \quad > \quad 3. \tag{8.13}$$

Figure 66 shows the $\ln \mathcal{L}$ separation between $K^\pm$ and $\pi^\pm$, and between $K^\pm$ and $p/\overline{p}$, and Figure 67 shows the purity as a function of momentum of the identified $K^\pm$ sample [92].

8.3 Λ and K_S^0 Identification

A pair of oppositely charged particles originating at a neutral decay vertex is generically called a "V^0." The charged decay modes of the Λ ($\mathcal{B}(\Lambda \to p\pi^-) = (63.9 \pm 0.5)\%$) and the K_S^0 ($\mathcal{B}(K_S^0 \to \pi^+\pi^-) = (68.60 \pm 0.27)\%$) are of particular interest as several features of their decays can assist in their reconstruction: Long flight distance; accuracy of pointing back to the IP; and the possibility of reconstructing the vertex mass.

Once a Λ or K_S^0 candidate V^0 has met the criteria listed in Table 8, one more cut is applied to reduce the combinatorial background: In the plane transverse to the beam, the angle ϕ_{xy} between the vertex axis and the vertex momentum p_{xy}
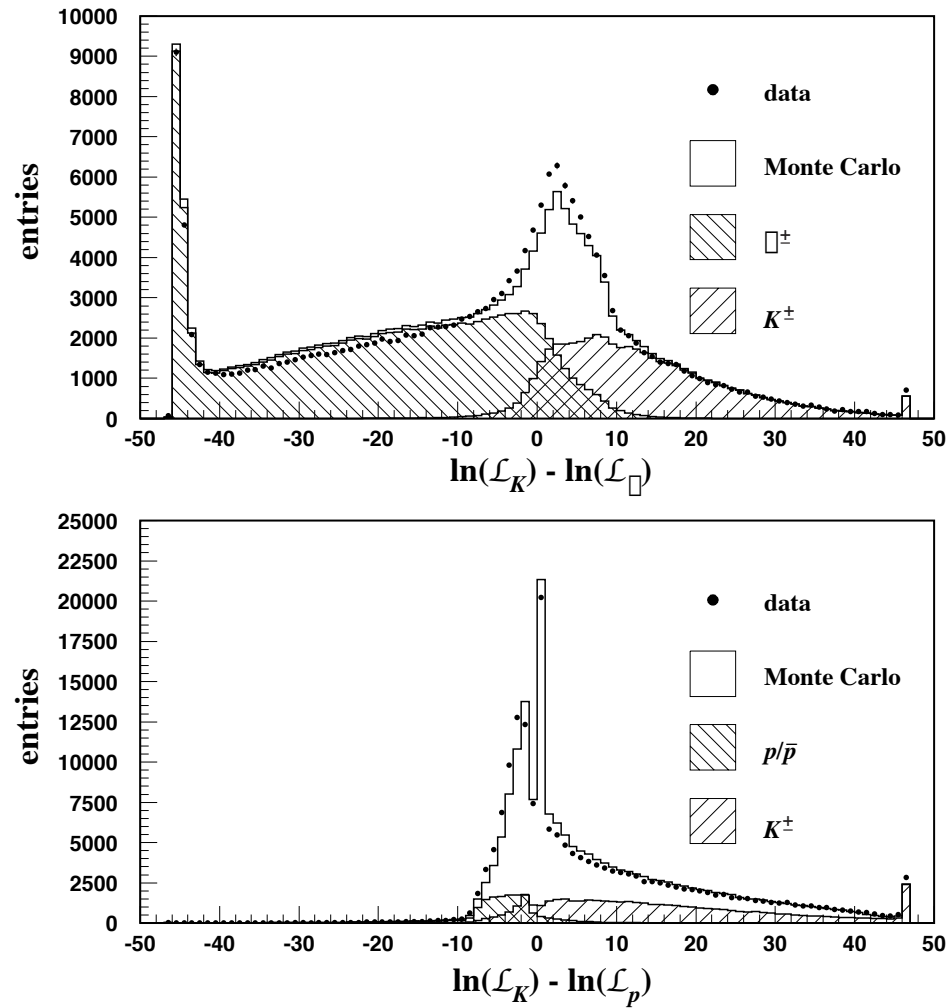
FIGURE 66. The log-likelihood separation between Kaons, Pions, and Protons. In the plots, the histogram represents the Monte Carlo and the dots represent the data.
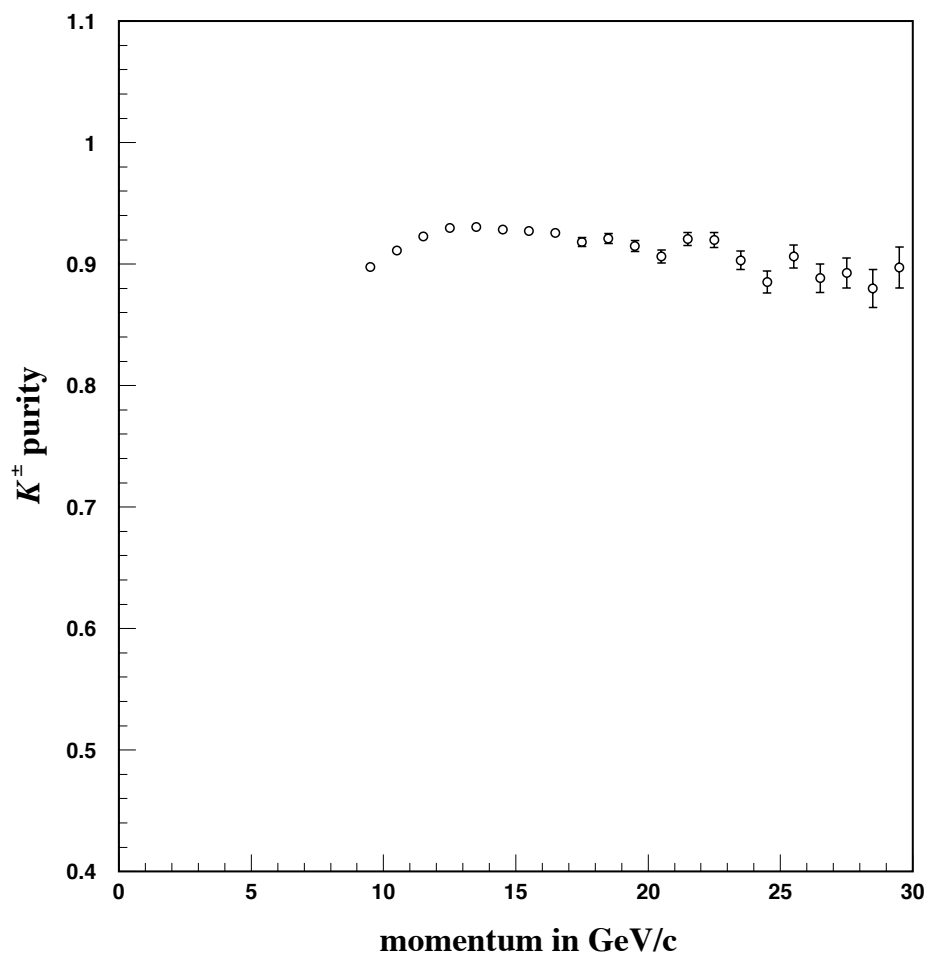
FIGURE 67. Purity as a function of momentum of the identified $K^{\pm}$ sample as estimated from the Monte Carlo simulation. The uncertainties are statistical only.

must obey the following relation:

$$\phi_{xy} \ < \ C_{V^0} \left(2 \text{ mrad} + \frac{20 \text{ mrad GeV}}{p_{xy}} + \frac{5 \text{ mrad GeV}^2}{p_{xy}^2} \right) \quad (8.14)$$

where $C_\Lambda = 1.75$ and $C_{K_S^0} = 2.50$.

For the remaining Λ and K_S^0 candidate V^0s, the invariant vertex mass is computed assuming three different hypotheses and corresponding masses for the two tracks; $\gamma \rightarrow e^+ e^-$, $\Lambda \rightarrow p\pi^-$, and $K_S^0 \rightarrow \pi^+\pi^-$:

$$m_{e^+e^-} = \sqrt{\left(\sqrt{p_1^2 + m_e^2} + \sqrt{p_2^2 + m_e^2} \right)^2 - (\vec{p}_1 + \vec{p}_2)^2} \quad (8.15)$$

$$m_{p\pi} = \sqrt{\left(\sqrt{p_1^2 + m_p^2} + \sqrt{p_2^2 + m_\pi^2} \right)^2 - (\vec{p}_1 + \vec{p}_2)^2} \quad (8.16)$$

$$m_{\pi\pi} = \sqrt{\left(\sqrt{p_1^2 + m_\pi^2} + \sqrt{p_2^2 + m_\pi^2} \right)^2 - (\vec{p}_1 + \vec{p}_2)^2}. \quad (8.17)$$

Figures 68 and 69 show the invariant vertex masses for $m_{p\pi}$ and $m_{\pi\pi}$ respectively.

The Monte Carlo simulation predicted a surplus of low momentum Λ and K_S^0 candidates, as shown in Figures 70 and 71 respectively. These discrepancies were corrected in the simulation by applying a momentum independent correction factor to the number of simulated true Λ candidates with $p < 15$ GeV and K_S^0 candidates with $p < 10$ GeV which rejected a total of 12.5% of the simulated Λ sample and 6.9% of the simulated K_S^0 sample within these momentum regions. This procedure maintained the absolute background which is seen from the $m_{p\pi}$ and $m_{\pi\pi}$ sidebands (see Figures 68 and 69 respectively) to be well simulated [92].
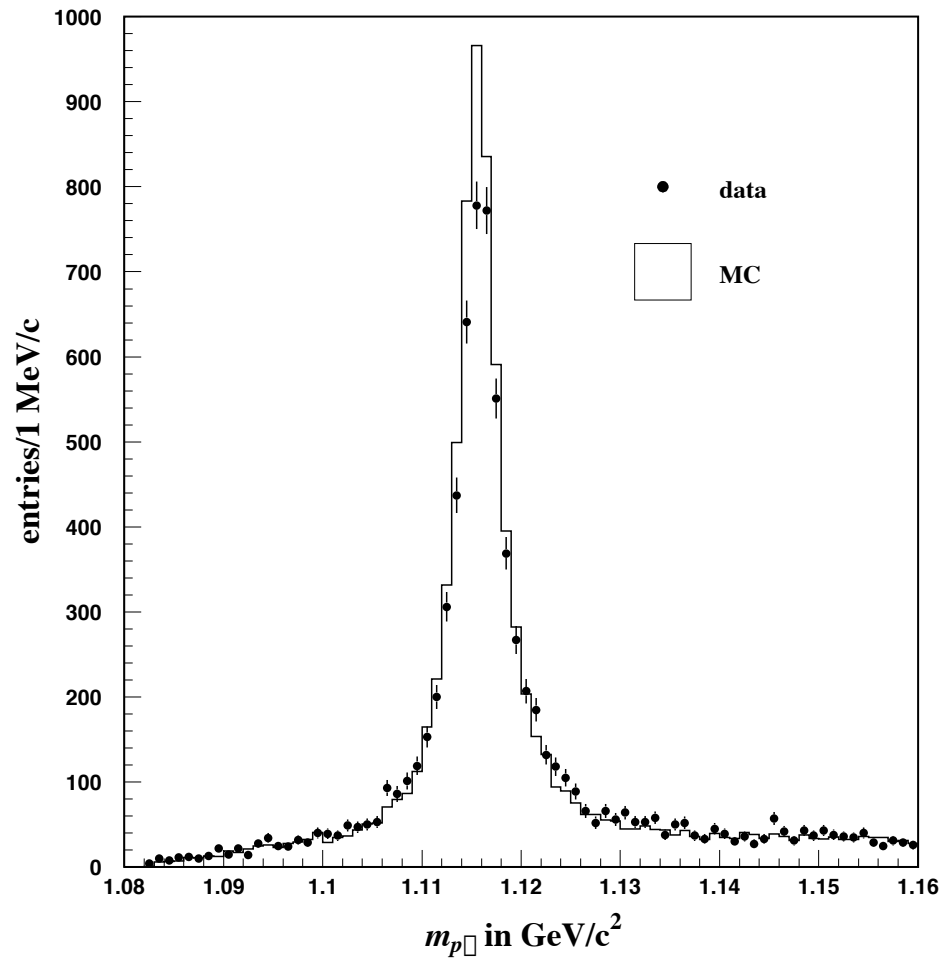
FIGURE 68. The invariant mass $m_{p\pi}$ of Λ candidates with momentum $p > 5$ GeV. The dots represent the data and the histogram represents the uncorrected Monte Carlo simulation.
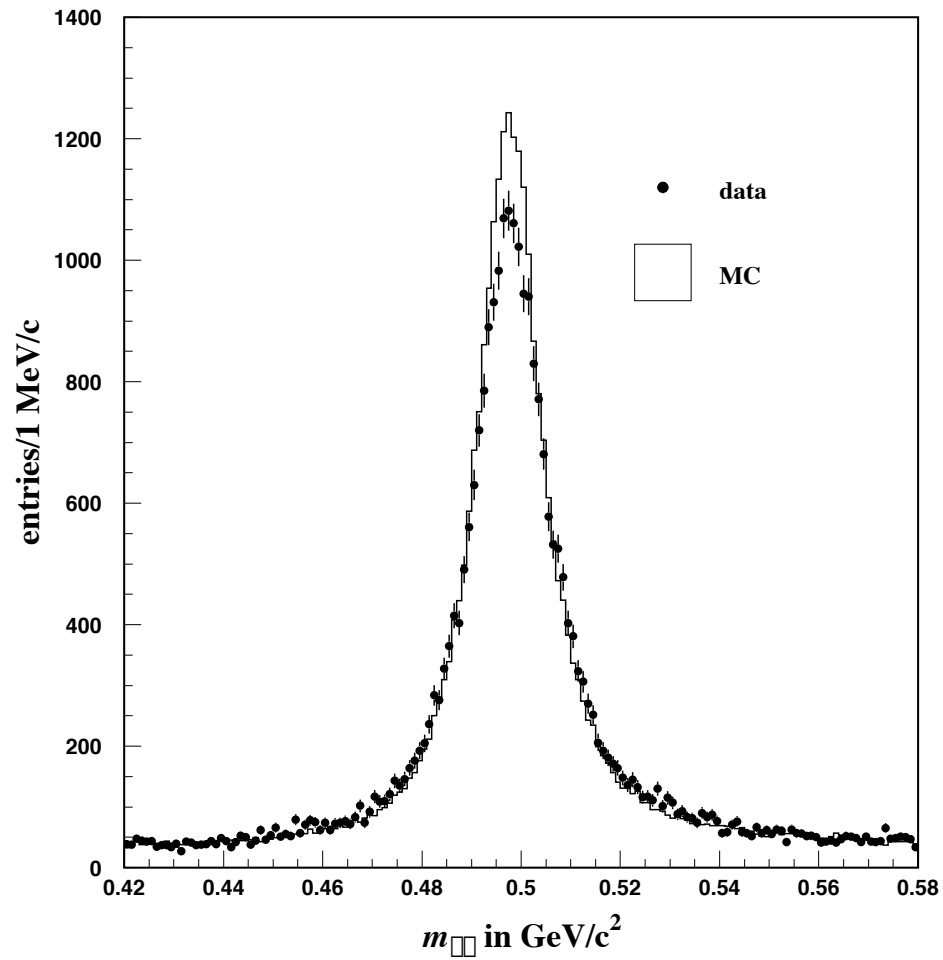
FIGURE 69. The invariant mass $m_{\pi\pi}$ of K_S^0 candidates with momentum $p > 5$ GeV. The dots represent the data and the histogram represents the uncorrected Monte Carlo simulation.

TABLE 9. Requirements for Λ identification

1. $m_{e^+e^-} > 0.1$ GeV
2. $\left\lvert m_{\pi\pi} - m_{K^0_S} \right\rvert > 2\sigma_{m_{\pi\pi}}$ where $\sigma_{m_{\pi\pi}} = 0.00063355 \times p_{V^0} + 0.0036430$ GeV
3. $\left\lvert m_{p\pi} - m_\Lambda \right\rvert < 2\sigma_{m_{p\pi}}$ where $\sigma_{m_{p\pi}} = 0.00024074 \times p_{V^0} + 0.00080625$ GeV
4. V^0 normalized flight distance $l/\sigma_l > 5$ and $\ln \mathcal{L}_{p/\bar{p}} - \ln \mathcal{L}_{\pi^\pm} > 0$ or V^0 normalized flight distance $l/\sigma_l > 10$ and no CRID information

For Λ identification, several conditions must be met: $m_{p\pi}$ must be within $2\sigma_{m_{p\pi}}$ of $m_\Lambda = 1.11568$ GeV where $\sigma_{m_{p\pi}}$ is the width of the $m_{p\pi}$ distribution and is a linear function of momentum; to rule out $\gamma \to e^+e^-$, $m_{e^+e^-}$ must be greater than 0.1 GeV, far from $2m_e = 0.001022$ GeV; to rule out K^0_Ss, $m_{\pi\pi}$ must be more than $2\sigma_{m_{\pi\pi}}$ away from $m_{K^0_S} = 0.49767$ GeV where $\sigma_{m_{\pi\pi}}$ is the width of the $m_{\pi\pi}$ distribution and is a linear function of momentum; if the proton can be identified with the CRID – i.e. $\ln \mathcal{L}_{p/\bar{p}} - \ln \mathcal{L}_{\pi^\pm} > 0$ – the normalized flight distance of the V^0 from the IP l/σ_l must be greater than 5; if the proton cannot be identified with the CRID, the normalized flight distance of the V^0 from the IP l/σ_l must be greater than 10. These conditions are summarized in Table 9.

For K^0_S identification, similar conditions must be met: $m_{\pi\pi}$ must be within $2\sigma_{m_{\pi\pi}}$ of $m_{K^0_S} = 0.49767$ GeV where $\sigma_{m_{\pi\pi}}$ is the width of the $m_{\pi\pi}$ distribution and is a linear function of momentum; to rule out $\gamma \to e^+e^-$, $m_{e^+e^-}$ must be greater than 0.1 GeV, far from $2m_e = 0.001022$ GeV; and the normalized flight distance of the V^0 from the IP l/σ_l must be greater than 5. These conditions are summarized in Table 10.
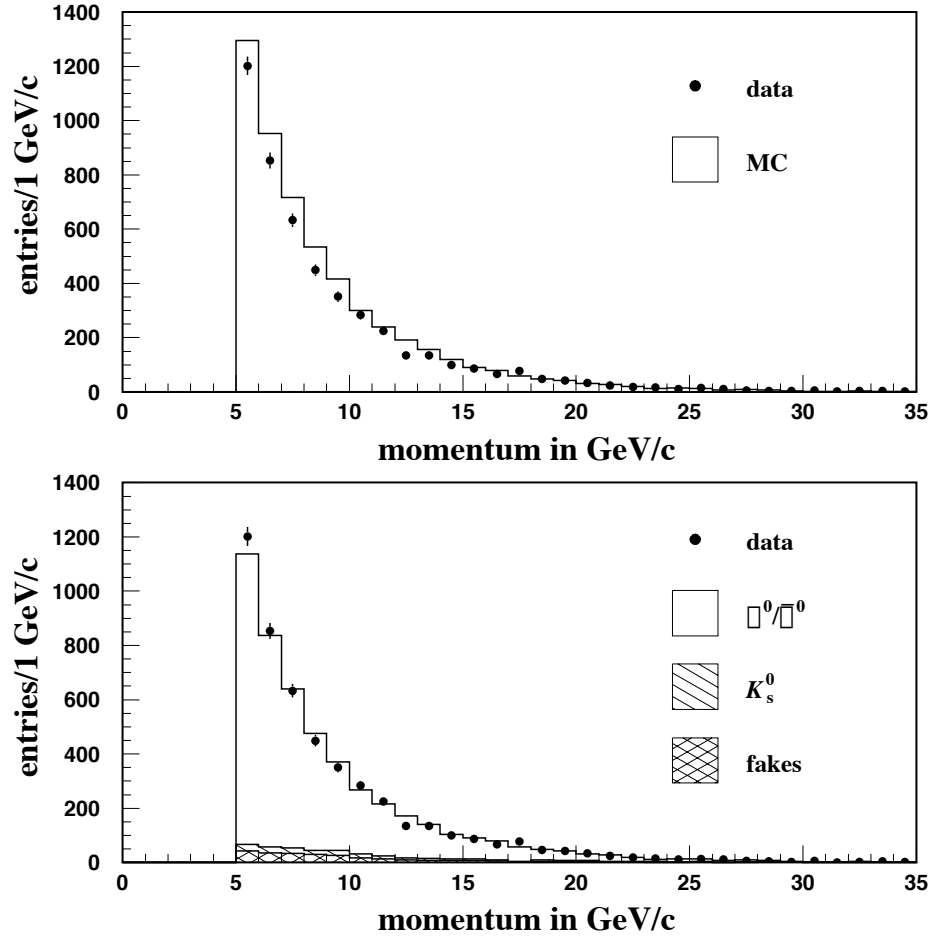
FIGURE 70. Momentum of Λ candidates before (top) and after (bottom) applying a momentum-independent correction to the number of simulated true Λ with $p < 15$ GeV. The dots represent the data and the histogram represents the Monte Carlo simulation. Fakes were reconstructed vertices which were not actually the result of a decay.

TABLE 10. Requirements for K_S^0 identification

1.	$m_{e^+e^-} > 0.1$ GeV
2.	$\left| m_{\pi\pi} - m_{K_S^0} \right| < 2\sigma_{m_{\pi\pi}}$ where $\sigma_{m_{\pi\pi}} = 0.00063355 \times p_{V^0} + 0.0036430$ GeV
3.	V^0 normalized flight distance $l/\sigma_l > 5$
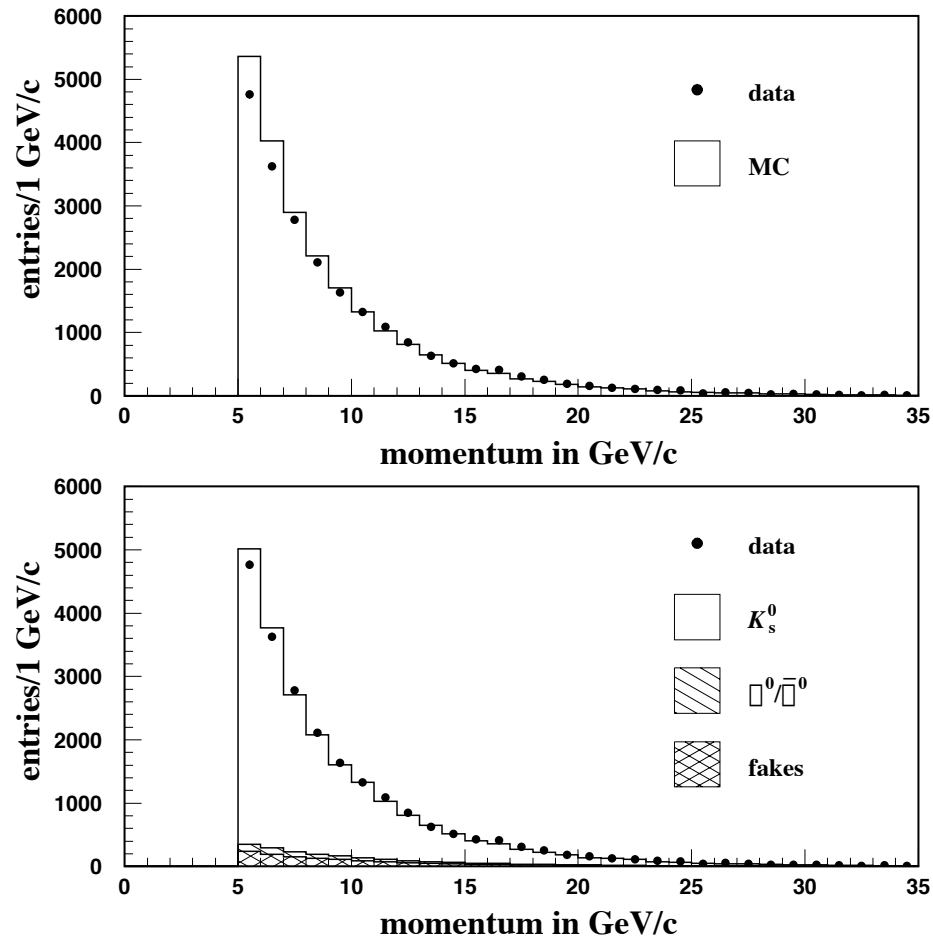
FIGURE 71. Momentum of K_S^0 candidates before (top) and after (bottom) apply-ing a momentum-independent correction to the number of simulated true K_S^0 with $p < 10$ GeV. The dots represent the data and the histogram represents the Monte Carlo simulation. Fakes were reconstructed vertices which were not actually the result of a decay.
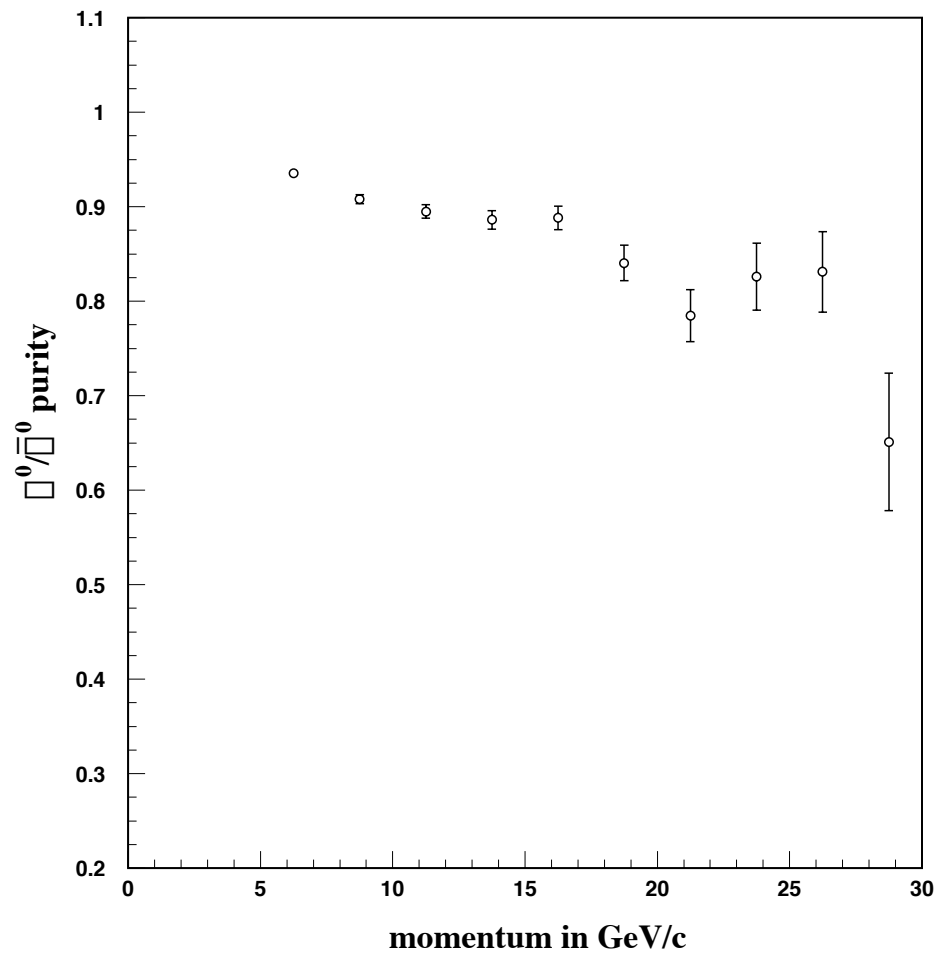
FIGURE 72. Purity as a function of momentum of the identified Λ sample as estimated from the Monte Carlo simulation. The uncertainties are statistical only.
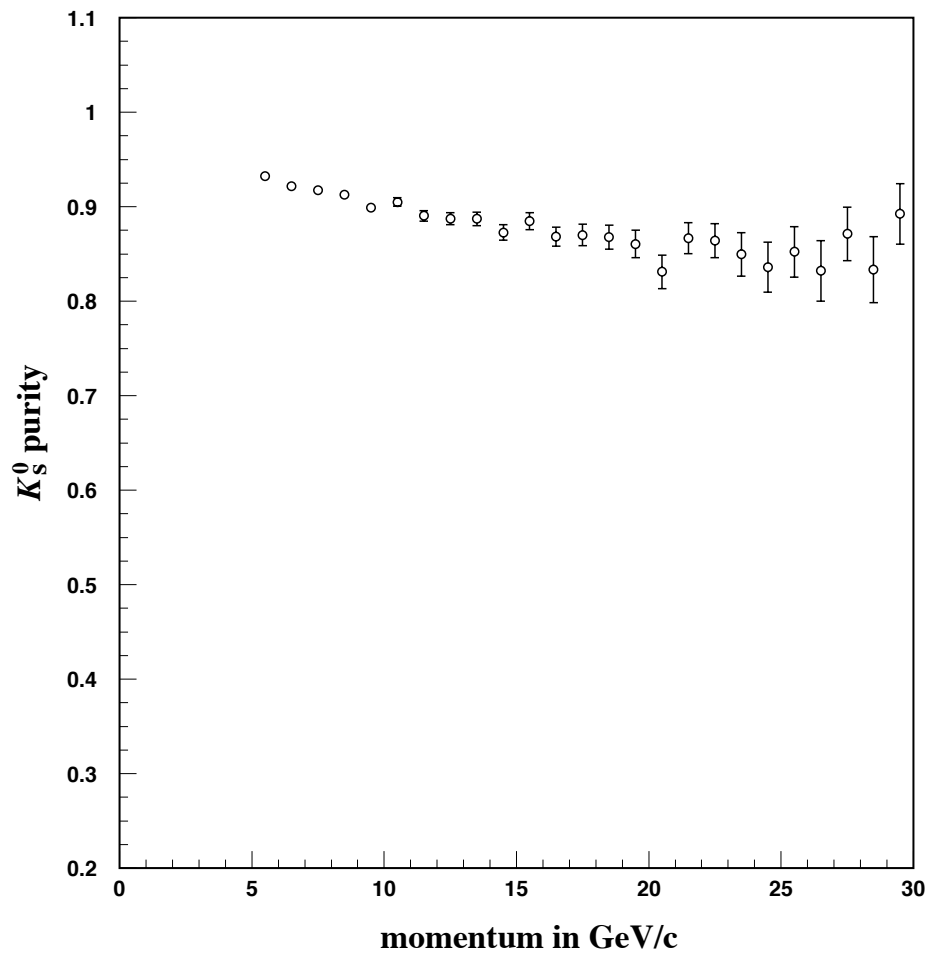
FIGURE 73. Purity as a function of momentum of the identified K_S^0 sample as estimated from the Monte Carlo simulation. The uncertainties are statistical only.

TABLE 11. Initial requirements for bs event identification.

1.	One hemisphere contains no significant tracks, no b or c candidate vertices, and has a $K^{\pm}$, Λ, or K_S^0
2.	Opposite Hemisphere contains an identified b decay vertex

Figures 72 and 73 show the purities as a function of momentum of the identified Λ and K_S^0 samples respectively [92]. The present scheme for identifying Λ and K_S^0 particles is discussed in greater detail by Stängle [92] and Baird [94].

8.4 Separating s Hemispheres from b Hemispheres

When searching for a small or nonexistent signal, as is the case with the R_{bs} measurement, it is crucial to suppress backgrounds. The identification of flavor-changing bs events begins with the requirements that one hemisphere must contain no significant tracks and have no b or c candidate vertices. This hemisphere must contain an identified s quark in the form of a $K^{\pm}$, Λ, or K_S^0. And the opposite hemisphere must contain an identified b quark. These are summarized in Table 11. Figure 74 shows the effects of each of these requirements in turn on the different Monte Carlo event flavors, including hypothetical bs events. The bar graphs represents the fractions of events which meet the corresponding requirements.

Some of the backgrounds are clearly easier to suppress than others: Figure 74 illustrates that the requirement to identify a b quark in the opposite hemisphere wipes out the vast majority of $u\bar{u}$, $d\bar{d}$, and $s\bar{s}$ events, as well as a significant portion of the $c\bar{c}$ events. This is due to the high purity obtained with the b identification scheme. But from the perspective of identifying bs events, the most insidious
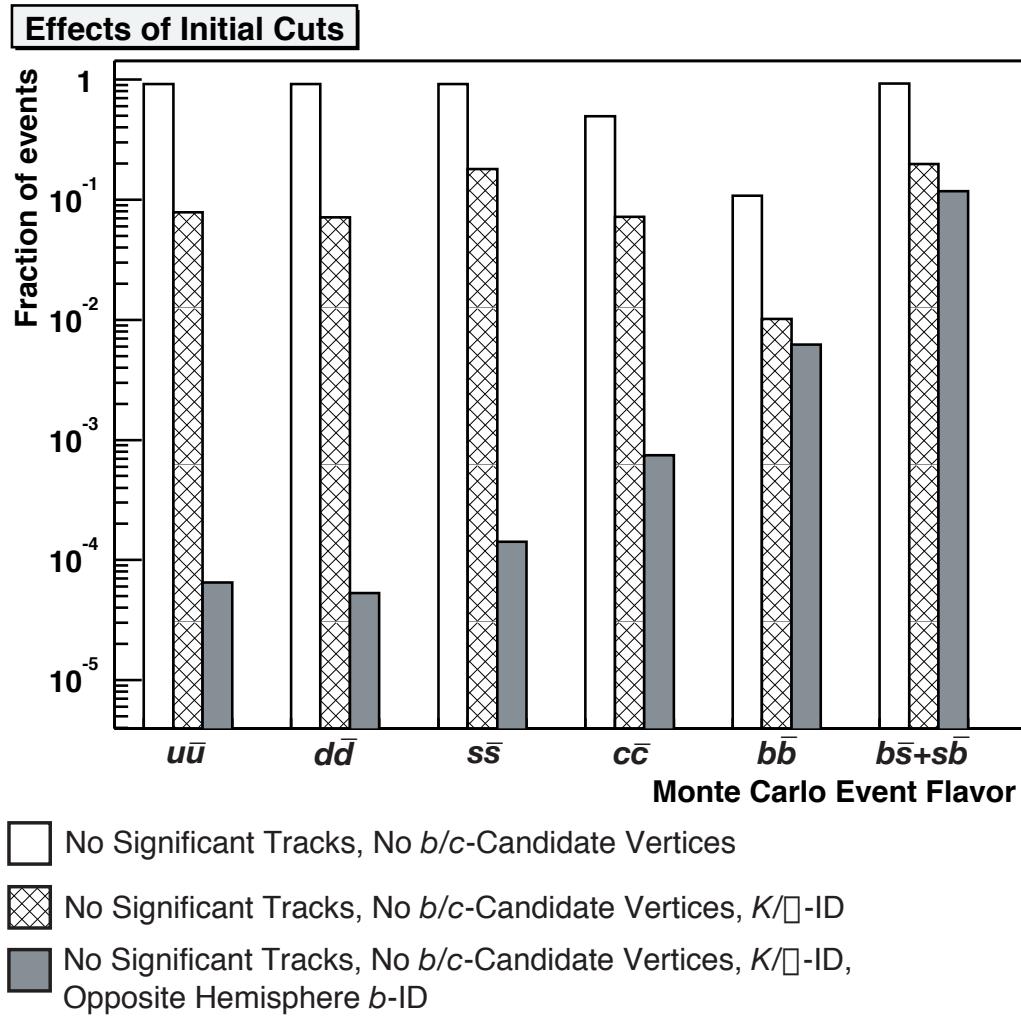
FIGURE 74. Comparison of the effects of each of the initial cuts on Monte Carlo event flavors.

source of background is $b\bar{b}$ events in which a b quark is seen in one hemisphere but missed in the other, and where an s quark is identified in the hemisphere containing the unseen b quark. The s quarks which conspire with the unseen b quarks have numerous sources: B meson decays are one problematic source, and fragmentation is another. In the literature, branching ratios of B meson decays into final states containing s quarks are specifically listed. All other sources are accounted for in average multiplicites which include fragmentation and any other process which results in a final state s quark [15]:

- B meson decays into final states containing s quarks:

  ○ $\mathcal{B}(B \rightarrow K^{\pm}) = 74 \pm 6\%$

  ○ $\mathcal{B}(B \rightarrow K_s^0) = 29 \pm 2.9\%$

  ○ $\mathcal{B}(B \rightarrow \Lambda/\overline{\Lambda}) = 5.9 \pm 0.6\%$

- Multiplicites of final state s quarks in Z^0 decays:

  ○ $\langle N_{K^{\pm}} \rangle = 2.25 \pm .05$

  ○ $\langle N_{K_s^0} \rangle = 2.039 \pm 0.025$

  ○ $\langle N_{\Lambda} \rangle = 0.388 \pm 0.009$

In order to suppress the treacherous backgrounds from $b\bar{b}$ events masquerading as bs events, three neural networks are employed – one corresponding to each species of strange particle identifiable in the detector. These neural networks are trained specifically to separate hemispheres containing a primary s quark from hemispheres containing both an unseen b quark and an identified s quark in the form of a $K^{\pm}$, Λ, or K_S^0. The three neural networks employed here, hereafter referred to as "sNN" meaning "strange neural net", all used an orthodox feed-forward architecture with an input layer containing four units, one hidden layer containing

$K^{\pm}$	Λ	K_S^0
p_s	p_s	p_s
n_{tracks}	n_{tracks}	n_{tracks}
$\sum_{tracks} \vec{p}$	$\sum_{tracks} \vec{p}$	$\sum_{tracks} \vec{p}$
$\frac{b_{xy}}{\sigma_b}$	θ_{xy}	θ_{xy}

TABLE 12. Strange particle species and their corresponding neural network inputs.

five units, and an output layer containing two units, as previously discussed in section 7.1 and illustrated in Figure 48.

Several parameters were identified which proved helpful in separating hemispheres containing a primary s quark from hemispheres containing an unseen b quark and a $K^{\pm}$, Λ, or K_S^0:

$$p_s = \text{Strange particle momentum}$$

$$n_{tracks} = \text{Number of charged tracks in the hemisphere}$$

$$\sum_{tracks} \vec{p} = \text{Momentum sum of charged tracks in the hemisphere}$$

$$\frac{b_{xy}}{\sigma_b} = \text{2D normalized impact parameter}$$

$$\theta_{xy} = \text{2D angle between } p_{K_S^0,\Lambda} \text{ and the vertex axis.}$$

Each neural network has four inputs. Table 12 details which parameters serve as inputs for each of the neural networks corresponding to each s particle species. The distributions for the input parameters are shown in Figures 75, 76, and 77. The agreement between data and Monte Carlo is not as good as one might hope, particularly for the hemisphere charged track momentum sum $\sum_{tracks} \vec{p}$, the 2D impact parameter b_{xy}/σ_b for $K^{\pm}$, and the 2D angle between the vertex axis and
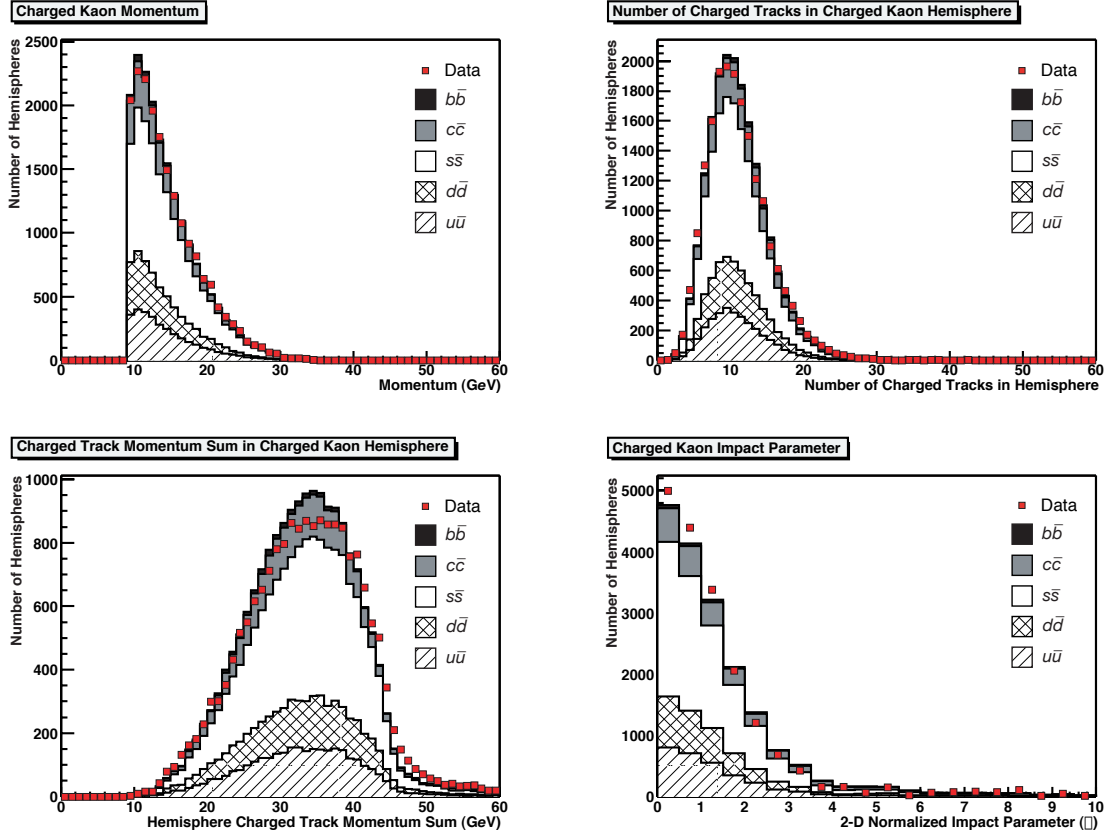
FIGURE 75. Input parameter distributions for the $K^{\pm}$ neural network. In the plots, the histogram represents the Monte Carlo and the dots represent the data.

the momentum θ_{xy} for Λ and K_S^0. The Monte Carlo is thus reweighted by the ratio of data/Monte Carlo for both $\sum_{tracks} \vec{p}$ and the b_{xy}/σ_b for $K^{\pm}$, and by $\sum_{tracks} \vec{p}$ and θ_{xy} for Λ and K_S^0. Only events with a hemisphere meeting the first requirement in Table 11 are reweighted. If the event contains two hemispheres which meet the first requirement in Table 11, the event weight is the product of the two hemisphere weights. The reweighted distributions with improved agreement between Monte Carlo and data are shown in Figures 78, 79, and 80. All Monte Carlo derived quantities are calculated from the reweighted Monte Carlo.
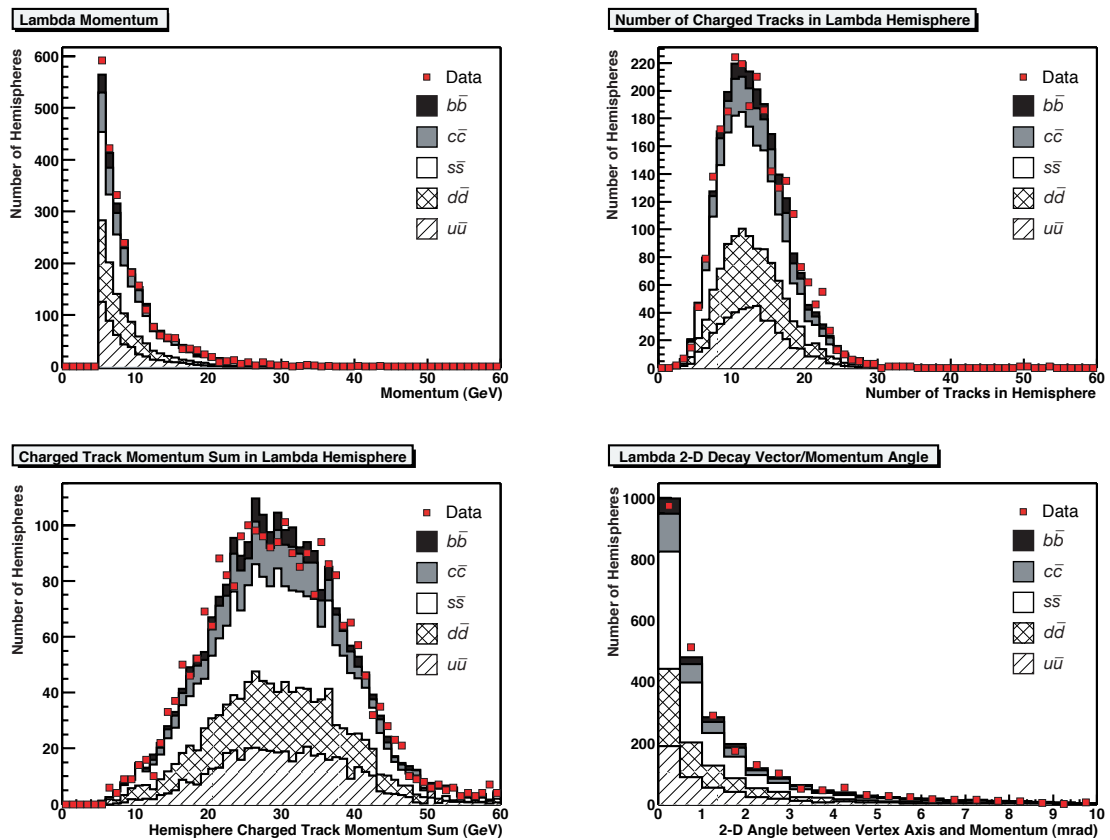
FIGURE 76. Input parameter distributions for the Λ neural network. In the plots, the histogram represents the Monte Carlo and the dots represent the data.
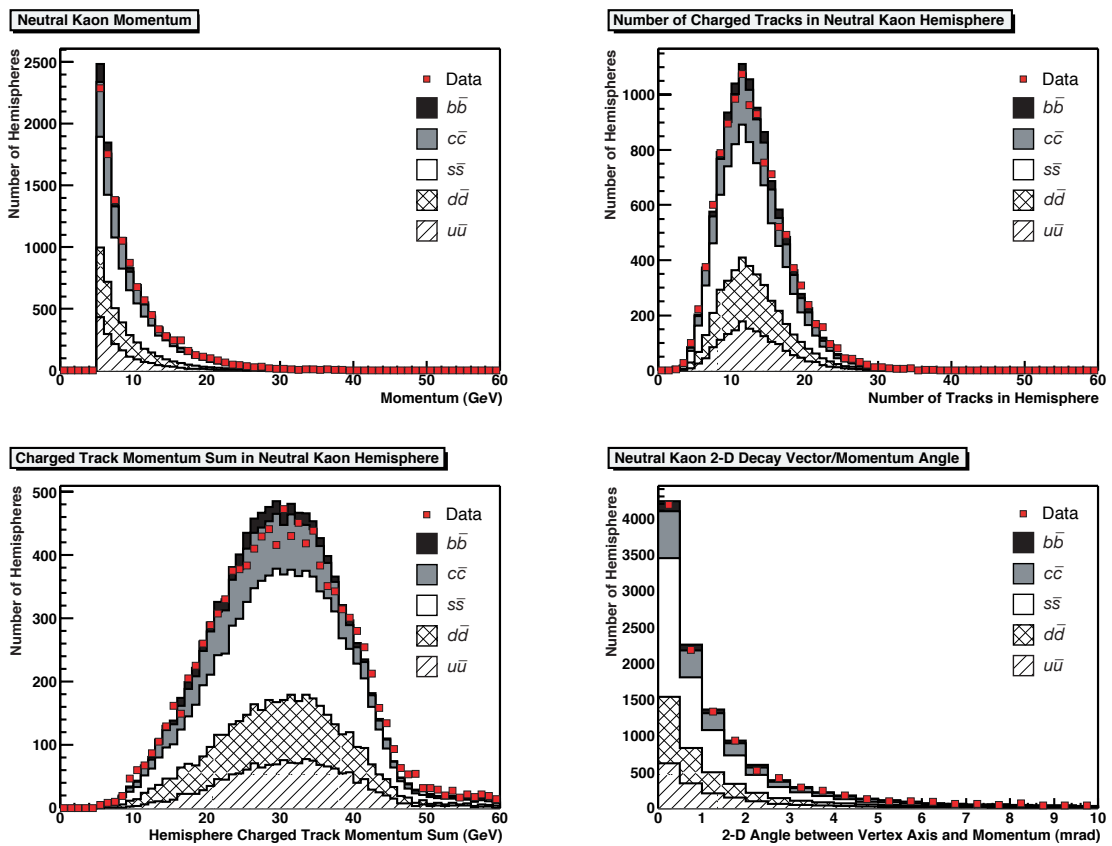
FIGURE 77. Input parameter distributions for the K_S^0 neural network. In the plots, the histogram represents the Monte Carlo and the dots represent the data.
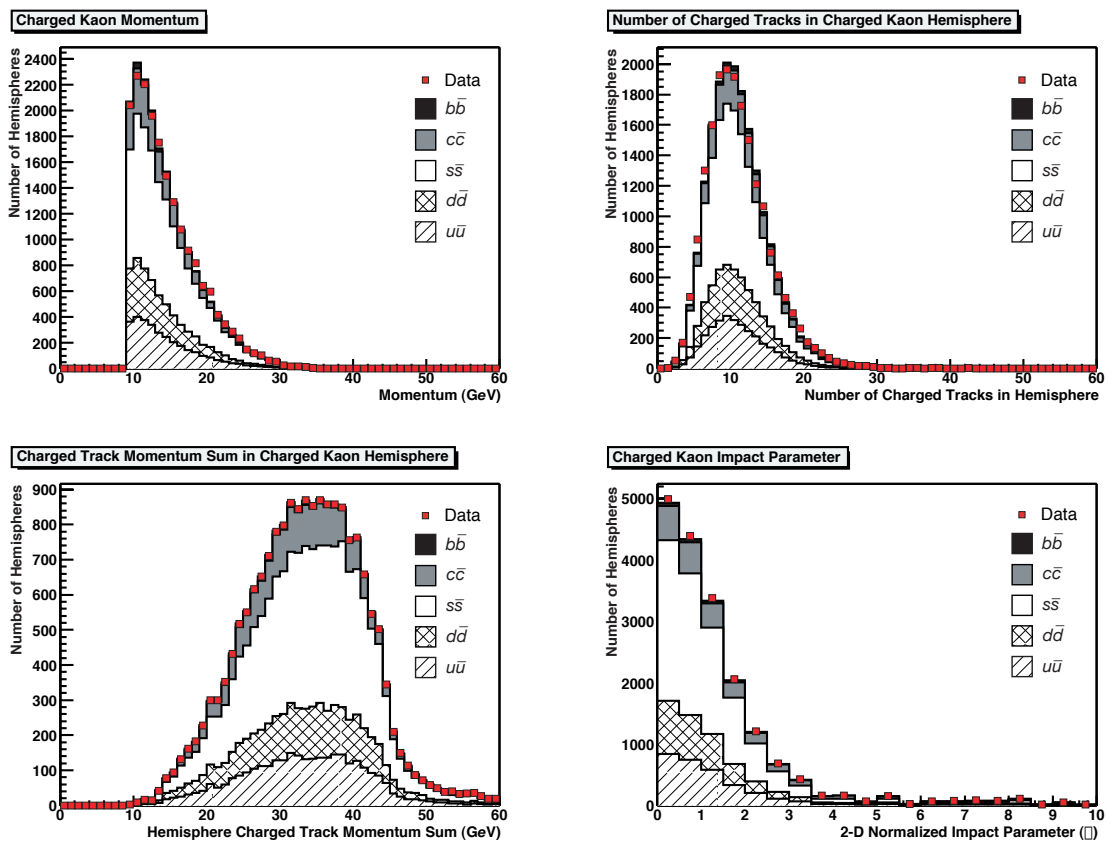
FIGURE 78. Monte Carlo reweighted input parameter distributions for the $K^{\pm}$ neural network. In the plots, the histogram represents the Monte Carlo and the dots represent the data.
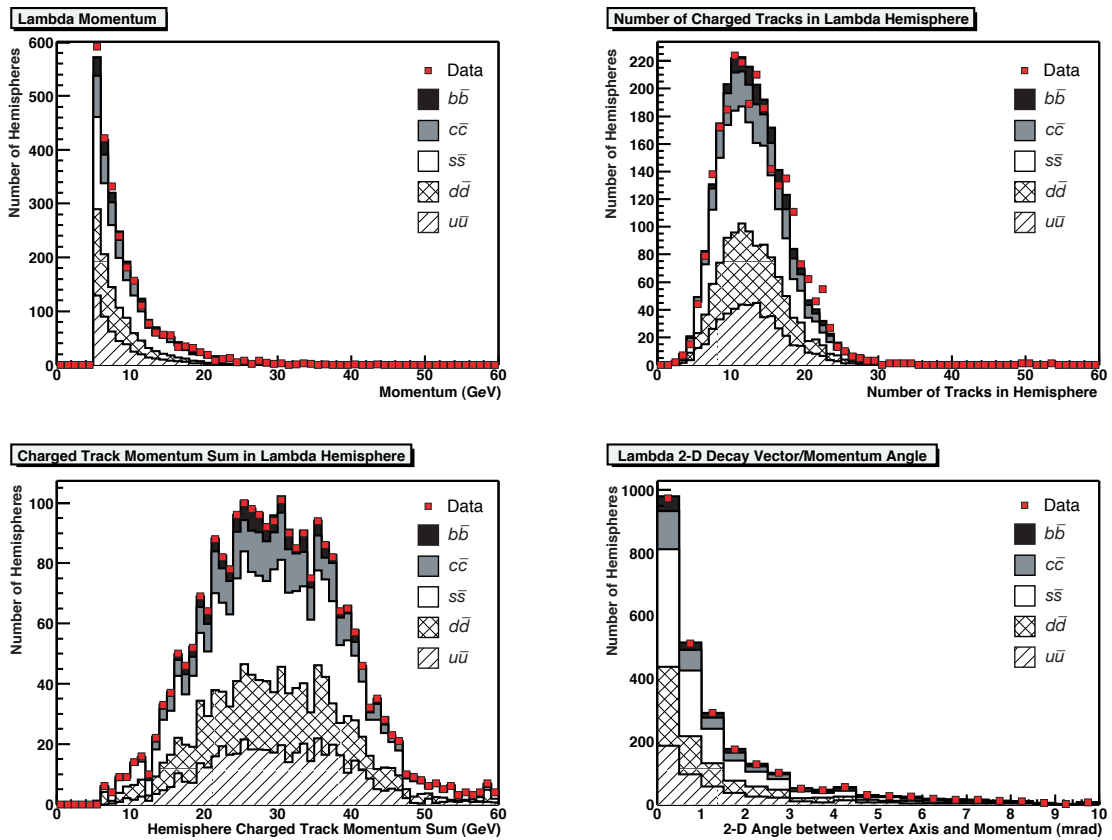
FIGURE 79. Monte Carlo reweighted input parameter distributions for the Λ neural network. In the plots, the histogram represents the Monte Carlo and the dots represent the data.
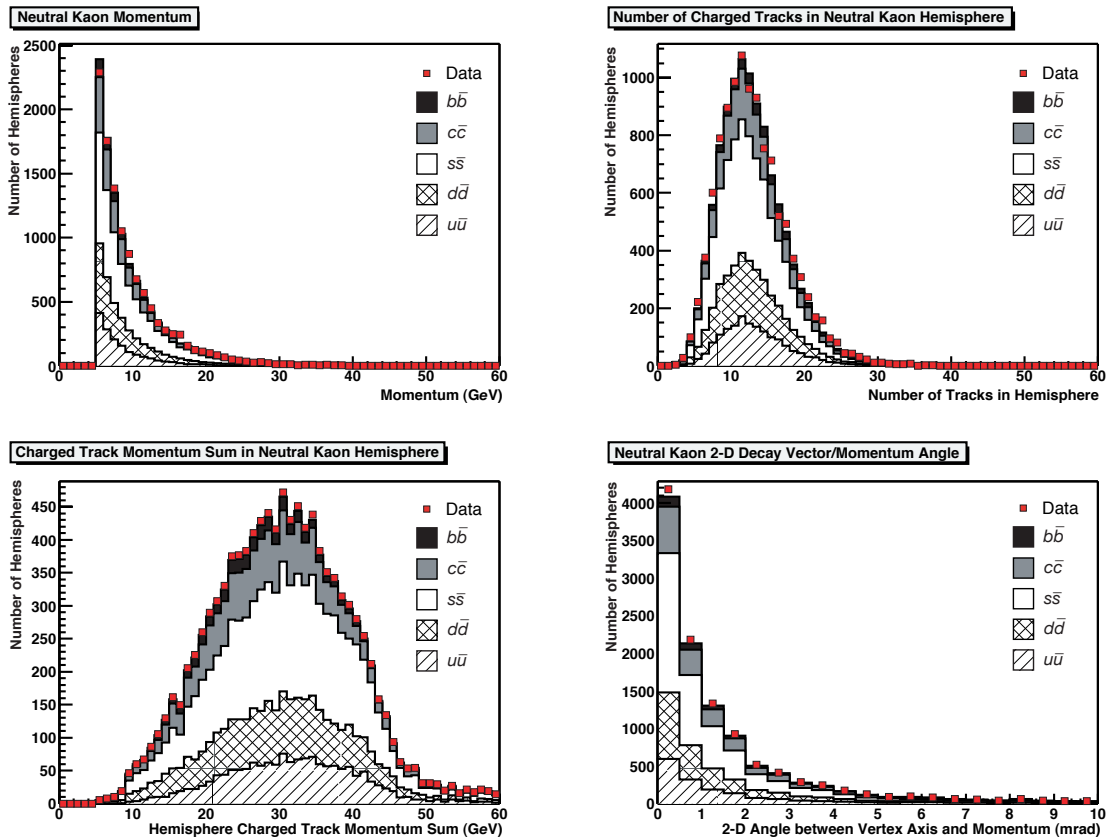
FIGURE 80. Monte Carlo reweighted input parameter distributions for the K_S^0 neural network. In the plots, the histogram represents the Monte Carlo and the dots represent the data.
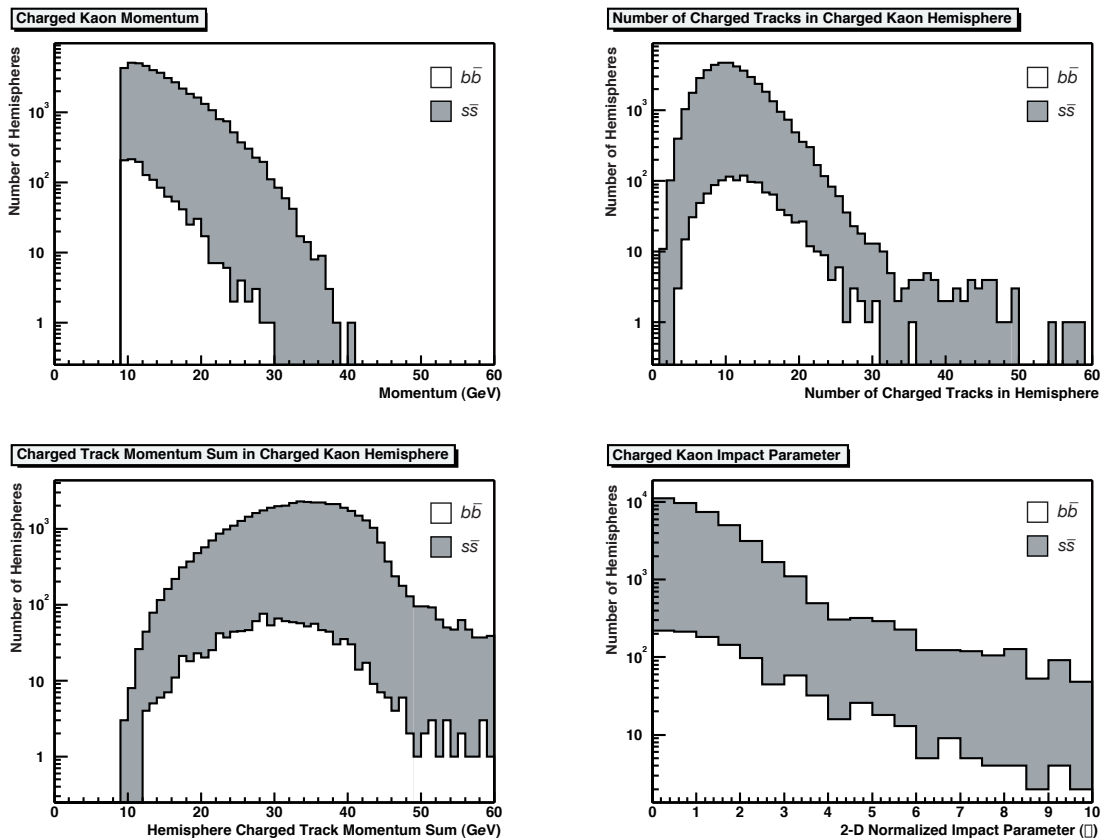
FIGURE 81. Comparison of primary s and b input parameter distributions for the $K^{\pm}$ neural network.
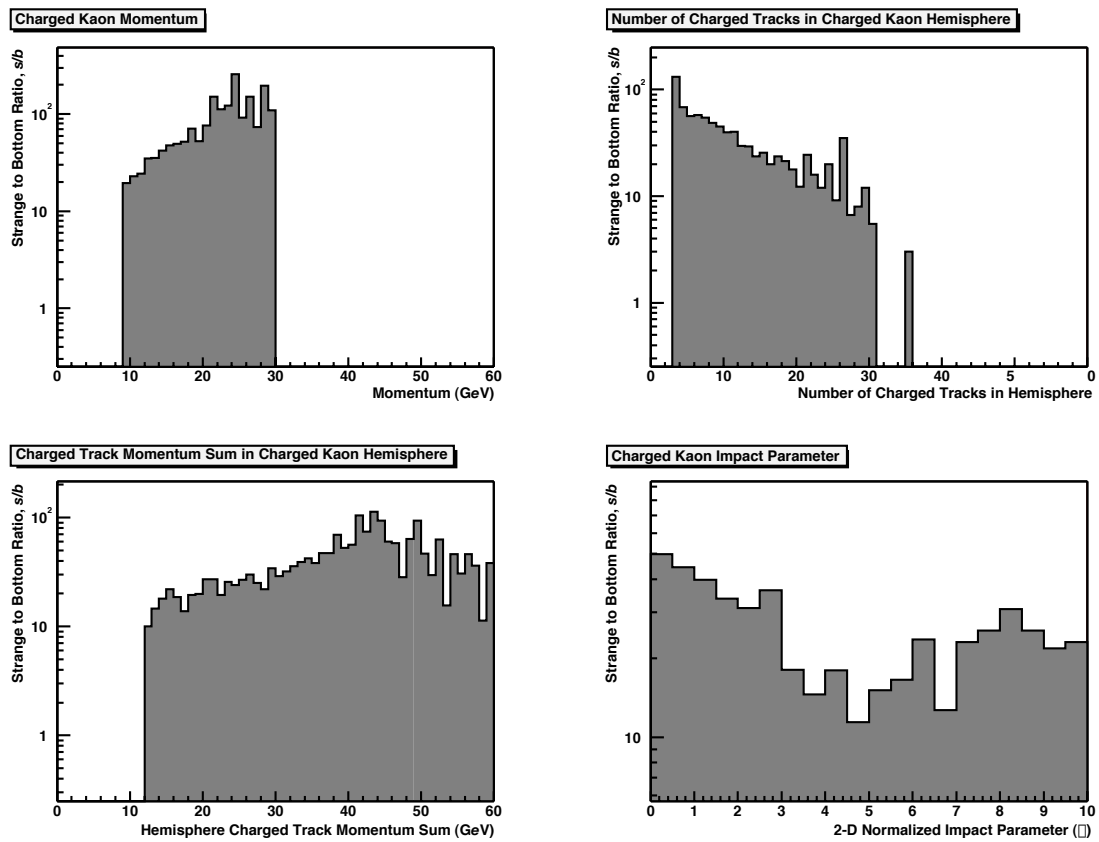
FIGURE 82. Ratio of s to b input parameter distributions for the $K^{\pm}$ neural network.
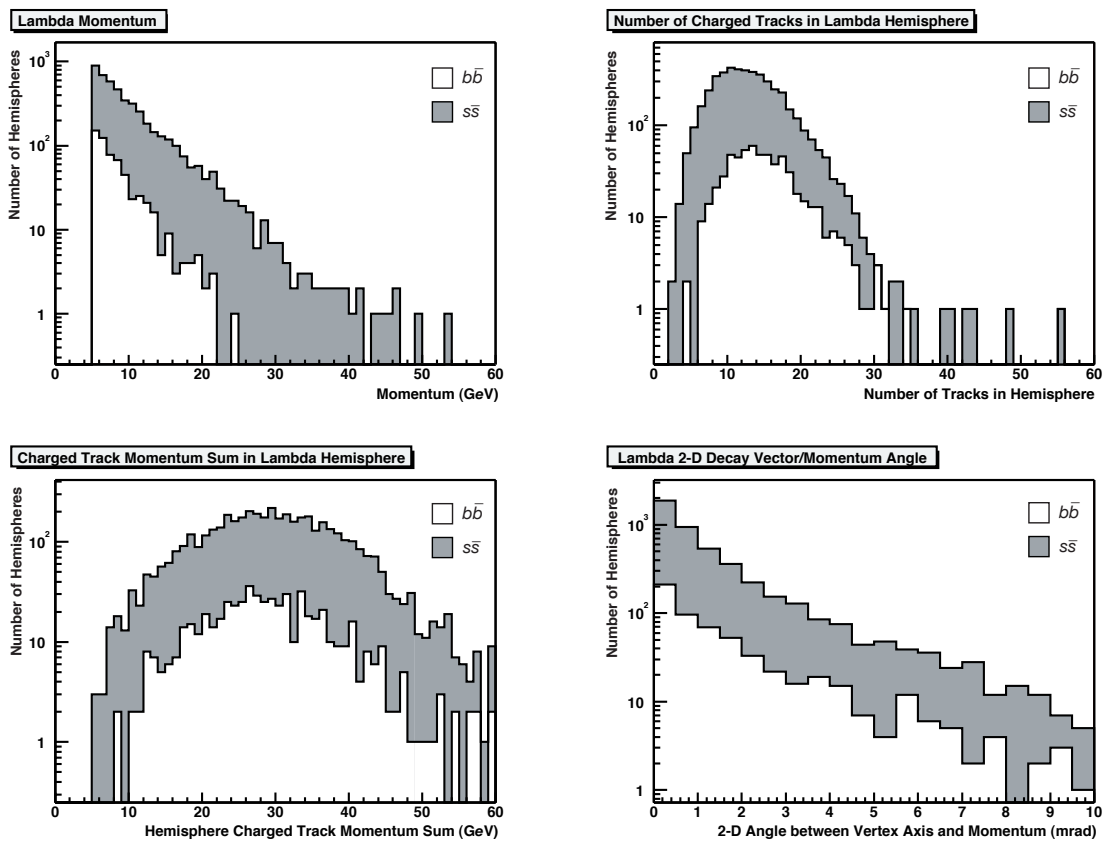
FIGURE 83. Comparison of just the s and b input parameter distributions for the Λ neural network.
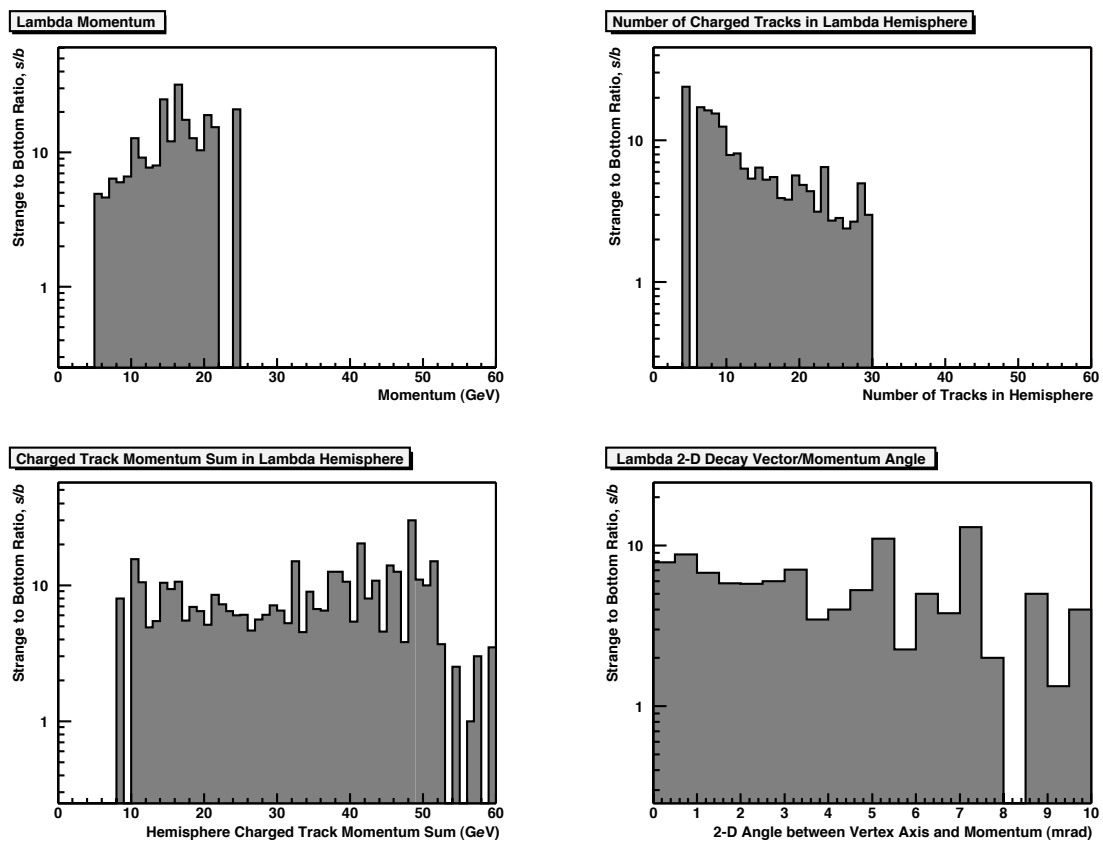
FIGURE 84. Ratio of s to b input parameter distributions for the Λ neural network.
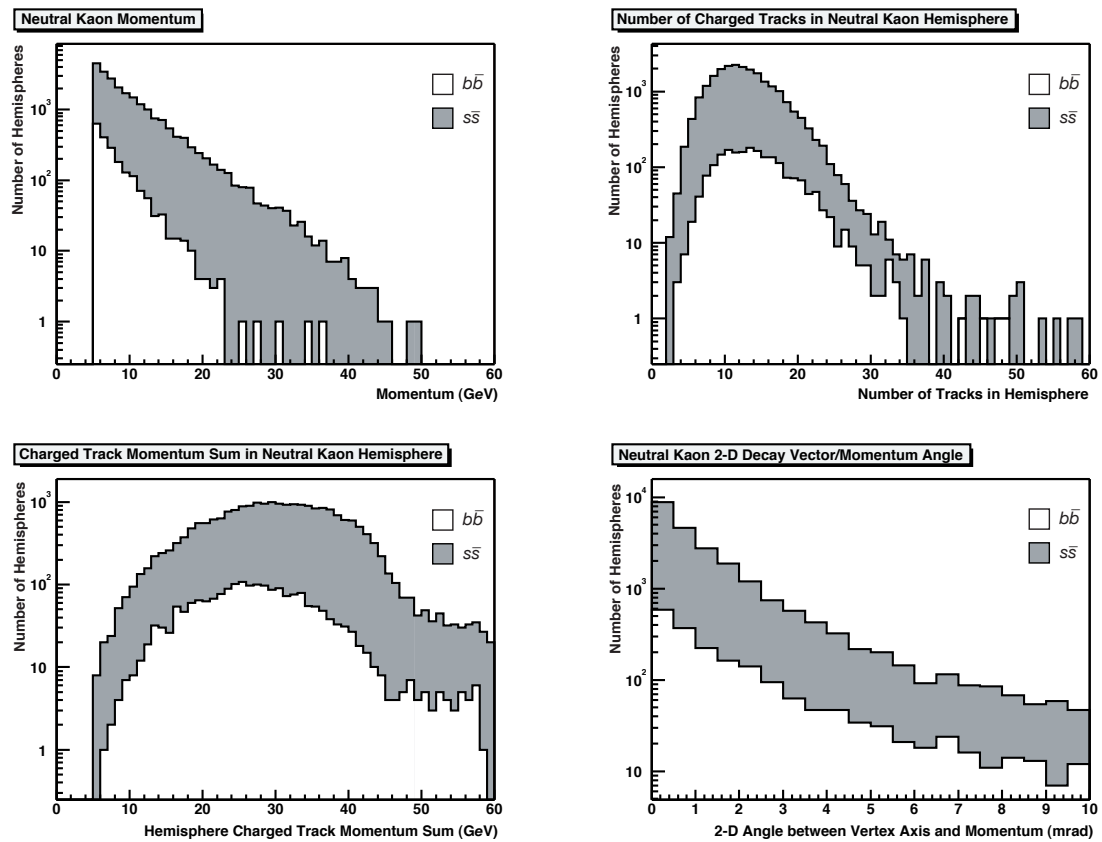
FIGURE 85. Comparison of just the s and b input parameter distributions for the K_S^0 neural network.
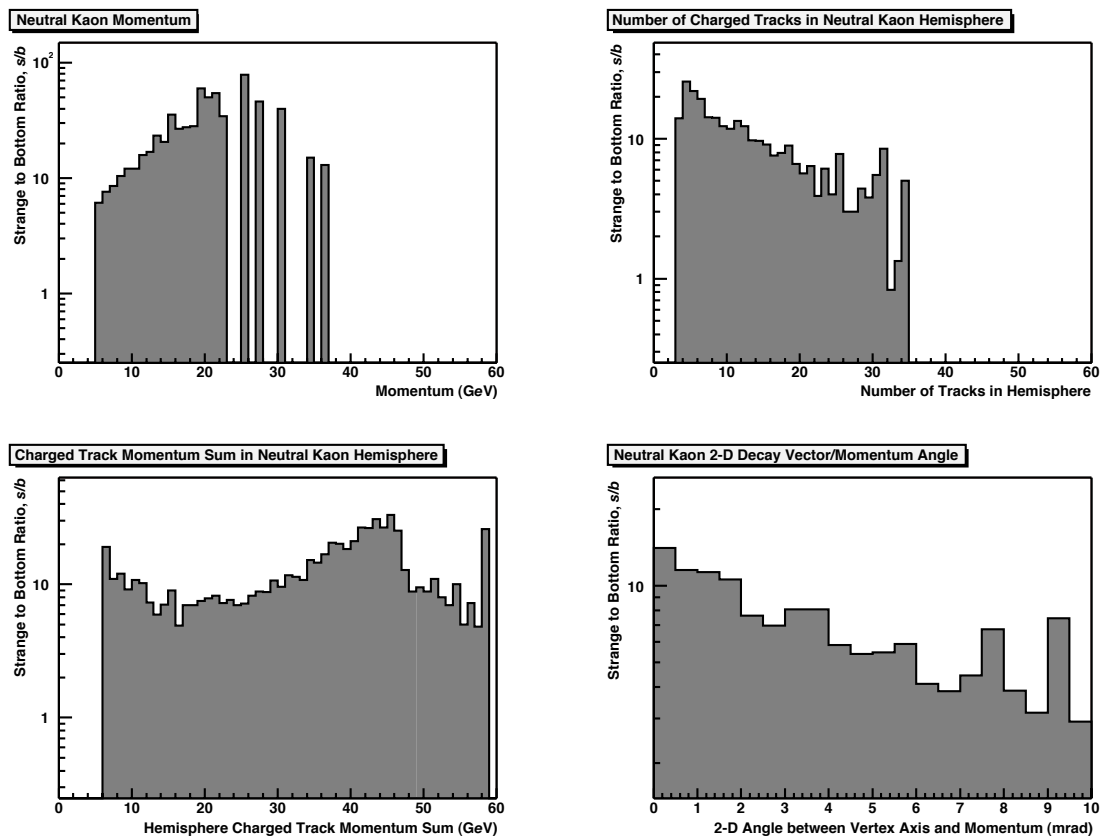
FIGURE 86. Ratio of s to b input parameter distributions for the K_S^0 neural network.

The initial cuts are fairly successful in eliminating b hemispheres (see Figure 74), and it is difficult to make out the $b\bar{b}$ backgrounds in Figures 75 through 80. Figures 81, 83, and 85 better illustrate the differences in the distributions of true s and true b hemispheres. But to really illustrate the effectiveness of the input parameters in separating s hemispheres from b hemispheres, the ratios of the s and b distributions are plotted in Figures 82, 84, and 86: The larger the value of the signal/background ratio, the more likely the hemisphere is to be s rather than b.

The three sNN were naturally trained specifically to separate Monte Carlo $b\bar{b}$ events from Monte Carlo bs events. The sNN output distributions are shown in Figures 87, 88, and 89. The best results were obtained using a training set that included roughly equal numbers of signal and background events randomly distributed throughout the set. Only Monte Carlo $b\bar{b}$ and bs events which met all the requirements listed in Table 11 were included. One neural net output unit was set to 1 and the other to zero for bs (signal) events, and vice-versa (0, 1) for $b\bar{b}$ (background) events. The second output unit turned out to be redundant, and the unit which was set to 1 for signal and 0 for background was used in the end. A separate validation set was used to test the performance of each neural network, and training was stopped once the error development in the validation set had leveled off. No examples of over-training were encountered.

The three neural networks were then tuned simultaneously, examining the entire parameter space of all possible combinations of the three cuts to find that unique set of optimum cuts which minimizes the limit we can set on R_{bs} assuming
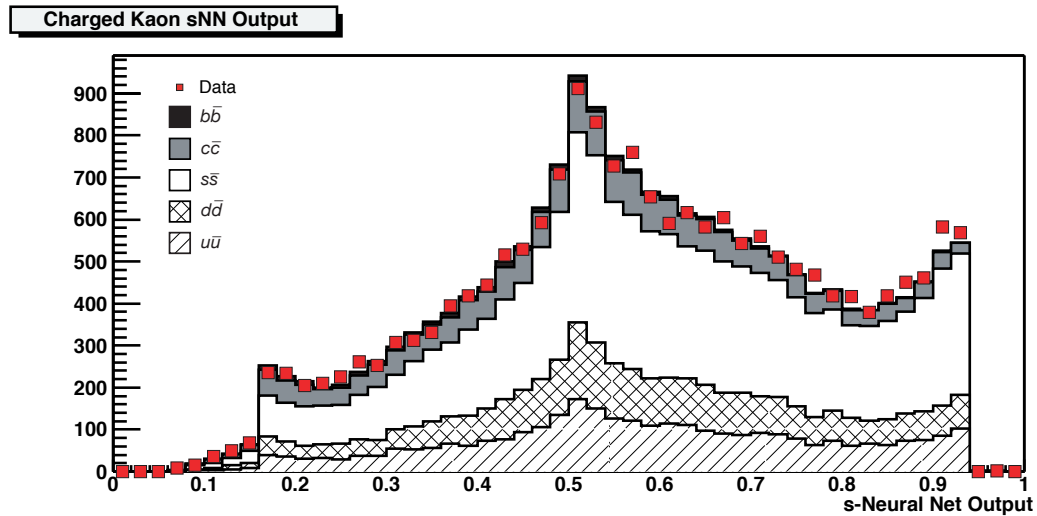
FIGURE 87. Output distribution of the $K^{\pm}$ sNN. In the plots, the histogram represents the Monte Carlo and the dots represent the data. Hemispheres with sNN output closer to 1 are more likely to be s while hemispheres with sNN output closer to 0 are more likely to be b.
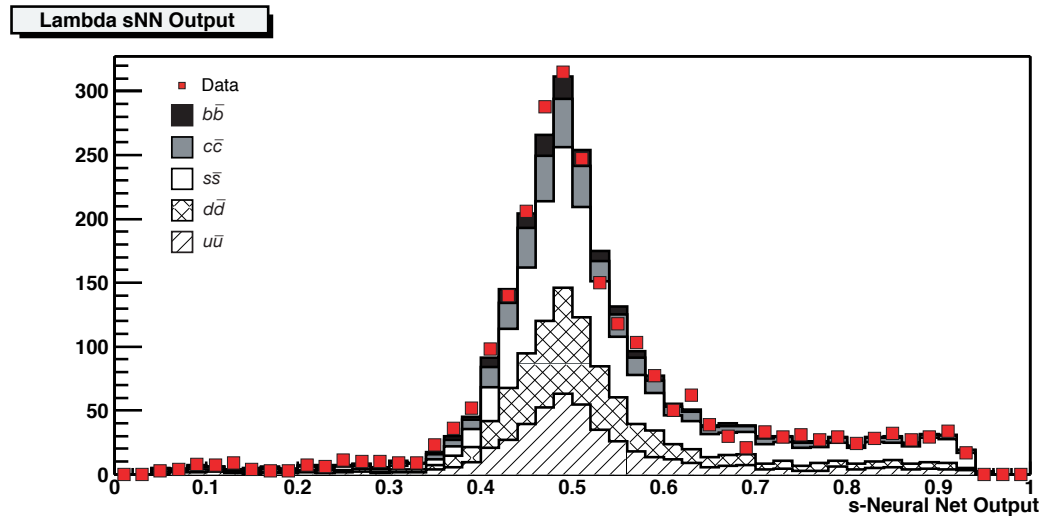
FIGURE 88. Output distribution of the Λ sNN. In the plots, the histogram represents the Monte Carlo and the dots represent the data. Hemispheres with sNN output closer to 1 are more likely to be s while hemispheres with sNN output closer to 0 are more likely to be b.
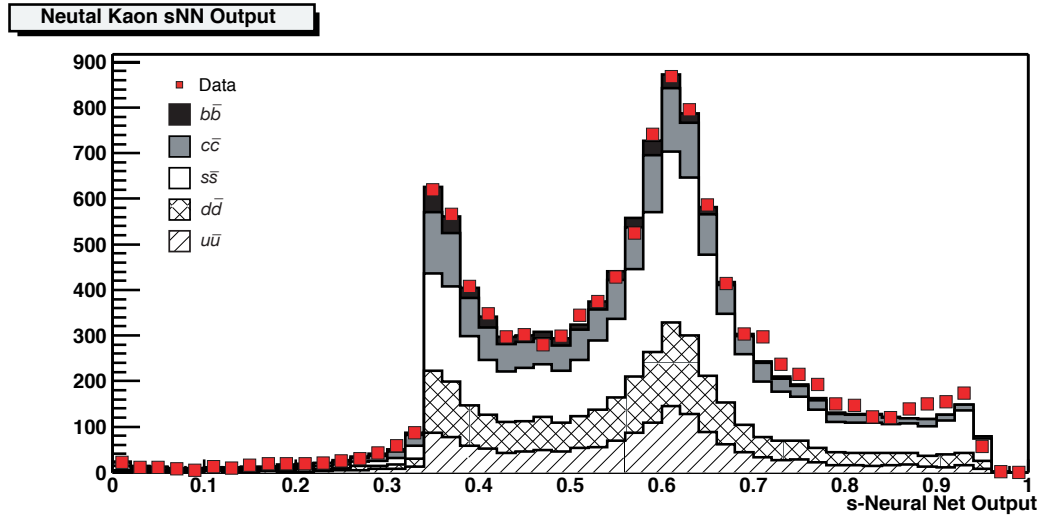
FIGURE 89. Output distribution of the K_S^0 sNN. In the plots, the histogram represents the Monte Carlo and the dots represent the data. Hemispheres with sNN output closer to 1 are more likely to be s while hemispheres with sNN output closer to 0 are more likely to be b.

zero signal events:

$$90\% \text{ C.L. Limit on } R_{bs} \quad = \quad \frac{1.64\sigma}{N_{had}(\epsilon_b\epsilon_s + \mu_{bs}\mu_{sb})} \qquad (8.18)$$

where

$$\sigma \quad = \quad \sqrt{N_{had}p(1-p)} \qquad (8.19)$$

$$p \quad = \quad R_b\epsilon_b\mu_{bs} + R_s\mu_{sb}\epsilon_s + \sum_{q\neq b,s} R_q\mu_{qb}\mu_{qs}. \qquad (8.20)$$

The cuts on the three neural networks are shown in Table 13.

It is interesting to note that the K_S^0 and Λ sNN have harder cuts than the $K^\pm$ sNN. This is because leading s-particles found in $s\bar{s}$ events and bs events strongly
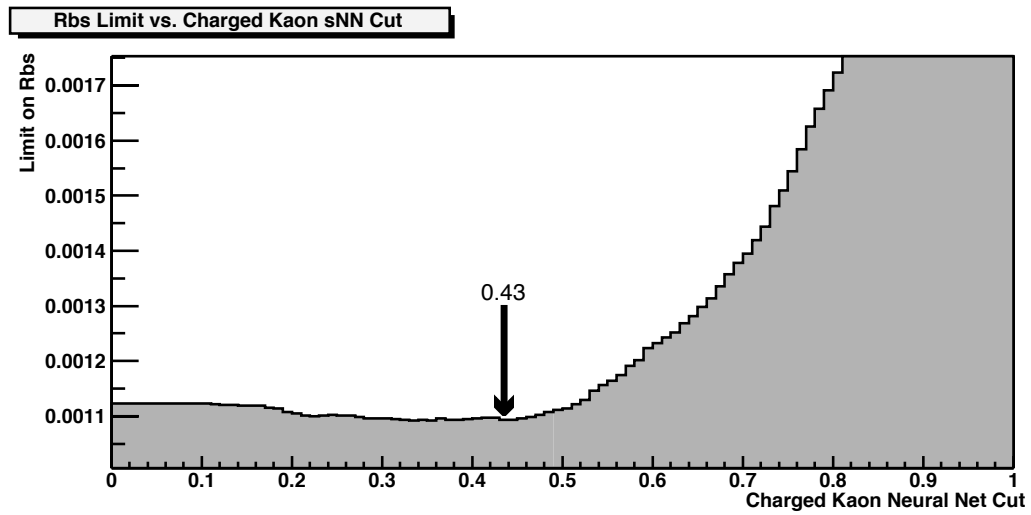
FIGURE 90. Estimated 90% confidence limit (statistics only) on R_{bs} vs. $K^{\pm}$ sNN Cut. Other cuts are held constant at their optimum values.
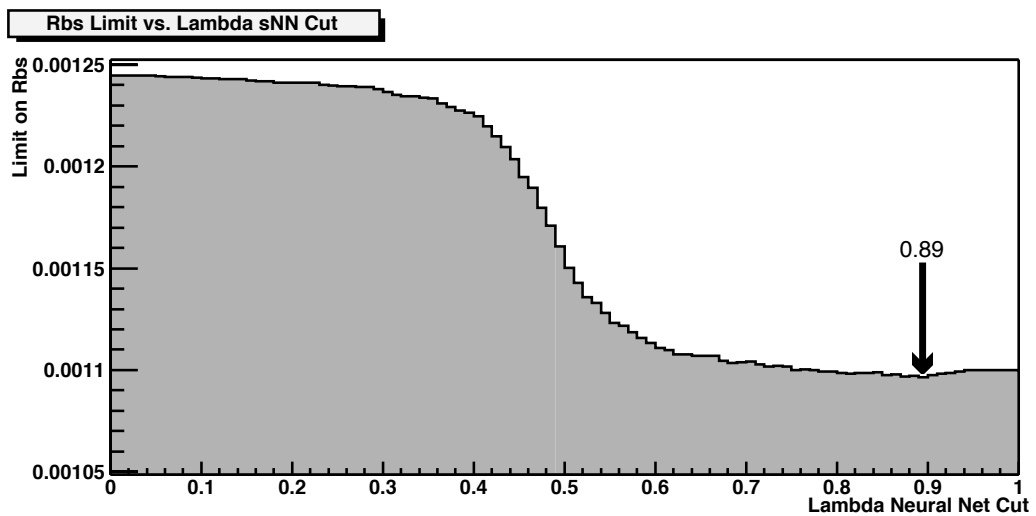
FIGURE 91. Estimated 90% confidence limit (statistics only) on R_{bs} vs. Λ sNN Cut. Other cuts are held constant at their optimum values.
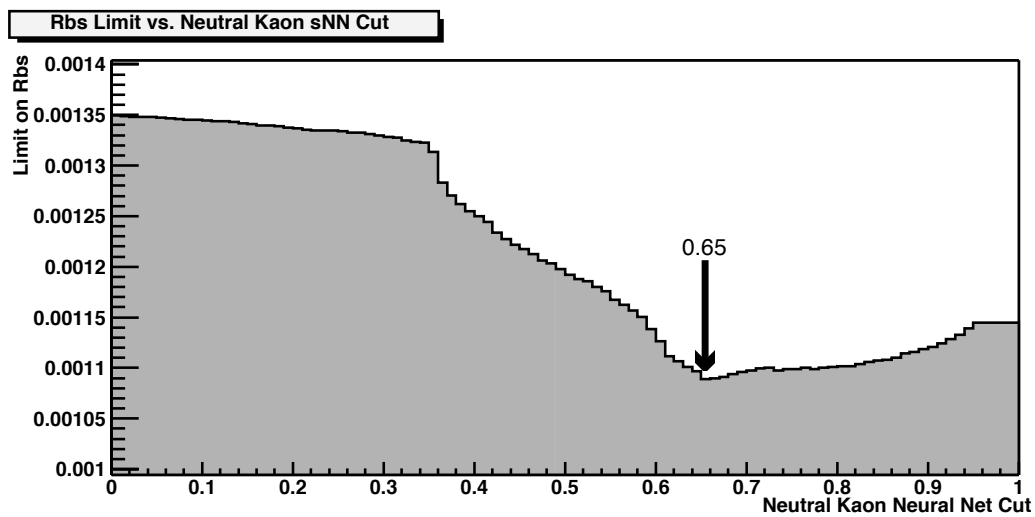
FIGURE 92. Estimated 90% confidence limit (statistics only) on R_{bs} vs. K_S^0 sNN Cut. Other cuts are held constant at their optimum values.

Species	sNN Output
$K^{\pm}$	> 0.43
Λ	> 0.89
K_S^0	> 0.65

TABLE 13. sNN Cuts

Effects of Initial Cuts and sNN
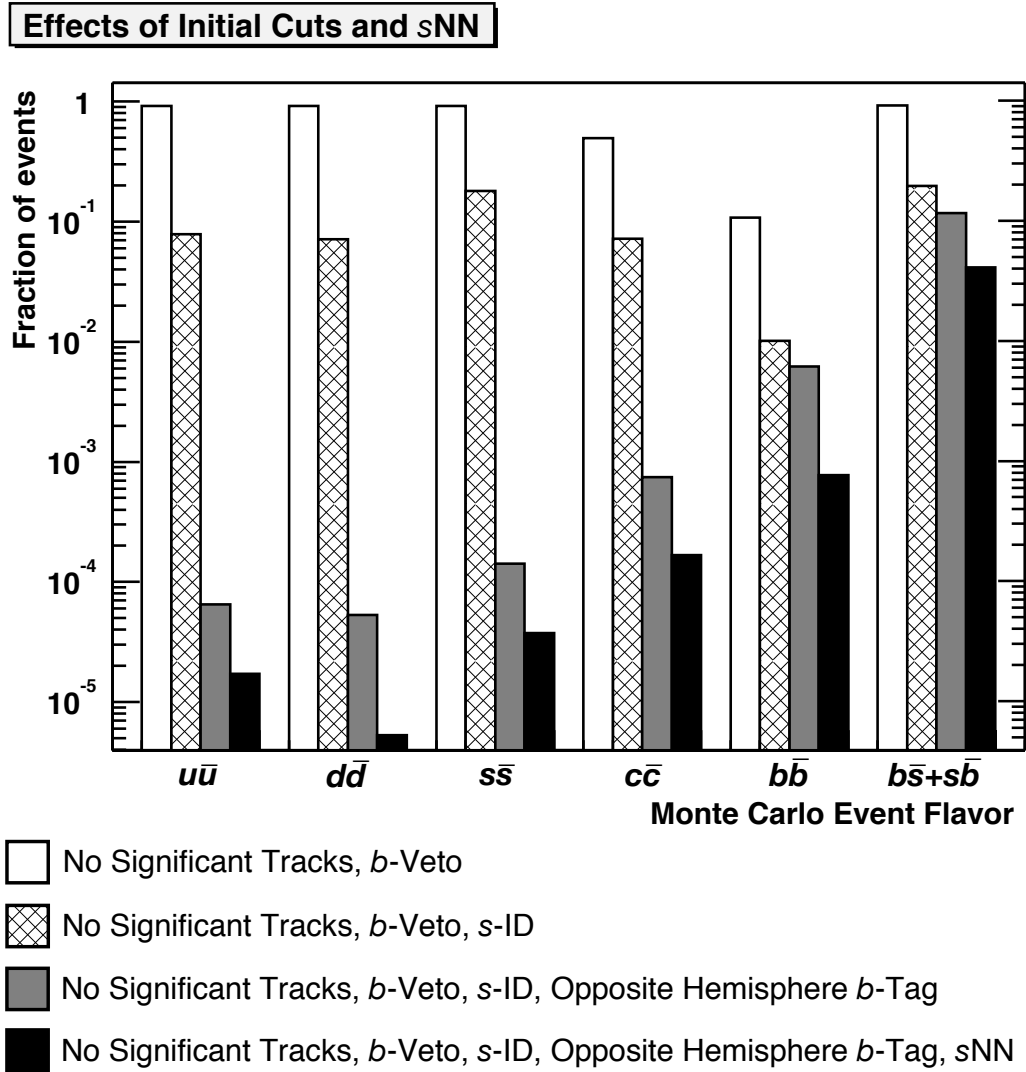
FIGURE 93. Comparison of the effects of all cuts on Monte Carlo event flavors.
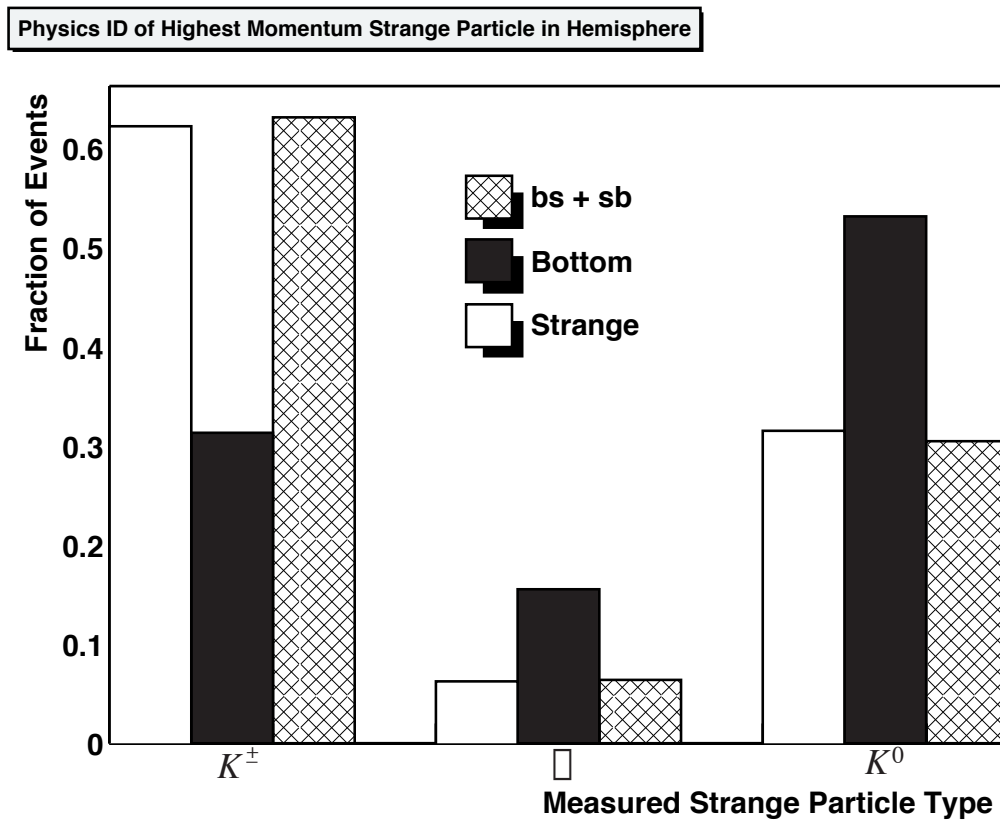
FIGURE 94. Comparison of the fractions of each strange particle species for $b\bar{s}+s\bar{b}$, $b\bar{b}$, and $s\bar{s}$ events

favor $K^{\pm}$ whilst the leading s-particles found in $b\bar{b}$ events strongly favor K_S^0 (See Figure 94). Likewise, Λ are also found more often in true $b\bar{b}$ events than in $s\bar{s}$ and bs events.

On the surface, this may appear non-intuitive as leading strange particles from s-jets are equally likely to be charged or neutral. However, B-decays favor $K^{\pm}$ over K_S^0 by approximately 74% to 29%.

This bias is to do with the momentum distributions of the various species of s-particles for $b\bar{b}$ events compared to $s\bar{s}$ and bs events. The leading s-particles found coming from $b\bar{b}$ events have a softer momentum spectrum than those coming from $s\bar{s}$ and bs events. The s-quark identification scheme tags $K^{\pm}$ down to 9 GeV and K_S^0 and Λ down to 5 GeV. Softer $K^{\pm}$ from B decays therefore aren't seen by the detector, while softer K_S^0 and Λ are. Above 9 GeV, the identification efficiency for $K^{\pm}$ is higher than for K_S^0 and Λ. This accounts for the bias.

Ultimately, the Monte Carlo predicts that the effect of the sNN on s hemisphere identification efficiency and the rate to mis-identify a b as an s, independent of any opposite hemisphere b tag, is as follows:

- sNN effect on s hemisphere identification efficiency ϵ_s : 18.0% $\rightarrow$ 10.7%.

- sNN effect on the rate of b hemispheres mis-identified as s, μ_{bs} : 1.01% $\rightarrow$ 0.137%.

The overall efficiency to identify bs events went from 11.8% $\rightarrow$ 6.56%.

CHAPTER IX

RESULTS

9.1 Summary of Results

The measurements for R_{bs}, R_b, and R_c are summarized in Tables 16, 19, and 22 respectively. These tables include the raw and corrected measurements, the corrections, and the statistical and systematic uncertainties.

These measurements of R_{bs}, R_b, and R_c require some inputs from simulated events. These inputs include two hemisphere correlation coefficients, C_{cc} and C_{bb}, about which much more will be said in section 9.9. The inputs from simulated events also include a number of mistag rates, $\mu_{qq'}$, which is the rate to mistag a quark of flavor q as a quark of flavor q'. All of these inputs, along with their statistical uncertainties, are detailed in Table 14.

The tags for b, c, and s flavored quarks are all self calibrating in that their efficiencies ϵ_q are measured using the data. The data was also used to measure two mistag rates. These efficiencies and mistag rates, along with their statistical uncertainties, which were measured in the data are listed in Table 15.

The quantities derived from simulation are affected by uncertainties related to the limited knowledge of the physics processes that are simulated. These sources of uncertainty are common to all electroweak measurements and, in order to pro-

duce consistent averages, the input physics parameters and models used in the simulation must be the same for all analyses in all experiments. To that end, the LEP/SLD Heavy Flavor Working Group has produced a set of input parameters [96], [97] that are used for all heavy flavor electroweak measurements. The systematic uncertainties in the measurements of R_{bs}, R_b, and R_c which are associated with this set of input parameters from the LEP/SLD Heavy Flavor Working Group are shown in Tables 17, 20, and 23 respectively.

Uncertainties associated with the modeling of the detector response produce attendant uncertainties in the measurements of R_{bs}, R_b, and R_c as well. These detector related systematic uncertainties along with other uncertainties unique to this analysis are summarized in Tables 18, 21, and 24. The Monte Carlo statistical uncertainty is included here as well.

Detailed discussions of each uncertainty in turn follow in the succeeding sections.

9.2 Calculating the Statistical Uncertainties

Suppose $y(\vec{x})$ is a function of some set of n random variables $\vec{x} = (x_1 \cdots x_n)$, that all the mean values μ_i for each of the variables x_i are known, and that the covariance matrix V_{ij} is either known or has at least been estimated. The expectation values of y can be approximated by expanding the function $y(\vec{x})$ about the mean values μ_i of the variables x_i [98],

$$y(\vec{x}) \approx y(\vec{\mu}) + \sum_{i=1}^{n} \left[\frac{\partial y}{\partial x_i} \right]_{\vec{x}=\vec{\mu}} (x_i - \mu_i). \qquad (9.1)$$

TABLE 14. Input parameters and their statistical uncertainties determined from the Monte Carlo simulation for the 1996 and 1997-98 run periods.

	1996	1997-98
C_{cc}	1.06374 ± 0.04883	1.01292 ± 0.01637
C_{bb}	0.99970 ± 0.01071	1.00278 ± 0.00394
μ_{us}	0.04015 ± 0.00089	0.04252 ± 0.00037
μ_{uc}	0.00053 ± 0.00010	0.00038 ± 0.00004
μ_{ub}	0.00083 ± 0.00013	0.00075 ± 0.00005
μ_{ds}	0.03365 ± 0.00072	0.03572 ± 0.00030
μ_{dc}	0.00047 ± 0.00009	0.00032 ± 0.00003
μ_{db}	0.00069 ± 0.00011	0.00082 ± 0.00005
ϵ_s	0.10150 ± 0.00122	0.10899 ± 0.00051
μ_{sc}	0.00077 ± 0.00011	0.00036 ± 0.00003
μ_{sb}	0.00065 ± 0.00010	0.00073 ± 0.00004
μ_{cs}	0.02965 ± 0.00077	0.03061 ± 0.00032
ϵ_c	0.15191 ± 0.00163	0.18165 ± 0.00072
μ_{cb}	0.01170 ± 0.00049	0.01119 ± 0.00020
μ_{bs}	0.00277 ± 0.00021	0.00219 ± 0.00008
μ_{bc}	0.02078 ± 0.00057	0.02380 ± 0.00025
ϵ_b	0.56996 ± 0.00198	0.61543 ± 0.00080

TABLE 15. Tagging efficiencies and mistag rates and their statistical uncertainties measured using the data for the 1996 and 1997-98 run periods.

	1996	1997-98
ϵ_b	0.57514 ± 0.00769	0.61586 ± 0.00265
ϵ_c	0.14593 ± 0.01149	0.17937 ± 0.00469
ϵ_s	0.10842 ± 0.00493	0.11570 ± 0.00179
μ_{cs}	0.02931 ± 0.00427	0.02778 ± 0.00151
μ_{bc}	0.02382 ± 0.00189	0.02550 ± 0.00073

TABLE 16. R_{bs} results, corrections, and statistical and systematic uncertainties for the 1996 and 1997-98 run periods.

	1996	1997-98	Combined
Raw R_{bs}	0.00513	0.00005	
$\delta R_{bs}(g \to b\bar{b})$	-0.00025	-0.00022	
$\delta R_{bs}(g \to c\bar{c})$	-0.00024	-0.00039	
Corrected R_{bs}	0.00464	-0.00056	-0.00017
$\sigma_{R_{bs}}^{stat}$	0.00316	0.00090	0.00087
$\sigma_{R_{bs}}^{sys}$(Total)	0.00098	0.00049	0.00048

TABLE 17. LEP/SLD Heavy Flavor Working Group systematics associated with the R_{bs} measurement for the 1996 and 1997-98 run periods.

	1996	1997-98	Combined
$\sigma_{R_{bs}}^{sys}(x_b \pm 0.008)$	0.00004	< 0.00001	0.00001
$\sigma_{R_{bs}}^{sys}(x_c \pm 0.008)$	0.00005	0.00006	0.00006
$\sigma_{R_{bs}}^{sys}(g \to b\bar{b} \pm 0.00051)$	0.00012	0.00010	0.00011
$\sigma_{R_{bs}}^{sys}(g \to c\bar{c} \pm 0.0038)$	0.00006	0.00010	0.00009
$\sigma_{R_{bs}}^{sys}(\langle n_b^{ch} \rangle \pm 0.062)$	0.00013	0.00015	0.00015
$\sigma_{R_{bs}}^{sys}(\langle n_{D^0}^{ch} \rangle)$	0.00003	0.00002	0.00002
$\sigma_{R_{bs}}^{sys}(\langle n_{D^\pm}^{ch} \rangle)$	0.00003	0.00002	0.00002
$\sigma_{R_{bs}}^{sys}(\langle n_{D_s}^{ch} \rangle)$	0.00008	0.00007	0.00007
$\sigma_{R_{bs}}^{sys}(\mathcal{B}(D^\pm \to K^0) \pm 7.0\%)$	0.00006	0.00003	0.00003
$\sigma_{R_{bs}}^{sys}(\mathcal{B}(D^0 \to K^0) \pm 5.0\%)$	0.00007	0.00003	0.00003
$\sigma_{R_{bs}}^{sys}(\mathcal{B}(D_s \to K^0) \pm 28\%)$	< 0.00001	0.00007	0.00006
$\sigma_{R_{bs}}^{sys}(\mathcal{B}(D^\pm \to \pi^0) \pm 10\%)$	0.00002	0.00002	0.00002
$\sigma_{R_{bs}}^{sys}(\mathcal{B}(D^0 \to \pi^0) \pm 10\%)$	0.00007	0.00003	0.00004
$\sigma_{R_{bs}}^{sys}(\mathcal{B}(D_s \to \pi^0) \pm 10\%)$	0.00001	< 0.00001	< 0.00001
$\sigma_{R_{bs}}^{sys}(\tau_b \pm 0.05 \text{ ps})$	0.00022	0.00016	0.00017
$\sigma_{R_{bs}}^{sys}(\tau_{D^0} \pm 0.004 \text{ ps})$	0.00001	0.00001	0.00001
$\sigma_{R_{bs}}^{sys}(\tau_{D^\pm} \pm 0.015 \text{ ps})$	0.00001	0.00001	0.00001
$\sigma_{R_{bs}}^{sys}(\tau_{D_s} \pm 0.017 \text{ ps})$	0.00001	0.00001	0.00001
$\sigma_{R_{bs}}^{sys}(\tau_{\Lambda_c} \pm 0.012 \text{ ps})$	< 0.00001	< 0.00001	< 0.00001
$\sigma_{R_{bs}}^{sys}(\text{Charm Hadron Production})$	0.00007	0.00008	0.00008
$\sigma_{R_{bs}}^{sys}(b \text{ Hemisphere Correlation})$	0.00001	< 0.00001	< 0.00001
$\sigma_{R_{bs}}^{sys}(c \text{ Hemisphere Correlation})$	0.00006	0.00001	0.00001

TABLE 18. Detector and other systematics associated with the R_{bs} measurement for the 1996 and 1997-98 run periods.

	1996	1997-98	Combined
$\sigma_{R_{bs}}^{sys}(\mathcal{B}(B \to K^{\pm}) \pm 6.0\%)$	0.00014	0.00009	0.00010
$\sigma_{R_{bs}}^{sys}(\mathcal{B}(B \to \Lambda) \pm 0.6\%)$	0.00002	0.00001	0.00002
$\sigma_{R_{bs}}^{sys}(\mathcal{B}(B \to K_S^0) \pm 2.9\%)$	0.00017	0.00004	0.00006
$\sigma_{R_{bs}}^{sys}(\langle N_{K^{\pm}}\rangle \pm 5.0\%)$	0.00006	0.00009	0.00008
$\sigma_{R_{bs}}^{sys}(\langle N_{\Lambda}\rangle \pm 0.9\%)$	0.00005	0.00002	0.00002
$\sigma_{R_{bs}}^{sys}(\langle N_{K_S^0}\rangle \pm 2.5\%)$	0.00002	0.00003	0.00003
$\sigma_{R_{bs}}^{sys}(R_d)$	< 0.00001	< 0.00001	< 0.00001
$\sigma_{R_{bs}}^{sys}(R_s)$	< 0.00001	< 0.00001	< 0.00001
$\sigma_{R_{bs}}^{sys}(\text{Tracking Efficiency Correction})$	0	0.00021	0.00018
$\sigma_{R_{bs}}^{sys}(\text{Track Resolution Correction})$	0.00039	0.00003	0.00008
$\sigma_{R_{bs}}^{sys}(\langle IP \rangle \text{ Tail})$	0.00003	0	< 0.00001
$\sigma_{R_{bs}}^{sys}(s\text{NN Input Reweighting})$	0.00003	0.00002	0.00002
$\sigma_{R_{bs}}^{sys}(\text{Monte Carlo Statistics})$	0.00083	0.00030	0.00028

TABLE 19. R_b results, corrections, and statistical and systematic uncertainties for the 1996 and 1997-98 run periods.

	1996	1997-98	Combined
Raw R_b	0.21014	0.21952	
$\delta R_b(g \to b\bar{b})$	−0.00032	−0.00029	
$\delta R_b(g \to c\bar{c})$	−0.00063	−0.00043	
$\delta R_b(\text{Event Selection Bias})$	−0.00151	−0.00188	
$\delta R_b(\text{Running } b\text{-mass})$	0.00035	0.00024	
$\delta R_b(\text{Photon Exchange})$	0.00020	0.00020	
Corrected R_b	0.20823	0.21736	0.21645
$\sigma_{R_b}^{stat}$	0.00413	0.00138	0.00131
$\sigma_{R_b}^{sys}(\text{Total})$	0.00185	0.00107	0.00111

TABLE 20. LEP/SLD Heavy Flavor Working Group systematics associated with the R_b measurement for the 1996 and 1997-98 run periods.

	1996	1997-98	Combined
$\sigma_{R_b}^{sys}(x_b \pm 0.008)$	0.00019	0.00011	0.00012
$\sigma_{R_b}^{sys}(x_c \pm 0.008)$	0.00015	0.00012	0.00013
$\sigma_{R_b}^{sys}(g \to b\bar{b} \pm 0.00051)$	0.00015	0.00013	0.00014
$\sigma_{R_b}^{sys}(g \to c\bar{c} \pm 0.0038)$	0.00015	0.00011	0.00011
$\sigma_{R_b}^{sys}(\langle n_b^{ch} \rangle \pm 0.062)$	0.00010	0.00018	0.00017
$\sigma_{R_b}^{sys}(\langle n_{D^0}^{ch} \rangle)$	0.00007	0.00007	0.00007
$\sigma_{R_b}^{sys}(\langle n_{D^\pm}^{ch} \rangle)$	0.00007	0.00007	0.00007
$\sigma_{R_b}^{sys}(\langle n_{D_s}^{ch} \rangle)$	0.00022	0.00023	0.00023
$\sigma_{R_b}^{sys}(\mathcal{B}(D^\pm \to K^0) \pm 7.0\%)$	0.00015	0.00007	0.00008
$\sigma_{R_b}^{sys}(\mathcal{B}(D^0 \to K^0) \pm 5.0\%)$	0.00020	0.00007	0.00008
$\sigma_{R_b}^{sys}(\mathcal{B}(D_s \to K^0) \pm 28\%)$	0.00005	0.00020	0.00018
$\sigma_{R_b}^{sys}(\mathcal{B}(D^\pm \to \pi^0) \pm 10\%)$	0.00005	0.00005	0.00005
$\sigma_{R_b}^{sys}(\mathcal{B}(D^0 \to \pi^0) \pm 10\%)$	0.00015	0.00009	0.00010
$\sigma_{R_b}^{sys}(\mathcal{B}(D_s \to \pi^0) \pm 10\%)$	0.00002	0.00001	0.00001
$\sigma_{R_b}^{sys}(\tau_b \pm 0.05 \text{ ps})$	0.00028	0.00020	0.00021
$\sigma_{R_b}^{sys}(\tau_{D^0} \pm 0.004 \text{ ps})$	0.00003	0.00002	0.00002
$\sigma_{R_b}^{sys}(\tau_{D^\pm} \pm 0.015 \text{ ps})$	0.00003	0.00002	0.00002
$\sigma_{R_b}^{sys}(\tau_{D_s} \pm 0.017 \text{ ps})$	0.00002	0.00003	0.00003
$\sigma_{R_b}^{sys}(\tau_{\Lambda_c} \pm 0.012 \text{ ps})$	< 0.00001	< 0.00001	< 0.00001
$\sigma_{R_b}^{sys}(\text{Charm Hadron Production})$	0.00017	0.00018	0.00018
$\sigma_{R_b}^{sys}(b \text{ Hemisphere Correlation})$	0.00038	0.00005	0.00009
$\sigma_{R_b}^{sys}(c \text{ Hemisphere Correlation})$	0.00013	0.00002	0.00004

TABLE 21. Detector and other systematics associated with the R_b measurement for the 1996 and 1997-98 run periods.

	1996	1997-98	Combined
$\sigma_{R_b}^{sys}(\mathcal{B}(B \to K^{\pm}) \pm 6.0\%)$	0.00009	0.00010	0.00010
$\sigma_{R_b}^{sys}(\mathcal{B}(B \to \Lambda) \pm 0.6\%)$	0.00005	0.00020	0.00017
$\sigma_{R_b}^{sys}(\mathcal{B}(B \to K_S^0) \pm 2.9\%)$	0.00005	0.00035	0.00031
$\sigma_{R_b}^{sys}(\langle N_{K^{\pm}} \rangle \pm 5.0\%)$	0.00013	0.00002	0.00004
$\sigma_{R_b}^{sys}(\langle N_{\Lambda} \rangle \pm 0.9\%)$	0.00005	0.00008	0.00008
$\sigma_{R_b}^{sys}(\langle N_{K_S^0} \rangle \pm 2.5\%)$	0.00005	0.00009	0.00008
$\sigma_{R_b}^{sys}(R_d)$	< 0.00001	< 0.00001	< 0.00001
$\sigma_{R_b}^{sys}(R_s)$	< 0.00001	< 0.00001	< 0.00001
$\sigma_{R_b}^{sys}$(Event Selection Bias)	0.00136	0.00056	0.00067
$\sigma_{R_b}^{sys}$(Running b-quark mass)	0.00034	0.00024	0.00025
$\sigma_{R_b}^{sys}$(Tracking Efficiency Correction)	0	0.00041	0.00035
$\sigma_{R_b}^{sys}$(Track Resolution Correction)	0.00094	0.00003	0.00016
$\sigma_{R_b}^{sys}(\langle IP \rangle$ Tail)	0.00022	0	0.00003
$\sigma_{R_b}^{sys}(s$NN Input Reweighting)	0.00004	0.00002	0.00003
$\sigma_{R_b}^{sys}$(Monte Carlo Statistics)	0.00101	0.00035	0.00033

TABLE 22. R_c results, corrections, and statistical and systematic uncertainties for the 1996 and 1997-98 run periods.

	1996	1997-98	Combined
Raw R_c	0.18689	0.17649	
$\delta R_c(g \to b\bar{b})$	0.00026	0.00027	
$\delta R_c(g \to c\bar{c})$	−0.00073	−0.00172	
δR_c(Event Selection Bias)	0.00042	0.00001	
δR_c(Photon Exchange)	−0.00020	−0.00020	
Corrected R_c	0.18664	0.17484	0.17588
$\sigma_{R_c}^{stat}$	0.01462	0.00452	0.00432
$\sigma_{R_c}^{sys}$(Total)	0.00943	0.00306	0.00352

TABLE 23. LEP/SLD Heavy Flavor Working Group systematics associated with the R_c measurement for the 1996 and 1997-98 run periods.

	1996	1997-98	Combined
$\sigma_{R_c}^{sys}(x_b \pm 0.008)$	0.00007	0.00003	0.00003
$\sigma_{R_c}^{sys}(x_c \pm 0.008)$	0.00033	0.00002	0.00006
$\sigma_{R_c}^{sys}(g \to b\bar{b} \pm 0.00051)$	0.00012	0.00013	0.00013
$\sigma_{R_c}^{sys}(g \to c\bar{c} \pm 0.0038)$	0.00018	0.00042	0.00039
$\sigma_{R_c}^{sys}(\langle n_b^{ch} \rangle \pm 0.062)$	0.00001	0.00001	0.00001
$\sigma_{R_c}^{sys}(\langle n_{D^0}^{ch} \rangle)$	0.00081	0.00013	0.00023
$\sigma_{R_c}^{sys}(\langle n_{D^\pm}^{ch} \rangle)$	0.00013	0.00015	0.00015
$\sigma_{R_c}^{sys}(\langle n_{D_s}^{ch} \rangle)$	0.00337	0.00074	0.00111
$\sigma_{R_c}^{sys}(\mathcal{B}(D^\pm \to K^0) \pm 7.0\%)$	0.00071	0.00001	0.00011
$\sigma_{R_c}^{sys}(\mathcal{B}(D^0 \to K^0) \pm 5.0\%)$	0.00080	0.00036	0.00042
$\sigma_{R_c}^{sys}(\mathcal{B}(D_s \to K^0) \pm 28\%)$	0.00268	0.00183	0.00195
$\sigma_{R_c}^{sys}(\mathcal{B}(D^\pm \to \pi^0) \pm 10\%)$	0.00037	0.00005	0.00009
$\sigma_{R_c}^{sys}(\mathcal{B}(D^0 \to \pi^0) \pm 10\%)$	0.00086	0.00023	0.00032
$\sigma_{R_c}^{sys}(\mathcal{B}(D_s \to \pi^0) \pm 10\%)$	0.00064	0.00009	0.00017
$\sigma_{R_c}^{sys}(\tau_b \pm 0.05 \text{ ps})$	0.00002	0.00001	0.00001
$\sigma_{R_c}^{sys}(\tau_{D^0} \pm 0.004 \text{ ps})$	0.00011	0.00004	0.00005
$\sigma_{R_c}^{sys}(\tau_{D^\pm} \pm 0.015 \text{ ps})$	0.00014	0.00002	0.00003
$\sigma_{R_c}^{sys}(\tau_{D_s} \pm 0.017 \text{ ps})$	0.00019	0.00004	0.00006
$\sigma_{R_c}^{sys}(\tau_{\Lambda_c} \pm 0.012 \text{ ps})$	0.00006	0.00003	0.00003
$\sigma_{R_c}^{sys}(\text{Charm Hadron Production})$	0.00064	0.00048	0.00050
$\sigma_{R_c}^{sys}(b \text{ Hemisphere Correlation})$	0.00012	0.00001	0.00003
$\sigma_{R_c}^{sys}(c \text{ Hemisphere Correlation})$	0.00496	0.00079	0.00139

TABLE 24. Detector and other systematics associated with the R_c measurement for the 1996 and 1997-98 run periods.

	1996	1997-98	Combined
$\sigma_{R_c}^{sys}(\mathcal{B}(B \to K^{\pm}) \pm 6.0\%)$	0.00008	0.00003	0.00003
$\sigma_{R_c}^{sys}(\mathcal{B}(B \to \Lambda) \pm 0.6\%)$	0.00001	0.00005	0.00004
$\sigma_{R_c}^{sys}(\mathcal{B}(B \to K_S^0) \pm 2.9\%)$	0.00003	0.00010	0.00009
$\sigma_{R_c}^{sys}(\langle N_{K^{\pm}} \rangle \pm 5.0\%)$	0.00016	0.00009	0.00010
$\sigma_{R_c}^{sys}(\langle N_{\Lambda} \rangle \pm 0.9\%)$	0.00014	0.00008	0.00009
$\sigma_{R_c}^{sys}(\langle N_{K_S^0} \rangle \pm 2.5\%)$	0.00051	0.00010	0.00016
$\sigma_{R_c}^{sys}(R_d)$	< 0.00001	< 0.00001	< 0.00001
$\sigma_{R_c}^{sys}(R_s)$	< 0.00001	< 0.00001	< 0.00001
$\sigma_{R_c}^{sys}$(Event Selection Bias)	0.00123	0.00051	0.00061
$\sigma_{R_c}^{sys}$(Tracking Efficiency Correction	0	0.00014	0.00012
$\sigma_{R_c}^{sys}$(Track Resolution Correction	0.00119	0.00033	0.00045
$\sigma_{R_c}^{sys}(\langle IP \rangle \text{Tail})$	0.00026	0	0.00004
$\sigma_{R_c}^{sys}(s\text{NN Input Reweighting})$	0.00046	0.00002	0.00008
$\sigma_{R_c}^{sys}$(Monte Carlo Statistics)	0.00620	0.00209	0.00198

To first order, the expectation value of y is

$$\langle y(\vec{x}) \rangle \approx y(\vec{\mu}). \qquad (9.2)$$

since $\langle x_i - \mu_i \rangle = 0$. The expectation value of y^2 is

$$
\begin{aligned}
\langle y^2(\vec{x}) \rangle &\approx y^2(\vec{\mu}) + 2y(\vec{\mu}) \cdot \sum_{i=1}^{n} \left[\frac{\partial y}{\partial x_i} \right]_{\vec{x}=\vec{\mu}} \langle x_i - \mu_i \rangle \\
&+ \left\langle \left(\sum_{i=1}^{n} \left[\frac{\partial y}{\partial x_i} \right]_{\vec{x}=\vec{\mu}} (x_i - \mu_i) \right) \left(\sum_{j=1}^{n} \left[\frac{\partial y}{\partial x_j} \right]_{\vec{x}=\vec{\mu}} (x_j - \mu_j) \right) \right\rangle \\
&\approx y^2(\vec{\mu}) + \sum_{i,j=1}^{n} \left[\frac{\partial y}{\partial x_i} \frac{\partial y}{\partial x_j} \right]_{\vec{x}=\vec{\mu}} V_{ij}. \qquad (9.3)
\end{aligned}
$$

The variance of y, $V[y] = \sigma_y^2$ is then

$$\sigma_y^2 \approx \sum_{i,j=1}^{n} \left[\frac{\partial y}{\partial x_i} \frac{\partial y}{\partial x_j} \right]_{\vec{x}=\vec{\mu}} V_{ij}. \qquad (9.4)$$

For the case where the x_i are not correlated, i.e. $V_{ii} = \sigma_i^2$ and $V_{ij} = 0$ for $i \neq j$, equation 9.4 becomes

$$\sigma_y^2 \approx \sum_{i=1}^{n} \left[\frac{\partial y}{\partial x_i} \right]_{\vec{x}=\vec{\mu}}^2 \sigma_i^2. \qquad (9.5)$$

This analysis rests on the following variables:

$$
\begin{aligned}
H_b &= \text{number of } b\text{-tagged hemispheres} \\
E_{bb} &= \text{number of double } b\text{-tagged events} \\
H_c &= \text{number of } c\text{-tagged hemispheres} \\
E_{cc} &= \text{number of double } c\text{-tagged events} \\
H_s &= \text{number of } s\text{-tagged hemispheres} \\
E_{cs} &= \text{number of } cs\text{-tagged events} \\
E_{bs} &= \text{number of } bs\text{-tagged events} \\
E_{bc} &= \text{number of } bc\text{-tagged events} \\
N_{had} &= \text{number of hadronic events.}
\end{aligned}
$$

These nine variables, however, are not statistically independent, and the covariance matrix V_{ij} is not known. But with the addition of the variable E_{ss} for double s-tagged events, these variables can be exchanged for a set of new variables which are statistically independent, making the covariance matrix simply $V_{ii} = \sigma_i^2$ and $V_{ij} = 0$ for $i \neq j$. The new variables are then:

$$E_b = \text{number of single } b\text{-tagged events}$$

$$E_{bb} = \text{number of double } b\text{-tagged events}$$

$$E_c = \text{number of single } c\text{-tagged events}$$

$$E_{cc} = \text{number of double } c\text{-tagged events}$$

$$E_s = \text{number of single } s\text{-tagged events}$$

$$E_{ss} = \text{number of double } s\text{-tagged events}$$

$$E_{cs} = \text{number of } cs\text{-tagged events}$$

$$E_{bs} = \text{number of } bs\text{-tagged events}$$

$$E_{bc} = \text{number of } bc\text{-tagged events}$$

$$E_0 = \text{number of un-tagged events.}$$

Note that with the new variables E_q, there is no overlap with E_{qq} – an event is either tagged once or twice, but not both. With H_q on the other hand, a double tagged event for example would contribute to both H_q and E_{qq}. With the new set of variables, each variable counts an independent subset of the data. The new variables can be calculated as follows:

$$E_b = H_b - 2E_{bb} - E_{bs} - E_{bc} \tag{9.6}$$

$$E_c = H_c - 2E_{cc} - E_{cs} - E_{bc} \tag{9.7}$$

$$E_s = H_c - 2E_{ss} - E_{cs} - E_{bs} \tag{9.8}$$

$$E_0 = N_{had} - E_b - E_{bb} - E_c - E_{cc} - E_s - E_{ss} - E_{cs} - E_{bs} - E_{bc}. \tag{9.9}$$

Because an event either increments a given variable ("success") or it doesn't ("failure"), the statistical uncertainties on these variables come from binomial

TABLE 25. Statistical uncertainties for R_{bs}, R_b, and R_c.

	1996	1997-98	Combined
$\sigma_{R_{bs}}^{stat}$	0.00316	0.00090	0.00087
$\sigma_{R_b}^{stat}$	0.00413	0.00138	0.00131
$\sigma_{R_c}^{stat}$	0.01462	0.00452	0.00432

statistics and are simply

$$\sigma_i \;=\; \sqrt{E_i\left(1 - \frac{E_i}{N_{had}}\right)}. \tag{9.10}$$

From equation 9.5, the statistical uncertainty on the unknown y can then be estimated by varying each of these new variables by $\pm 1\sigma$ in turn, and summing differences in quadrature, as follows:

$$\sigma_y^2 \;\approx\; \sum_{i=1}^{10}\left[\frac{y(E_i + \sigma_i) - y(E_i - \sigma_i)}{2}\right]^2. \tag{9.11}$$

The statistical uncertainties are shown in Table 25

The Monte Carlo statistical uncertainty is estimated in an analogous way, except that there is a set of ten E_i for each Monte Carlo event flavor: Thus, $E_i^{u\bar{u}}$, $E_i^{d\bar{d}}$, $E_i^{s\bar{s}}$, $E_i^{c\bar{c}}$, and $E_i^{b\bar{b}}$. All of these $E_i^{q\bar{q}}$ must be varied by $\pm 1\sigma$ in turn, and the differences summed in quadrature, as above.

$$\sigma_y^2 \;\approx\; \sum_{q\bar{q}}\sum_{i=1}^{10}\left[\frac{y(E_i^{q\bar{q}} + \sigma_i^{q\bar{q}}) - y(E_i^{q\bar{q}} - \sigma_i^{q\bar{q}})}{2}\right]^2. \tag{9.12}$$

The Monte Carlo statistical uncertainties are shown in Table 26.

TABLE 26. Monte Carlo Statistical uncertainties for R_{bs}, R_b, and R_c.

	1996	1997-98	Combined
$\sigma_{R_{bs}}^{sys}$(Monte Carlo Statistics)	0.00083	0.00030	0.00028
$\sigma_{R_b}^{sys}$(Monte Carlo Statistics)	0.00101	0.00035	0.00033
$\sigma_{R_c}^{sys}$(Monte Carlo Statistics)	0.00620	0.00209	0.00198

9.3 Heavy Quark Fragmentation

The process of hadronization is modelled as the convolution of a perturbative part – hard gluon radiation, and a non-perturbative part, called fragmentation, which is described by phenomenological models. In the JETSET simulation, the fragmentation model by Peterson *et al.* is used. The model contains one free parameter, ϵ_q, which varies the cut-off for the transition between the perturbative and the non-perturbative parts, although ϵ_q cannot be given an absolute meaning beyond this. In any case, ϵ_q is tuned to reproduce the observed value of the mean energy of the heavy hadrons. The energy spectrum of the heavy hadrons is more conveniently expressed in terms of the variable x_q, defined as the energy of the heavy hadron normalized to the beam energy.

The LEP/SLD Heavy Flavor Working Group provides values for the mean energies of b and c hadrons [96]:

$$\langle x_b \rangle = 0.702 \pm 0.008 \tag{9.13}$$

$$\langle x_c \rangle = 0.484 \pm 0.008. \tag{9.14}$$

To vary $\langle x_b \rangle$ and $\langle x_c \rangle$ within their uncertainties, events in the Monte Carlo data sample are reweighted in the following way. Begin with the definitions below:

$$\int n(x_q)dx_q = N \tag{9.15}$$

$$\int n(x_q)w(x_q)dx_q = N \tag{9.16}$$

$$\int x_q n(x_q)dx_q = \overline{x_q}N \tag{9.17}$$

$$\int x_q n(x_q)w(x_q)dx_q = \overline{x'_q}N \tag{9.18}$$

where $n(x_q)$ is the number of events having x_q between x_q and $x_q + dx_q$, N is the total number of events, and $w(x_q)$ is the weighting factor used to tweak $\overline{x_q}$ to $\overline{x'_q}$. Let $w(x_q) = (x_q - \overline{x_q})w_0 + w_1$. Substituting into the above equations yields

$$\int n(x_q)[(x_q - \overline{x_q})w_0 + w_1]dx_q = N \tag{9.19}$$

$$w_0 \int x_q n(x_q)dx_q + w_0 \overline{x_q} \int n(x_q)dx_q + w_1 \int n(x_q)dx_q = N \tag{9.20}$$

$$w_0 \overline{x_q}N - w_0 \overline{x_q}N + w_1 N = N \tag{9.21}$$

$$w_1 = 1 \tag{9.22}$$

$$\int x_q n(x_q)[(x_q - \overline{x_q})w_0 + 1]dx_q = \overline{x'_q}N \tag{9.23}$$

$$w_0 \int x_q^2 n(x_q)dx_q - w_0 \overline{x_q} \int x_q n(x_q)dx_q + \int x_q n(x_q)dx_q = \overline{x'_q}N \tag{9.24}$$

$$w_0 N(\overline{x_q^2} - \overline{x_q}^2) + \overline{x_q}N = \overline{x'_q}N \tag{9.25}$$

$$w_0 = \frac{\overline{x'_q} - \overline{x_q}}{\overline{x_q^2} - \overline{x_q}^2}. \tag{9.26}$$

Finally, $w(x_q)$ becomes

$$w(x_q) = (x_q - \overline{x_q})\frac{\overline{x'_q} - \overline{x_q}}{\overline{x_q^2} - \overline{x_q}^2} + 1 \tag{9.27}$$

TABLE 27. Uncertainties associated with heavy quark fragmentation.

	1996	1997-98	Combined
$\sigma_{R_{bs}}^{sys}(x_b \pm 0.008)$	0.00004	< 0.00001	0.00001
$\sigma_{R_{bs}}^{sys}(x_c \pm 0.008)$	0.00005	0.00006	0.00006
$\sigma_{R_b}^{sys}(x_b \pm 0.008)$	0.00019	0.00011	0.00012
$\sigma_{R_b}^{sys}(x_c \pm 0.008)$	0.00015	0.00012	0.00013
$\sigma_{R_c}^{sys}(x_b \pm 0.008)$	0.00007	0.00003	0.00003
$\sigma_{R_c}^{sys}(x_c \pm 0.008)$	0.00033	0.00002	0.00006

and is computed event by event to determine how the event in question should be weighted. The uncertainties associated with x_b and x_c are listed in Table 27.

9.4 Adjusting Branching Ratios and Multiplicities

Implicit in the Monte Carlo are assumptions about the values for many different branching ratios, multiplicities, and so on that are, fundamentally, determined by averaging integers, i.e. the number of a certain particle coming from the decay of another certain particle in a given event, for example. Such assumptions may affect other assumptions about the levels of backgrounds, identification efficiencies, mis-identification rates, and so on. For the purposes of establishing systematic uncertainties, it will be important to reweight the Monte Carlo data event by event in order to alter certain average values and determine the effect the changes have on the final values of R_{bs}, R_b, and R_c.

Consider as an example the case of the branching ratio $\mathcal{B}(B \rightarrow K^{\pm})$. A B meson decay can produce $0, 1, 2, ... K^{\pm}$. The branching ratio can be calculated by

$$\mathcal{B}(B \rightarrow K^{\pm}) \;\; = \;\; \sum_n nP(n) \tag{9.28}$$

where n is the number of $K^{\pm}$s originating from a particular B meson, and $P(n)$ is the probability that a particular B meson contained n $K^{\pm}$s.

For the purpose of determining its systematic effect, the branching ratio (multiplicity, or whatever) must be varied by an amount $\pm\Delta$ to cover the range of possible values encompassed by its uncertainty. The new value for the branching ratio may be expressed thus

$$\mathcal{B}(B \rightarrow K^{\pm}) + \Delta \ = \ \sum_n nP'(n) \tag{9.29}$$

where $P'(n)$ is the adjusted probability distribution. $P'(n)$ may be determined from $P(n)$ by

$$P'(n) \ = \ f_1 P(n) + f_2 P(n-1). \tag{9.30}$$

A fraction $1 - f_1$ of the B mesons containing n $K^{\pm}$s are in effect being given one extra $K^{\pm}$, as are a fraction f_2 of the B mesons containing $n-1$ $K^{\pm}$s. The new branching ratio becomes

$$\mathcal{B}(B \rightarrow K^{\pm}) + \Delta \ = \ \sum_n n\left[f_1 P(n) + f_2 P(n-1)\right] \tag{9.31}$$

$$= \ f_1 \mathcal{B}(B \rightarrow K^{\pm}) + f_2 \sum_n nP(n-1) \tag{9.32}$$

$$= \ f_1 \mathcal{B}(B \rightarrow K^{\pm}) + f_2 \sum_n (n+1)P(n) \tag{9.33}$$

$$= \ f_1 \mathcal{B}(B \rightarrow K^{\pm}) + f_2 \sum_n \left[nP(n) + P(n)\right] \tag{9.34}$$

$$= \ f_1 \mathcal{B}(B \rightarrow K^{\pm}) + f_2 \mathcal{B}(B \rightarrow K^{\pm}) + f_2 \sum_n P(n). \tag{9.35}$$

It is not desired to change the overall number of events, so

$$f_1 + f_2 \;=\; 1 \tag{9.36}$$

and

$$\sum_n P(n) \;=\; 1. \tag{9.37}$$

The fractions f_1 and f_2 can be solved for as follows:

$$f_1 \;=\; 1 - \Delta \tag{9.38}$$

$$f_2 \;=\; \Delta. \tag{9.39}$$

The weight for a particular B meson decay is then

$$w(n) \;=\; \frac{P'(n)}{P(n)} \tag{9.40}$$

and the overall weight for the entire event is the product of the weights associated with each B meson decay in the event.

9.5 Heavy Quarks from Gluon Splitting

Hard gluons can occasionally split into heavy quark pairs, and this contribution must be subtracted. The rates $g_{b\bar{b}}$ and $g_{c\bar{c}}$ are defined thus, with average published result compiled by the LEP/SLD Heavy Flavor Working Group [96]:

$$g_{b\bar{b}} \quad = \quad \frac{\Gamma(Z^0 \rightarrow g \rightarrow b\bar{b})}{\Gamma(Z^0 \rightarrow \text{hadrons})} = 0.00254 \pm 0.00051 \tag{9.41}$$

$$g_{c\bar{c}} \quad = \quad \frac{\Gamma(Z^0 \rightarrow g \rightarrow c\bar{c})}{\Gamma(Z^0 \rightarrow \text{hadrons})} = 0.0296 \pm 0.0038. \tag{9.42}$$

The value for $g_{b\bar{b}}$ in the Monte Carlo generator is calculated by considering the number of non-$b\bar{b}$ events which contain b quarks, plus $b\bar{b}$ events containing more than the orthodox two b quarks, divided by the total number of hadronic events. Similarly, the value for $g_{c\bar{c}}$ is calculated by considering the number of non-$c\bar{c}$ events which contain c quarks, excluding c quarks coming from B meson decays, plus $c\bar{c}$ events containing more than the orthodox two c quarks, divided by the total number of hadronic events. The Monte Carlo generator produces values of

$$g_{b\bar{b}}^{MC} \quad = \quad 0.00145 \tag{9.43}$$

$$g_{c\bar{c}}^{MC} \quad = \quad 0.0141. \tag{9.44}$$

Since the Monte Carlo generator's values for $g_{b\bar{b}}$ and $g_{c\bar{c}}$ do not agree with the latest average values compiled by the LEP/SLD Heavy Flavor Working Group, corrections to R_{bs}, R_b and R_c must be applied.

The Monte Carlo events are first reweighted, using the method detailed in section 9.4, such that $g_{b\bar{b}}$ and $g_{c\bar{c}}$ in the Monte Carlo are increased by 100%, effectively doubling the number of gluon splitting events. R_{bs}, R_b and R_c are then computed on this basis. The corrections are evaluated by scaling the $g_{b\bar{b}} + 100\%$ and $g_{c\bar{c}} + 100\%$ changes in R_{bs}, R_b and R_c as follows:

$$\delta R_{bs}(g_{b\bar{b}}) = \left[R_{bs}(g_{b\bar{b}}^{MC} + 100\%) - R_{bs}(g_{b\bar{b}}^{MC}) \right] \frac{g_{b\bar{b}} - g_{b\bar{b}}^{MC}}{g_{b\bar{b}}^{MC}} \tag{9.45}$$

$$\delta R_{bs}(g_{c\bar{c}}) = \left[R_{bs}(g_{c\bar{c}}^{MC} + 100\%) - R_{bs}(g_{c\bar{c}}^{MC}) \right] \frac{g_{c\bar{c}} - g_{c\bar{c}}^{MC}}{g_{c\bar{c}}^{MC}} \tag{9.46}$$

$$\delta R_b(g_{b\bar{b}}) = \left[R_b(g_{b\bar{b}}^{MC} + 100\%) - R_b(g_{b\bar{b}}^{MC}) \right] \frac{g_{b\bar{b}} - g_{b\bar{b}}^{MC}}{g_{b\bar{b}}^{MC}} \tag{9.47}$$

$$\delta R_b(g_{c\bar{c}}) = \left[R_b(g_{c\bar{c}}^{MC} + 100\%) - R_b(g_{c\bar{c}}^{MC}) \right] \frac{g_{c\bar{c}} - g_{c\bar{c}}^{MC}}{g_{c\bar{c}}^{MC}} \tag{9.48}$$

$$\delta R_c(g_{b\bar{b}}) = \left[R_c(g_{b\bar{b}}^{MC} + 100\%) - R_c(g_{b\bar{b}}^{MC}) \right] \frac{g_{b\bar{b}} - g_{b\bar{b}}^{MC}}{g_{b\bar{b}}^{MC}} \tag{9.49}$$

$$\delta R_c(g_{c\bar{c}}) = \left[R_c(g_{c\bar{c}}^{MC} + 100\%) - R_c(g_{c\bar{c}}^{MC}) \right] \frac{g_{c\bar{c}} - g_{c\bar{c}}^{MC}}{g_{c\bar{c}}^{MC}}. \tag{9.50}$$

The systematic uncertainties are calculated the same way by further scaling the $g_{b\bar{b}} + 100\%$ and $g_{c\bar{c}} + 100\%$ changes in R_{bs}, R_b and R_c to account for the uncertainties in $g_{b\bar{b}}$ and $g_{c\bar{c}}$. The corrections and uncertainties associated with gluon splitting are listed in Table 28.

9.6 Multiplicities in Heavy Flavor Decays

Heavy flavor quarks are identified based on the presence in a jet or hemisphere of charged tracks with significant impact parameter from the primary vertex. In this analysis, the b and c identification efficiencies as well as the rate to mis-tag

TABLE 28. Corrections and systematic uncertainties associated with gluons splitting into heavy flavors.

	1996	1997-98	Combined
$\delta R_{bs}(g \to b\bar{b})$	-0.00025	-0.00022	
$\delta R_{bs}(g \to c\bar{c})$	-0.00024	-0.00039	
$\sigma_{R_{bs}}^{sys}(g \to b\bar{b} \pm 0.00051)$	0.00012	0.00010	0.00011
$\sigma_{R_{bs}}^{sys}(g \to c\bar{c} \pm 0.0038)$	0.00006	0.00010	0.00009
$\delta R_b(g \to b\bar{b})$	-0.00032	-0.00029	
$\delta R_b(g \to c\bar{c})$	-0.00063	-0.00043	
$\sigma_{R_b}^{sys}(g \to b\bar{b} \pm 0.00051)$	0.00015	0.00013	0.00014
$\sigma_{R_b}^{sys}(g \to c\bar{c} \pm 0.0038)$	0.00015	0.00011	0.00011
$\delta R_c(g \to b\bar{b})$	0.00026	0.00027	
$\delta R_c(g \to c\bar{c})$	-0.00073	-0.00172	
$\sigma_{R_c}^{sys}(g \to b\bar{b} \pm 0.00051)$	0.00012	0.00013	0.00013
$\sigma_{R_c}^{sys}(g \to c\bar{c} \pm 0.0038)$	0.00018	0.00042	0.00039

b as c are all measured directly in the data using the fraction of double b and c tagged events and the fraction of bc mixed-tag events, respectively. However, the rate to mis-tag c as b is taken from the Monte Carlo simulation, and it is therefore important to propagate the uncertainties associated with the multiplicities of charged particles in the decays of heavy hadrons. These uncertainties also enter the analysis through the hemisphere correlation coefficients C_{cc} and C_{bb}.

The LEP/SLD Heavy Flavor Working Group has obtained for the mean B-hadron charged multiplicity [96]

$$\langle n_b^{ch} \rangle = 4.955 \pm 0.062. \tag{9.51}$$

This value is adjusted in the Monte Carlo within its uncertainty using the method described in section 9.4.

TABLE 29. Topological rates for the different charm-meson species, with estimated errors and correlation coefficients. The subscripts indicate the number of charged particles produced.

D^0	$f_0 = 0.054$	$f_2 = 0.634$	$f_4 = 0.293$	$f_6 = 0.019$
	$\sigma_0 = 0.011$		$\sigma_4 = 0.023$	$\sigma_6 = 0.009$
	$C_{04} = 0.07$	$C_{46} = -0.46$	$C_{06} = 0$	
$D^\pm$	$f_1 = 0.384$	$f_3 = 0.541$	$f_5 = 0.075$	
	$\sigma_1 = 0.023$		$\sigma_5 = 0.015$	
	$C_{15} = -0.33$			
D_s	$f_1 = 0.37$	$f_3 = 0.42$	$f_5 = 0.21$	
	$\sigma_1 = 0.10$		$\sigma_5 = 0.11$	
	$C_{15} = -0.02$			

The different charmed hadron species are each done separately due to the significant differences in their lifetimes. Varying the individual D-hadron multiplicities is somewhat more complex than for B-hadrons. For each species, D^0, $D^\pm$, and D_s, each channel (i.e. 0, 1, 2... charged particles) is varied within its uncertainty, except for the channel with the highest rate, which is used to compensate the variation [96]. This is again accomplished by reweighting the Monte Carlo events using the method described in section 9.4. The resulting uncertainties are combined using the corresponding correlation coefficients. For each species of D hadron, the fractions decaying into i charged particles f_i, the corresponding uncertainties σ_i, and the associated correlation coefficients C_{ij}, are given in Table 29 [96]. (No uncertainty is listed for the channel with the highest rate as it is used to compensate the other variations.)

The identification efficiencies and mis-tag rates also depend on the number of neutral particles accompanying the charged particles in a given topological decay channel. The uncertainties associated with neutral particle production are

TABLE 30. R_{bs} systematic uncertainties associated with multiplicities in heavy flavor decays.

	1996	1997-98	Combined
$\sigma_{R_{bs}}^{sys}(\langle n_b^{ch}\rangle \pm 0.062)$	0.00013	0.00015	0.00015
$\sigma_{R_{bs}}^{sys}(\langle n_{D^0}^{ch}\rangle)$	0.00003	0.00002	0.00002
$\sigma_{R_{bs}}^{sys}(\langle n_{D^\pm}^{ch}\rangle)$	0.00003	0.00002	0.00002
$\sigma_{R_{bs}}^{sys}(\langle n_{D_s}^{ch}\rangle)$	0.00008	0.00007	0.00007
$\sigma_{R_{bs}}^{sys}(\mathcal{B}(D^\pm \to K^0) \pm 7.0\%)$	0.00006	0.00003	0.00003
$\sigma_{R_{bs}}^{sys}(\mathcal{B}(D^0 \to K^0) \pm 5.0\%)$	0.00007	0.00003	0.00003
$\sigma_{R_{bs}}^{sys}(\mathcal{B}(D_s \to K^0) \pm 28\%)$	< 0.00001	0.00007	0.00006
$\sigma_{R_{bs}}^{sys}(\mathcal{B}(D^\pm \to \pi^0) \pm 10\%)$	0.00002	0.00002	0.00002
$\sigma_{R_{bs}}^{sys}(\mathcal{B}(D^0 \to \pi^0) \pm 10\%)$	0.00007	0.00003	0.00004
$\sigma_{R_{bs}}^{sys}(\mathcal{B}(D_s \to \pi^0) \pm 10\%)$	0.00001	< 0.00001	< 0.00001

TABLE 31. R_b systematic uncertainties associated with multiplicities in heavy flavor decays.

	1996	1997-98	Combined
$\sigma_{R_b}^{sys}(\langle n_b^{ch}\rangle \pm 0.062)$	0.00010	0.00018	0.00017
$\sigma_{R_b}^{sys}(\langle n_{D^0}^{ch}\rangle)$	0.00007	0.00007	0.00007
$\sigma_{R_b}^{sys}(\langle n_{D^\pm}^{ch}\rangle)$	0.00007	0.00007	0.00007
$\sigma_{R_b}^{sys}(\langle n_{D_s}^{ch}\rangle)$	0.00022	0.00023	0.00023
$\sigma_{R_b}^{sys}(\mathcal{B}(D^\pm \to K^0) \pm 7.0\%)$	0.00015	0.00007	0.00008
$\sigma_{R_b}^{sys}(\mathcal{B}(D^0 \to K^0) \pm 5.0\%)$	0.00020	0.00007	0.00008
$\sigma_{R_b}^{sys}(\mathcal{B}(D_s \to K^0) \pm 28\%)$	0.00005	0.00020	0.00018
$\sigma_{R_b}^{sys}(\mathcal{B}(D^\pm \to \pi^0) \pm 10\%)$	0.00005	0.00005	0.00005
$\sigma_{R_b}^{sys}(\mathcal{B}(D^0 \to \pi^0) \pm 10\%)$	0.00015	0.00009	0.00010
$\sigma_{R_b}^{sys}(\mathcal{B}(D_s \to \pi^0) \pm 10\%)$	0.00002	0.00001	0.00001

evaluated by varying the K^0 and π^0 production rates in charmed hadron decays: $\mathcal{B}(D^\pm \to K^0)$, $\mathcal{B}(D^0 \to K^0)$, and $\mathcal{B}(D_s \to K^0)$ are varied within their uncertainties as listed in the Review of Particle Physics; the branching ratios $\mathcal{B}(D^\pm \to \pi^0)$, $\mathcal{B}(D^0 \to \pi^0)$, $\mathcal{B}(D_s \to \pi^0)$ are varied by a conservative $\pm 10\%$. The uncertainties associated with multiplicities in heavy flavor decays are listed in tables 30, 31, and 32.

TABLE 32. R_c systematic uncertainties associated with multiplicities in heavy flavor decays.

	1996	1997-98	Combined
$\sigma_{R_c}^{sys}(\langle n_b^{ch}\rangle \pm 0.062)$	0.00001	0.00001	0.00001
$\sigma_{R_c}^{sys}(\langle n_{D^0}^{ch}\rangle)$	0.00081	0.00013	0.00023
$\sigma_{R_c}^{sys}(\langle n_{D^\pm}^{ch}\rangle)$	0.00013	0.00015	0.00015
$\sigma_{R_c}^{sys}(\langle n_{D_s}^{ch}\rangle)$	0.00337	0.00074	0.00111
$\sigma_{R_c}^{sys}(\mathcal{B}(D^\pm \to K^0) \pm 7.0\%)$	0.00071	0.00001	0.00011
$\sigma_{R_c}^{sys}(\mathcal{B}(D^0 \to K^0) \pm 5.0\%)$	0.00080	0.00036	0.00042
$\sigma_{R_c}^{sys}(\mathcal{B}(D_s \to K^0) \pm 28\%)$	0.00268	0.00183	0.00195
$\sigma_{R_c}^{sys}(\mathcal{B}(D^\pm \to \pi^0) \pm 10\%)$	0.00037	0.00005	0.00009
$\sigma_{R_c}^{sys}(\mathcal{B}(D^0 \to \pi^0) \pm 10\%)$	0.00086	0.00023	0.00032
$\sigma_{R_c}^{sys}(\mathcal{B}(D_s \to \pi^0) \pm 10\%)$	0.00064	0.00009	0.00017

9.7 Heavy Flavor Lifetimes

The lifetimes of heavy hadrons are relevant to this analysis because the further from the primary vertex the heavy hadron is when it decays, the easier the secondary vertex is to resolve, which in turn affects the identification efficiency. For R_b, the lifetimes of charm hadrons affect the degree of charm contamination whereas bottom lifetimes only enter through the hemisphere correlations because the b identification efficiency is measured in the data with the double b-tagged events. For R_c, the charm and bottom lifetimes enter only through the hemisphere correlations because both the c identification efficiency and the rate to mis-tag b as c are measured in the data.

The LEP/SLD Heavy Flavor Working Group takes the average lifetime of b hadrons to be [96]

$$\tau_b = 1.576 \pm 0.016 \text{ ps.} \tag{9.52}$$

The lifetime difference between the various b species has been found in general to have very little impact and is considered as a source of uncertainty in the R_b analyses by enlarging the error to 0.05 ps.

The lifetimes of the various charm hadron species are considered as individual sources of uncertainties. The values and errors are [96]

$$\tau_{D^0} = 0.415 \pm 0.004 \text{ ps} \tag{9.53}$$

$$\tau_{D^\pm} = 1.057 \pm 0.015 \text{ ps} \tag{9.54}$$

$$\tau_{D_s} = 0.467 \pm 0.017 \text{ ps} \tag{9.55}$$

$$\tau_{\Lambda_c} = 0.206 \pm 0.012 \text{ ps}. \tag{9.56}$$

The Monte Carlo events are reweighted in order to adjust the average lifetimes of the various heavy flavor hadrons by their corresponding uncertainties. Recall that the number $N(t)$ of particles having lifetime τ remaining after time t is

$$N(t) = N_0 e^{-\frac{t}{\tau}}. \tag{9.57}$$

The weight that a particular hadron having lifetime t should be given to make the average lifetime change by an amount $\delta\tau$ (i.e. lifetime $\tau \to \tau + \delta\tau$) can be calculated as

$$dN(t) = \frac{N_0}{\tau} e^{-\frac{t}{\tau}} dt \tag{9.58}$$

$$dN'(t) = \frac{N_0}{\tau + \delta\tau} e^{-\frac{t}{\tau+\delta\tau}} dt \tag{9.59}$$

TABLE 33. Systematic uncertainties associated with the lifetimes of heavy hadrons.

	1996	1997-98	Combined
$\sigma_{R_{bs}}^{sys}(\tau_b \pm 0.05 \text{ ps})$	0.00022	0.00016	0.00017
$\sigma_{R_{bs}}^{sys}(\tau_{D^0} \pm 0.004 \text{ ps})$	0.00001	0.00001	0.00001
$\sigma_{R_{bs}}^{sys}(\tau_{D^\pm} \pm 0.015 \text{ ps})$	0.00001	0.00001	0.00001
$\sigma_{R_{bs}}^{sys}(\tau_{D_s} \pm 0.017 \text{ ps})$	0.00001	0.00001	0.00001
$\sigma_{R_{bs}}^{sys}(\tau_{\Lambda_c} \pm 0.012 \text{ ps})$	< 0.00001	< 0.00001	< 0.00001
$\sigma_{R_b}^{sys}(\tau_b \pm 0.05 \text{ ps})$	0.00028	0.00020	0.00021
$\sigma_{R_b}^{sys}(\tau_{D^0} \pm 0.004 \text{ ps})$	0.00003	0.00002	0.00002
$\sigma_{R_b}^{sys}(\tau_{D^\pm} \pm 0.015 \text{ ps})$	0.00003	0.00002	0.00002
$\sigma_{R_b}^{sys}(\tau_{D_s} \pm 0.017 \text{ ps})$	0.00002	0.00003	0.00003
$\sigma_{R_b}^{sys}(\tau_{\Lambda_c} \pm 0.012 \text{ ps})$	< 0.00001	< 0.00001	< 0.00001
$\sigma_{R_c}^{sys}(\tau_b \pm 0.05 \text{ ps})$	0.00002	0.00001	0.00001
$\sigma_{R_c}^{sys}(\tau_{D^0} \pm 0.004 \text{ ps})$	0.00011	0.00004	0.00005
$\sigma_{R_c}^{sys}(\tau_{D^\pm} \pm 0.015 \text{ ps})$	0.00014	0.00002	0.00003
$\sigma_{R_c}^{sys}(\tau_{D_s} \pm 0.017 \text{ ps})$	0.00019	0.00004	0.00006
$\sigma_{R_c}^{sys}(\tau_{\Lambda_c} \pm 0.012 \text{ ps})$	0.00006	0.00003	0.00003

$$w(t) \;=\; \frac{dN'(t)}{dN(t)} \tag{9.60}$$

$$=\; \frac{\tau e^{-\frac{t}{\tau+\delta\tau}}}{(\tau+\delta\tau)e^{-\frac{t}{\tau}}}. \tag{9.61}$$

The systematic uncertainties associated with the lifetimes of heavy hadrons are given in Table 33

9.8 Charm Hadron Production

Because of the differences in the lifetimes between the various species of charmed hadrons, their individual identification efficiencies and mis-tag rates tend to be substantially different, and therefore their relative abundances in $Z^0 \to c\bar{c}$

TABLE 34. Charm hadron production fractions.

Species	Value	Uncertainty
f_{D^0}	0.600	
$f_{D^\pm}$	0.233	± 0.028
f_{D_s}	0.102	± 0.037
f_{Λ_c}	0.065	± 0.029

events affects the overall charm identification efficiency and the various mis-tag rates.

In order to estimate the systematic uncertainty, the D^0 fraction is written as $f_{D^0} = 1 - f_{D^\pm} - f_{D_s} - f_{\Lambda_c}$. The errors on the last three parameters and their correlation matrix are used to evaluate the uncertainty. The values of f_{D^0}, $f_{D^\pm}$, f_{D_s}, and f_{Λ_c} along with their uncertainties are listed in Table 34 [97]. When varying the charm production fractions in the Monte Carlo, the variation of each of the three fractions $f_{D^\pm}$, f_{D_s}, and f_{Λ_c} is always compensated by the fraction f_{D^0}, so no uncertainty is listed for f_{D^0}.

The correlation matrix used to combine the uncertainties for each charm species is [97]

$$
C \;=\; \begin{pmatrix} C_{D^\pm,D^\pm} & C_{D^\pm,D_s} & C_{D^\pm,\Lambda_c} \\ C_{D_s,D^\pm} & C_{D_s,D_s} & C_{D_s,\Lambda_c} \\ C_{\Lambda_c,D^\pm} & C_{\Lambda_c,D_s} & C_{\Lambda_c,\Lambda_c} \end{pmatrix} = \begin{pmatrix} 1 & -0.36 & -0.24 \\ -0.36 & 1 & -0.14 \\ -0.24 & -0.14 & 1 \end{pmatrix}. \tag{9.62}
$$

The systematic uncertainties associated with production rates for different charm species are listed in Table 35.

TABLE 35. Systematic uncertainties associated with production rates for different charm species.

	1996	1997-98	Combined
$\sigma_{R_{bs}}^{sys}$(Charm Hadron Production)	0.00007	0.00008	0.00008
$\sigma_{R_b}^{sys}$(Charm Hadron Production)	0.00017	0.00018	0.00018
$\sigma_{R_c}^{sys}$(Charm Hadron Production)	0.00064	0.00048	0.00050

9.9 Hemisphere Correlations

In this analysis, the fractions of double b- and c-tagged events are used to determine the bottom and charm quark identification efficiencies, respectively. The efficiency to double-tag an event is taken to be the square of the hemisphere tag efficiency times a correlation coefficient. The bottom and charm hemisphere correlation coefficients are defined as

$$C_{bb} = \frac{\epsilon_{bb}}{\epsilon_b^2} \tag{9.63}$$

$$C_{cc} = \frac{\epsilon_{cc}}{\epsilon_c^2} \tag{9.64}$$

where ϵ_{qq} is the efficiency to identify a quark in both hemispheres of a $q\bar{q}$ event. These correlation coefficients must be estimated from the Monte Carlo simulation.

To evaluate the systematic uncertainty on this quantity, we consider three effects which can give rise to correlations: (1) detector inhomogeneities, (2) the common primary vertex, and (3) kinematic correlations from final state gluon radiation.

In general, correlations arise when the identification efficiency ϵ_q depends on some variable x which is correlated between the two hemispheres of the event. The

resulting hemisphere correlation can be estimated as

$$C_{qq}^x = \frac{\langle \epsilon_q(x_1)\epsilon_q(x_2)\rangle}{\langle \epsilon_q(x_1)\rangle\langle \epsilon_q(x_2)\rangle} \tag{9.65}$$

where $x_{1,2}$ are the values of x in the two hemispheres of the event and the average is taken over all the $q\bar{q}$ events in the Monte Carlo data sample. The efficiencies are evaluated in small bins of x.

The two heavy quarks tend to be produced back to back, and as a result, their decay products tend to go into geometrically opposite regions of the detector. The thrust axis is taken as an estimator of the heavy quark direction of flight. The cylindrical geometry of the detector causes the identification efficiency for heavy quarks to be directionally nonuniform and to depend on the polar angle θ. As $cos\,\theta$ of the thrust axis approaches 1 or -1, decay products must travel through more intervening material, and multiple scattering degrades the tracking resolution and thus the identification efficiency. The correlation due to detector inhomogeneities is evaluated as

$$C_{qq}^{cos\,\theta} = \frac{\langle \epsilon_q^{\text{Hem 1}}(cos\,\theta)\epsilon_q^{\text{Hem 2}}(cos\,\theta)\rangle}{\langle \epsilon_q^{\text{Hem 1}}(cos\,\theta)\rangle\langle \epsilon_q^{\text{Hem 2}}(cos\,\theta)\rangle}. \tag{9.66}$$

The identification of heavy flavors is dependent on knowledge of the location of the primary vertex. The further a secondary vertex is from the primary vertex, the easier it is to resolve. Also, the vertex decay vector is determined from the locations of both the primary vertex and the secondary decay vertex, and is important for calculating the p_T corrected vertex mass. Because information regarding the primary vertex is common to both hemispheres in an event, it is important to

consider this as a source of correlation. The correlation due to imprecise knowledge of the primary vertex is evaluated by simply taking the difference between the correlation determined using the ordinary primary vertex, and the correlation determined using the true Monte Carlo location of the primary vertex.

Heavy flavor identification efficiencies depend on the momenta of the associated heavy hadrons: High momentum particles tend to travel further before decaying, making the secondary vertex easier to resolve from the primary vertex; and the tracks associated with the heavy flavor decays are of higher momentum, and can thus be measured with better resolution. Final state gluon radiation reduces the momentum of both heavy quarks in the event. Because of conservation of momentum, the momentum of the heavy hadron in one hemisphere is to a degree correlated with the momentum of the heavy hadron in the opposite hemisphere. As a result, the heavy flavor identification efficiencies are to a degree correlated between the two hemispheres. This kinematic correlation is evaluated by

$$C_{qq}^{p_1,p_2} = \frac{\langle \epsilon_q(p_1)\epsilon_q(p_2) \rangle}{\langle \epsilon_q(p_1) \rangle \langle \epsilon_q(p_2) \rangle}. \tag{9.67}$$

All of the component correlations are given in Table 36.

The uncertainties associated with the hemisphere correlations are evaluated by letting the each correlation coefficient assume the value of its component sum and running the analysis. The uncertainties were then taken as half the difference of the measurements using the component sum and using the overall direct Monte Carlo correlation coefficient. These uncertainties are given in Table 37.

TABLE 36. Component Correlations, the component sum, and the overall direct Monte Carlo correlation coefficient values.

	1996	1997-98
$C_{bb}^{\cos\theta} - 1$	-0.0002	0.0005
$C_{bb}^{\mathrm{IP}} - 1$	0.0026	0.0008
$C_{bb}^{p_1,p_2} - 1$	0.0009	0.0019
$1 + (C_{bb}^{\mathrm{IP}} - 1) + (C_{bb}^{p_1,p_2} - 1) + (C_{bb}^{\cos\theta} - 1)$	1.0033	1.0032
Monte Carlo C_{bb}	0.9997	1.0028
$C_{cc}^{\cos\theta} - 1$	0.0040	0.0020
$C_{cc}^{\mathrm{IP}} - 1$	-0.0391	-0.0074
$C_{cc}^{p_1,p_2} - 1$	0.0432	0.0093
$1 + (C_{cc}^{\mathrm{IP}} - 1) + (C_{cc}^{p_1,p_2} - 1) + (C_{cc}^{\cos\theta} - 1)$	1.0080	1.0039
Monte Carlo C_{cc}	1.0637	1.0129

TABLE 37. Systematic uncertainties associated with hemisphere correlations.

	1996	1997-98	Combined
$\sigma_{R_{bs}}^{sys}$ (b Hemisphere Correlation)	0.00001	< 0.00001	< 0.00001
$\sigma_{R_{bs}}^{sys}$ (c Hemisphere Correlation)	0.00006	0.00001	0.00001
$\sigma_{R_b}^{sys}$ (b Hemisphere Correlation)	0.00038	0.00005	0.00009
$\sigma_{R_b}^{sys}$ (c Hemisphere Correlation)	0.00013	0.00002	0.00004
$\sigma_{R_c}^{sys}$ (b Hemisphere Correlation)	0.00012	0.00001	0.00003
$\sigma_{R_c}^{sys}$ (c Hemisphere Correlation)	0.00496	0.00079	0.00139

9.10 $\gamma - Z^0$ Interference

R_b and R_c actually measure the ratio of production cross sections $R_q = \sigma_{q\bar{q}}/\sigma_{\text{Hadronic}}$. To obtain the ratios of partial widths $R_q^0 = \Gamma_{q\bar{q}}/\Gamma_{\text{Hadronic}}$, small corrections for photon exchange and $\gamma - Z^0$-interference have to be applied. These corrections are typically $+0.0002$ for R_b and -0.0002 for R_c [96].

9.11 Strange Quark Final States

Events with final states containing strange particles are an important background for $Z^0 \rightarrow bs$ events, particularly $b\bar{b}$ events containing a final state $K^{\pm}$, K_S^0, or Λ particle. If such a final state strange particle in a $b\bar{b}$ event has sufficient momentum to be identified, and if it happens to reside in the same hemisphere as a B meson that failed to be identified, the event will have the same signature as a true $Z^0 \rightarrow bs$ event. There are two important sources of these particles; B mesons can decay to them, or they can be produced in the fragmentation process.

In order to estimate systematic uncertainties, the branching ratios $\mathcal{B}(B \rightarrow K^{\pm})$, $\mathcal{B}(B \rightarrow \Lambda)$, and $\mathcal{B}(B \rightarrow K_S^0)$ and the average multiplicities in Z^0 decays $\langle N_{K^{\pm}} \rangle$, $\langle N_{\Lambda} \rangle$, and $\langle N_{K_S^0} \rangle$ are varied within their uncertainties using the method detailed in section 9.4.

The uncertainties associated with final state $K^{\pm}$, K_S^0, and Λ particles are listed in Table 38.

TABLE 38. Systematic uncertainties associated with final state $K^{\pm}$, K^0_S, and Λ particles.

	1996	1997-98	Combined
$\sigma^{sys}_{R_{bs}}(\mathcal{B}(B \to K^{\pm}) \pm 6.0\%)$	0.00014	0.00009	0.00010
$\sigma^{sys}_{R_{bs}}(\mathcal{B}(B \to \Lambda) \pm 0.6\%)$	0.00002	0.00001	0.00002
$\sigma^{sys}_{R_{bs}}(\mathcal{B}(B \to K^0_S) \pm 2.9\%)$	0.00017	0.00004	0.00006
$\sigma^{sys}_{R_{bs}}(\langle N_{K^{\pm}} \rangle \pm 5.0\%)$	0.00006	0.00009	0.00008
$\sigma^{sys}_{R_{bs}}(\langle N_{\Lambda} \rangle \pm 0.9\%)$	0.00005	0.00002	0.00002
$\sigma^{sys}_{R_{bs}}(\langle N_{K^0_S} \rangle \pm 2.5\%)$	0.00002	0.00003	0.00003
$\sigma^{sys}_{R_b}(\mathcal{B}(B \to K^{\pm}) \pm 6.0\%)$	0.00009	0.00010	0.00010
$\sigma^{sys}_{R_b}(\mathcal{B}(B \to \Lambda) \pm 0.6\%)$	0.00005	0.00020	0.00017
$\sigma^{sys}_{R_b}(\mathcal{B}(B \to K^0_S) \pm 2.9\%)$	0.00005	0.00035	0.00031
$\sigma^{sys}_{R_b}(\langle N_{K^{\pm}} \rangle \pm 5.0\%)$	0.00013	0.00002	0.00004
$\sigma^{sys}_{R_b}(\langle N_{\Lambda} \rangle \pm 0.9\%)$	0.00005	0.00008	0.00008
$\sigma^{sys}_{R_b}(\langle N_{K^0_S} \rangle \pm 2.5\%)$	0.00005	0.00009	0.00008
$\sigma^{sys}_{R_c}(\mathcal{B}(B \to K^{\pm}) \pm 6.0\%)$	0.00008	0.00003	0.00003
$\sigma^{sys}_{R_c}(\mathcal{B}(B \to \Lambda) \pm 0.6\%)$	0.00001	0.00005	0.00004
$\sigma^{sys}_{R_c}(\mathcal{B}(B \to K^0_S) \pm 2.9\%)$	0.00003	0.00010	0.00009
$\sigma^{sys}_{R_c}(\langle N_{K^{\pm}} \rangle \pm 5.0\%)$	0.00016	0.00009	0.00010
$\sigma^{sys}_{R_c}(\langle N_{\Lambda} \rangle \pm 0.9\%)$	0.00014	0.00008	0.00009
$\sigma^{sys}_{R_c}(\langle N_{K^0_S} \rangle \pm 2.5\%)$	0.00051	0.00010	0.00016

9.12 Uncertainties associated with R_d and R_s

The values for R_d and R_s used in this analysis are taken to be

$$R_d = R_s \;=\; \frac{\Gamma^{SM}_{d\bar{d}}}{\Gamma^{SM}_{b\bar{b}}} R_b \tag{9.68}$$

where

$$\Gamma^{SM}_{d\bar{d}} \;=\; 383.1 \pm 0.2 \text{ MeV} \tag{9.69}$$

$$\Gamma^{SM}_{b\bar{b}} \;=\; 375.9 \pm 0,1 \text{ MeV}. \tag{9.70}$$

$\Gamma^{SM}_{d\bar{d}}$ and $\Gamma^{SM}_{b\bar{b}}$ are each varied within their uncertainties as follows

$$R_d^+ = R_s^+ \;=\; \frac{\Gamma^{SM}_{d\bar{d}} + \sigma_{\Gamma^{SM}_{d\bar{d}}}}{\Gamma^{SM}_{b\bar{b}} - \sigma_{\Gamma^{SM}_{b\bar{b}}}} R_b = \frac{383.3}{375.8} R_b \tag{9.71}$$

$$R_d^- = R_s^- \;=\; \frac{\Gamma^{SM}_{d\bar{d}} - \sigma_{\Gamma^{SM}_{d\bar{d}}}}{\Gamma^{SM}_{b\bar{b}} + \sigma_{\Gamma^{SM}_{b\bar{b}}}} R_b = \frac{382.9}{376.0} R_b. \tag{9.72}$$

The uncertainties on the measurements are then evaluated by taking

$$\sigma^{sys}_{R_{bs}}(R_d) \;=\; \frac{|R_{bs}(R_d^+) - R_{bs}(R_d^-)|}{2} \tag{9.73}$$

$$\sigma^{sys}_{R_{bs}}(R_s) \;=\; \frac{|R_{bs}(R_s^+) - R_{bs}(R_s^-)|}{2} \tag{9.74}$$

$$\sigma^{sys}_{R_b}(R_d) \;=\; \frac{|R_b(R_d^+) - R_b(R_d^-)|}{2} \tag{9.75}$$

$$\sigma^{sys}_{R_b}(R_s) \;=\; \frac{|R_b(R_s^+) - R_b(R_s^-)|}{2} \tag{9.76}$$

$$\sigma^{sys}_{R_c}(R_d) \;=\; \frac{|R_c(R_d^+) - R_c(R_d^-)|}{2} \tag{9.77}$$

$$\sigma^{sys}_{R_c}(R_s) \;=\; \frac{|R_c(R_s^+) - R_c(R_s^-)|}{2}. \tag{9.78}$$

TABLE 39. Uncertainties associated with R_d and R_s.

	1996	1997-98	Combined
$\sigma^{sys}_{R_{bs}}(R_d)$	< 0.00001	< 0.00001	< 0.00001
$\sigma^{sys}_{R_{bs}}(R_s)$	< 0.00001	< 0.00001	< 0.00001
$\sigma^{sys}_{R_b}(R_d)$	< 0.00001	< 0.00001	< 0.00001
$\sigma^{sys}_{R_b}(R_s)$	< 0.00001	< 0.00001	< 0.00001
$\sigma^{sys}_{R_c}(R_d)$	< 0.00001	< 0.00001	< 0.00001
$\sigma^{sys}_{R_c}(R_s)$	< 0.00001	< 0.00001	< 0.00001

The uncertainties associated with R_d and R_s are given in Table 39.

9.13 Event Selection Bias and the Running b-mass Effect

The hadronic event selection scheme was designed to accept all flavors of hadronic Z^0 decays equally. In practice however, $b\bar{b}$ events and to a lesser degree $c\bar{c}$ events are slightly favored over the other flavors. To avoid contamination from leptonic events, we must live with this bias. As such, corrections to R_b and R_c are estimated by subtracting the values for R_b and R_c calculated from the events in the Monte Carlo generator from the values obtained after the hadronic event selection scheme and the < 4-jet cut:

$$\delta R_b(\text{Event Selection Bias}) = R_b^{\text{Generator}} - R_b^{\text{H.E.S., <4 Jets}} \tag{9.79}$$

$$\delta R_c(\text{Event Selection Bias}) = R_c^{\text{Generator}} - R_c^{\text{H.E.S., <4 Jets}} \tag{9.80}$$

where $R_q^{\text{Generator}}$ is the value of R_q at the generator level and $R_q^{\text{H.E.S., <4 Jets}}$ is the value of R_q after the the hadronic event selection scheme and the < 4-jet cut. The uncertainties associated with the two event selection biases are simply the

statistical uncertainties from bionomial statistics on $R_q^{\text{Generator}}$ and $R_q^{\text{H.E.S., } <4 \text{ Jets}}$ added in quadrature. See Table 42.

A large fraction of the overall event selection bias is due to the requirement that considered events have less than four jets, and this part is defined as

$$\delta R_b(< 4 \text{ Jet Cut}) \;\; = \;\; R_b^{\text{H.E.S.}} - R_b^{\text{H.E.S., } <4 \text{ Jets}}. \tag{9.81}$$

It turns out that the four jet rate for $b\bar{b}$ events is affected by the b quark mass, which has been measured by SLD [99] among others at $m_b(M_Z) \approx 3 \pm 1$ GeV.

The jet algorithms JADE, E0, Durham, and Geneva are iterative clustering algorithms which begin with a set of final-state particles (partons in QCD calculations, charged tracks at the detector level) and cluster the pair of particles (i, j) with the smallest value of a dimensionless measure y_{ij} into a single "protojet." The procedure is repeated until all the y_{ij} exceed the value of the jet resolution parameter y_{cut}, at which point the protojets are declared to be jets. The algorithms differ in the measure y_{ij} used and/or in the rule for recombining two clustered momenta.

Several studies were done where the mass of the b quark was varied in the Monte Carlo generator JETSET, and the four jet rate for $b\bar{b}$ events was calculated. These results were then compared with LO calculations of the four jet rate for $b\bar{b}$ events as a function of b quark mass m_b done by Arnd Brandenburg [100]. The leading order calculation is known to differ from both the data and the next-to-leading-order calculation by as much as 100%. The comparison is none-the-less valid as it is the relative change in the four-jet rate as a function of m_b – i.e. the

TABLE 40. 4-Jet rate for $b\bar{b}$ events, $y_{\text{cut}} = 0.02$.

Source	Jet Algorithm	m_b	f_4^b	$\frac{f_4^b(0) - f_4^b(m_b)}{f_4^b(0)}$
LO calculation	E0 Parton	0	4.27%	0
LO calculation	E0 Parton	3 GeV	4.03%	5.6%
LO calculation	E0 Parton	5 GeV	3.65%	14.5%
JETSET	JADE Parton	0	$8.882 \pm 0.028\%$	0
JETSET	JADE Parton	3 GeV	$8.492 \pm 0.028\%$	4.4%
JETSET	JADE Parton	5 GeV	$7.415 \pm 0.026\%$	16.5%
JETSET	JADE Track	0	$7.711 \pm 0.027\%$	0
JETSET	JADE Track	3 GeV	$7.441 \pm 0.026\%$	3.5%
JETSET	JADE Track	5 GeV	$7.369 \pm 0.026\%$	4.4%

TABLE 41. 4-Jet rate for $b\bar{b}$ events with $m_b = 0$ compared to uds events, $y_{\text{cut}} = 0.02$.

Source	Jet Algorithm	f_4^{uds}	f_4^b	$\frac{f_4^{uds} - f_4^b(0)}{f_4^b(0)}$
JETSET	JADE Parton	$8.110 \pm 0.035\%$	$7.711 \pm 0.027\%$	5.18%

last column in Table 40 – that we are interested in rather than the absolute value of the four-jet rate.

Judging from the last column of Table 40, it appears that at the parton level the dependence of the four jet rate for $b\bar{b}$ events on b quark mass m_b in JETSET is approximately correct and suggests that JETSET is mimicking the effect of the b mass in the leading order calculation rather nicely. The effect is diluted somewhat at the track level.

There is a B hadron phase space effect even when $m_b = 0$ which causes the four jet rate $f_4^b(m_b = 0)$ and f_4^{uds} to be different. To compute a correction, we wish only to scale that part of the < 4 jet event selection bias, $\delta R_b(< 4 \text{ Jet Cut})$, which is due to the b-mass effect.

The correction can be estimated by scaling the change in R_b from the < 4 jet cut:

$$\delta R_b(b\text{-mass effect}) = \delta R_b(< 4 \text{ Jet Cut}) \times \text{Scale Factor} \tag{9.82}$$

$$\text{Scale Factor} = \frac{b \text{ Phase Space Effect} + \text{Corrected } b\text{-mass Effect}}{b \text{ Phase Space Effect} + b\text{-mass Effect}} \tag{9.83}$$

where

$$b \text{ Phase Space Effect} = \frac{f_4^{uds} - f_4^b(0)}{f_4^b(0)} = 5.18\% \tag{9.84}$$

$$b\text{-mass Effect} = \frac{f_4^b(0) - f_4^b(5 \text{ GeV})}{f_4^b(0)} = 4.4\%. \tag{9.85}$$

The corrected b-mass effect is calcuated in two different ways. The first is to scale the b-mass effect by the four-jet rate difference assuming $m_b = 3$ GeV from the LO calculation,

$$\text{Corrected } b\text{-mass Effect} = b\text{-mass Effect} \left[\frac{\left(\frac{f_4^b(0) - f_4^b(3 \text{ GeV})}{f_4^b(0)} \right)}{\left(\frac{f_4^b(0) - f_4^b(5 \text{ GeV})}{f_4^b(0)} \right)} \right]_{\text{LO Calculation}} \tag{9.86}$$

$$= 4.4\% \left[\frac{5.6\%}{14.5\%} \right] = 1.7\% \tag{9.87}$$

or directly using the Monte Carlo track level four-jet rate

$$\text{Corrected } b\text{-mass Effect} = \left[\frac{f_4^b(0) - f_4^b(3 \text{ GeV})}{f_4^b(0)} \right] = 3.5\%. \tag{9.88}$$

TABLE 42. Corrections and systematic uncertainties associated with the event selection bias and the running b-mass effect.

	1996	1997-98	Combined
δR_b(Event Selection Bias)	-0.00151	-0.00188	
δR_b(Running b-mass)	0.00035	0.00024	
$\sigma_{R_b}^{sys}$(Event Selection Bias)	0.00136	0.00056	0.00067
$\sigma_{R_b}^{sys}$(Running b-quark mass)	0.00034	0.00024	0.00025
δR_c(Event Selection Bias)	0.00042	0.00001	
$\sigma_{R_c}^{sys}$(Event Selection Bias)	0.00123	0.00051	0.00061

The correction is taken as the average of the two, and the uncertainty as half the difference:

$$\text{Scale Factor} = \frac{b \text{ Phase Space Effect} + \overline{\text{Corrected } b\text{-mass Effect}}}{b \text{ Phase Space Effect} + b\text{-mass Effect}} \tag{9.89}$$

$$= \frac{5.18\% + (2.6\% \pm 0.9\%)}{5.18 + 4.4\%} = 81\% \pm 9\%. \tag{9.90}$$

9.14 Corrections to the Monte Carlo Simulation

The corrections to the tracking efficiency and track resolution were discussed in their respective sections in Chapter V. The analysis was run with and without these corrections applied, and the uncertainty was taken as half the difference.

$$\sigma_{R_{bs}}^{sys}(\text{Tracking Efficiency Correction}) = \frac{|R_{bs} - R_{bs}(\text{Correction off})|}{2} \tag{9.91}$$

$$\sigma_{R_b}^{sys}(\text{Tracking Efficiency Correction}) = \frac{|R_b - R_b(\text{Correction off})|}{2} \tag{9.92}$$

$$\sigma_{R_c}^{sys}(\text{Tracking Efficiency Correction}) = \frac{|R_c - R_c(\text{Correction off})|}{2}. \tag{9.93}$$

$$\sigma_{R_{bs}}^{sys}(\text{Track Resolution Correction}) = \frac{|R_{bs} - R_{bs}(\text{Correction off})|}{2} \quad (9.94)$$

$$\sigma_{R_b}^{sys}(\text{Track Resolution Correction}) = \frac{|R_b - R_b(\text{Correction off})|}{2} \quad (9.95)$$

$$\sigma_{R_c}^{sys}(\text{Track Resolution Correction}) = \frac{|R_c - R_c(\text{Correction off})|}{2}. \quad (9.96)$$

Because no track efficiency correction is made to the 1996 Monte Carlo, the systematic uncertainty is taken as zero.

The Monte Carlo distributions of the input parameters for the three strange neural networks, the sNN, did not match the data exactly, and so the Monte Carlo distributions were reweighted in order to match the data. The systematic uncertainties were evaluated by running the analysis without reweighting the Monte Carlo sNN input distributions, and were taken as half the difference of the measurements with and without the sNN input reweighting. Table 43 shows these uncertainties.

$$\sigma_{R_{bs}}^{sys}(s\text{NN Input Reweighting}) = \frac{|R_{bs} - R_{bs}(\text{Reweighting off})|}{2} \quad (9.97)$$

$$\sigma_{R_b}^{sys}(s\text{NN Input Reweighting}) = \frac{|R_b - R_b(\text{Reweighting off})|}{2} \quad (9.98)$$

$$\sigma_{R_c}^{sys}(s\text{NN Input Reweighting}) = \frac{|R_c - R_c(\text{Reweighting off})|}{2}. \quad (9.99)$$

TABLE 43. Systematic uncertainties associated with tracking efficiency and track resolution.

	1996	1997-98	Combined
$\sigma_{R_{bs}}^{sys}$(Tracking Efficiency Correction)	0	0.00021	0.00018
$\sigma_{R_{bs}}^{sys}$(Track Resolution Correction)	0.00039	0.00003	0.00008
$\sigma_{R_{bs}}^{sys}$(sNN Input Reweighting)	0.00003	0.00002	0.00002
$\sigma_{R_{b}}^{sys}$(Tracking Efficiency Correction)	0	0.00041	0.00035
$\sigma_{R_{b}}^{sys}$(Track Resolution Correction)	0.00094	0.00003	0.00016
$\sigma_{R_{b}}^{sys}$(sNN Input Reweighting)	0.00004	0.00002	0.00003
$\sigma_{R_{c}}^{sys}$(Tracking Efficiency Correction	0	0.00014	0.00012
$\sigma_{R_{c}}^{sys}$(Track Resolution Correction	0.00119	0.00033	0.00045
$\sigma_{R_{c}}^{sys}$(sNN Input Reweighting)	0.00046	0.00002	0.00008

9.15 Uncertainties associated with the IP

For purposes of assigning a systematic uncertainty, the event Y_T is evaluated. There is evidence of a non-Gaussian tail in the 1996 data (Figure 47, lower left). As has been done in the past, this tail is represented by a second Gaussian IP spread with a $\sigma = 100$ μm for 0.5% of the events. The systematic uncertainty is estimated by smearing the entire Monte Carlo sample to a Gaussian with $\sigma = 100$ μm, and then recombining this smeared sample, using a weight of 0.5% with the unsmeared sample, using an event weight of 99.5%. The uncertainty is taken as half the difference:

$$\sigma_{R_{bs}}^{sys}(\langle \text{IP} \rangle \text{ Tail}) = \frac{|R_{bs} - R_{bs}(0.5\%, 100\mu\text{m IP smear})|}{2} \tag{9.100}$$

$$\sigma_{R_{b}}^{sys}(\langle \text{IP} \rangle \text{ Tail}) = \frac{|R_{b} - R_{b}(0.5\%, 100\mu\text{m IP smear})|}{2} \tag{9.101}$$

$$\sigma_{R_{c}}^{sys}(\langle \text{IP} \rangle \text{ Tail}) = \frac{|R_{c} - R_{c}(0.5\%, 100\mu\text{m IP smear})|}{2}. \tag{9.102}$$

TABLE 44. Systematic uncertainties associated with $\langle IP \rangle$ tail.

	1996	1997-98	Combined
$\sigma_{R_{bs}}^{sys}(\langle IP \rangle \text{ Tail})$	0.00003	0	< 0.00001
$\sigma_{R_b}^{sys}(\langle IP \rangle \text{ Tail})$	0.00022	0	0.00003
$\sigma_{R_c}^{sys}(\langle IP \rangle \text{Tail})$	0.00026	0	0.00004

As this is considered a conservative estimate, no correction is made to the Monte Carlo.

The 1997-98 data on the other hand shows virtually no evidence of a non-Gaussian tail (Figure 47, upper left). Therefore, no systematic uncertainty is taken for the 1997-98 data. These uncertainties are given in Table 44.

CHAPTER X

CONCLUSIONS

The defining characteristic of the scientific method is the principle that observation is the sole arbiter of whether something is so or not. Richard Feynman says that "if there is an exception to any rule, and if it can be proved by observation, that rule is wrong" [101]. The rules which collectively constitute the Standard Model make precise predictions for numerous Z^0 pole observables, and this analysis has precisely tested three of those predictions. The relevant Standard Model predictions may be summarized as follows

$$R_{bs}^{SM} = 5.8 \times 10^{-8} \tag{10.1}$$

$$R_{b}^{SM} = 0.21569 \pm 0.00016 \tag{10.2}$$

$$R_{c}^{SM} = 0.17230 \pm 0.00007. \tag{10.3}$$

The results presented in this analysis, summarized for comparison, are as follows:

$$R_{bs} = -0.00017 \pm 0.00087 \pm 0.00048 \tag{10.4}$$

$$R_{b} = 0.21645 \pm 0.00131 \pm 0.00111 \tag{10.5}$$

$$R_{c} = 0.17588 \pm 0.00432 \pm 0.00352. \tag{10.6}$$

Agreement with the Standard Model is clearly quite good.

It is desirable at this point to make a statement about the range of values of R_{bs} that likely include the true value, but because the true value cannot be negative, this innocently conceived objective is fraught with subtleties. Problems arise because R_{bs} is small and the uncertainty on the measurement is large by comparison. As is the case here, the result of a given experiment will often be negative – that is a necessary and natural consequence of statistical fluctuations. We can set an upper limit by excluding the region above $\mu + \delta$ where μ is the measured value and t is the true value. For an uncertainty σ, the confidence level (or probability) that the true value t will fall below $\mu + \delta$ is determined as follows: Because the true value of R_{bs} is non-negative, the physical region P and unphysical region U are defined as

$$P \quad = \quad \frac{1}{\sqrt{2\pi}\sigma} \int_0^\infty e^{-\frac{(t-\mu)^2}{2\sigma^2}} dt \qquad (10.7)$$

$$U \quad = \quad \frac{1}{\sqrt{2\pi}\sigma} \int_{-\infty}^0 e^{-\frac{(t-\mu)^2}{2\sigma^2}} dt = 1 - P. \qquad (10.8)$$

We wish to scale the physical region P by the desired confidence level (see illustration in Figure 95), and then determine the corresponding δ:

$$\text{Confidence Level} \times P + U \quad = \quad \frac{1}{\sqrt{2\pi}\sigma} \int_{-\infty}^{\mu+\delta} e^{-\frac{(t-\mu)^2}{2\sigma^2}} dt. \qquad (10.9)$$

There are tables based on equation 10.9 for looking up the corresponding value of δ (see for example the CRC Standard Mathematical Tables [102]). Adding the statistical and systematic uncertainties in quadrature, the measurement presented here is $R_{bs} = -0.171\sigma$ and corresponds to a physical region $P = 0.4325$. A 90% confidence limit corresponds to $\delta = 1.71\sigma$; a 95% confidence level limit corresponds
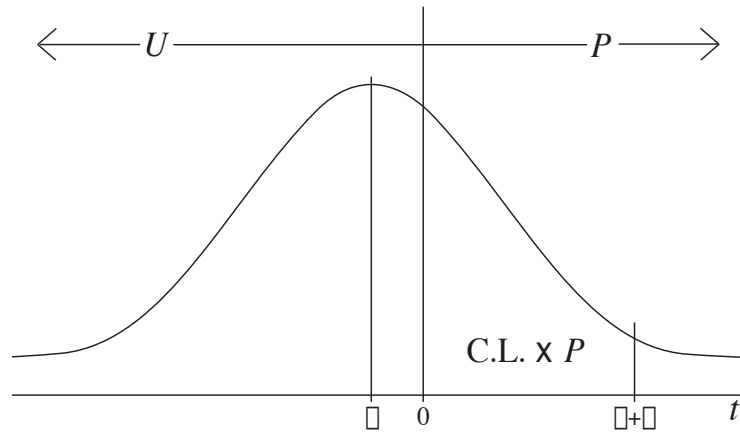
FIGURE 95. Illustration of a Gaussian showing the physical and unphysical regions P and U respectively. Only the physical region is scaled by the desired confidence level, C.L., in the determination of δ in the upper limit $\mu + \delta$.

to $\delta = 2.02\sigma$. Upper limits on R_{bs} at the 90% and 95% confidence levels are

$$90\% \text{ Confidence Level Upper Limit: } R_{bs} \;<\; 0.00153 \qquad (10.10)$$

$$95\% \text{ Confidence Level Upper Limit: } R_{bs} \;<\; 0.00184. \qquad (10.11)$$

An upper limit on R_{bs} may also be determined using the method suggested by Feldman and Cousins [103] for Gaussian errors with a bounded physical region and yields for the upper limits at the 90% and 95% confidence levels

$$90\% \text{ Confidence Level Upper Limit: } R_{bs} \;<\; 0.00147 \qquad (10.12)$$

$$95\% \text{ Confidence Level Upper Limit: } R_{bs} \;<\; 0.00179. \qquad (10.13)$$

The limits resulting from the two different methods are negligibly different, and in any case are consistent with the Standard Model.

To this author's knowledge, this is the only existing measurement of R_{bs} at the Z^0 resonance. However, two of the LEP experiments, DELPHI and L3, have made measurements of R_{bq} where $q = d, s$ at the Z^0 [104]:

$$\text{DELPHI: } R_{bq} = 0.00013 \pm 0.00061 \pm 0.00055 \tag{10.14}$$

$$\text{L3: } R_{bq} = -0.0008 \pm 0.0015 \pm 0.0032. \tag{10.15}$$

A combined upper limit for these measurements, as reported at DPF '99 [104], is

$$\text{Combined LEP 90\% Confidence Level Upper Limit: } R_{bq} < 0.00240. \tag{10.16}$$

The results of this analysis are compared graphically with the results from the two LEP measurements in Figure 96.

The present state of R_b and R_c shows agreement between theory and experiment that goes well beyond just this analysis. Figures 97 and 98 summarize the latest results as reported by the LEP Electroweak Working Group (LEPEWWG). The results from this analysis have been added at the bottom of each plot for comparison.

The SLD experiment finished taking data in 1998, and with LEP and its four experiments having been disassembled to make room for the LHC, it seems likely that these measurements will be the last of their kind on the Z^0 resonance for some time to come. But as we reach the denouement, the Standard Model still appears to be doing just fine.
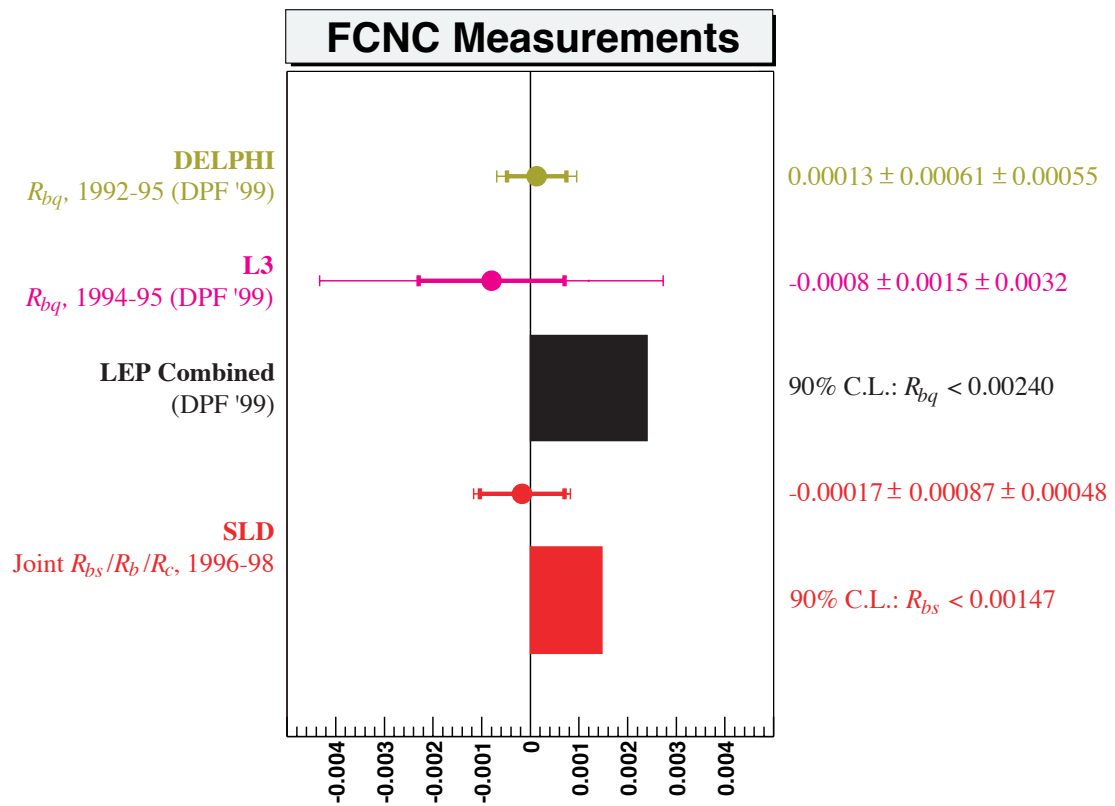
FIGURE 96. Measurements of R_{bq} and corresponding 90% confidence upper limits from LEP compared with the measurement of R_{bs} and corresponding 90% confidence upper limit from this analysis.

R_b Measurements

ALEPH Mult., 1992-95	$0.2159 \pm 0.0009 \pm 0.0011$
DELPHI Mult., 1992-95	$0.21634 \pm 0.00067 \pm 0.00060$
L3 Mult., 1994-95	$0.2174 \pm 0.0015 \pm 0.0028$
OPAL Mult., 1992-95	$0.2176 \pm 0.0011 \pm 0.0014$
SLD Vtx Mass, 1993-98	$0.21627 \pm 0.00092 \pm 0.00075$
LEP + SLD Summer 2003	0.21638 ± 0.00066
Standard Model	
SLD Joint $R_{bs}/R_b/R_c$, 1996-98	$0.21645 \pm 0.00131 \pm 0.00111$

FIGURE 97. The latest measurements of R_b.

FIGURE 98. The latest measurements of R_c.

APPENDIX

THE SLD COLLABORATION

Kenji Abe,[15] Koya Abe,[24] T. Abe,[21] I. Adam,[21] H. Akimoto,[21] D. Aston,[21] K.G. Baird,[11] C. Baltay,[30] H.R. Band,[29] T.L. Barklow,[21] J.M. Bauer,[12] G. Bellodi,[17] R. Berger,[21] G. Blaylock,[11] J.R. Bogart,[21] G.R. Bower,[21] J.E. Brau,[16] M. Breidenbach,[21] W.M. Bugg,[23] D. Burke,[21] T.H. Burnett,[28] P.N. Burrows,[17] A. Calcaterra,[8] R. Cassell,[21] A. Chou,[21] H.O. Cohn,[23] J.A. Coller,[4] M.R. Convery,[21] V. Cook,[28] R.F. Cowan,[13] G. Crawford,[21] C.J.S. Damerell,[19] M. Daoudi,[21] N. de Groot,[2] R. de Sangro,[8] D.N. Dong,[21] M. Doser,[21] R. Dubois,[21] I. Erofeeva,[14] V. Eschenburg,[12] S. Fahey,[5] D. Falciai,[8] J.P. Fernandez,[26] K. Flood,[11] R. Frey,[16] E.L. Hart,[23] K. Hasuko,[24] S.S. Hertzbach,[11] M.E. Huffer,[21] X. Huynh,[21] M. Iwasaki,[16] D.J. Jackson,[19] P. Jacques,[20] J.A. Jaros,[21] Z.Y. Jiang,[21] A.S. Johnson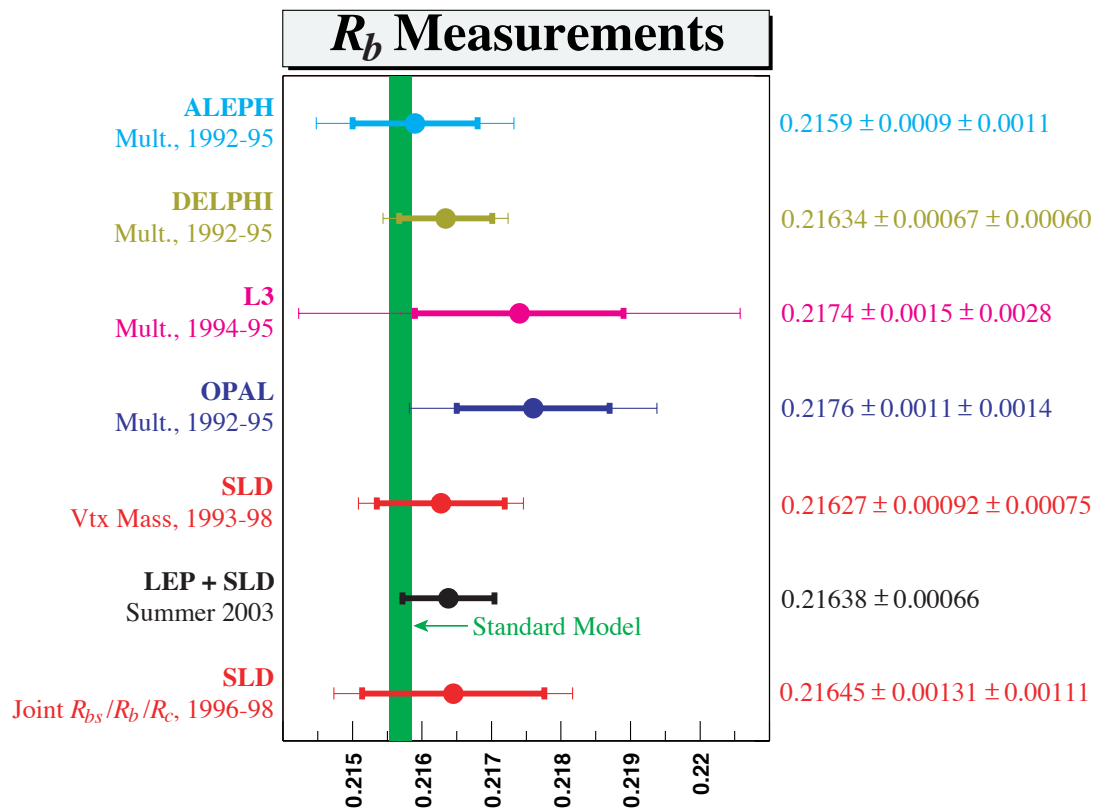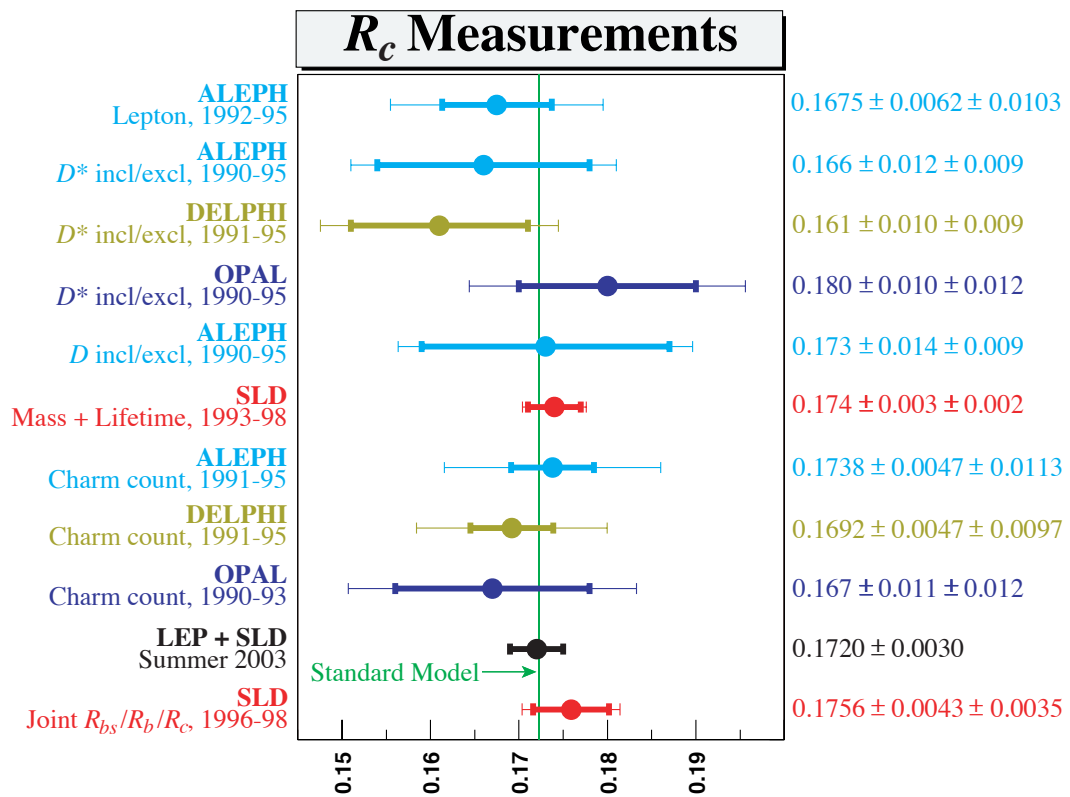,[21] J.R. Johnson,[29] R. Kajikawa,[15] M. Kalelkar,[20] H.J. Kang,[20] R.R. Kofler,[11] R.S. Kroeger,[12] M. Langston,[16] D.W.G. Leith,[21] V. Lia,[13] C. Lin,[11] G. Mancinelli,[20] S. Manly,[30] G. Mantovani,[18] T.W. Markiewicz,[21] T. Maruyama,[21] A.K. McKemey,[3] R. Messner,[21] K.C. Moffeit,[21] T.B. Moore,[30] M. Morii,[21] D. Muller,[21] V. Murzin,[14] S. Narita,[24] U. Nauenberg,[5] H. Neal,[30] G. Nesom,[17] N. Oishi,[15] D. Onoprienko,[23] L.S. Osborne,[13] R.S. Panvini,[27] C.H. Park,[22] I. Peruzzi,[8] M. Piccolo,[8] L. Piemontese,[7] R.J. Plano,[20] R. Prepost,[29] C.Y. Prescott,[21] B.N. Ratcliff,[21]

J. Reidy,[12] P.L. Reinertsen,[26] L.S. Rochester,[21] P.C. Rowson,[21] J.J. Russell,[21] O.H. Saxton,[21] T. Schalk,[26] B.A. Schumm,[26] J. Schwiening,[21] V.V. Serbo,[21] G. Shapiro,[10] N.B. Sinev,[16] J.A. Snyder,[30] H. Staengle,[6] A. Stahl,[21] P. Stamer,[20] H. Steiner,[10] D. Su,[21] F. Suekane,[24] A. Sugiyama,[15] S. Suzuki,[15] M. Swartz,[9] F.E. Taylor,[13] J. Thom,[21] E. Torrence,[13] T. Usher,[21] J. Vavra,[21] R. Verdier,[13] D.L. Wagner,[5] A.P. Waite,[21] S. Walston,[16] A.W. Weidemann,[23] E.R. Weiss,[28] J.S. Whitaker,[4] S.H. Williams,[21] S. Willocq,[11] R.J. Wilson,[6] W.J. Wisniewski,[21] J.L. Wittlin,[11] M. Woods,[21] T.R. Wright,[29] R.K. Yamamoto,[13] J. Yashima,[24] S.J. Yellin,[25] C.C. Young,[21] H. Yuta.[1]

(The SLD Collaboration)

[1] *Aomori University, Aomori , 030 Japan,*

[2] *University of Bristol, Bristol, United Kingdom,*

[3] *Brunel University, Uxbridge, Middlesex, UB8 3PH United Kingdom,*

[4] *Boston University, Boston, Massachusetts 02215,*

[5] *University of Colorado, Boulder, Colorado 80309,*

[6] *Colorado State University, Ft. Collins, Colorado 80523,*

[7] *INFN Sezione di Ferrara and Universita di Ferrara, I-44100 Ferrara, Italy,*

[8] *INFN Lab. Nazionali di Frascati, I-00044 Frascati, Italy,*

[9] *Johns Hopkins University, Baltimore, Maryland 21218-2686,*

[10] *Lawrence Berkeley Laboratory, University of California, Berkeley, California 94720,*

[11] *University of Massachusetts, Amherst, Massachusetts 01003,*

[12] *University of Mississippi, University, Mississippi 38677,*

[13] *Massachusetts Institute of Technology, Cambridge, Massachusetts 02139,*

[14] *Institute of Nuclear Physics, Moscow State University, 119899, Moscow Russia,*

[15] *Nagoya University, Chikusa-ku, Nagoya, 464 Japan,*

[16] *University of Oregon, Eugene, Oregon 97403,*

[17] *Oxford University, Oxford, OX1 3RH, United Kingdom,*

[18] *INFN Sezione di Perugia and Universita di Perugia, I-06100 Perugia, Italy,*

[19] *Rutherford Appleton Laboratory, Chilton, Didcot, Oxon OX11 0QX United Kingdom,*

[20] *Rutgers University, Piscataway, New Jersey 08855,*

[21] *Stanford Linear Accelerator Center, Stanford University, Stanford, California 94309,*

[22] *Soongsil University, Seoul, Korea 156-743,*

[23] *University of Tennessee, Knoxville, Tennessee 37996,*

[24] *Tohoku University, Sendai 980, Japan,*

[25] *University of California at Santa Barbara, Santa Barbara, California 93106,*

[26] *University of California at Santa Cruz, Santa Cruz, California 95064,*

[27] *Vanderbilt University, Nashville,Tennessee 37235,*

[28] *University of Washington, Seattle, Washington 98105,*

[29] *University of Wisconsin, Madison,Wisconsin 53706,*

[30] *Yale University, New Haven, Connecticut 06511.*

BIBLIOGRAPHY

[1] James Burke. *The Day the Universe Changed.* Little, Brown and Company, Boston, 1985.

[2] Timothy Ferris. *Coming of Age in the Milky Way.* Doubleday, New York, 1988.

[3] S. Peter Rosen. The march toward higher energies. *Los Alamos Science*, Number 11:146–151, Summer/Fall 1984.

[4] High Energy Physics Advisory Panel. HEPAP white paper on planning for U.S. high-energy physics. White paper, U.S. Department of Energy Office of Science, Division of High Energy Physics, Germantown, MD, October 2000. DOE/SC-0027.

[5] Richard Slansky. Lecture notes: From simple field theories to the Standard Model. *Los Alamos Science*, pages 54–71, Summer/Fall 1984.

[6] Richard Slansky, Stuart Raby, Terry Goldman, Gerry Garvey, and Necia Grant Cooper. The oscillating neutrino: An introduction to neutrino masses and mixings. *Los Alamos Science*, Number 25:28–63, 1997.

[7] Stuart Raby and Richard Slansky. Neutrino masses: How to add them to the Standard Model. *Los Alamos Science*, Number 25:64–70, 1997.

[8] Chris Quigg. *Gauge Theories of the Strong, Weak and Electromagnetic Interactions.* Benjamin-Cummings, 1983.

[9] Stuart Raby. Family mixing and the origin of mass. *Los Alamos Science*, Number 25:72–77, 1997.

[10] R. G. Hamish Robertson. Private communication.

[11] Karen Lingel, Tomasz Skwarnicki, and James G. Smith. Penguin decays of B mesons. *Annu. Rev. Nucl. Part. Sci.*, **48**:253–306, December 1998.

[12] Mikhail A. Shifman. *ITEP Lectures in Particle Physics.* World Sci., 1996.

[13] Dimitri Nanopoulous John Ellis, Mary. K. Gaillard and Serge Rudaz. The phenomenology of the next left-handed quarks. *Nucl. Phys. B*, **131**:285–307, 1977.

[14] M. Clements, C. Footman, A. Kronfeld, S. Narasimhan, and D. Photiadis. Flavor changing decays of the Z^0. *Phys. Rev. D*, **27**(3):570–578, February 1983.

[15] Particle Data Group Collaboration, K. Hagiwara, et al. Review of particle physics. *Phys. Rev. D*, **66**(1):010001, July 2002.

[16] Lincoln Wolfenstein. Parametrization of the kobayashi-maskawa matrix. *Phys. Rev. Lett.*, **51**(21):1945–1947, November 1983.

[17] SLD Collaboration, K. Abe, et al. Measurements of R_b with impact parameters and displaced vertices. *Phys. Rev. D*, **53**(3):1023–1036, February 1996.

[18] OPAL Collaboration, K. Ackerstaff, et al. An improved measurement of r(b) using a double tagging method. *Z. Phys. C*, **74**(1):1–17, March 1997.

[19] Bryan W. Lynn and Robin G. Stuart. Electroweak radiative corrections to b-quark production. *Phys. Lett. B*, **252**(4):676–682, December 1990.

[20] Particle Data Group Collaboration, H. Hikasa, et al. Review of particle properties. *Phys. Rev. D*, **45**(11), June 1992.

[21] Particle Data Group Collaboration, L. Montanet, et al. Review of particle properties. *Phys. Rev. D*, **50**(3):1173–1826, August 1994.

[22] Particle Data Group Collaboration, R. M. Barnet, et al. Review of particle physics. *Phys. Rev. D*, **54**(1):1–720, July 1996.

[23] Particle Data Group Collaboration, C. Caso, et al. Review of particle physics. *Eur. Phys. J. C*, **3**(1-4):1–794, 1998.

[24] Particle Data Group Collaboration, D. E. Groom, et al. Review of particle physics. *Eur. Phys. J. C*, **15**(1-4):1–878, 2000.

[25] P.S. Wells. Electroweak results from EPS-HEP 95. Cern particle physics seminar, CERN, 29 August 1995.

[26] Dong Su. Private communication.

[27] Dong Su. Vertex detectors and R_b, R_c measurements. In *SLD Collaboration Meeting*, St. Francis Yacht Club, San Fransisco, CA, 5 October 2001.

[28] Donald H. Rumsfeld. News transcript. DoD News Briefing - Secretary Rumsfeld and Gen. Myers, February 12, 2002.

[29] J. Hewett. New physics in b decays at SLD. In *Notes from the SLD Collaboration Meeting held at Chateau La Cresta*, Saratoga, CA, 10-12 February 1998. SLAC-WP-009.

[30] J. L. Hewett, S. Nandi, and T. G. Rizzo. $B \to \mu^+\mu^-$ in the two-Higgs doublet model. *Phys. Rev. D*, **39**(1):250–256, 1989.

[31] David Atwood, Laura Reina, and Amarjit Soni. Phenomenology of two Higgs doublet models with flavor changing neutral currents. *Phys. Rev. D*, **55**(5):3156–3176, March 1997.

[32] Biswarup Mukhopadhyaya and Amitava Raychaudhuri. Can flavor-changing Z decay provide a test for supersymmetry? *Phys. Rev. D*, **39**(1):280–286, January 1989.

[33] N. G. Deshpande. Private communication.

[34] Decio Cocolicchio and Michael Dittmar. The radiative and hadronic flavor changing decays of the Z. CERN-TH-5753-90, April 1990.

[35] Anjan S. Joshipura. Flavor changing neutral currents and seesaw masses for quarks. *Phys. Rev. D*, **39**(3):878–887, February 1989.

[36] N. G. Deshpande and Dilip Kumar Ghosh. Flavor and CP violating Z exchange and the rate asymmetry in $B \to \phi K_S$. hep-ph/0311332, November 2003.

[37] Stephen F. King. Dynamical electroweak symmetry breaking. *Rep. Prog. Phys.*, **58**:263–309, March 1995.

[38] Markus A. Luty, John Terning, and Aaron K. Grant. Electroweak symmetry breaking by strong supersymmetric dynamics at the TeV scale. *Phys. Rev. D*, **63**:075001, 2001. hep-ph/0006224.

[39] Nan Phinney. The SLC. In *SLD Collaboration Meeting*, St. Francis Yacht Club, San Fransisco CA, 5 October 2001.

[40] K. T. Pitts. *Electroweak Coupling Measurements from Polarized Bhabha Scattering at the Z^0 Resonance*. Dissertation, University of Oregon, Eugene OR, 1994.

[41] Matthew D. Langston. *A Measurement of the Effective Electron Neutral Current Coupling Parameters from Polarized Bhabha Scattering at the Z^0 Resonance*. Dissertation, University of Oregon, Eugene OR, 2003.

[42] S. C. Berridge et al. The small angle electromagnetic calorimeter at SLD: A $2m^2$ application of silicon detector diodes. *IEEE Trans. Nucl. Sci.*, **36**:339–343, 1989.

[43] S.C. Berridge et al. Beam test of the SLD silicon-tungsten luminosity monitor. *IEEE Trans. Nucl. Sci.*, **37**:1191–1199, 1990.

[44] S. C. Berridge et al. First results from the SLD silicon calorimeters. *IEEE Trans. Nucl. Sci.*, **39**:1242–1248, 1992.

[45] SLD Collaboration, K. Abe, et al. Design and performance of the SLD vertex detector, a 307 mpixel tracking system. *Nucl. Instrum. Meth.*, **A400**:287–343, 1997.

[46] The CCDs were manufactured by the EEV Company. Chelmsford, Essex, United Kingdom.

[47] David J. Jackson, Dong Su, and Fred J. Wickens. Internal alignment of the SLD vertex detector using a matrix singular value decomposition technique. *Nucl. Instrum. Meth.*, **A491**:351–365, 2002. SLAC-PUB-9092.

[48] Toshinori Abe. Current performance of the SLD VXD3. *Nucl. Instrum. Meth.*, **A447**:90–99, 2000. SLAC-PUB-8239.

[49] M. J. Fero et al. Performance of the SLD central drift chamber. *Nucl. Instrum. Meth.*, **A367**:111–114, 1995. SLAC-PUB-6656.

[50] T. W. Markiewicz. Private communication.

[51] Glenn F. Knoll. *Radiation Detection and Measurement.* John Wiley and Sons, New York, second edition edition, 1989.

[52] Byron P. Roe. *Particle Physics at the New Milennium.* Springer, New York, 1996.

[53] SLD Collaboration. *The SLD Design Report.* Stanford Linear Accelerator Center, Stanford, CA, 1984. SLAC-R-273.

[54] SLD Collaboration, D. Muller, et al. Physics results from SLD using the CRID. *Nucl. Instrum. Meth.*, **A433**(1-2):314–327, August 1999. SLAC-PUB-8046.

[55] S. Gonzalez. *A Calorimetric Measurement of the Strong Coupling Constant in Electron-Positron Annihilation at a Center-of-Mass Energy of 91.6 GeV.* Dissertation, Massachusetts Institute of Technology, Cambridge, MA, 1994. SLAC-R-439.

[56] C. W. Fabjan, W. Struczinzki, W. J. Willis, C Kourkoumelis, A. J. Lankford, and P. Rehak. Hadron cascades in iron and uranium. *Phys. Lett. B*, **60**(1):105–108, December 1975.

[57] James. E. Brau and Tony A. Gabriel. Theoretical studies of hadronic calorimetry for high luminosity, high energy colliders. *Nucl. Instrum. Meth.*, **A279**(1,2):40–56, July 1989.

[58] James. E. Brau and Tony A. Gabriel. Monte Carlo studies of uranium calorimetry. *Nucl. Instrum. Meth.*, **A238**(2,3):489–495, August 1985.

[59] Torbjörn Sjöstrand. High-energy-physics event generation with PYTHIA 5.7 and JETSET 7.4. *Comput. Phys. Commun.*, **82**(1):74–89, August 1994.

[60] Torbjörn Sjöstrand, Leif Lönnblad, and Stephen Mrenna. *PYTHIA 6.2 Physics and Manual*, August 2001. http://www.thep.lu.se/ torbjorn/Pythia.html.

[61] P. Burrows and H. Masuda. An optimised QCD parameter set for the JETSET 7.4 Monte Carlo program. SLD Physics Note 36, Stanford Linear Accelerator Center, Stanford, CA, 10 May 1995.

[62] C. Peterson, D. Schlatter, I. Schmitt, and P. M. Zerwas. Scaling violations in inclusive e^+e^- annihilation spectra. *Phys. Rev. D*, **27**(1):105–111, January 1983.

[63] CLEO Collaboration. *QQ - the CLEO event generator*. http://www.lns.cornell.edu/public/CLEO/soft/QQ.

[64] CLEO Collaboration, B. Barish, et al. Measurement of the B semileptonic branching fraction with lepton tags. *Phys. Rev. Lett.*, **76**(10):1570–1574, March 1996.

[65] Nathan Isgur, Daryl Scora, Benjamin Grinstein, and Mark B. Wise. Semileptonic B and D decays in the quark model. *Phys. Rev. D*, **39**(3):799–818, February 1989.

[66] Application Software Group, Computing and Networks Division. *GEANT Detector Description and Simulation Tool*. CERN.

[67] Torbjörn Sjöstrand. Special thanks for his valuable assistance.

[68] W. K. H. Panofsky and M. Breidenbach. Accelerators and detectors. *Rev. Mod. Phys.*, **71**(2):S121–S132, March 1999.

[69] M. Tigner. Possible apparatus for electron clashing beam experiments. *Il Nuovo Cimento*, **37**(3):1228–1231, June 1965.

[70] Nan Phinney. Lessons learned from the SLC. In *Proceedings of the Symposium on Electron Linear Accelerators in Honor of Richard B. Neals 80th Birthday*, 1997. SLAC-R-526.

[71] Roger Erickson, editor. *SLC Design Handbook*, Stanford, CA, December 1984. Stanford Linear Accelerator Center.

[72] J. Kent et al. Precision measurement of the SLC beam energy. In *IEEE Particle Accelerator Conference*, Chicago, IL, 20-23 March 1989. IEEE. SLAC-PUB-4922.

[73] P. C. Rowson et al. Calibration of the WISRD spectrometer with a Z peak scan. SLD Note 264, Stanford Linear Accelerator Center, Stanford, CA, 6 July 2000.

[74] D. C. Carey. *The Optics of Charged Particle Beams*, volume **6** of *Accelerators and Storage Rings*. Harwood Academic Publishers GmbH, Chur, Switzerland, 1992.

[75] P. Raimondi et al. New techniques for emittance tuning in the SLC. In *XIX International Linear Accelerator Conference*, Chicago, IL, 23-28 August 1998.

[76] P. Raimondi et al. Luminosity upgrades for the SLC. In *Particle Accelerator Conference (PAC99)*, New York, 29 Mar - 2 Apr 1999. IEEE. SLAC-PUB-8042.

[77] Draft version of the damping ring chapter of the entire SLC performance summary, 1 May 1999. http://www.slac.stanford.edu/grp/ad/addr/home.html.

[78] R. Assmann et al. SLC – the end game. In *Seventh European Particle Accelerator Conference, EPAC 2000*, Austria Center Vienna (AVC), Vienna, Austria, 26 to 30 June 2000. Institute of High Energy Physics of the Austrian Academy of Sciences.

[79] V. Balakin, A. Novakhatsky, and V. Smirnov. Transverse beam dynamics. In *Proceedings of the 12th International Conference of High-Energy Accelerators (HEAC83)*, Batavia, IL, 1983. Fermilab.

[80] SLACspeak: Glossary of SLAC-related and HEP-related acronyms and terms. http://www.slac.stanford.edu/spires/slacspeak/.

[81] Nan Phinney. Private communication.

[82] J. J. Russell. Private communication.

[83] P. N. Burrows, H. Park, K. T. Pitts, and J. M. Yamartino. Estimate of combined triggering and selection efficiency for hadronic events. SLD Note 229, Stanford Linear Accelerator Center, Stanford, CA, 13 January 1993.

[84] J. M. Yamartino. Hadronic event selection using the lac. SLD Physics Note 14, Stanford Linear Accelerator Center, Stanford, CA, 11 April 1992.

[85] Jeffrey D. Richman. Heavy quark physics and CP violation. In R. Gupta, A Morel, E. de Rafael, and F. David, editors, *Probing the Standard Model of Particle Interactions*, Les Houches, Session LXVIII, New York, 1997. Elsevier.

[86] E. Presley. Private communication.

[87] B. Denby. Neural networks in high energy physics: A ten year perspective. *Comput. Phys. Commun.*, **119**:219–231, 1999.

[88] Andreas Zell, , et al. *SNNS, Stuttgart Neural Network Simulator User Manual, Version 4.2*. University of Stuttgart Institute for Parallel and Distributed High Performance Systems and University of Tübingen Wilhelm-Schickard-Institute for Computer Science, Stuttgart, Germany, 1998. http://www-ra.informatik.uni-tubingen.de/SNNS/.

[89] Thomas R. Wright. *Parity Violation in decays of Z^0 Bosons into Heavy Quarks at SLD*. Dissertation, University of Wisconsin-Madison, Madison, WI, 2002. SLAC-R-602.

[90] David J. Jackson. A topological vertex reconstruction algorithm for hadronic jets. *Nucl. Instrum. Meth.*, **A388**:247–253, 1997. SLAC-PUB-7215.

[91] SLD Collaboration, K. Abe, et al. Measurement of leading particle effects in decays of Z^0 bosons into light flavors. *Phys. Rev. Lett.*, **78**:3442–3446, 1997.

[92] Hermann Stängle. *Measurement of the $Z^0 \rightarrow s\bar{s}$ Coupling at SLD*. Dissertation, Colorado State University, Fort Collins, CO, 1999. SLAC-R-549.

[93] Tomas Josef Pavel. *Measurement of Charged Hadron Spectra at the Z^0 with Cherenkov Ring Imaging*. Dissertation, Stanford University, Stanford, CA, 1996.

[94] Kenneth G. Baird. *Strange Particle Production in Hadronic Z^0 Decays at SLD.* Dissertation, Rutgers University, Piscataway, NJ, 1997. SLAC-R-483.

[95] SLD Collaboration, K. Abe, et al. Obtaining physics results from the SLD CRID. *Nucl. Instrum. Meth.*, **A371**:195–199, 1996.

[96] D. Abbaneo et al. Final input parameters for the LEP/SLD heavy flavor analyses. SLD Physics Note 270, LEP/SLD Heavy Flavor Working Group, Summer 2001.

[97] D. Abbaneo et al. Presentation of LEP electroweak heavy flavor results for summer 1996 conferences. Technical Report LEPHF/96-01, LEP Electroweak Working Group, Summer 1996.

[98] Glen Cowan. *Statistical Data Analysis.* Oxford University Press, Oxford, 1998.

[99] A. Brandenburg, P. N. Burrows, D. Muller, N. Oishi, and P. Uwer. Measurement of the running b-quark mass using $e^+e^- \rightarrow b\bar{b}g$ events. *Phys. Lett. B*, **468**:168–177, 1999. SLAC-PUB-7915.

[100] Arnd Brandenburg. Private communication.

[101] Richard P. Feynman. *The Meaning of it All*, chapter I, The Uncertainty of Science, pages 15–16. Addison-Wesley, 1998.

[102] William H. Beyer. *CRC Standard Mathematical Tables.* CRC Press, Boca Raton, FL, 28 edition, 1987.

[103] Gary J. Feldman and Robert D. Cousins. Unified approach to the classical statistical analysis of small signals. *Phys. Rev. D*, **57**(7):3873–3889, April 1998.

[104] Fernando Martínez-Vidal. Heavy quark production at the Z. In Katsushi Arisaka and Zvi Bern, editors, *1999 Meeting of the Division of Particles and Fields of the American Physical Society (DPF '99)*, Talk 1-06, 1999. http://www.dpf99.library.ucla.edu.